Title

Understanding Planetesimal Evolution: Bulk Chemistry, Petrology, and O-Isotope Studies of the Rumuruti Chondrite Group.

Author

Isa, Junko

Publication Date

2017

Peer reviewed|Thesis/dissertation

UNIVERSITY OF CALIFORNIA

Los Angeles

Understanding Planetesimal Evolution:

Bulk Chemistry, Petrology, and O-Isotope Studies of the Rumuruti Chondrite Group.

A dissertation in partial satisfaction of the

requirements of the degree of Doctor of Philosophy

in Geochemistry

by

Junko Isa

2017

ABSTRACT OF THE DISSERTATION

Understanding Planetesimal Evolution:

Bulk Chemistry, Petrology, and O-Isotope Studies of the Rumuruti Chondrite Group.

by

Junko Isa

Doctor of Philosophy in Geochemistry

University of California, Los Angeles, 2017

Professor John T. Wasson, Co-Chair
Professor Kevin D. McKeegan, Co-Chair

This thesis presents cosmochemical discoveries coupled with improvements of analytical techniques focused on deepening our understanding of the formation of rocky planetary bodies during the early evolution of the solar system. Chondrite meteorites and their components have been utilized to study the early stages of planetary body formation since they are thought to be samples of these bodies. Previous attempts to construct a comprehensive model for planetesimal evolution that explains cosmochemical signatures have relied on the well-known chondrite groups, such as ordinary and carbonaceous chondrites, that had been studied for over a hundred years. In this thesis, I primarily focused on studies of a relatively new and unstudied meteorite group, the Rumuruti (R) chondrites. The bulk chemistry, petrology and O-isotope studies

presented in this thesis have revealed evidence that the chondrite parent object(s) are formed through chaotic accretionary processes. In addition to the studies of R chondrites detailed here, another study designed to further our understanding of the petrology of iron meteorite inclusions is presented. The main thesis findings include the following:

The quantification of oxygen isotope SIMS matrix effects in olivine samples (from Mg-rich to Fe-rich) were investigated by using the UCLA CAMECA ims 1270 and 1290 instruments in order to improve the accuracy of *in situ* O-isotope measurements in geochemical/cosmochemical olivine samples. One of the main findings was that oxygen isotope SIMS matrix effects are reproducible. With this knowledge in hand, a model curve was developed that can be used for correcting observations of instrumental mass fractionation in olivine samples of intermediate chemical composition. The model curve was calibrated by utilizing data from SIMS analysis on a San Carlos olivine, which was chosen to be the primary standard in O-isotope studies in the R chondrite chondrules.

R chondrite parent body evolutionary processes were explored by analyzing the bulk chemistry and petrology of R chondrites from petrologic types 3 to 6. I confirmed that R chondrites have a monolithic bulk composition and that R chondrites are closely related in terms of composition to ordinary chondrites. However, R-chondrite volatile abundances are much higher in comparison to those found in ordinary chondrites. And, it was found that metamorphosed R chondrites recorded different degrees of oxidation within their olivine and spinel components. These results suggest that local environment conditions on the parent asteroid were not uniform but instead were diverse.

The oxygen isotope composition of different chondrite components in one of the least equilibrated R chondrites, PRE 95404, was examined in order to investigate the apparent heterogeneity, as evidenced just above, in the parent body formation conditions. The results show that the different chondrite components present in PRE95404 experienced a variety of metamorphic processes suggesting that material from different proto bodies were incorporated into the fine grain matrix before they were finally lithified in the R parent bodies. These results conflict with the conventional ordinary chondrite accretionary model, which starts from chondrule formations followed by immediate accretion yielding the chondritic asteroids that subsequently underwent *in situ* metamorphism. Instead the thesis results support a model that the R chondrite parent body formed by accretion of pre-existing planetesimal materials. The studies presented in the thesis also clarify the relationships between the R chondrites and other chondrite groups.

Lastly, a new a mineral, $MnCr_2S_4$, was discovered during an investigation of Cr-bearing inclusions found in iron meteorites. The new mineral has been given the name Joegoldsteinite.

The dissertation of Junko Isa is approved.

Delroy A. Baugh

Edward Donald. Young

John T. Wasson, Co-Chair

Kevin D. McKeegan, Co-Chair

University of California, Los Angeles,

2017

Table of Contents

List of Figures

List of Tables

Acknowledgments

Most importantly, I am deeply obligated to my advisers John Wasson and Kevin McKeegan for their expertise, patience and supports. This PhD thesis is fundamentally supported by their commitment to my education and research. I am truly happy and fortunate to have both very different types of excellent scientists as my advisors. Thank you all the lessons. John is truly one of a legendary individual in cosmochemistry field. At the "red table", he told me about many stories. One of my favorite was "geochemists never agree each other except of a few occasions". That is, indeed true. I would like to thank John for letting me use meteorites from UCLA collection for my research. Kevin has been extremely generous, supportive and encouraging in any point of my PhD. He helped preparing me to be a scientist throughout of my PhD education. I very much enjoyed learning from someone who has great scientific insight and skills. I have learned early solar system chronology, SIMS, O-isotope in the solar system and some American humor. Also, I have learned so much through writing a paper with him.

I would like to express my gratitude to my committee members Edward Young and Delroy Baugh. Ed is always enthusiastic about discussing broad scientific problems with me. I have learned isotope-geochemistry through your class and at your lab. Ed's broad interest in isotope-geochemistry and cosmochemistry with challenging spirit inspired me and influenced to my research directions. I greatly appreciate Ed's generosity and let me join at his lab. I solved so many problems when I tried to explain to him what my problems are because Ed always gave some thoughtful comments.

I am grateful to my committee member Delroy Baugh for his time and effort. Del's comments lead me to discuss my research subjects to many people inside and outside of committee members.

I would like to make appreciation to the "fourth floor cosmochemistry group". Alan Rubin corrected and edited my English in abstracts and papers. In science, he taught me "chondrites 101" and "chondrule 101". Paul Warren gave extremely generous financial supports during my time in UCLA. Without his help, I was not able to become a PhD student. I always very much enjoyed discussing achondrite projects over the thin section images. I also learned how to make a simple curiosity turning into a scientific project. Frank Kyte helped me learning electron microprobe. With his advice to get proper standard, I was able to discover a new mineral.

I would like to thank Johanna Marin-Carbonne, Rita Economos, and Ming-Chang Liu for helping and training me for using the ion microprobes. Thank you for maintaining instruments and the lab in good conditions.

I also would like to thank UCLA colleagues, Issaku Kohl and Rosario Esposito. You two are such a great mentor! They showed me what kind of attitude is required to obtain good data, for example.

I would like to thank Chi Ma for wonderful collaboration and helping me using EBSD and discovering a new mineral. I thank V. Tsurkan for providing a synthesized $FeCr_2S_4$ crystal that greatly facilitated analysis of the new mineral by EPMA. I am also thankful to members of a group at the UCI research reactor. Thank you for safely operating the reactor and providing an opportunity to use it for scientific research purpose.

Here I would like to list of all collaboration works in this thesis. I thank to my colleagues for their wonderful collaboration.

Chapter 3 is a version of the manuscript that has been accepted for publication: Isa et al. (2017): J. Isa, I.E. Kohl, M.-C. Liu, J.T. Wasson, E.D. Young, K.D. McKeegan, Quantification of oxygen isotope SIMS matrix effects in olivine samples: Correlation with sputter rate, *Chemical Geology*, (2017). DOI: 10.1016/j.chemgeo.2017.03.020. I thank my co-authors Issaku Kohl, Ming-Chang Liu, John Wasson, Edward Young and Kevin McKeegan.

Chapter 4 is a version of the paper by Isa et al. (2014), which is already in publication: Isa, J., Rubin, A. E., and Wasson, J. T. R-chondrite bulk-chemical compositions and diverse oxides: Implications for parent-body processes. *Geochimica et Cosmochimica Acta*, (2014) *124*, 131-151, DOI:10.1016/j.gca.2013.09.018. I thank my co-authors Alan Rubin and John Wasson.

Chapter 6 is a version of Isa et al. (2016): Isa, J., Ma, C., and Rubin, A. E. (2016). Joegoldsteinite: A new sulfide mineral ($MnCr_2S_4$) from the Social Circle IVA iron meteorite. *American Mineralogist*, (2016) *101*(5), 1217-1221. DOI: 10.2138/am-2016-5594. I wish to thank Chi Ma and Alan Rubin as co-authors on the paper.

I appreciate all who have helped me to finish the thesis and to prepare me as a scientist. It is impossible to list them all here.

I also thank to my undergraduate and masters advisor Mitsuru Ebihara in Tokyo for asking me if I would be interested in working at Professor Wasson's laboratory at UCLA. It was an unexpected suggestion and I am very appreciating the doors that were opened by his suggestion.

Lee Bargatze has been my strongest and the closest supporter throughout my Ph.D. I would like to thank Lee for all his love and encouragement. I am glad that I met you. It would not be possible for me to finish this thesis without so much help and encouragement from my friends and colleagues. During my time at UCLA, I have had a lot of fun and many precious times. I am particularly grateful to Mojhgan Haghnegahdar, Patrick Boehnke, Katie Dyl, Haolan Tang, and Robert Steele.

I am thankful to my sisters, Naoko Suzuki and Yuko Isa. You two are responsible of my multifaceted perspective towards problem solving. Thank you for supporting my family while I am so far away pursuing my dream. Finally, I thank to my mother, Reiko Isa. I truly appreciate that you let me be whatever I wanted to be. I cannot imagine how many things you had to undergo while raising me and letting me go abroad for my higher education.

VITA

Junko Isa

Education

2013 **Master of Science,** Geochemistry, University of California Los Angeles, Los Angeles, CA, USA.

2009 **Master of Science,** Chemistry, Tokyo Metropolitan University, Tokyo, Japan.

2007 **Bachelor of Science,** Chemistry, Tokyo Metropolitan University, Tokyo, Japan.

Other Education Experience

2016 Special Student, Division of Geology and Planetary Sciences, California Institute of Technology

2007 STINT (The Swedish Foundation for International Cooperation in Research and Higher Education) Summer School on Nanoparticles in Interactive Environments, at the University of Gothenburg, Sweden.

Professional Experience

2011-2017 **Graduate Student Researcher,** UCLA, Dept. of Earth Planetary and Space Sciences, UCLA.

2009-2011 **Staff Research Associate** (full time), UCLA
- INAA of meteorite samples for cosmochemical survey

Teaching Experience

Teaching Assistant
- UCLA, EPSS 15 Blue Planet: Introduction to Oceanography (2016, 2015, and 2014)
- UCLA, EPSS 51 Mineralogy (2016)
- UCLA, EPSS C107/C207 Geochemistry (2014)

High School Science Teaching License granted by Minister of Education, Culture, Sports, Science and Technology in Japan (2007)

Middle School Science Teaching License granted by Minister of Education, Culture, Sports, Science and Technology in Japan (2007)

Peer-Reviewed Publications

Warren, P.H., Isa, J., Ebihara, M., Yamaguchi, A., Baecker, B., (2017). Secondary-volatiles linked metallic iron in eucrites: the dual-origin metals of Camel Donga. *Meteoritics & Planetary Science.*

Isa, J., Ma, C., Rubin, A., (2016). Joegoldsteinite: A new sulfide mineral (MnCr2S4) from the Social Circle IVA iron meteorite. *American Mineralogist*, *101*(5), 1217-1221.

Rubin, A.E., Breen, J.P., Isa, J., Tutorow, S. (2016). NWA 10214–An LL3 chondrite breccia with an assortment of metamorphosed, shocked, and unique chondrite clasts. *Meteoritics & Planetary Science*, *52*, 372–390.

Warren, P.H., Rubin, A.E., Isa, J., Gessler, N., Ahn, I., Choi, B.G., (2014). Northwest Africa 5738: Multistage fluid-driven secondary alteration in an extraordinarily evolved eucrite. *Geochimica et Cosmochimica Acta*, *141*, 199-227.

Isa, J., Rubin, A.E., Wasson, J.T., (2014) R-chondrite bulk-chemical compositions and diverse oxides: Implications for parent-body processes. *Geochimica et Cosmochimica Acta*, *124*, 131–151.

Warren, P.H., Rubin, A.E., Isa, J., Brittenham, S., Ahn, I., Choi, B.-G., (2013). Northwest Africa 6693: A new type of FeO-rich, low-$\Delta^{17}O$, poikilitic cumulate achondrite. *Geochimica et Cosmochimica Acta*, *107*, 135–154.

Wasson, J.T., Isa, J., Rubin, A.E. (2013). Compositional and petrographic similarities of CV and CK chondrites: A single group with variations in textures and volatile concentrations attributable to impact heating, crushing and oxidation. *Geochimica et Cosmochimica Acta*, *108*, 45–62.

Peer-Reviewed Manuscripts Accepted

Isa, J., Kohl, I.E., Liu, M.-C., Wasson, J.T., Young, E.D., McKeegan K.D., (2017). Quantification of oxygen isotope SIMS matrix effects in olivine samples: correlation with sputter rate. *Chemical Geology*.

Manuscripts in Preparation

Isa, J., Rubin, A.E., Marin-Carbonne, J., McKeegan, K.D., Wasson, J.T., O-isotopic composition of R-chondrite components.

Chapter 1: Introduction

Background and Motivation

The solar system is a research subject that has fascinated humanity since antiquity. It has been at the frontier of science for thousands of years, —human interest in the development of calendars is one of the reflections—, and is still so today. The modern view of the evolution of the solar system began with the Kant-Laplace nebular hypothesis (Kant, 1755 and Laplace, 1796) in the 18th century. About the same time, meteorites began to be recognized as extraterrestrial samples by scientists such as Jean-Baptiste Biot (Gounelle, 2006). Scientific meteorite research started to bloom in the early 19th century with series of meteorite falls: l'Aigle (L6), Alais (CI), and Orgueil (CI) chondrites, and with careful chemical analyses.

One of the early debates focused on the origins of meteorites and also on differences among meteorites, and one conclusion was that Orgueil was a sample of "primitive" material in the solar system (summarized in Gounelle and Zolensky, 2014). Over the last century, with improvements in electronics and in the availability of extraterrestrial samples, in particular by the sample return missions in addition to meteorite collections, it has been to empirically study extraterrestrial materials in laboratories with high precision. Especially since 1969, the year of "the modern revolution in cosmochemistry" (MacPherson and Boss, 2011), it has become clear that solar system materials have isotopic and chemical diversity, reflecting their parent planetary body characteristics including their source composition, condition, material conveyance, and thermal and differentiation histories. It became clear that meteorites are samples from igneous planetary basalts and gabbro, planetary metallic cores, partially differentiated planetary materials, and undifferentiated components of the solar system (See **Section 1.1 Meteorite Taxonomy**). Planetary scale (bulk meteorite) stable isotope variations in the solar system had been known to

be homogeneous. However, inter-planetary isotope variations become apparent in sub-per mill to a few percent level for some elements such as oxygen.

Among the numerous research topics investigated during the last two decades, three new planetary science research results have motivated cosmochemists to re-visit and re-evaluate planetary evolution processes.

The first is the study of the oxygen isotope composition of the Sun. The isotope ratios precisely reveal a ^{16}O-rich isotopic composition on the Δ^{17}O scale equal to -25‰ that is the clearly different from that of the Earth and other inner planetary materials (McKeegan et al., 2011). Three oxygen isotope studies in cosmochemistry began finding ^{16}O-rich isotope anomalies in refractory chondritic components in a relative sense with respect to the terrestrial standards (Clayton, 1976). However, those components had become, indeed, normal in the solar system standard considering that the Sun contains ~98% of oxygen in the solar system (Davis et al., 2008). Because the Sun dominates the mass of the solar system, the initial composition of the solar system and of the protoplanetary nebular gas likely had an ^{16}O-rich isotopic composition. The fundamental origin of the O-isotope composition variation amongst planetary bodies is not yet understood. Studying the meteorite components that have the most ^{17}O- and ^{18}O-rich anomalous O-isotope components in the solar system, therefore, may provide insight concerning the origin of the O-isotope compositional variation within the different planetary bodies.

The second new set of results involves Hf-W geochronology data that revealed magmatic meteorites accreted and differentiated before chondrule formation and the subsequent occurrence of chondrite parent body formation. The results indicate that magmatic iron meteorites have low ^{182}W/^{184}W ratios with ^{182}W being a decay product of ^{182}Hf (half-life $t_{1/2}$ = 8.9 Myr) (e.g., Kleine

et al., 2009). The results were inconsistent with the traditional "standard" model for asteroid accretion, which held that chondrites are the precursors of differentiated bodies. The results of Hf-W studies shed light on to iron meteorites that had not been extensively studied as compared to chondrite and achondrite meteorites. Also, the results lead to the questioning the fundamental concept of "primordial" rocks in cosmochemistry and increased community interest in the study of the late stage of accretion when chondrites finally formed.

The third set of new results was derived by the study of material from sample return missions from an asteroid and a comet. The Hayabusa mission confirmed that the spectroscopically identified S-type asteroid 25143 Itokawa assumed to be LL chondrite compositions was indeed an equilibrated LL4-6 chondrite via chemical analyses in laboratories (Nakamura, 2011). Chemical analyses of solid material returned by the Stardust mission to comet Wild 2 showed that the mineralogical chemistry and isotope composition variation of the samples overlapped with that of meteorites; i.e., asteroids, and interplanetary dust particles (IDPs), and yet the components are somehow more diverse (e.g., Snead, 2016). The asteroid-comet continuum is consistent with the observation of active asteroids (Hsieh and Jewitt, 2006). The diversity in cometary materials motivated to further look and pay attention to the degree of diversities themselves in chondrites attribute to conveyance/mixing during the formation of asteroids.

Finally, in addition to the current cosmochemistry research results, the rapid increase of interests into astrobiology in the planetary science community motivates, in part, the studies in this thesis focused on chondritic meteorite groups that can put constraints that are relevant to future astrobiology studies. As it has been known since 19th century, meteorites contain organic matter and some has been found in carbonaceous chondrites such as complex compounds similar to kerogen (Kwok, 2016). The implications on astrobiology studies are clear.

1.1 Meteorite Taxonomy

Meteorites are traditionally defined as "solid objects that have fallen to Earth from space" and an extended definition of meteorites is found in Rubin and Grossman (2010). The majority of meteorites appear to originate from asteroids that are remnants of solar system formation and planetary accretion processes. The study of meteorites started with taxonomy (e.g. Grewingk and Schmidt, 1864; Prior, 1916). The nature of meteorites as rocks was separated from the geological context. Individual chondrite groups are thought to have each originated from a single asteroid that had been broken into pieces by impact events. Therefore, in order to reassemble the pieces and their individual geological context, meteorite taxonomy is rather crucial in the field of cosmochemistry. From the meteorite classification scheme, we hope to reveal genetic relationships between meteorite groups and to understand their sources and the processes that took place on their parent bodies. Meteorites are classified into two major categories: chondrites (Figure 1-1) and non-chondritic (Figure 1-2) meteorites based on their bulk compositions and textures.

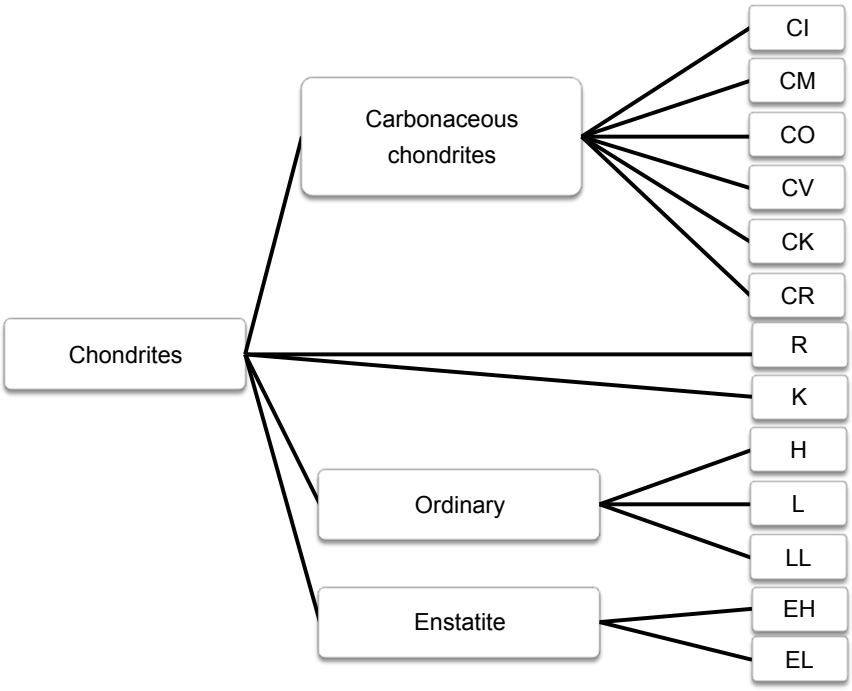

Figure 1-1. Classification of chondrites excluding ungrouped meteorites.

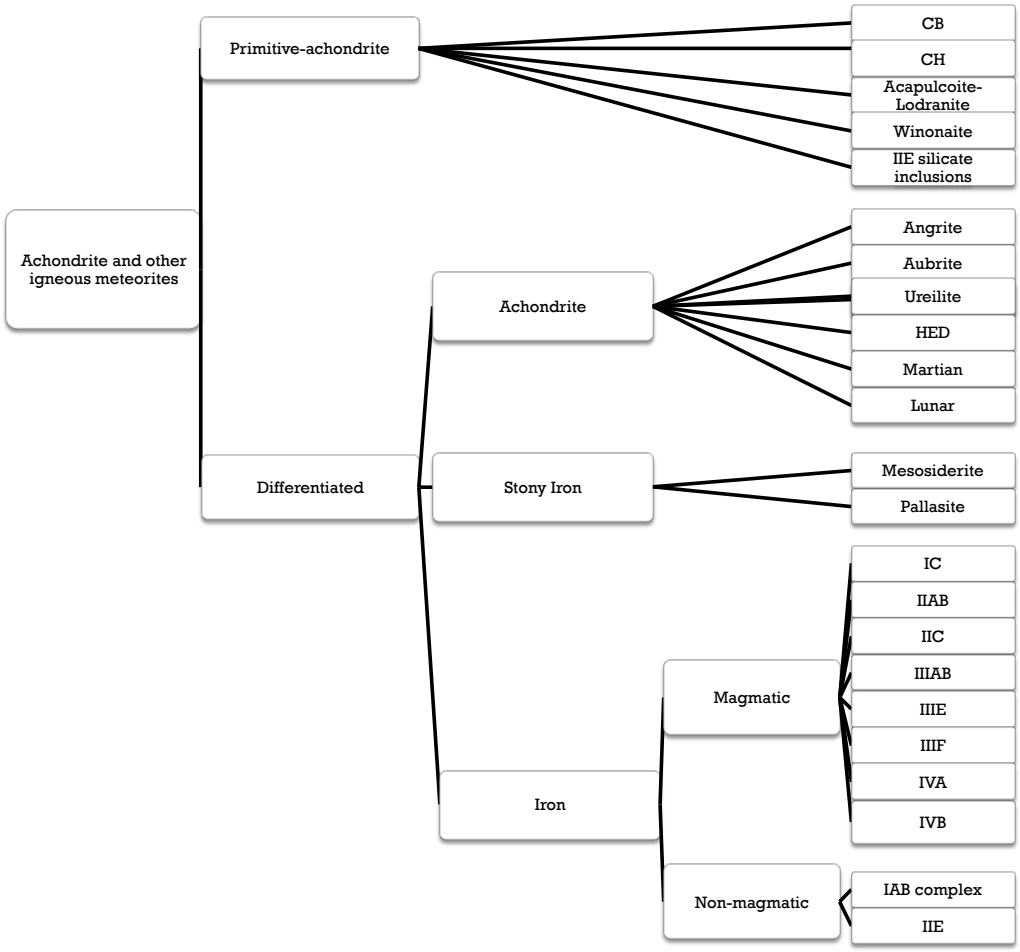

Figure 1-2. Classification of meteorites excluding major chondrites and ungrouped meteorites.

Chondrites represent undifferentiated components of the solar system that are excellent samples of various components that have existed since the early stages of solar nebula formation. For instance, Calcium and Aluminum-rich Inclusion (CAIs) are the oldest yet dated material that formed in the solar system (Gray et al., 1973). Other examples include volatile-rich, fine-grain matrix material, pre-solar grains, and other igneous components including chondrules.

Primitive achondrites have undergone small degrees of partial melting events that did not result in complete differentiation and they often contain metal and silicates that retain their chondritic composition. Igneous silicate meteorites and achondrites appear to have originated from several differentiated planetary bodies. They consist of either basalt or gabbro with compositions that are similar with that of terrestrial cognates but they have different elemental and isotopic ratios. The origin of achondrites is thought to include a range of objects from large planetary bodies to small yet differentiated planetary bodies. Magmatic iron meteorites represent samples from proto-planetary metallic cores. The parent bodies of stony iron meteorites also must be differentiated.

The chondrites span a range of several taxonomic categories: carbonaceous (C) chondrite groups, ordinary (O) chondrite groups, enstatite (E) chondrite groups, and Rumuruti (R) chondrite groups. In addition to these categories, there are also relatively rare chondrites that fall into other taxonomic groups. Chondrite groups are further classified into subgroups and petrologic types based on their degree of thermal and aqueous metamorphism (see Fig 1-3) (Van Schmus and Wood, 1967).

Figure 1-3. The chondrite petrologic types for most of chondrite groups.

Type 3 chondrites are also called "unequilibrated" chondrites and the type 3 chondrites have the experienced least amount of metamorphism on their parent body. The sequence of type 3 to type 6 represents the degree of thermal metamorphism. Their chemical compositions become more uniform and the mineral texture becomes more re-crystalized in higher petrologic type. The sequence of type 3 to 1 represents the degree of aqueous alterations applied to some carbonaceous chondrites. However, this scheme does not work for several chondrites. For example, R chondrites have experienced aqueous alterations and thermal alterations. Nevertheless, this petrological scheme has been used for all chondrite groups including R chondrites.

Mass-independent stable isotopic variations are also useful classification tools. Across the meteorite groups, regardless of differentiation or non-differentiation, it became clear that the solar system rocky materials are classified by composition as either similar to carbonaceous chondrites or of other composition (see Figure 6 in Warren, 2011). The speculation is that the bimodality clustering of composition can be explained by the formation location of carbonaceous chondrites in the outer solar system while non-carbonaceous chondrites originate in the inner solar system (e.g., Walsh et al., 2011). And then, a question arises, what is the connection between the two? The connection could be found in the materials sit between the two.

1.2 Previous Studies of Rumuruti Chondrites

Rumuruti chondrite groups represent the end member or extreme among the current chondrite collections in some respects (as summarized in a review by (Bischoff et al., 2011)). R chondrites share some properties both with ordinary chondrites (OC) and with carbonaceous chondrites (CC).

R chondrites (along with CK carbonaceous chondrites) constitute one of the two most oxidized chondrite groups. The R group has been studied for more than 20 years (Bischoff et al., 1994, 2011; Greenwood et al., 2000; Isa et al., 2014; Kallemeyn et al., 1996; Khan et al., 2015; Lingemann et al., 2000; Righter et al., 2016; Righter and Neff, 2007; Rubin, 2014; Rubin and Kallemeyn, 1989; Schulze et al., 1994; Weisberg et al., 1991). R chondrites are characterized by low chondrule/matrix modal abundance ratios (0.9 in unbrecciated Carlisle Lakes), moderate chondrule sizes (~400 μm), abundant sulfides (typically 6-10 wt. % pyrrhotite and pentlandite), high $\Delta^{17}O$ values (~2.9‰), rare refractory inclusions (~0.04 vol. %). The majority of R chondrites are breccias (Bischoff et al., 2011); however, relatively non-disturbed $^{40}Ar/^{39}Ar$ ages of 4.34–4.38 Ga in amphibole-bearing equilibrated R chondrites have been reported (Righter et al., 2016). R chondrites also contain amino acids that were known to exist in other carbonaceous chondrites (Burton et al., 2015). The hydrogen isotope ratio in amphiboles from one R6 chondrite (LAP 04840) shows an extremely heavy δD value equal to about +3700 ‰ (c.f. ~+2400‰ in the highest D/H ratio in the Jupiter family comet 67P/CG; Altwegg et al., 2014).

The R chondrites have high $\Delta^{17}O$ values and their proportions of chondrule textural types are similar to the properties of ordinary chondrites; in contrast, their high matrix abundance resembles that of carbonaceous chondrite. Magnesium- and CI-normalized refractory lithophile

abundances in R chondrites (~0.97) are similar to those in OC; refractory and common siderophile abundances are at CI levels; and volatiles (especially Se and Zn) are significantly enriched relative to OC (Kallemeyn et al., 1996). The mean bulk R-chondrite $\Delta^{17}O$ value of ~3‰ is the highest among chondrite groups and the most anomalous ^{16}O-poor oxygen isotope composition across planetary materials as compared to that of the Sun. Most R whole rocks have similar $\Delta^{17}O$ values. The O-isotopic compositions of chondrules scatter around a mass-fractionation line with $\Delta^{17}O$ = ~3‰; however, chondrules from Carlisle Lakes and PCA 91241 plot close to the OC region: $\Delta^{17}O$ = 0.68‰ (Weisberg et al., 1991); and -0.4 to 0.7‰ (Greenwood et al., 2000), respectively. Similarities in O-isotope compositions between magnetite in R3.8 PCA 91241 and LL3.0 Semarkona imply that these oxides formed in both chondrites by alteration of metallic Fe by high-$\Delta^{17}O$ water (Choi et al., 1998; Greenwood et al., 2000). Most individual olivine and pyroxene grains in R chondrites plot near an R-chondrite mass-fractionation-line (RFL), defining the intercept ($\Delta^{17}O$ = ~3‰), or in the region of unequilibrated ordinary chondrites (UOC) (Greenwood et al., 2000). A few refractory forsterite grains in DAG 013 have low $\Delta^{17}O$ values of ~-3‰ (Pack et al., 2004). Most individual minerals in most R-chondrite CAIs plot along a slope-1 line and have lower $\Delta^{17}O$ values, ~-23 to -26‰ (Rout et al., 2009).

Previous hypotheses concerning R-chondrule formation held that their precursors had OC-chondrule O-isotopic compositions that later acquired higher $\Delta^{17}O$ values by reaction with nebular gas (Weisberg et al., 1991) or water derived from parent body fluids associated with the matrix (Greenwood et al., 2000).

Despite their accuracy, bulk R-chondrule O-isotope data are not ideal for testing these hypotheses because they lose the specific information as many chondrule mesostases were

altered by Δ^{17}O-rich parent-body fluids. It is more instructive to approximate the original O-isotopic compositions of R-chondrule precursors by using *in situ* analyses of relict olivine phenocrysts in minimally altered R chondrules. In Chapter 4 of this thesis, I analyzed the chemical compositions and performed petrologic observations of R chondrites. And in chapter 5 of this thesis, I studied O-isotopes in the one of the least metamorphosed R chondrites to test these hypotheses.

1.3 Magmatic Iron Meteorites and their Inclusions

Magmatic iron meteorites are the best samples for examining the diversity of extensively melted and homogenized planetary materials. Given that direct sampling of the cores of planetary bodies is not possible, one can turn instead to iron meteorites as a valuable proxy as they are readily accessible and are certainly relevant in the context of planetary building blocks.

Iron meteorites are more resistant to destruction than stony meteorites in space. Their long exposure ages and multistep exposure histories prove their toughness. And, there are far fewer differentiated stony and stony-iron groups than there are iron meteorite groups. Iron meteorites seem to represent at least 26 distinct fully-differentiated parent bodies based on their chemical compositions (Wasson, 2013); the number of asteroids responsible for the formation of non-magmatic irons is more difficult to assess but probably similar. Therefore, there is a good chance that iron meteorites provide samples from a large fractions of planetary bodies that underwent core formation. These samples can provide insight into individual body sizes, crystallization histories, and event timings that will help put constraints on models of planetary formation.

Although magmatic iron meteorites mainly consist of Fe-Ni alloys, some sulfide, phosphide, graphite, nitride and silicate inclusions are found in iron meteorites ranging in size from less than

one micron up to several centimeters. These inclusions contain potentially important information about their parent bodies and relationships to other meteorite groups. For example, the mineral assemblages could reveal the diversity of possible crystallization sequences of planetary cores and suitable inclusion minerals offer opportunities to determine the crystallization ages of solid metallic cores. In previous studies using the silicate inclusions, several researchers have tested relationships between iron meteorites and stony meteorites through analysis of O-isotope compositions (Clayton and Mayeda, 1996). In another study, the presence of S, P, and C in iron meteorites was shown to play an important role in controlling elemental partitioning of crystal fractionations (Wasson et al., 1999).

In Chapter 6 of this thesis, I extend upon prior research (Buchwald, 1975) by searching for Cr-bearing inclusions in IVA iron meteorites with the hope of discovering the phases that control bulk Cr concentrations and volatile abundances during fractional crystallizations. Cr is known to be one of the elements that undergo anomalous partitioning during fractional crystallization. Experimentally determined partition coefficients of Cr are very small, and yet Cr behaves as if it is compatible in bulk iron meteorites. For example, the observed bulk Cr abundance is negatively correlated with bulk Au abundances. Therefore, determining the Cr-bearing phase is important because it can mainly control the Cr concentrations in solid and liquid metal phases. In previous studies, Cr-enriched samples were explained by heterogeneity or extraction of chromite grains from metallic melts (Wasson and Richardson, 2001; Chabot et al., 2009).

1.2 Oxygen: A General Overview

Oxygen is one of the most important elements in planetary science due to its abundance, chemical properties, and variable isotope-composition. Oxygen is the third abundant elements in

the solar system, and is the most abundant element in stony meteorites, asteroids and the terrestrial planets (Anders and Ebihara, 1982; Anders and Grevesse, 1989; Lodders and Katharina, 2003) and thus oxygen is a key element in the building blocks of planets. Oxygen is reactive element and widely distributed in planetary materials so it is possible to determine the range in O-isotope compositions of planetesimals by analyzing O-isotope compositions in stony, stony-iron, and iron meteorites. To understand the evolution of the planetary objects, understanding the behavior of oxygen is necessary.

Oxygen has three stable isotopes: ^{16}O, ^{17}O, and ^{18}O. The most common isotope of oxygen is ^{16}O; this isotope is created by H and He burning. The other two oxygen isotopes, ^{17}O and ^{18}O, are secondary isotopes that can only be produced in second generation stars. Their abundances change with the chemical evolution of the Galaxy (e.g., Clayton, 1988). The terrestrial abundances of ^{16}O, ^{17}O, and ^{18}O are 99.762%, 0.038%, and 0.200%, respectively. Isotope compositions are normally expressed on a conventional normalized scale. In case of oxygen, the ratios are converted to delta-notation by normalizing to the accepted value of $^{18}O/^{16}O$ in standard mean ocean water, SMOW, yielding: $(^{18}O/^{16}O)_{SMOW} = 0.00200520$ (Baertschi, 1976) and $(^{17}O/^{16}O)_{SMOW} = 0.000383925$ (Fahey et al., 1987). The delta isotope equations list below refer to the per mil (‰) differences of the ratio with respect to a reference line:

$$\delta^{18}O = [(^{18}O/^{16}O)_{sample} / (^{18}O/^{16}O)_{SMOW} - 1] \times 1000$$

$$\delta^{17}O = [(^{17}O/^{16}O)_{sample} / (^{17}O/^{16}O)_{SMOW} - 1] \times 1000$$

In a three isotope diagram, $\delta^{17}O$ versus $\delta^{18}O$, the oxygen isotopic compositions of nearly all terrestrial samples plots on a single linear line of slope ~0.52 and is called the terrestrial

fractionation line (TFL). The "big delta" (or "capital delta") notation $\Delta^{17}O$ (*i.e.*, Clayton et al., 1991) is also commonly used and defined as:

$$\Delta^{17}O = \delta^{17}O - 0.52 \times \delta^{18}O$$

The $\Delta^{17}O$ represents the degree of deviations from a mass-independent fractionation relative to a reference oxygen reservoir. In this thesis, I refer to absolute $\Delta^{17}O$ values as mass-independent deviations from the TFL ($\Delta^{17}O=0$).

Despite its large abundance and the occurrence of its three stable isotopes, oxygen shows the most extreme mass-independent variations of any element that has at least three isotopes (see Figure 1-3, left). Most differentiated achondrites have $\Delta^{17}O$ values within ± ~1 ‰ of 0; they are thus similar in $\Delta^{17}O$ value with those of the Earth and Mars. One might infer that the O-isotope compositions of all differentiated bodies have $\Delta^{17}O$ values similar to the Earth. In contrast one might assume the undifferentiated bodies would be outliers with respect to $\Delta^{17}O$. However, there are some exceptions with O-isotope compositions for differentiated bodies that significantly different from those of the Earth and Mars (see Figure 1-3, right).

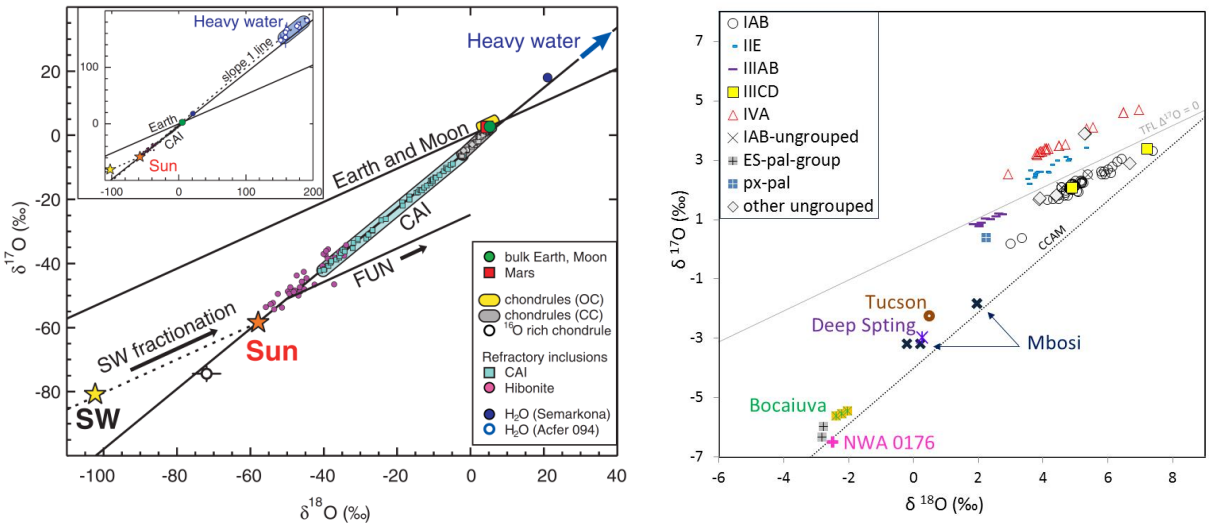

Figure 1-4. The oxygen compositions variability of solar system materials in three oxygen isotope diagrams. The left hand panel of this figure is from McKeegan et al., (2011), reprinted with permission from AAAS. The data plotted in the right hand panel are from Clayton and Mayeda (1978), Mayeda and Clayton, (1980), Clayton et al., (1983), Olsenl et al., (1996), Clayton and Mayeda (1996), Liu et al., (2001), Wang et al., (2004).

The O-isotope data can provide important constraints on mixing during the early stage of the solar system formation because the observed mass-independent isotope heterogeneities are likely due to processes driving the evolution of the proto solar nebula. Mass-independent isotope fractionations among nebular materials are due to photolysis of their parent molecular constituent, CO, (Clayton, 2002; Yurimoto and Kuramoto, 2004; Lyons and Young, 2005). The most abundant isotopologue, C^{12}-O^{16}, was optically thick in the nebula gas compared to the other rare isotopologues: C^{12}-O^{17}, C^{12}-O^{18}, C^{13}-O^{16}, C^{13}-O^{17}, and C13-O^{18}. The self-shielding of UV-light drove mass-independent fractionation of O and lead to the enriched abundance of H_2O^{17} and H_2O^{18} in the gas phase and in condensed water ice. The gas and ice-coated dust decoupled (e.g., Ciesla and Cuzzi, 2006; Yurimoto and Kuramoto, 2004). If this hypothesis is true, water concentrates the heavy isotope components in reactions between solar nebular gas and dust. The model predicts that H_2O should be enriched in ^{17}O and ^{18}O by 30 – 100% relative to disk CO for the same irradiated environment (Lyons and Young, 2005). Empirical measurements have revealed evidence of extremely heavy O-isotope compositions in cosmic symplectites in the Acfer 094 meteorite (Sakamoto et al., 2007), in insoluble organic material in a CR chondrite (Hashizume et al., 2011), and for slightly elevated $\Delta^{17}O$ values in LL3 magnetite (Choi et al., 1998).

Since water is considered to be the main oxidant in the nebula, the same hypotheses predict that the planetary materials that formed in oxidized conditions would have higher $\Delta^{17}O$ values. Correlations of the oxidation states and oxygen isotopes have been studied for chondrules. The previous studies suggested that the chondrules with higher $\Delta^{17}O$ values are analogously FeO-rich and oxidized which may be caused by an oxidant (e.g. H_2O) or by a dust enriched environment (Fedkin and Grossman, 2006; Connolly and Huss, 2010; Ushikubo et al., 2012; Tenner et al.,

2013). Therefore, R chondrites can a valuable meteorite group to study in order to understand the nebular environment present during chondrule formation. As yet, R chondrites have not been studied as extensively as O, C, or E chondrites.

1.5 Overview of Thesis

The subject of this thesis consists of new cosmochemical discoveries coupled with improvements of analytical techniques focused on deepening our understanding of the formation of rocky planetary bodies during the early evolution of the solar system. The thesis is primarily focused on studies of meteorite samples from the Rumuruti chondrite group. The focus on R chondrites is motivated by several factors including:

1) R chondrites are known to be one of the most oxidized chondrite groups with the highest bulk $\Delta^{17}O$ values. They are anomalous in this respect to other rocky objects found in our solar system.

2) The R chondrite groups, in comparison with other chondrites, have received relatively little research interest. As a result, their compositional variations are not well sampled or understood.

3) It is generally accepted that proto solar system materials can be divided into two components: carbonaceous chondrites and all others. Prior studies show that R chondrites buck this general trend. They seem to share characteristics of both of these components and they may provide a link to reconcile their evolutionary histories.

4) R chondrites also may help put limits on the state of the environment present during the early evolution of the solar system, constraints that would excite biochemists searching

for what might be the spark of life in the universe. R chondrites are enriched in matrix materials, contain amino acids, are abundant in sulfides, contain a rich mixture of multiple valance components, and show clear evidence for the presence of water and for natural heat sources.

In order to achieve high-accuracy oxygen isotope compositional measurements, it is necessary to account for instrumental "matrix effects" when interpreting data collected via SIMS. Studies (see Chapter 2) were performed in order to calibrate a correction technique. In addition to the investigation of Rumuruti chondrites, I investigated IVA iron meteorites to find non-metallic inclusions that contain phases rich in Cr.

The thesis outline includes:

Chapter 1 is this introduction.

Chapter 2 details oxygen isotope analytical techniques. The techniques include fluorination techniques and overview of SIMS O-isotope analyses.

Chapter 3, which has been accepted for publication (Isa et al. 2017), details investigations of SIMS O-isotope matrix effects on olivine that can then be utilized to more accurately analyze Fe-rich olivine in R chondrite chondrules. The correction technique that we have developed to account for O-isotope matrix effects is applicable to the CAMECA IMS 1270, 1280 and 1290 instruments.

Chapter 4, which has already been published (Isa et al., 2014), presents measurements that define the general characteristics of R chondrite group through a comprehensive study of meteorites via bulk chemistry and petrology. The chapter provides a summary of chemical and petrologic

comparisons of the R chondrite group with other chondrite groups. Contrasting differences are also outlined.

Chapter 5 presents O-isotope compositional data for components from a pristine type 3 R chondrite named PRE 9544. Evolutionary scenarios and the timings of processes leading to the formation of an R chondrite parent body as discussed in the context of the empirical compositional variations.

Chapter 6, which also appears in publication (Isa et al., 2016), highlights one of the results found during the investigation of Cr-bearing inclusions present in iron meteorites. This chapter presents the evidence that supports the discovery of new a mineral, $MnCr_2S_4$. The new mineral has been given the name Joegoldsteinite; the name designation has been approved and recognized by the International Mineralogical Association.

Chapter 7 summarizes the studies presented in this thesis and provides advice for future projects related to the study of the complex relationships between meteorite groups and the study of early solar system evolution.

1.6 References

Altwegg, K., Balsiger, H., Bar-Nun, A., Berthelier, J.J., Bieler, A., Bochsler, P., Briois, C., Calmonte, U., Combi, M., De Keyser, J., Eberhardt, P., Fiethe, B., Fuselier, S., Gasc, S., Gombosi, T.I., Hansen, K.C., Hassig, M., Jackel, A., Kopp, E., Korth, A., LeRoy, L., Mall, U., Marty, B., Mousis, O., Neefs, E., Owen, T., Reme, H., Rubin, M., Semon, T., Tzou, C.-Y., Waite, H., Wurz, P., (2014). 67P/Churyumov-Gerasimenko, a Jupiter family comet with a high D/H ratio. *Science* **347** *(6220), 1261952.*

Anders, E., Ebihara, M., (1982). Solar-system abundances of the elements. *Geochim. Cosmochim. Acta* **46**, 2363–2380.

Anders, E., Grevesse, N., (1989). Abundances of the elements: Meteoritic and solar. *Geochim. Cosmochim. Acta* **53**, 197–214.

Baertschi, P., (1976). Absolute ^{18}O content of standard mean ocean water. *Earth Planet. Sci. Lett.* **31**, 341–344.

Bischoff, A., Geiger, T., Palme, H., Spettel, B., Schultz, L., Scherer, P., Loeken, T., Bland, P., Clayton, R.N., Mayeda, T.K., Herpers, U., Meltzow, B., Michel, R., Dittrich-Hannen, B., (1994). Acfer 217-A new member of the Rumuruti chondrite group (R). *Meteoritics* **29**, 264–274.

Bischoff, A., Vogel, N., Roszjar, J., (2011). The Rumuruti chondrite group. *Chemie der Erde - Geochemistry* **71**, 101–133.

Buchwald, V.F., (1975). Handbook of iron meteorites: Their history, distribution, composition, and structure. Volumes 1, 2 & 3. *Arizona State Univ. Cent. Meteor. Stud. Berkeley Univ. Calif. Press 1975*.

Burton, A.S., McLain, H., Glavin, D.P., Elsila, J.E., Davidson, J., Miller, K.E., Andronikov, A.V., Lauretta, D., Dworkin, J.P., (2015). Amino acid analyses of R and CK chondrites. *Meteorit. Planet. Sci.* **50**, 470–482.

Chabot, N.L., Saslow, S.A., McDonough, W.F., Jones, J.H., (2009). An investigation of the behavior of Cu and Cr during iron meteorite crystallization. *Meteorit. Planet. Sci.* **44**, 505–519.

Choi, B.-G., McKeegan, K.D., Krot, A.N., Wasson, J.T., (1998). Extreme oxygen-isotope compositions in magnetite from unequilibrated ordinary chondrites. *Nature* **392**, 577–579.

Ciesla, F.J., Cuzzi, J.N., (2006). The evolution of the water distribution in a viscous protoplanetary disk. *Icarus* **181**, 178–204.

Clayton, R.N., (2002). Solar System: Self-shielding in the solar nebula. *Nature* **415**, 860–861.

Clayton, R.N., Mayeda, T.K., (1978). Genetic relations between iron and stony meteorites. *Earth Planet. Sci. Lett.* **40**, 168–174.

Clayton, R.N., Mayeda, T.K., (1996). Oxygen isotope studies of achondrites. *Geochim. Cosmochim. Acta* **60**, 1999–2017.

Clayton, R.N., Mayeda, T.K., Goswami, J., Olsen, E.J., (1991). Oxygen isotope studies of ordinary chondrites. *Geochim. Cosmochim. Acta* **55**, 2317–2337.

Clayton, R.N., Mayeda, T.K., Olsen, E.J., Prinz, M., (1983). Oxygen isotope relationships in iron meteorites. *Earth Planet. Sci. Lett.* **65**, 229–232.

Connolly, H.C., Huss, G.R., (2010). Compositional evolution of the protoplanetary disk: Oxygen isotopes of type-II chondrules from CR2 chondrites. *Geochim. Cosmochim. Acta* **74**, 2473–2483.

Davis, A.M., Hashizume, K., Chaussidon, M., Ireland, T.R., Prieto, C.A., Lambert, D.L., (2008). Oxygen in the Sun. *Rev. Mineral. Geochemistry* **68**, 73–92.

Fahey, A.J., Goswami, J.N., McKeegan, K.D., Zinner, E.K., (1987). ^{16}O Excesses in Murchison and Murray hibonites: A case against a late supernova injection origin of isotopic anomalies in O, Mg, Ca, and Ti. *Astrophys. J.* **323**, L91–L95.

Fedkin, A.V., Grossman, L., (2006). The Fayalite content of chondritic olivine: Obstacle to understanding the condensation of rocky material. *Meteorites Early Sol. Syst. II, D. S. Lauretta H. Y. McSween Jr. (eds.), Univ. Arizona Press. Tucson, 943 pp., p.279-294*, 279–294.

Gounelle, M., (2006). The meteorite fall at L'Aigle and the Biot report: Exploring the cradle of meteoritics. *Geol. Soc. London, Spec. Publ.* **256**, 73–89.

Gounelle, M., Zolensky, M.E., (2014). The Orgueil meteorite: 150 years of history. *Meteorit. Planet. Sci.* **49**, 1769–1794.

Gray, C.M., Papanastassiou, D.A., Wasserburg, G.J., (1973). The identification of early condensates from the solar nebula. *Icarus* **20**, 213–239.

Greenwood, J.P., Rubin, A.E., Wasson, J.T., (2000). Oxygen isotopes in R-chondrite magnetite and olivine: Links between R chondrites and ordinary chondrites. *Geochimica et Cosmochimica Acta*, **64**, 3897-3911.

Grewingk, C., Schmidt, C., (1864). Ueber die Meteoritenfälle von Pillistfer, Buschhof und Igast in Liv-und Kurland. *Dorpat: Laakmann.*

Hashizume, K., Takahata, N., Naraoka, H., Sano, Y., (2011). Extreme oxygen isotope anomaly with a solar origin detected in meteoritic organics materials formed in the early Solar System generally exhibit a characteristic oxygen isotopic signature known as the non- mass-dependent oxygen isotope anomaly. *Nat. Geosci.* **4**.

Isa, J., Kohl, I.E., Liu, M.-C., Wasson, J.T., Young, E.D., McKeegan, K.D., (2017). Quantification of Oxygen isotope SIMS matrix effects in olivine samples: Correlation with sputter rate. *Chemical Geology,* (in press).

Isa, J., Ma, C., Rubin, A.E., (2016). Joegoldsteinite: A new sulfide mineral (MnCr2S4) from the Social Circle IVA iron meteorite. *Am. Mineral.* **101***, 1217-1221.*

Isa, J., Rubin, A.E., Wasson, J.T., (2014). R-chondrite bulk-chemical compositions and diverse oxides: Implications for parent-body processes. *Geochim. Cosmochim. Acta* **124**, 131–151.

Kallemeyn, G.W., Rubin, A.E., Wasson, J.T., (1996). The compositional classification of chondrites : VII. The R chondrite group. *Geochemica Cosmochem. Acta* **60**, 2243–2256.

Kant, I., (1755). Universal natural history and theory of the heavens: Or, an essay on the constitution and the mechanical origin of the entire structure of the universe based on Newtonian Principles. tr. by Ian Johnston. *Vancouver Island University, Nanaimo, British Columbia Canada* (2008).

Khan, R., Shirai, N., Ebihara, M., (2015). Chemical characteristic of R chondrites in the light of P, REEs, Th and U abundances. *Earth Planet. Sci. Lett.* **422**, 18–27.

Kleine, T., Touboul, M., Bourdon, B., Nimmo, F., Mezger, K., Palme, H., Jacobsen, S.B., Yin, Q.-Z., Halliday, A.N., (2009). Hf–W chronology of the accretion and early evolution of asteroids and terrestrial planets. *Geochim. Cosmochim. Acta* **73**, 5150–5188.

Kwok, S., (2016). Complex organics in space from Solar System to distant galaxies. *Astron. Astrophys. Rev.* **24**, 8.

Laplace, P.S., (1796). The system of the world. tr. by J. Pond. *London: Phillips* (1809).

Lingemann, C.M., Berlin, J., Stöffler, D., (2000). Rumuruti chondrite: Origin and evolution of primitive components. *Meteorit. Planet. Sci.* **Supplement**, A98.

Liu, M., Scott, E.R.D., Keil, K., Wasson, J.T., Clayton, R.N., Mayeda, T., Eugster, O., Crozaz, G., Floss, C., (2001). Northwest Africa 176: A unique iron meteorite with silicate inclusions related to Bocaiuva. *Lunar Planet. Sci. XXXII*, abstract #2152.

Lodders, K., (2003). Solar System Abundances and Condensation Temperatures of the Elements. *Astrophys. J.* **591**, 1220–1247.

Lyons, J.R., Young, E.D., (2005). CO self-shielding as the origin of oxygen isotope anomalies in the early solar nebula. *Nature* **435**, 317–20.

MacPherson, G.J., Boss, A., (2011). Cosmochemical evidence for astrophysical processes during the formation of our solar system. *Proc. Natl. Acad. Sci. U. S. A.* **108**, 19152–19158.

Mayeda, T.K., Clayton, R.N., (1980). Oxygen isotopic compositions of aubrites and some unique meteorites. *Proc. Lunar Planet. Sci. Conf. 11th*, 1145–1151.

McKeegan, K.D., Kallio, A.P.A., Heber, V.S., Jarzebinski, G., Mao, P.H., Coath, C.D., Kunihiro, T., Wiens, R.C., Nordholt, J.E., Moses, R.W., Reisenfeld, D.B., Jurewicz, A.J.G., Burnett, D.S., (2011). The oxygen isotopic composition of the Sun inferred from captured solar wind. *Science* **332**, 1528–32.

Olsen, E.J., Clayton, R.N., Mayeda, T.K., Davis, A.M., Clarke, R.S., Wasson, J.T., (1996). Mbosi: An anomalous iron with unique silicate inclusions. *Meteorit. Planet. Sci.* **31,** 633-639.

Pack, A., Yurimoto, H., Palme, H., (2004). Petrographic and oxygen-isotopic study of refractory forsterites from R-chondrite Dar al Gani 013 (R3.5-6), unequilibrated ordinary and carbonaceous chondrites. *Geochim. Cosmochim. Acta* **68**, 1135–1157.

Prior, D.J., (1916). On the genetic relationship and classification of meteorites. *Miner. Mag.* **18**, 26–44.

Righter, K., Cosca, M.A., Morgan, L.E., (2016). Preservation of ancient impact ages on the R chondrite parent body: $^{40}Ar/^{39}Ar$ age of hornblende-bearing R chondrite LAP 04840. *Meteorit. Planet. Sci.* **51**, 1678–1684.

Righter, K., Neff, K.E., (2007). Temperature and oxygen fugacity constraints on CK and R chondrites and implications for water and oxidation in the early solar system. *Polar Sci.* **1**, 25–44.

Rout, S.S., Bischoff, A., Nagashima, K., Krot, A.N., Huss, G.R., Keil, K., (2009). Oxygen- and magnesium-isotope compositions of calcium–aluminum-rich inclusions from Rumuruti (R) chondrites. *Geochim. Cosmochim. Acta* **73**, 4264–4287.

Rubin, A.E., (2014). Shock and annealing in the amphibole- and mica-bearing R chondrites. *Meteorit. Planet. Sci.* **49***, 1057-1075.*

Rubin, A.E., Grossman, J.N., (2010). Meteorite and meteoroid: New comprehensive definitions. *Meteorit. Planet. Sci.* **45**, 117–125.

Rubin, A.E., Kallemeyn, G.W., (1989). Carlisle Lakes and Allan Hills 85151: Members of a new chondrite grouplet. *Geochim. Cosmochim. Acta* **53**, 3035–3044.

Sakamoto, N., Seto, Y., Itoh, S., Kuramoto, K., Fujino, K., Nagashima, K., Krot, A.N., Yurimoto, H., (2007). Remnants of the early solar system water enriched in heavy oxygen isotopes. *Science* **317**, 231–3.

Schulze, H., Bischoff, A., Palme, H., Spettel, B., Dreibus, G., Otto, J., (1994). Mineralogy and chemistry of Rumuruti: The first meteorite fall of the new R chondrite group. *Meteoritics* **29**, 275–286.

Tenner, T.J., Ushikubo, T., Kurahashi, E., Kita, N.T., Nagahara, H., (2013). Oxygen isotope systematics of chondrule phenocrysts from the CO3.0 chondrite Yamato 81020: Evidence for two distinct oxygen isotope reservoirs. *Geochim. Cosmochim. Acta* **102**, 226–245.

Ushikubo, T., Kimura, M., Kita, N.T., Valley, J.W., (2012). Primordial oxygen isotope reservoirs of the solar nebula recorded in chondrules in Acfer 094 carbonaceous chondrite. *Geochim. Cosmochim. Acta* **90**, 242–264.

Van Schmus, W.R., Wood, J.A., (1967). A chemical-petrologic classification for the chondritic meteorites. *Geochim. Cosmochim. Acta* **31**, 747–765.

Wang, P.-L., Rumble, D., McCoy, T.J., (2004). Oxygen isotopic compositions of IVA iron meteorites: implications for the thermal evolution derived from in situ ultraviolet laser microprobe analyses. *Geochim. Cosmochim. Acta* **68**, 1159–1171.

Warren, P.H., (2011). Stable-isotopic anomalies and the accretionary assemblage of the Earth and Mars: A subordinate role for carbonaceous chondrites. *Earth Planet. Sci. Lett.* **311**, 93–100.

Wasson, J.T., (2013). Vesta and extensively melted asteroids: Why HED meteorites are probably not from Vesta. *Earth Planet. Sci. Lett.* **381**, 138–146.

Wasson, J.T., Lange, D.E., Francis, C.A., Ulff-Møller, F., (1999). Massive chromite in the Brenham pallasite and the fractionation of Cr during the crystallization of asteroidal cores. *Geochim. Cosmochim. Acta* **63**, 1219–1232.

Wasson, J.T., Richardson, J.W., (2001). Fractionation trends among IVA iron meteorites: Contrasts with IIIAB trends. *Geochim. Cosmochim. Acta* **65**, 951–970.

Weisberg, M.K., Prinz, M., Kojima, H., Yanai, K., Clayton, R.N., Mayeda, T.K., (1991). The Carlisle Lakes-type chondrites : A new grouplet with high Al70 and evidence for nebular oxidation. **55**, 2657–2669.

Yurimoto, H., Kuramoto, K. (2004). Molecular cloud origin for the oxygen isotope heterogeneity in the solar system. *Science* **305**, 1763–6.

Chapter 2: Analytical Techniques: Oxygen Isotope Measurements

2.1 Overview of Secondary Ion Mass Spectrometry

All O-isotope analyses in R chondrites addressed in this thesis were performed at UCLA by secondary ion mass spectrometry (SIMS) on the UCLA CAMECA IMS 1270 ion microprobe. The SIMS instrument is a magnetic sector mass spectrometer/ion microscope and analyzes the target elements or isotopes as secondary ions sputtered from the solid samples with a focused primary ion beam. SIMS are composed of six components: (1) a primary column, (2) a transfer section, (3) an electrostatic analyzer (ESA), (4) a coupling section, (5) an electromagnet (mass analyzer) and (6) a detection chamber.

Samples are typically sputtered with a 10 to 20 keV primary beam of usually Cs^+ or $^{16}O^-$. The ion beam is generated by an ion source and focused into a small spot with a diameter of a few to dozens of μm on the sample surface by lenses and deflectors in the primary column. The primary beam produces a collision cascade and sputters off material from the sample surface as various chemical species (neutral atoms, ions, electrons, and molecules). The secondary ions then become accelerated into the mass spectrometer and are collected by separate detectors based on their mass/charge ratios. Detailed descriptions about CAMECA-type SIMS machines were extensively addressed in Ph.D. theses of McKeegan (1987) and Fahey (1988). A detailed description of the CAMECA IMS 1270 instrument appears in the Ph.D. thesis written by Liu (2008).

2.2 SIMS Oxygen Isotope Measurements and Data Reduction

All data reductions of SIMS O-isotope measurements were carried out by applying corrections for (1) Instrumental Mass fractionation (IMF), (2) detector efficiency and background effects.

2.2.1 Instrumental Mass Fractionation

The determination of the absolute degree of IMF is not straightforward and it probably varies from session to session. The determination of the absolute degree of IMFs is, however, unnecessary. This is because all SIMS measurements are taken relative to a standard just as typically done with all types of mass spectrometry. Instrumental biases (e.g., mass-dependent fractionations) are calibrated by the use of standard materials. Problems can arise due to a lack of appropriate standard materials; such problems can be particularly acute for SIMS limiting both precision and accuracy of isotopic analyses. Inaccuracies generated by a mismatch between the matrix of the sample that is the subject of research study and that of the standard utilized to calibrate instrumental fractionation is referred to as the "matrix effect". The O-isotope SIMS matrix effect on olivine samples will be discussed later in Chapter 3 of this thesis.

2.2.2 Detector Efficiency and Background

Individual detectors have different physical properties and these properties have to be rigorously determined and characterized. Faraday cups (FCs) have backgrounds and these are measured during the pre-sputtering time prior to when a run is performed to analyze a sample. The electron multipliers (EMs) have dead times and pulse height distributions that are inherent to the ion counting system. The dead times were separately measured by analyzing a glass slide under different primary beam conditions. And, the pulse height distributions of the ion counting system were monitored every couple of hours during analysis runs. The high voltage (HV) supply running the system was adjusted as needed to provide reliable measurements.

2.3 Theoretical Approach to SIMS Oxygen Isotope Matrix Effects

The goal of this section is to theoretically explain empirical variations in the observed sputtering rate and primary beam (Cs ion) concentration at the sputtering surface that arise due to matrix effects.

2.3.1 Previous Empirical Observations

The SIMS sputter rate, Cs ion (primary beam ion) concentrations at the sputtered area, and useful ion yields are known to be correlated (Deline et al., 1978). The useful yields are proportional to the Cs concentration at the sputtering surface but they are inversely proportional to the sputtering rate. These relationships can be expressed as $n^-/n_0 \propto [Cs]_v^{x-} \propto (1/S_l)^{x-}$ where n^-/n_0 is the relative negative ion yield of a specie n, $[Cs]_v$ is the Cs volume concentration (atom/cm^3), S_l is the linear sputtering rate (Å/s), and *x*- is an exponential factor. This equation above was empirically tested by Chelgren et al., (1979). They concluded that sputtered substrate ion yields (useful yield) are proportional to $[Cs]_v^{x-}$ and that the surface Cs concentration increases with increases in the inverse of the sputtering yield thus confirming the Deline et al., (1978) equation. The useful yield was enhanced by Cs implantation in the target sample surface because the implanted Cs decreases the work function and increases the formation probability of secondary ions (Philipp et al., 2007). Chelgren et al., (1979) also found that $(1+S_a)^{-1}$ (S_a is the sputtering yield of the substrate ion/atom) was unexpectedly correlated in a non-linear fashion with the measured Cs concentration.

2.3.2: Matrix Effect Assumptions

During SIMS analyses with the use of a constant primary ion beam flux, a sputtering equilibrium is achieved and the primary ion concentration reaches a steady state near the sputtering surface. Here, I assume that the sputtering surface consists of arbitrary distinct sites in each of which a maximum of one primary beam ion can be allocated. I also assume that individual sites do not chemically interact with each other. If a site has acquired one implanted primary beam ion, the site acquires energy equal to q. The temperature of the system is also taken to be constant. Given these assumptions, I use a statistical mechanical approach to treat ions at these sites on the solid surface.

2.3.3: Grand Canonical Ensembles

The grand partition function, Ξ, is given by:

$$\Xi = \sum_{N} \lambda^{N} \sum_{n} e^{-\beta E_N^n} \qquad (2-1)$$

where λ is the fugacity ($\lambda = e^{\beta\mu}$: μ is chemical potential), β is the thermodynamic beta ($\beta = 1/k_B T$: k_B is the Boltzmann constant and T is temperature), and E_N^n is the total energy of a canonical ensemble containing N particles in microscopic states n. A site (n=1) is either occupied by one particle (number of particles N = 1 and thus $E_1 = q$) or vacant (N = 0 and thus $E_1 = 0$).

$$\Xi_1 = 1 + e^{\beta(\mu+q)} \qquad (2-2)$$

Using this grand partition function, I consider total number of sites, N_{total}, which are all equivalent to Ξ_1. Then, the total grand partition function is given by the product of the grand partition functions of independent portions: $\Xi = \prod_{i=1}^{N_{total}} \Xi_i$. Therefore, I can describe the

probability that the sites are vacant or occupied by a primary ion (atom). And, the coverage of implanted primary ions on the sputtering surface θ is given by:

$$\theta = \frac{e^{\beta(\mu+q)}}{1+e^{\beta(\mu+q)}} = \frac{1}{1+e^{-\beta(\mu+q)}} \qquad (2-3)$$

Given that the system is assumed to be isothermal, the chemical potential is a free parameter of Equation (2-3). And, the chemical potential in this system is primarily controlled by the sputtering rates of materials under our assumption that the primary ion flux (implanting rate) is constant and that the primary beam ion concentration is at a steady state condition. Equation (2-3) predicts that the mass-dependent SIMS isotope effects would obey a non-linear dependence on the sputtering rate. According to our experimental results (see Chapter 3 of this thesis), the sputtering rates and O-isotope SIMS matrix effects in olivine are well correlated when a sigmoid model curve is used to fit the dat. These experimental observations and the Equation (2-3) also confirmed previous results that useful ionization yields are enhanced by the reactive primary beam ions (e.g., Andersen, 1970; Yu, 1986).

The relationship expressed in Equation (2-3) is based on the assumptions that the ions are implanted in the sample substrate at shallow depths and that the implanted ions do not develop multiple layers. If the system does not fulfill these assumptions, the Cs concentration versus sputtering rate may not follow the curve predicted by Equation (2-3). Several cases can arise in the SIMS analytical settings that would degrade the model relationship. For example, sample materials with an extremely low mass density would allow primary beam ions to be implanted deeply within the sample. Likewise, extremely low sputtering rates can lead to the development of a thick layer of primary beam ions or implanted ions may have a significant chemical reactive with the sample material. The crystalline nature of the sample may also provide complications.

The O-isotope matrix effects in other minerals (garnet, carbonates, etc.) aside from olivine may exhibit different dependencies on sputtering rate as a consequence of any of these factors.

2.3.4: Summary of the Theoretical Work

This study demonstrates that the experimental observations exhibit a non-linear relationship between sputtering rate and Cs concentration. This work explains that ionization processes can be reasonably understood by the Cs concentration distribution on the sputter surface. Researchers have paid attention to chemical compositions and crystalline structure of the target samples that match standards. As chemical composition and crystal morphology affect the beam sputtering rates, it is vitally important to carefully pair matching standards and samples in order to obtain accurate SIMS measurements. It is also useful to analyze the crater depth after an analytical session to determine the sputtering rate found for individual SIMS pits and checking to see if chemical matrix matching between the sample and standard is maintained.

2.4 SRIM Simulation of Sputtering of Oxygen Isotopes in Olivine

The Stopping and Range of Ions in Matter (SRIM) computer code (Ziegler et al., 2010) is a well known binary collision approximation (BCA) simulation code. It was originally developed for nuclear physics applications. The SRIM code is based on a Monte Carlo method to provide the statistical distribution of sample damage (defects) created by energetic particles bombardment. The code is widely applied for interpreting the results of studies that ion implantations/sputtering processes to collect observational data and to develop theoretical models.

The detailed description of the SRIM programs can be found in (Ziegler et al., 2010; Ziegler and Biersack, 1985). The TRansport of Ions in Matter (TRIM) program of the SRIM code set was

adopted to understand our SIMS empirical results. This program tracks the stopping range of ions into materials with recoils of target atoms caused by collision cascade. The TRIM program models ion and material collisional interactions by assuming that incident ions interact with electrons of target atoms by Coulomb collisions and collides with the nucleus of target atoms. In this simulation code, the sputtering yield is calculated by counting the number of atoms that escape from the target. Atoms can be sputtered if the kinetic energy along the normal direction to the sample is higher than surface binding energy of the target.

2.4.1 Conditions and Assumptions

To reconcile SIMS sputtering processes, we chose the incident ion, incident angle of the ion, and its impact energy, as Cs, 30 degrees, and 20 keV, respectively, to use as input parameters to TRIM. We also set the density of Forsterite (Fo) and Fayalite (Fa). The sputtering results are sensitive to several important parameters (atomic displacement energy, Ed, surface binding energy, Es, and the binding energy of a lattice atom to its site, Eb) that set the bonding conditions in the target materials. Sputtering atoms are only counted when atoms are knocked out from the surface of the target material. We discuss how these conditions affect the TRIM predictions in the following sections.

2.4.2 List of TRIM Simulation Initial Conditions

The following initial condition settings were utilized as input to the TRIM code to perform calculations that simulate SIMS analyses performed in the context of my thesis research project.

Ion Data:

Element:	Cs atom
Energy:	20 keV

Incident Angle: 30 degree
Total Number of Ions: 1000

Target Data #1 (compositionally forsterite)

Width: 1000 Ångstrom
Density: 3.27 g/cm^3

Element #1: Mg
Atom Stoichiometry: 2
Damage:
Displacement: 25 eV
Lattice: 3 eV
Surface: 1.54 eV

Element #2: Si
Atom Stoichiometry: 1
Damage:
Displacement: 15 eV
Lattice: 2 eV
Surface: 4.7 eV

Element #3: O
Atom Stoichiometry: 4
Damage:
Displacement: 28 eV
Lattice: 3 eV
Surface: 2 eV

Target Data #2 (compositionally fayalite)

Width: 1000 Ångstrom
Density: 4.66 g/cm^3

Element #1: Fe
Atom Stoichiometry: 2
Damage:
Displacement: 25 eV
Lattice: 3 eV
Surface: 4.34 eV

Element #2: Si
Atom Stoichiometry: 1
Damage:
Displacement: 15 eV
Lattice: 2 eV

Surface: 4.7 eV

Element #3: O
Atom Stoichiometry: 4
Damage:
Displacement: 28 eV
Lattice: 3 eV
Surface: 2 eV

2.4.3 Results

The results indicate that Cs ions are implanted deeper in forsterite, peak depth 116 Å, than fayalite, peak depth 92 Å (see Figures 1 and 2). This is mainly due to the mass differences between Mg and Fe. Also, the total sputtering yields for fayalite and forsterite are nearly identical (see Table 1). This is inconsistent with the volume sputtering rates that were obtained in our SIMS analyses. The results showed a nearly factor of two difference between the sputtering rate for fayalite at 86 μm^3/min versus forsterite at 44 μm^3/min.

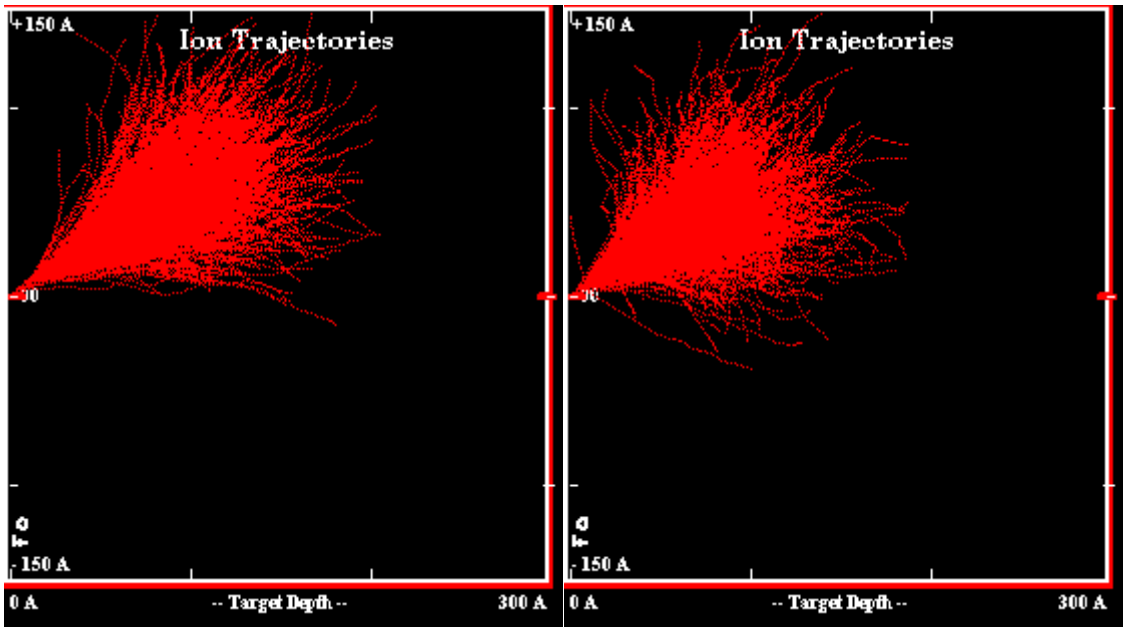

Figure 2-1. Ion depth penetration for Forsterite (left) and Fayalite (right).

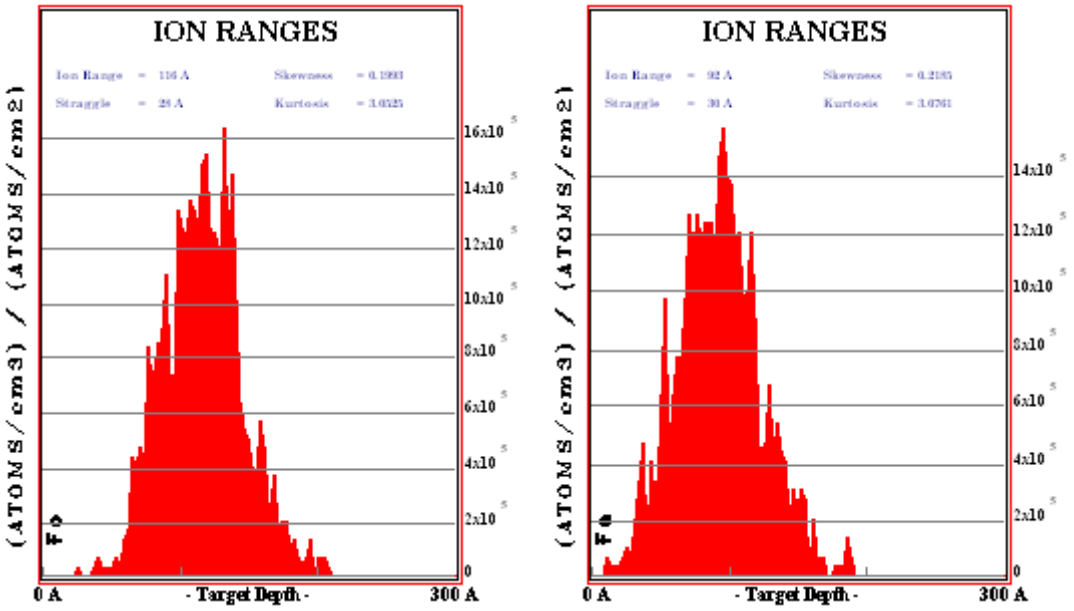

Figure 2-2. Implanted ion depth for Forsterite (left) and Fayalite (right).

Table 2-1. Sputtering yields. Note: Back scattering ions were 0 for Forsterite and 1 for Fayalite.

Forsterite	Atom/Ion	eV/Atom
O	6.53	25.39
Mg	3.77	19.84
Si	0.9660	38.18

Fayalite	Atom/Ion	eV/Atom
O	7.37	21.47
Fe	2.33	38.62
Si	1.11	36.05

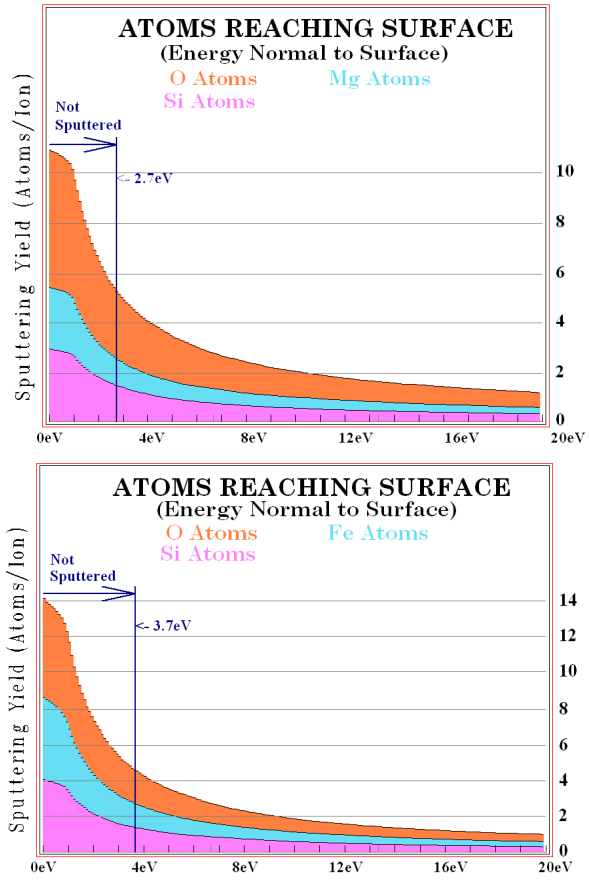

Figure 2-3. Sputtering yields for Forsterite (top) and Fayalite (bottom).

2.4.4 Summary of the TRIM Simulation

The TRIM simulation results suggest that one can reasonably assume that primary ions sputter off target materials and then become implanted themselves into a shallow surface layer on the sample. This validates one of the key assumptions we made in order to model SIMS results by applying the grand canonical ensemble formula (Equation 2-3). However, the sputtering yields of the TRIM simulations were not consistent with our experimental SIMS results. The discrepancy between the simulation results and empirical results can probably explained by the crystalline structure of our sample material, olivine, versus the virtual TRIM sample, which is assumed to

be amorphous. Therefore, the TRIM input settings we chose for the damage parameters (e.g. lattice energy) were likely inaccurate. Also, SRIM does not simulate any chemical sputtering phenomena that would include any chemical modification of the sample surface due to implanted materials. These factors help disagreements between the experimental and simulated results.

2.5 Laser Fluoridation Technique

The Oxygen isotope compositions of olivine samples presented in Chapter 3 of this thesis were measured via laser fluorination analysis. This section outlines the theory and methods of laser fluorination technique as related to oxygen isotope measurement. The description given below is based on the following references (Rumble et al., 1997; Sharp, 1990; Young et al., 1998a; Young et al., 1998b, Young et al., 2016), and hands-on training from Issaku Kohl at UCLA Young lab.

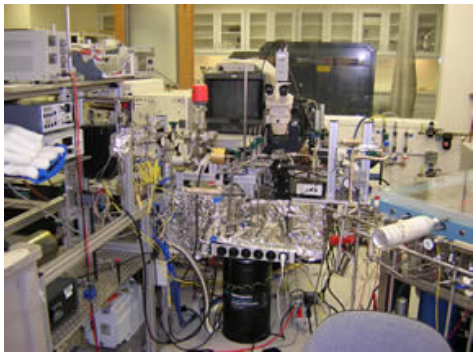

Figure 2-4. The laser fluorination line located in the Young laboratory at UCLA. This image was downloaded from the laboratory website: http://sims.ess.ucla.edu/eyoung/Young_lab.htm.

2.5.1 Laser Fluoridation Sample Compatibility

Mineral samples which react with fluorine gas, during CO_2-laser induced melting, are suitable for this technique. Note that alkali elements are highly reactive with fluorine gas such that they react without the assistance of CO_2-laser. If one wants to analyze alkali-rich feldspar, only a

single sample can be analyzed in the sample chamber at any given time. Fluorine is the most electron negative element and it reacts with most elements. Accordingly, the gas reacts with most geological samples. One exception is that apatite minerals are difficult to fluorinate by this technique. The Young lab utilizes a CO_2 laser made by GEO-Feinmechanik with a wavelength of 10.6 μm that operates at a frequency in the range between 10 to 50 Hz. The laser has maximum output strength of 25 W with pulse durations between 1 to 170 μs.

2.5.2 Sample Laser Heating: No Differences for Fe-rich and Mg-rich Olivine

The wavelength of our laser is 10.6 μm, which is in the thermal infrared and the SiO_4 tetrahedral structure has strong vibrational modes at this wavelength. Luckily, most geological samples, including Fe-rich and Mg-rich olivine, can be efficiently heated with this laser.

Crystals only absorb infrared light if the wavelength resonates with the bonds in the crystal. This interaction occurs when the lattice vibrations accompany periodic changes in the dipole moment. These changes are due to oscillation of the atoms. The periodic oscillation of the atoms in the crystals can couple with the frequency of the electromagnetic fields of incident photons. In the case of olivine, 35 out of 84 normal lattice modes are infrared active (Reynard, 1991). Thermal infrared studies show that olivine has strong absorption bands facilitated by Si-O around ~10 to 11.8 μm (three bands), 12.1 μm, and 16.4 to 21.7 μm (three or four bands) due to the v3, v1, and v4 modes, respectively. At lower energies in the wavelength range of 20 to 50 μm, there is absorption due to activation of the v2 symmetric bending mode, rotations and translations of the SiO_4 tetrahedron, and translations of Fe^{2+} or Mg^{2+}. In the far-infrared region, 50 to 117.6 μm, additional translational modes and combinations of SiO_4 and Mg^{2+} and Fe^{2+} translations can also be excited (Hofmeister, 1997). Extensive studies of olivine band positions for the Mg-Fe solid

solution series (Hamilton (2010) and references therein) show that Mg-Fe substitution leads to a change in the absolute positions of the bands. The position of each absorption band shifts towards longer wavelength with the increasing proportion of the Fe concentration (Figure 2-5). Further detail concerning the thermal infrared spectroscopy of Mg-Fe olivine in can be found in an extensive review article written by Hamilton (2010).

Since, the wavelength of the major absorption bands are all longer than 10.6 μm, the laser heating of olivine does not likely differ significantly as a function of Fe-Mg compositions. CO_2 laser excitation is efficient enough to melt forsterite (1900 °C) and fayalite (1200 °C) samples thus enabling reactions with fluorine gas.

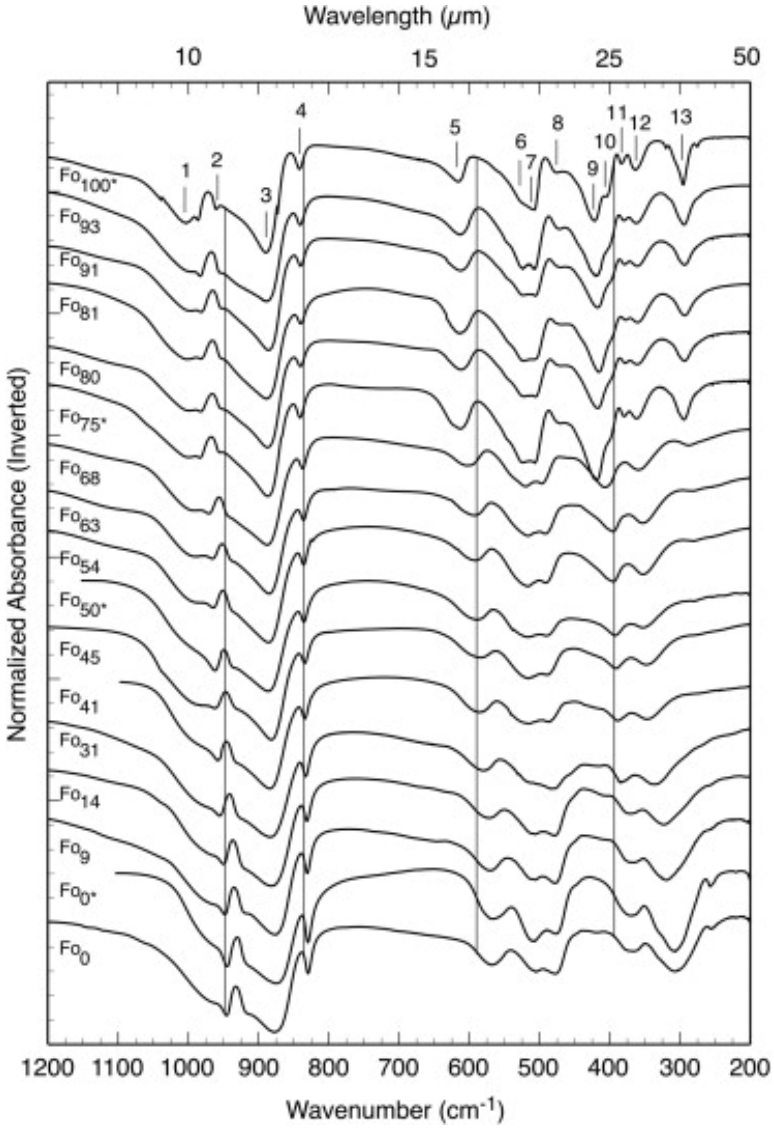

Figure 2-5. A figure from Hamilton (2010), reprinted with permission from Elsevier. (originally Hofmeister and Pitman, 2007). Thin-film transmission spectra of 17 Mg-Fe series olivines, offset for clarity. Numbers on the top of the spectra are band numbers from Burns and Huggins (1972). Vertical lines are for visual reference.

2.5.3 Vacuum Extraction Line of the Laser Fluoridation Instrument

The vacuum extraction line consists of an upstream section and a downstream section. The upstream section includes, in order: 1) an F_2 source, 2) a reaction chamber, 3) an F_2 trap via reaction with KBr, 4) an NF_3 molecular sieve trap, and 5) an O_2 trap. The downstream section incudes: 1) another KBr trap to remove remaining F_2 and a device to collect Br_2 before the gas is evacuated through a pump.

Upstream

Figure 2-6. A picture of the vacuum extraction line portion of the Young laboratory laser fluoridation instrument. The area indicated in yellow is upstream.

1) F_2 gas is provided from a source, which is generated by using double distillation with $K_3NiF_6 \cdot KF$ salt powder (Young et al., (2016) supplement) in a vacuum line. To release F_2 gas, the source needs to be heated at 200 °C. About 60 mbar of F_2 is used for a sample.

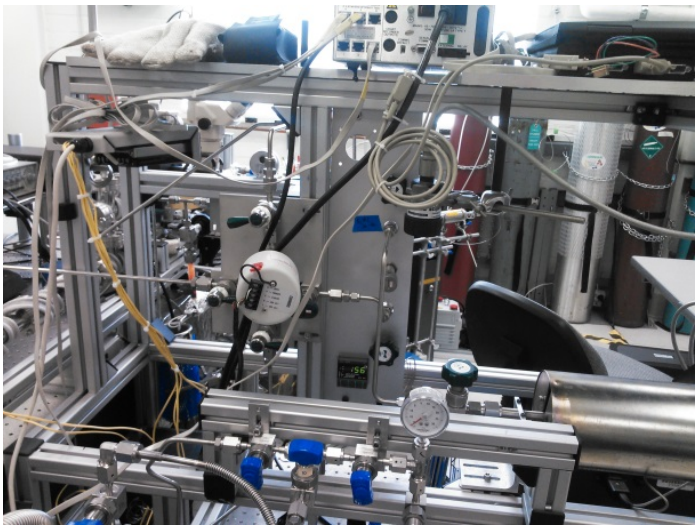

Figure 2-7. A picture of fluorine source in the Young laboratory.

2) A sample plate is made of electro polished 316-alloy stainless steel with seven sample holes. The ideal sample weight sizes are ~2.00 ± 0.5 mg, 2.5 ± 0.5 mg, and 7 ± 1 mg for silicates, meteorite-bulk samples, and sulfates, respectively. Note that the optimal sample weights were determined by Issaku Kohl. Larger oxide samples with weights greater than 3 mg may not sufficiently react with fluorine gas.

   The reaction chamber is also made of electro polished 316-alloy stainless steel. The laser window is made of zinc selenide, which has a high index of refraction, coated with a thorium fluoride coating, which has a low index of refraction. Both of these window materials are transparent at infrared wavelengths. The windows and the chamber are shielded by a Teflon O-ring. The laser pulse location is fixed so that a motorized sample stage needs to be constantly moved in order to align the laser to illuminate the sample and heat it uniformly. Low laser power is used at the beginning of the fluorination process and the laser power should be increased from there. The reaction of molten olivine $(Mg,Fe)_2SiO_4$ with F_2 gas yields MgF_2 (melting point, 1248-1263 °C at ambient pressure (p)), FeF_2 (melting point,

1000-1100 °C at ambient p), FeF_3 (1000-1030 °C at ambient p), SiF_4 (boiling point -86 °C) and O_2. That is, M_2SiO_4 (l) + 4 F_2 (g) → 2 MgF_2 (s or l) + SiF_4 (g) + $2O_2$ (g) where g, l, and s in the parentheses refer to gas, liquid, and solid, respectively. More details concerning the molecular properties of the reaction products can be found in an on-line reference index provided by ChemSpider located at http://www.chemspider.com/.

Note that while the window is opened, the reaction chamber is flooded with N_2 gas to purge the system. After all the measurements and before any measurements, the chamber is also heated with a portable heating light up to ~165 °C to clean the chamber. The baseline pressure of the chamber is 10^{-6} mbar.

3) The Young laboratory laser fluoridation extraction line is built by using 316-alloy stainless steel tubing, BCR stainless steel fittings, Nupro stainless steel bellows-sealed high vacuum valves, and a Swagelok diaphragm valve. The high reactivity of F_2 gas with KBr allows a convenient means of removing Fluorine from the desired portion of the measurement sample. Fluorine gas reacts quite readily with broken chips of crystalline, infrared (IR) grade KBr (typically heated to ~120 °C). The resultant Br_2 released from the reaction is subsequently trapped in cold fingers.

$$SiF_4\ (g) + 4\ KBr\ (s) \rightarrow SiBr_4\ (g) + 4\ KF\ (s),\ SiBr_4\ (s) + KBr\ (s) \rightarrow Si\ (s) + KBr\ (s) + Br_2\ (l)$$

$$F_2\ (g) + 2\ KBr\ (s) \rightarrow 2\ KF\ (s) + Br_2\ (l)$$

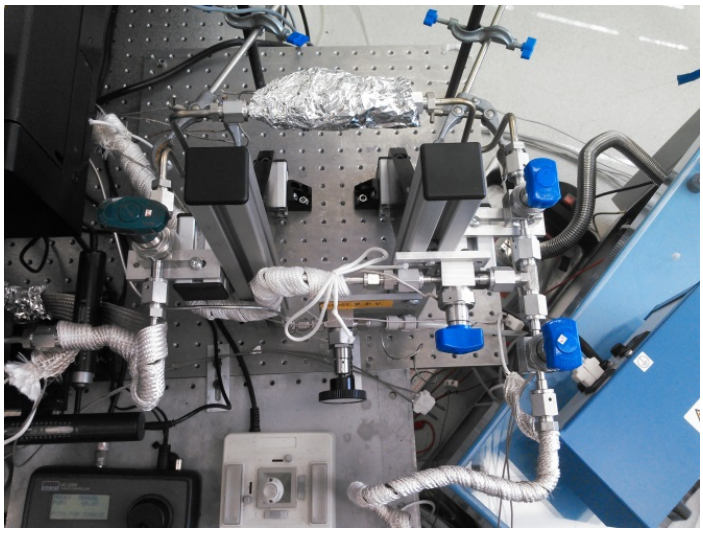

Figure 2-8. A picture of the KBr Fluorine trap.

4) Then, a molecular sieve is utilized to trap NF_3. All the sample gas is collected by a cold molecular sieve (13X) (zeorite) cooled by liquid N_2 (LN_2) to -196 °C. A pentene bath at a melting point temperature (sherbet-like texture) (-130 °C) is used to trap N_2 and NF_3 (the temperature choice was empirically determined by Mark Thiemens). This temperature does not trap O_2 so the oxygen gas must then be selectively collected by another molecular sieve, which is also cooled by liquid N_2 (-196 °C). After O_2 is trapped at the second molecular sieve, the glass tube is heated by heating tape (120 °C) to expand the gas to the mass spectrometer for 25 min. Those temperatures are measured by a thermocouple.

Downstream

Figure 2-9. A picture of the vacuum extraction line of the Young laboratory laser fluoridation. The area indicated in brown is downstream section.

The Br_2 sequestered in the cold traps is transferred to the other cold U finger traps at the lower end of the stream by heating the U traps (upper stream) with a heater.

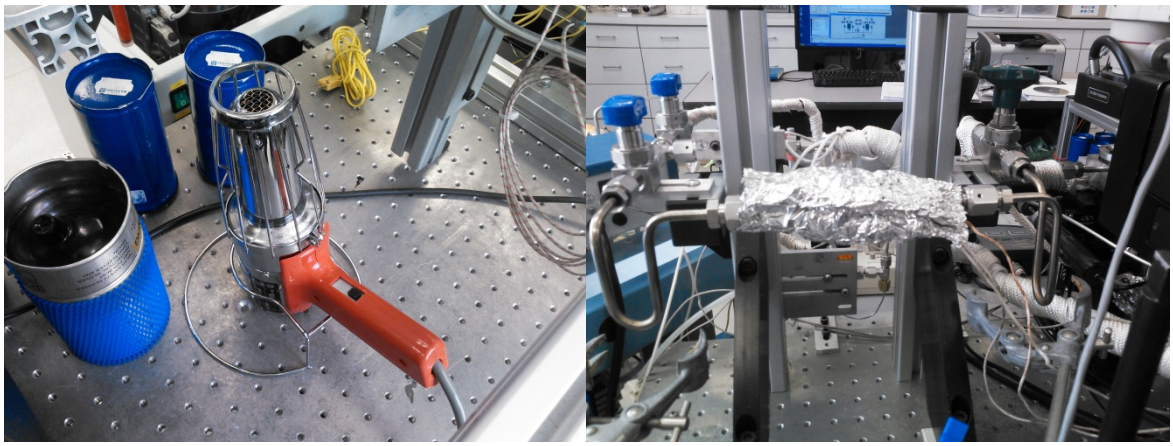

Figure 2-10. Pictures showing a portable heater (left) and the KBr and U traps (right).

Finally there is yet one more KBr trap that removes any remaining fluorine gas through an exchange reaction with Br. After all measurements are complete, the Br_2 is collected at a trap before the gas goes to a rotary pump (Pfeiffer Vacuum).

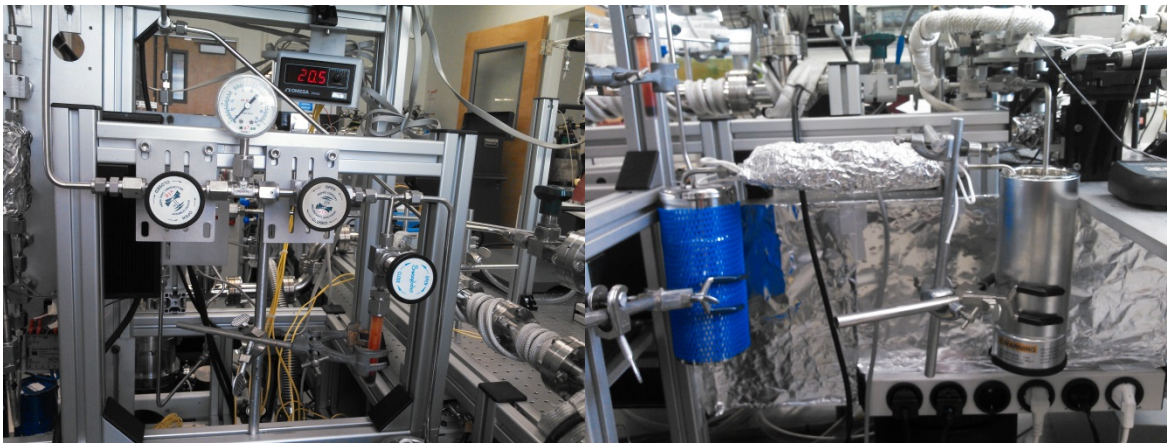

Figure 2-11. The Br_2 collector (right hand side, left picture) and the KBr trap (right picture).

2.5.4 Mass Spectrometer

The extraction line is connected directly to a Dual-inlet, sector-type mass spectrometer (Thermo Delta-plus isotope ratio mass spectrometer). The reference gas and sample gas are loaded in the variable bellows. The optimal pressures for the reference and sample gases are manually adjusted in the dual inlet to ensure well-balanced ion beams when averaged over 20 measurement cycles. The measurements repeat over 4 blocks and their average and standard deviation/standard error values are reported. Three Faraday cups are fixed that simultaneously measure at molecular weights of 32, 33, and 34. The sample gas is loaded in a completely stretched bellows, which is shown as “100%” on the control screen.

Relative sample yields can be calculated by using the pressure of the bellows, the sample weight, and stoichiometry. Assuming that the temperature of the gas is always constant, the sample

pressure of the O_2 gas fluorinated from San Carlos olivine in the bellows and the molar relationships are empirically related by X [μmol] = 2.9769 × Pressure [mbar] - 0.5564

One can be assured of the success of the fluorination completeness by checking this relative yield. However, I note that the relative yield is not a quantitative measure of the actual reaction yields and one should be aware of systematic errors and nature of samples (e.g. inclusions) when applying this equation. Also, this method cannot be applied for bulk samples with multiple mineral phase components.

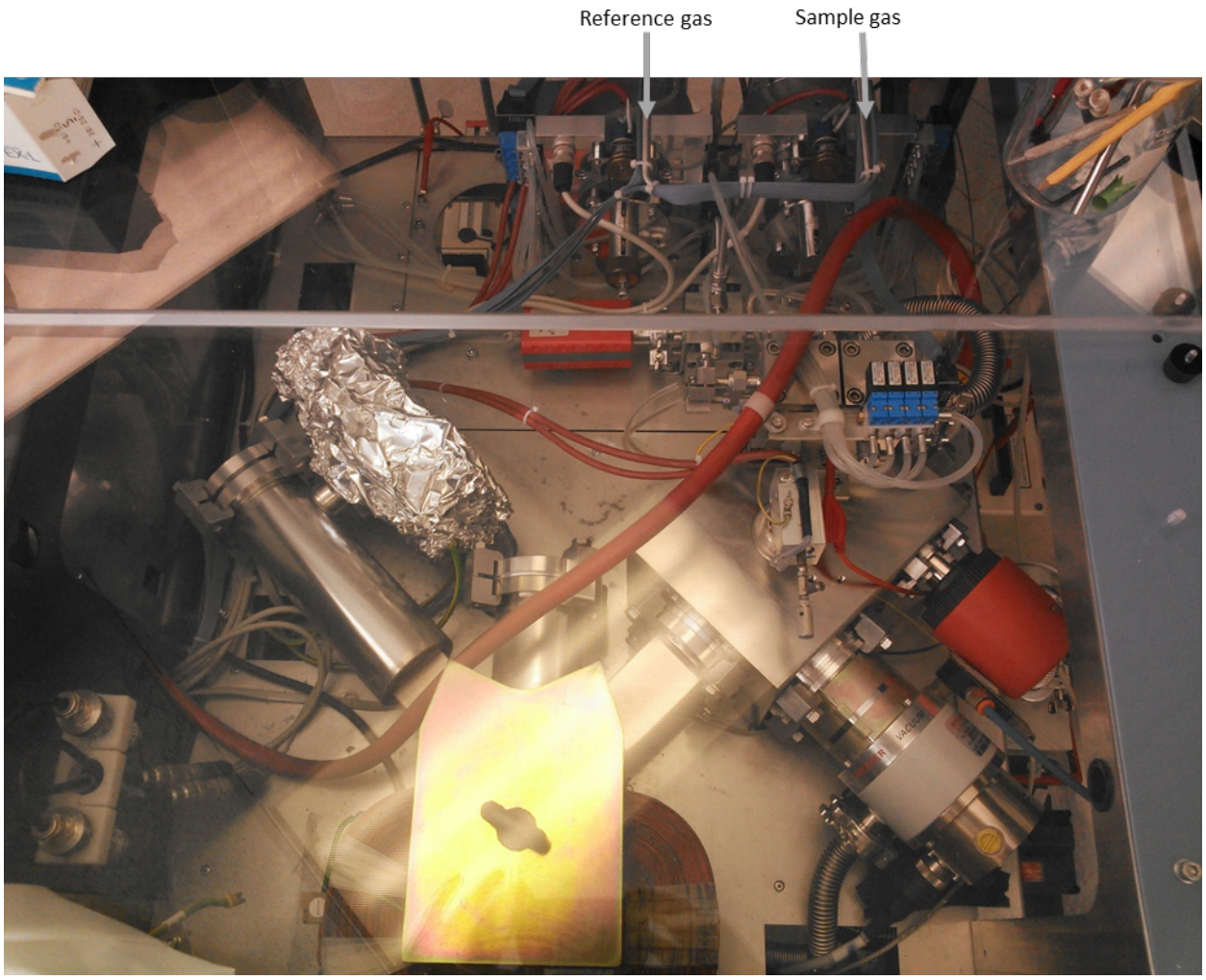

Figure 2-12. A picture of the mass spectrometer.

Interferences

It is important to note that NF has the same molecular mass, 32, as the most commonly occurring isotopic form of molecular (O^{16}_2). Thus, the presence of NF presents a potential source of error when performing laser fluoridation. This chemical species is decomposed from NF_3 molecule during a heating step (120 °C). To check for possible interference from NF, the amount of NF_3 (mass 71) in the system should be monitored before each sample measurement.

Reference Gas

A reference gas (from an O_2 tank) was calibrated against Vienna Standard Mean Ocean Water (VSMOW), which is accepted as an international standard for stable isotope analyses and measurements.

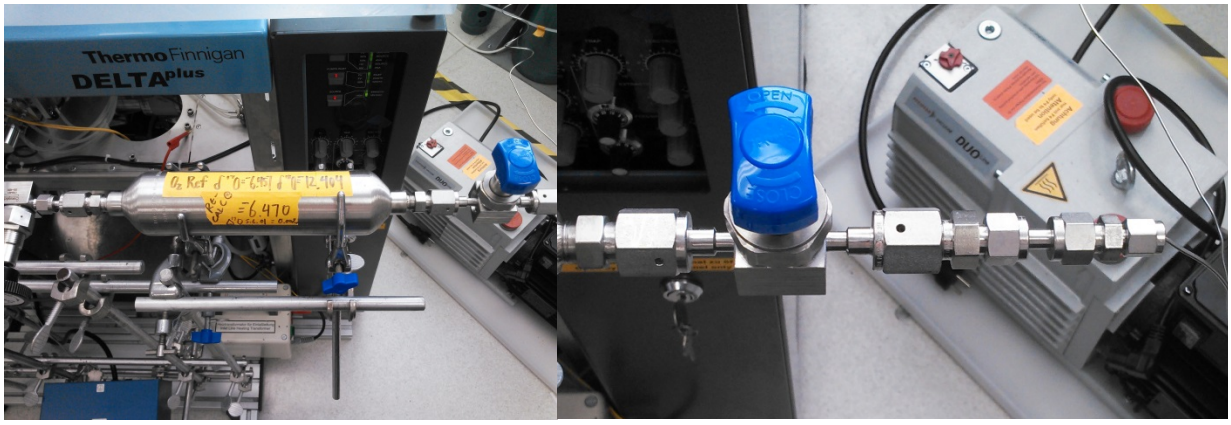

Figure 2-13. A picture of reference gas source (left) and its connection into the laser fluoridation line (right). Note that 316-alloy stainless steel tubing, BCR stainless steel fittings, and Swagelok diaphragm valves are used due to prevent leaking and any consequent isotope fractionation.

Step-by-Step Procedure

- Check pressures in the vacuum line.
- Isolate the sample chamber.

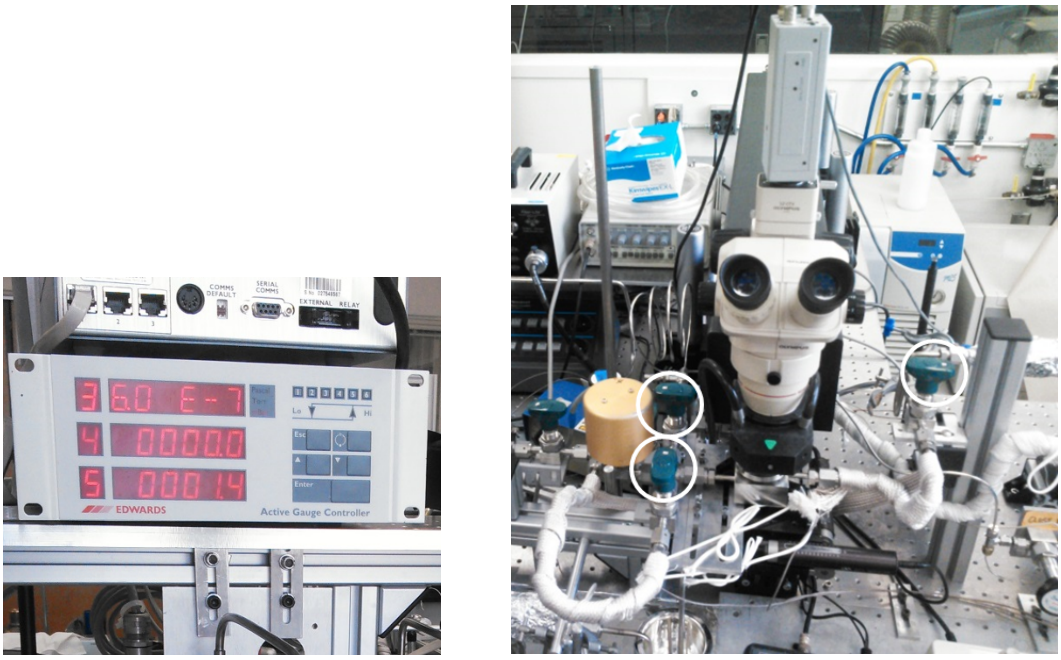

Figure 2-14. Pictures of the pressure display (left) and the vacuum line around the reaction chamber (right). The numbers on the display correspond to the vacuum gage numbers. Register #3 gives the pressure of the system located immediately above the pump. The regular base line pressure is equal to about 5×10^{-7} mbar. Register #4 displays the pressure of the sample chamber. Register #5 shows the fluorine pressure just on the downstream side of the Fluorine source. To isolate the chamber, the valves identified with white circles must be closed.

- Purge the sample chamber with N_2.
- Open the window of the chamber.
- Clean the residue by with a vacuum cleaner and Kimwipes.
- Remove the sample disk and close the window.
- Weigh the samples and place them on the sample disk.
- Place the sample disk, loaded with the samples, into the chamber and close the window.
- Stop N_2 gas.
- Use a roughing pump to remove N_2 from the chamber until the internal pressure reaches about 10^{-3} mbar.
- Use a turbo pump to take the pressure down to the base line.

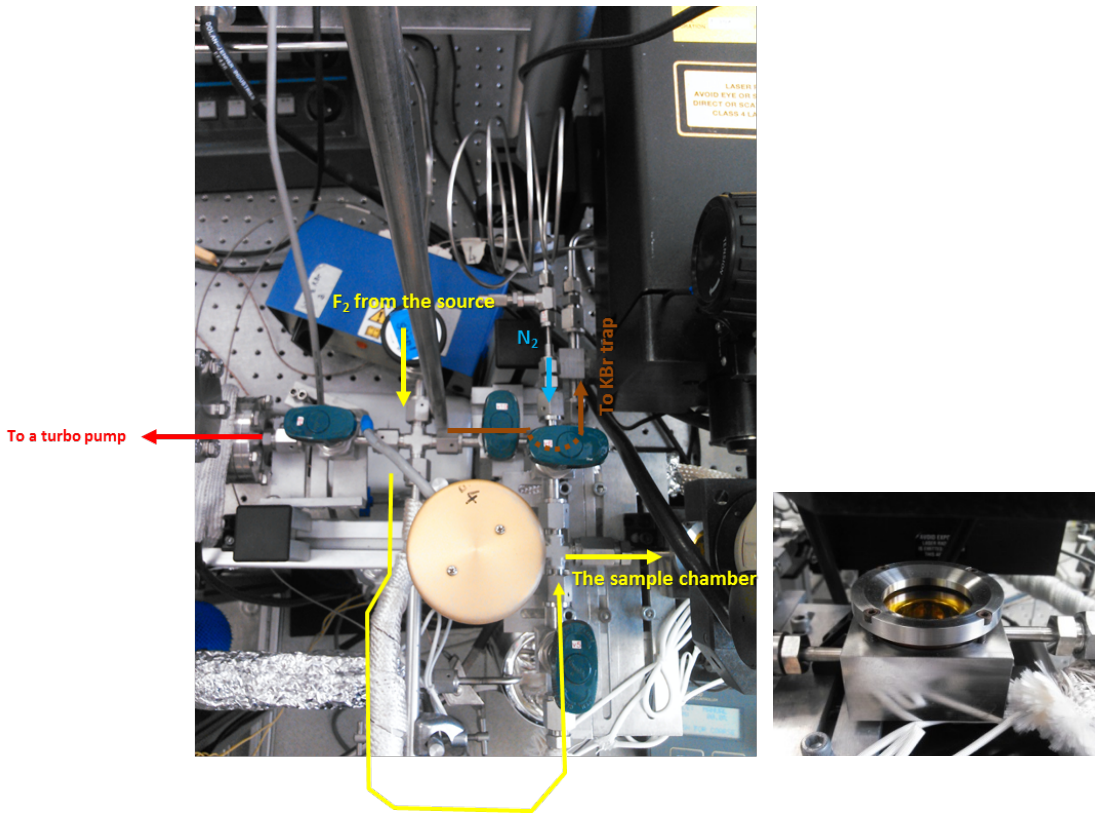

Figure 2-15. Picture of the vacuum line near the sample chamber (left) and of the sample chamber itself (right).

- Isolate the sample chamber.
- Load F_2 gas into the chamber. (About 60 mbar of F_2 is added to the sample chamber per sample). Leave the F_2 in the chamber overnight under IR lamp illumination.
- Start cooling the system for the laser. Turn on the laser once it is cooled.
- Begin using the laser with an output of 25% and then increase the output up to 50%.
- Moving the sample stage is a key to create a single molten droplet. The droplet will be gone after the complete reaction with F_2 gas.

Figure 2-16. Pictures of cooling system (left) and of the laser power and stage controller (right).

- Expand the gas into the KBr trap (10 min).
- For the left trap: It needs to take 10 min to raise a thermos cup with LN_2 completely
- For the right trap: It needs to take 15 min to raise a thermos cup with LN_2 (total 20 min).
- While waiting for the step above, prepare the cold molecular sieve for the next step.
- Use the zeorite molecular sieve-1, cooled by LN_2 to -196 °C, to trap the all gas (25 min).
- Prepare nearly frozen pentane.
- Using the sherbet-like texture of frozen pentane (temperature equal to about -130 °C) to trap the NF_3, but not the O_2, at molecular sieve-1 (30 min).
- Next open the line to molecular sieve-2, again cooled by LN_2 to -196 °C, to trap O_2 (25 min).
- Heat the second molecular sieve (120 °C) to allow the gas intomass spectrometer (30 min).
- Load the reference gas to the bellows (10 min).
- Load the sample gas to the bellows, expanded to 100%.
- Record the pressure in the bellows.
- Repeat expansion and contraction.
- Check for NF_3 in the sample by scanning for molecular mass 71.

- Equalize the pressures of the sample gas and reference gas.
- Start the measurements.

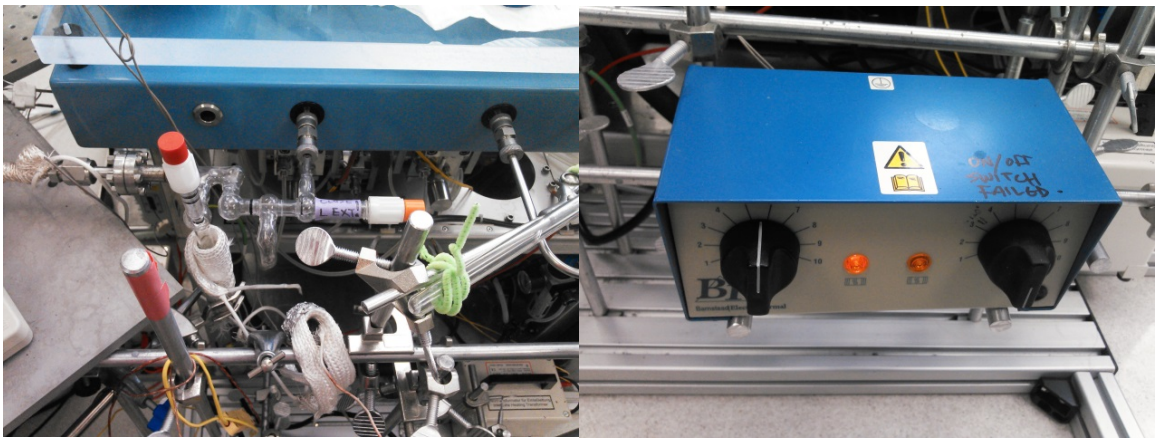

Figure 2-17. Pictures of the glass vacuum line with molecular sieves (left) and of the power supply for a thermocouple (right).

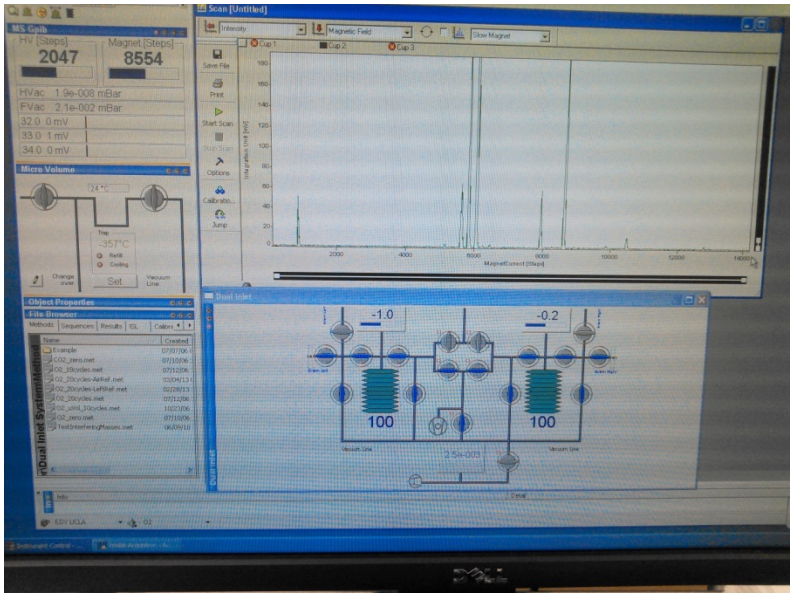

Figure 2-18. A picture showing the user interface of mass spectrometer. Valves and bellows inside of the mass spectrometer are controlled via this screen.

2.6 References

Andersen, C.A., (1970). Analytic methods for the ion microprobe mass analyzer. Part II. *Int. J. Mass Spectrom. Ion Phys*. **3**, 413–428. doi:10.1016/0020-7381(70)80001-8

Burns, R.G., Huggins, F.E. (1972). Cation determinative curves for Mg-Fe-Mn olivines from vibrational spectra. *American Mineralogist*, **57**, 967-985.

Chelgren, J.E., Katz, W., Deline, V.R., Evans, Jr., C.A., Blattner, R.J., Williams, P. (1979). Surface cesium concentrations in cesium-ion-bombarded elemental and compound targets. *Journal of Vacuum Science and Technology*, **16**, 324-327.

ChemSpider Home Page. http://www.chemspider.com/ (Access 2015 April)

Deline, V.R., Katz, W., Evans, C.A., Williams, P., (1978). Mechanism of the SIMS matrix effect. *Appl. Phys. Lett*. **33**, 832–835. doi:10.1063/1.90546

Fahey, A.J., (1988). Ion microprobe measurements of Mg, Ca, Ti and Fe isotopic ratios and trace element abundances in hibonite-bearing inclusions from primitive meteorites. Ph.D. thesis, Washington University.

Hamilton, V.E., (2010). Thermal infrared (vibrational) spectroscopy of Mg-Fe olivines: A review and applications to determining the composition of planetary surfaces. *Chemie der Erde - Geochemistry* **70**, 7-33. doi:10.1016/j.chemer.2009.12.005

Hofmeister, A.M., (1997). Infrared reflectance spectra of fayalite, and absorption data from assorted olivines, including pressure and isotope effects. *Phys. Chem. Miner*. **24**, 535–546. doi:10.1007/s002690050069

Hofmeister, A.M., Pitman, K.M. (2007). Evidence for kinks in structural and thermodynamic properties across the forsterite–fayalite binary from thin-film IR absorption spectra. *Physics and Chemistry of Minerals*, **34**, 319-333.

Liu, M.-C., (2008). Short-lived radionuclides and early solar system chronology. Ph.D. thesis, University of California, Los Angeles.

McKeegan, K.D., (1987). Ion microprobe measurements of H, C, O, Mg, and Si isotopic abundances in individual interplanetary dust particles. Ph.D. thesis, Washington University.

Philipp, P., Wirtz, T., Migeon, H.-N., Scherrer, H., (2007). Electron work function decrease in SIMS analysis induced by neutral cesium deposition. *Int. J. Mass Spectrom*. **264**, 70–83. doi:10.1016/j.ijms.2007.03.019

Reynard, B., (1991). Single-crystal infrared reflectivity of pure Mg_2SiO_2 forsterite and $(Mg_{0.86},Fe_{0.14})_2SiO_4$ olivine. *Phys. Chem. Miner*. **18**. 19-25. doi:10.1007/BF00199039

Rumble, D., Farquhar, J., Young, E.D., Christensen, C.P., (1997). In situ oxygen isotope analysis with an excimer laser using F_2 and BrF_5 reagents and O_2 gas as analyte. *Geochim. Cosmochim. Acta* **61**, 4229–4234. doi:10.1016/S0016-7037(97)00232-9

Sharp, Z.D., (1990). A laser-based microanalytical method for the in situ determination of oxygen isotope ratios of silicates and oxides. *Geochim. Cosmochim. Acta* **54**, 1353–1357. doi:10.1016/0016-7037(90)90160-M

Wittmaack, K., (1980). Aspects of quantitative secondary ion mass spectrometry. *Nucl. Instr. and Meth.* **168**, 343–356.

Young, E.D., Coutts, D.W., Kapitan, D., (1998). UV laser ablation and irm-GCMS microanalysis of $^{18}O/^{16}O$ and $^{17}O/^{16}O$ with application to a calcium-aluminium-rich inclusion from the Allende meteorite. *Geochim. Cosmochim. Acta* **62**, 3161–3168. doi:10.1016/S0016-7037(98)00216-6

Young, E.D., Fogel, M.L., Rumble, D., Hoering, T.C., (1998). Isotope-ratio-monitoring of O_2 for microanalysis of $^{18}O/^{16}O$ and $^{17}O/^{16}O$ in geological materials. *Geochim. Cosmochim. Acta* **62**, 3087–3094. doi:10.1016/S0016-7037(98)00215-4

Young, E.D., Kohl, I.E., Warren, P.H., Rubie, D.C., Jacobson, S.A., Morbidelli, A. (2016). Oxygen isotopic evidence for vigorous mixing during the Moon-forming giant impact. S*cience*, ***351***, 493-496.

Yu, M.L., (1986). Chemical enhancement effects in SIMS analysis. *Nucl. Instruments Methods Phys. Res. Sect. B Beam Interact. with Mater. Atoms* **15**, 151–158. doi:10.1016/0168-583X(86)90273-9

Ziegler, J.F., Biersack, J.P., (1985). The stopping and range of ions in matter, in: treatise on heavy-ion science. *Springer US, Boston, MA*, pp. 93–129. doi:10.1007/978-1-4615-8103-1_3

Ziegler, J.F., Ziegler, M.D., Biersack, J.P., (2010). SRIM – The stopping and range of ions in matter. *Nucl. Instruments Methods Phys. Res. Sect. B Beam Interact. with Mater. Atoms* **268**, 1818–1823. doi:10.1016/j.nimb.2010.02.091

Chapter 3: Quantification of Oxygen Isotope SIMS Matrix Effects in Olivine Samples: Correlation with Sputter Rate[1]

[1] This chapter is based on a manuscript accepted in Chemical Geology.

J. Isa, I.E. Kohl, M.-C. Liu, J.T. Wasson, E.D. Young and K.D. McKeegan.

Quantification of oxygen isotope SIMS matrix effects in olivine samples: Correlation with sputter rate.

3.1 Introduction

Secondary ion mass spectrometry (SIMS) is a useful technique for analyzing isotope abundances in cosmochemical and geochemical samples because of its excellent spatial resolution. For light elements (m < ~60 amu) with relatively high ionization yields, SIMS can provide high precision (sub-permil) analyses of isotope ratios. As with all mass spectrometers, instrumental biases (e.g., mass-dependent fractionations) are calibrated by the use of standard materials, thereby enabling isotope ratios to be reported on a conventional normalized scale (e.g., Standard Mean Ocean Water, SMOW, for oxygen or hydrogen isotopes). Problems can arise due to a lack of appropriate standard materials; such problems can be particularly acute for SIMS, limiting both precision and accuracy of isotopic analyses. Precision is, in part, dependent on the homogeneity of an isotopic standard at fine spatial scales, a characteristic that typically can be assessed only through repeated SIMS measurements. However, even after homogeneity of a material is established, its suitability as a standard for a given isotopic analysis depends on how well the material matches the mineralogical and chemical composition of the target sample(s). This is because elemental and isotopic fractionations in SIMS are inherent in the sputtering process and thus depend upon the interactions of the primary ion beam with the target material. Ionization yields of sputtered target atoms are a function of the near-surface chemical composition of the target and are generally <1%, even for sputtering with reactive primary ion beam species. Thus, instrumental fractionations can be discrepant for materials of differing chemical compositions or crystallinity, leading to inaccurate analyses should an inappropriate standard be used for calibration. The resultant error is referred to as a "matrix effect" since it is generated by a mismatch between the matrix of the sample being analyzed and that of the standard used to calibrate instrumental fractionation. In situ analysis of oxygen isotope abundances was

recognized as an important early application of SIMS, and this continues to the present day. Accordingly, significant efforts have been made to develop standard materials and to quantify matrix effects on SIMS oxygen isotope measurements. The most comprehensive work has involved oxygen isotope analyses of various silicate minerals made under energy filtering with selection of high-energy secondary ions (Eiler et al., 1997; Riciputi et al., 1998). This approach was taken in the hope that, by analyzing only secondary ions that were sputtered from a sample with high initial kinetic energy (typically >325 eV), matrix effects would be reduced and/or instrumental mass fractionation (IMF) would be more stable and could be modeled by systematic parameterization(s). These early investigations demonstrated some general trends between IMF and sample characteristics, for example mean atomic mass. Among related minerals, the IMF was found to correlate with simple chemical parameters; for example, within the olivine solid-solution series the magnitude of oxygen isotope IMF increased linearly with forsterite content by approximately 6‰/amu over a range of ~0.2 in molar Mg/(Mg + Fe) content (Eiler et al., 1997; Riciputi et al., 1998). Interpolation over this limited range in olivine chemistry permitted analytical accuracy in $\delta^{18}O$ of ~1‰, which was commensurate with the precision obtained with this method that utilized magnetic field peak-hopping and ion counting with electron multipliers. However, extrapolation to more Fe-rich compositions showed very large deviations from the linear relationship, resulting in a $\delta^{18}O$ error (matrix effect) ranging up to ~20‰ for pure fayalite (Eiler et al., 1997).

With the development of large-radius, forward-geometry ion microprobes (e.g., the CAMECA ims-1270 and ims-1280), rapid, high-precision (<0.5‰) oxygen isotope measurements became possible by measuring isotope beams simultaneously with Faraday cup detectors distributed along the instrument's mass focal plane (e.g., Kita et al., 2009; Kolodny et al., 2003; Treble et al.,

2007). To achieve the necessary high intensity signals from small (~10-25 μm) analytical spots, the mass spectrometer must be set to transmit the abundant, low-energy secondary ions, i.e., the peak of the sputtered ion energy distribution. These methods have supplanted the high energy-filtering approach because they enable much faster analyses (3-5 min vs. 15-30 min) that consume less sample while still yielding significantly improved precision. However, higher precision without an equivalent increase in accuracy is always problematic, and therefore today's analyses also require an improved quantification of matrix effects appropriate to the analytical conditions utilized.

In this contribution, we focus on oxygen isotope analyses of olivine. We are interested in meteoritic samples that often span a very wide range in FeO contents compared to terrestrial mantle olivines (Criss, 2008 and references therein); for example, olivine phenocrysts in unequilibrated carbonaceous chondrites range from ~Fa0 to Fa80 (e.g., Wasson and Rubin, 2003), olivine in Martian meteorites is intermediate from ~Fa20 to Fa50 (e.g., Mikouchi et al., 2001), olivine in HED meteorites is ~Fa30 to Fa90 (Warren et al., 2014, and references therein), and olivine in angrites goes from ~Fa10 to Fa86 (Keil, 2012). Previous studies of matrix effects in meteoritic olivine have come to different conclusions. Valley and Kita (2009) found significant matrix effects that varied non-linearly from forsterite to fayalite, however only a limited number of intermediate composition olivines were investigated with no samples analyzed between Fa40 and Fa100. In contrast, Jogo et al. (2012), using similar analytical methods and instrumentation, found no systematic differences in IMF among terrestrial (Fa11) and meteoritic (Fa35 and Fa63) olivine standards. The reasons for this discrepancy are not apparent. Our goal here is to investigate oxygen isotope IMF over the entire olivine Fe-Mg solid-solution series. We determined the oxygen isotope compositions of nine separate, homogeneous olivine samples by

laser-assisted fluorination isotope-ratio mass spectrometry and then made high precision SIMS analyses of the same samples to define a calibration curve between instrumental mass fractionation and sample compositions. We also investigated whether matrix effects correlate with the concentration of Cs ions implanted in the sample surface. Our results permit interpolation of matrix effects for intermediate olivines, thereby enabling high precision and high accuracy for investigations of cosmochemical samples.

We investigated the magnitude and reproducibility of instrumental mass-dependent fractionation of oxygen isotopes in secondary ion mass spectrometry (SIMS) analyses of olivine crystals of different major element chemistry (from Mg-rich to Fe-rich) in order to improve the accuracy of in-situ O-isotope measurements in geochemical/cosmochemical olivine samples. We found that oxygen isotope SIMS matrix effects are reproducible, and developed a model curve that can be used for correcting instrumental mass fractionation of olivine samples of intermediate chemical composition. The changes in instrumental mass fractionations were likely caused by differing Cs concentrations in the near surface regions of the samples due to different sample sputtering rates.

3.2 Samples and Analytical Technique

Seven terrestrial and two meteoritic olivine samples, covering a wide range of Fe/Mg compositions, were studied (Table 1). The sample descriptions are in the appendix. All samples were handpicked under a binocular microscope. The samples were carefully examined to avoid other phases such as opaque inclusions, or yellow brown to dark brown colored veins that probably consisted of carbonate and Fe-bearing oxide. Some grains were mounted in epoxy resin or indium for SIMS measurements, while other portions of selected grains were used for laser fluorination analysis. Several samples (Day Book dunite, Rockport, and those from the

Skaergaard intrusion) were washed prior to laser fluorination analysis to dissolve adhering opaque oxides and other weathering materials. The samples were washed in individual beakers by following a protocol of hydrochloric acid (3 mol/l overnight), deionized water in an ultrasonic bath, nitric acid (2 mol/l overnight), deionized water in an ultrasonic bath, and methanol in an ultrasonic bath. After the acid treatment, the samples looked transparent and had a uniform color (yellow to slightly green in the range Fa0 to Fa70). All samples were dried in an oven at 50 °C for three to five days prior to the laser fluorination analysis.

Quantitative mineral elemental compositions were obtained by electron microprobe analysis (EPMA) with the UCLA JEOL8200, with 20 s counting times for peaks and 5s counting time for backgrounds. The beam currents used were ~15 nA at 15 kV; ZAF corrections were made.

For laser-assisted fluorination, samples were melted in the presence of fluorine gas by irradiation with an infrared laser and the isotopic composition of liberated oxygen was measured with a Thermo Finnigan Delta Plus gas-source isotope ratio mass spectrometer (IRMS) in Dual Inlet mode at the Stable Isotope Lab, UCLA, following methods most recently described in Young et al. (2016). SIMS analyses were performed on the UCLA 1270 and 1290 ion microprobes by using a primary Cs^+ beam and analyzing low-energy (0-25eV) negative secondary ions. The measurements were carried out during four different analytical sessions, with the ims-1270 in 2012, 2013 and 2014, and with the ims-1290 in 2017. On the ims-1270, samples were sputtered with a 20 keV Cs^+ primary beam with intensities of 3, 4 and 6 nA focused to spots with a diameter in the range of 20-40 μm; on the ims-1290, primary beam intensities of 2.5 nA and 4 nA were used (spot sizes ~10-20 μm). A normal incidence electron gun was used to compensate for sample charging. Oxygen isotopes ^{16}O and ^{18}O were measured simultaneously by using two

Faraday cups (10^{10} and $10^{11}\Omega$ resistors) in the multicollector system. The acquisition times per analysis spot on the ims-1270 were 200 s (12 to 15 cycles of 10 s integration) and resulted in internal uncertainties less than 0.1‰. On the ims-1290, secondary ions were counted for ~1 min (10 cycles of 5 s integrations) and internal and external uncertainties between 0.1‰ and 0.2‰ were achieved. The relative sputter rates for individual samples were calculated based on the depths of crater pits sputtered in a 50 μm × 50 μm raster mode with a 5 nA primary Cs^+ beam by ims-1270. Each sample was sputtered for 20 min. The crater pits depths were measured with a MicroXAM interferometer.

For each SIMS analytical session, measurements of San Carlos olivine (hereafter, SC-olivine) were used to calibrate the instrumental mass fractionation and the relative yields of the two Faraday cup detectors used for the $^{18}O^-$ and $^{16}O^-$ beams. Although Faraday cup amplifier gains are calibrated electronically at the outset of each analysis session, this intercalibration is not necessarily accurate at the permil level. This is acceptable because the relative amplifier gains are stable on the time scale of an analytical session (typically 1 day) and thus the overall calibration is reliant on the reproducibility of analyses of the primary standard (SC-olivine). We thus define the overall correction factor as "instrumental mass fractionation" (IMF) according to:

$$IMF = (^{18}O/^{16}O)_{SC\text{-}SIMS} / (^{18}O/^{16}O)_{SC\text{-}LF} \quad (3\text{-}1)$$

where $(^{18}O/^{16}O)_{SC\text{-}SIMS}$ refers to the isotopic ratio in SC-olivine measured by SIMS and $(^{18}O/^{16}O)_{SC\text{-}LF}$ is the "true" value determined by laser-fluorination ($\delta^{18}O_{SMOW} = 5.19‰$). In the absence of matrix effects, the measured $^{18}O/^{16}O$ ratios of other olivine grains can be corrected for IMF obtained in each session by:

$$(^{18}O/^{16}O)_{SIMS,\ corrected} = (^{18}O/^{16}O)_{SIMS,\ measured} / IMF \quad (3\text{-}2)$$

The ratios can then be converted to delta-notation by normalizing to the accepted value of $^{18}O/^{16}O$ in standard mean ocean water ($(^{18}O/^{16}O)_{SMOW} = 0.00200520$; Baertschi, 1976):

$$\delta^{18}O = [(^{18}O/^{16}O)_{SIMS,\ corrected} / (^{18}O/^{16}O)_{SMOW} - 1] \times 1000 \quad (3\text{-}3)$$

The $\delta^{18}O$ values of all olivine standards measured in this study by laser-assisted fluorination are given in Table 3. The corresponding oxygen isotope ratios of these olivines can be calculated via:

$$(^{18}O/^{16}O)_{LF} = [\delta^{18}O/1000 + 1] \times (^{18}O/^{16}O)_{SMOW} \quad (3\text{-}4)$$

The gas-source Isotope Ratio Mass Spectrometry (IRMS) analyses are calibrated by sample standard bracketing with a reference gas, thus if the laser-assisted fluorination reactions go perfectly to completion (producing purified O_2 gas), analyses are free of matrix effects. Said another way, with 100% yield the gas in an IRMS measurement perfectly reflects the isotope ratio and molar amount of analyte contained within the starting material. Repeated measurements of San Carlos olivine in the UCLA IRMS laboratory coinciding with this study yielded results, precise and accurate at the level of ± 0.13 ‰ 1 S.D. or ± 0.033 ‰ at 1 standard error of the mean (n=17) (Young et al., 2016).

3.3 Results

The chemical compositions of the olivines investigated are given in Table 2 as the average of replicated electron microprobe analyses. Compositions range from magnesium-rich (Fa2) to nearly pure fayalite, with 4 samples spanning intermediate compositions between San Carlos (Fa9) and the Rockport end-member (Fa97). All samples are close to the forsterite-fayalite join, with only minor amounts of elements other than Mg, Fe, Si and O. Only the Rockport sample has an appreciable tephroite component, with 2.2 wt% MnO, and the Skaergaard samples EG

5108 and EG 1907 are the only others to have detectable MnO at ~0.4 and ~0.8 wt. %, respectively. Fayalite content is calculated as mol % Fe/(Mg + Mn + Fe); estimated uncertainties in the reported fayalite compositions are ~ 0.1% to 0.7%. The IMF-corrected $\delta^{18}O$ values on the SMOW-scale are given in Table 4. Repeated measurements of San Carlos olivine yielded an external reproducibility of ±0.2 ‰ 1 S.D. (n=77). It is readily observed (Figure 3-1) that the SIMS $\delta^{18}O$ values (calculated by eq. 3 and listed in Table 4) do not agree in all cases with the values determined by laser-fluorination (Table 3); the discrepancies are attributed to SIMS matrix effects.

The magnitude of the SIMS matrix effect for a given sample is calculated as the difference, expressed in permil, between the instrumental fractionation determined on a sample compared to that determined for the primary standard, San Carlos olivine, under the same experimental conditions. Thus, matrix effect is quantified by the expression:

$$1000\ (\ln(\alpha) - \ln(\mathrm{IMF})), \text{ where } \alpha = (^{18}O/^{16}O)_{SIMS} / (^{18}O/^{16}O)_{LF} \qquad (3\text{-}5)$$

and the IMF is defined for each analytical session by eq. (1). These matrix effects vary with olivine composition: they are relatively small to unresolvable within our experimental uncertainties among Mg-rich olivines (Fa<25), but they increase in magnitude with increasing Fe content, reaching values of -6 to -11‰ for Fe-rich olivines (Fa>95) under our experimental conditions. Relative sputter rates were determined for each olivine composition by measuring the crater depth resulting from sputtering by a ~5 nA Cs beam rastered over 50 × 50 μm for 20 min. The measured depths are normalized for small deviations in primary beam intensity from the intended 5 nA current (Table 5). The reported uncertainty in the calculated relative sputter rates is taken as the reproducibility of crater depths for repeated sputtering experiments on San Carlos olivine in different mounts.

3.4 Discussion

The primary goal of this work was to determine if systematic behavior of the SIMS IMF could be found such that precise and accurate measurements of oxygen isotopes for olivine of intermediate Fa content could be "routinely" achieved with an appropriate calibration for matrix effects. A fundamental requirement for this to be useful in a practical sense is that the matrix effect systematics be reproducible, at least over instrumental conditions that are sufficiently well-defined as to be routinely achievable. As can be seen in Table 4, analyses made years apart for five olivine samples (in addition to the primary standard, San Carlos) with two SIMS instruments yielded reproducible results within experimental uncertainties of typically a few tenths permil for all the samples except "Day Book dunite" and "Rockport". For example, analyses of olivine EG 5108 Skaergaard with composition Fa34 agreed within 0.1 ‰, allowing for precise calibration of a small matrix effect of -0.6‰ (relative to San Carlos). The Day Book dunite olivine Fa values are similar to that of San Carlos olivine, and therefore any matrix effect is expected to be small. Instead, a relatively large dispersion of the data was found, and this is likely attributable to the sample heterogeneity. We therefore excluded Day Book dunite olivine from further consideration as a standard suitable to calibrate matrix effects.

For the Rockport olivine, a nearly pure fayalite end-member, multiple SIMS analyses performed on the ims-1270 in 2013 and 2014 produced San Carlos normalized $\delta^{18}O$ values that disagreed by up to 3‰ (Table 4) suggesting either sample heterogeneity or irreproducibility in calibrating the matrix effect at this extreme iron content. Following a suggestion by Noriko Kita, we found that the dispersion in the data was associated with the primary beam intensity used in the analysis, which ranged from ~3 nA to ~6 nA in different analytical sessions (Figure 3-2a). Such an effect

is unexpected based on sputtering theory, so to investigate further we made a series of measurements with different Cs+ beam currents, this time using the ims-1290. Because a 6 nA Cs+ beam yielded $^{16}O^-$ signals that were too high, saturating the FC amplifier (10^{10} Ω resistor), we proceeded with the measurements using beams of 4.2 nA down to 2.5 nA. Charge compensation was achieved by a normal incidence electron gun, as in the previous experiments. However, this time we found no evidence for any correlation of IMF with primary beam intensity (Figure 3-2b). The matrix effect between Rockport and San Carols was a constant -9.3‰ over a dozen spots analyzed. We conclude that the apparent primary beam dependent matrix effects seen earlier were the result of improper charge compensation on very Fe-rich olivine under the relatively high primary beam currents used previously. The fact that this artifact only became apparent for the most Fe-rich sample makes sense because the charging condition in the analysis spot can be different for samples of differing conductivity if the electron cloud produced by the normal incidence electron gun is not tuned properly, thus producing insufficient density above the sample surface to neutralize all buildup of positive charge. In such a case, the sample high voltage supply may provide more or less negative charge depending on primary beam current and surface conductivity, which would lead to a shift in the energy spectrum of the sputtered ions, thus changing the IMF. This experience underscores the need to be very cautious, for example by exploring a range of instrumental parameters, when attempting to calibrate mass fractionation of oxygen in very Fe-rich samples (especially if Fe-poor San Carlos olivine is used as a primary standard). In the remainder of this discussion analyzing systematic behavior of IMF, we consider only those data for Rockport that showed a constant matrix effect, independent of primary beam current. The oxygen isotope matrix effects reported by various investigators utilizing different instruments and analytical approaches are shown as a

function of olivine sample composition in Figure 3-3a. The plot incorporates data obtained via Extreme Energy Filtering (EEF, Eiler et al., 1997; Riciputi et al., 1998) as well as data measured for low-energy secondary ions (Kita et al., 2010; Nakashima et al., 2013; Tenner et al., 2015, 2013; Valley and Kita, 2009) as was done in our study. As alluded to earlier, there is a wide variability in matrix effect behavior which depends strongly on the energy regime of the secondary ions analyzed. The magnitude of the matrix effect is in general much higher for analyses made via EEF, which is perhaps not surprising given that the overall magnitude of the IMF is also much higher for very high energy secondary ions.

The good reproducibility of the matrix effects that we observe for the analyses of low energy secondary ions allows us to define a systematic behavior dependent only on the Fa content of the olivine that is sufficiently precise to allow for interpolation to derive IMF for an olivine of intermediate composition for which a standard of closely matching Fe-content is unavailable (Figure 3-3b). The empirical correction curve can be fit by either a sigmoid or a quadratic expression. The matrix effect relative to San Carlos olivine can be expressed by either the sigmoid $-87.8 /(1 + \exp (2.14 \times (100/Fa))$ or the quadratic $-10.6 \times p^2$ with $p = (Fa/100 - 0.09)$, respectively. Note that SC-olivine Fe molar fraction is 0.09. The scatter about the calibration curve is shown as a function of Fa content in Figure 3-3c; the residual errors are characterized by a standard deviation of 0.4‰, which is a measure of the overall accuracy in $\delta^{18}O$ over the Fo-Fa solid solution. In principle, our empirical correction curve could be instrument-dependent. However, the fact that our data from both ims-1270 and ims-1290 plot within error of the model curve indicates that matrix effects measured for low-energy secondary ions are similar, regardless of the instrument used. As can be seen in Figure 3-3b, this expectation is confirmed by examining olivine O-isotope data from other studies measuring low-energy ions (Kita et al.,

2010; Nakashima et al., 2013; Tenner et al., 2015, 2013; Valley and Kita, 2009). Additional complications could arise due to the orientation of crystal faces relative to the sputtering beam which is thought to play a role in causing small variability in IMF for SIMS oxygen isotope measurements of Fe-oxides (Huberty et al., 2010). Although such effects have not been demonstrated in silicates, we minimized the possibility of systematic shifts due to crystallographic orientation by analyzing multiple grains at random orientations. The good agreement of our data, obtained over multiple analytical sessions, with data obtained under generally similar experimental conditions but in a different laboratory (Kita et al., 2010; Nakashima et al., 2013; Tenner et al., 2015, 2013; Valley and Kita, 2009) demonstrates that the major cause of matrix effects in the olivine solid-solution series is the Fa content and that SIMS IMF can be corrected empirically with an accuracy that is close to analytical precision.

Relationship to Sputter Rate: The fit shown in Figure 3-3b is purely empirical and the question arises whether there is some underlying physical reason for the dependence of oxygen isotope IMF on Fe concentrations in olivine. In the course of our investigations, we found that the sputter rate of olivine also varies systematically with Fe-content (Figure 3-4). For a given beam current, impact energy, focusing condition, etc., fayalite sputters more quickly than does forsterite. This is important because the ionization yield of negative secondary ions (like O^-) is a strong function of the concentration of Cs within the near surface of the sputtered area on the sample (e.g., Andersen, 1970; Yu and Mann, 1986). At steady-state, the concentration of Cs implanted from the primary ion beam is inversely proportional to sputter rate, so we might also expect that ionization yield would show a dependence on sputter rate. For Cs bombardment of simple matrices (metals and metal silicides), Deline et al. (1978) found a non-linear relationship between negative ion useful yield (defined as number of ions detected/ number of atoms

sputtered) and inverse sputtering rate. Using Auger spectroscopy, Chelgren and colleagues quantified the measured surface Cs atom fraction and the useful yield of Si^- which varied by a factor of several thousand between Pt_2Si and Si metal (Chelgren et al., 1979). Although these studies were conducted to quantify matrix effects in the yield of negative ions for elemental analysis, similar principles must also apply to isotopic measurements, i.e., to SIMS IMF. The reasoning can be seen clearly by considering the limiting case: as useful yield approaches unity, instrumental mass fractionation must go to zero, and if IMF is zero, then matrix effects vanish. We did not directly measure absolute useful yields in this study, however a correlation of useful yield with matrix effect can be inferred from our data. As can be seen in Figure 3-4, the sputter rate of Rockport is approximately 2 times faster than that of SC-olivine and therefore one would expect that the secondary ion intensity of oxygen from Rockport should be nearly double of that of SC-olivine (per nA Cs+ bombardment). However, $^{16}O^-$ count rates of Rockport increased by only approximately 10 to 20% compared to that of SC-olivine, thus indicating that ionization yields of O^- are lower in fayalite than in Mg-rich olivine. We find that in olivine, O-isotope SIMS matrix effects are inversely correlated with sputter rate according to a sigmoid curve (Figure 3-5). This is explained as a result of the difference in useful yield of O^- between Mg-rich and Fe-rich olivine, which is largely due to the difference in Cs concentration at the surface of the sputtered area. Fayalitic olivine, with its relatively high sputter rate, has a correspondingly low concentration of Cs and thus a relatively lower ionization for O^- and therefore a larger instrumental mass fractionation. The nonlinear dependence of ionization probability on Cs concentration (Chelgren et al., 1979) results in a high sensitivity of the matrix effect for Fe-rich olivine. On the other hand, for sufficiently slow sputter rates (as in Mg-rich olivine), a threshold Cs concentration is achieved such that matrix effects become relatively insensitive to small

changes in sputter rate due to changing Fa content. The phenomenon of Cs concentration reaching an effective saturation level for low sputter rates is consistent with a sigmoid curve as shown in Figure 3-5.The correlation of matrix effect with sputter rate, effectively a correlation with Cs concentration, is clear in a simple, essentially binary, solid solution series as in olivine. However, it is not straightforward to generalize this result to other mineral systems. For example, Page et al. (2010), found more complicated O-isotope matrix effects in garnet where sputter rate was not correlated with the magnitude of instrumental mass fractionation. Matrix effects in carbonates are also complicated (e.g., Rollion-Bard and Marin-Carbonne, 2011; Śliwiński et al., 2016a, 2016b) although Śliwiński and colleagues were able to fit the IMF data as a function of Fe/(Fe+Mg) content of the carbonates along the dolomite – anchorite solid solution to a Hill equation, which has a similar functional form to the sigmoid that we used relating change in IMF to sputter rate in olivine.

The primary purpose of this contribution was to develop a useful calibration scheme for the accurate measurements of oxygen isotope ratios in olivine over a wide range of chemical compositions. Although the exact physics leading to matrix-dependent mass fractionation in SIMS have not been uncovered, we can nevertheless see that achieving high ionization yields by supplying more Cs at the sputtering surface may help to decrease O-isotope SIMS matrix effects. Such a strategy may provide practical benefits in improving accuracy and precision of other isotopic measurements as well.

There have been several technical approaches tried for the purpose of increasing negative secondary ionization yields for reducing matrix effects. For example, flooding the sample surface with neutral Cs has been suggested (*e.g.* Bernheim et al., 1979; Wirtz and Migeon, 2004) to

enhance negative ion counts. Alternatively, reducing primary beam impact energy might increase useful yield (and thus reduce the matrix effect) by reducing both the sputter rate and the range (depth) of the implanted Cs. Changing the angle of incidence to be closer to normal to the sample surface (as in the CAMECA NanoSIMS) would also reduce sputter rate and improve Cs saturation, however the primary beam angle is not adjustable independent of impact energy in the CAMECA ims 1270 and 1290 ion microprobes. It is also worth noting that there is a practical limit to reducing sputter rates because low secondary ion intensities may prohibit use of Faraday cup detectors necessary for achieving high precision analyses.

3.5 Conclusions

SIMS matrix effects on instrumental mass fractionation of oxygen isotopes in olivine are reproducible between two different instruments in four different sessions and can therefore be accurately calibrated. The correlation between Fa content and instrumental mass fractionation implies that matrix effects can be corrected for in intermediate composition olivines by using a model curve and a reference IMF calibrated for a given analytical session on a primary standard (e.g., San Carlos olivine). Precision and accuracy of ~0.4‰ in $\delta^{18}O$ is achievable at the ~10-25 μm spatial scale. Accurate knowledge of the chemical composition (Fa content) of an olivine sample is required in order to correct matrix effects.

A higher Cs concentration at the sputtered surface helps reduce SIMS oxygen isotope matrix effects. Because sputter rate is the main control on the Cs concentration in the sputtered surface for a given matrix, it may be possible in principle to develop a correction for matrix effects in IMF by comparing relative sputter rates between an unknown and a standard sample; however, measuring chemical compositions of the samples is generally easier and more precise. For SIMS

isotopic analyses of samples for which no matching mineral standards exist, one should exercise particular caution due to the potential for large matrix effects especially when very different sputter rates are found between the samples and standards.

3.6 Acknowledgements

The authors thank Frank Kyte and Rosario Esposito for assistance with EPMA. We also thank Axel Schmitt and Rita Economos for assistance with SIMS analyses. The paper has benefitted from constructive reviews by Noriko Kita and an anonymous reviewer which we appreciate. This work was supported by NASA NNX 13 AH49G and NNX 14 AJ84G (JTW), NASA NNX09AG89G (KDM), and NASA Emerging Worlds NNX15AH43G (EDY). The UCLA ion microprobe laboratory is partially supported by a grant from the NSF Instrumentation and Facilities Program.

3.7 Figures

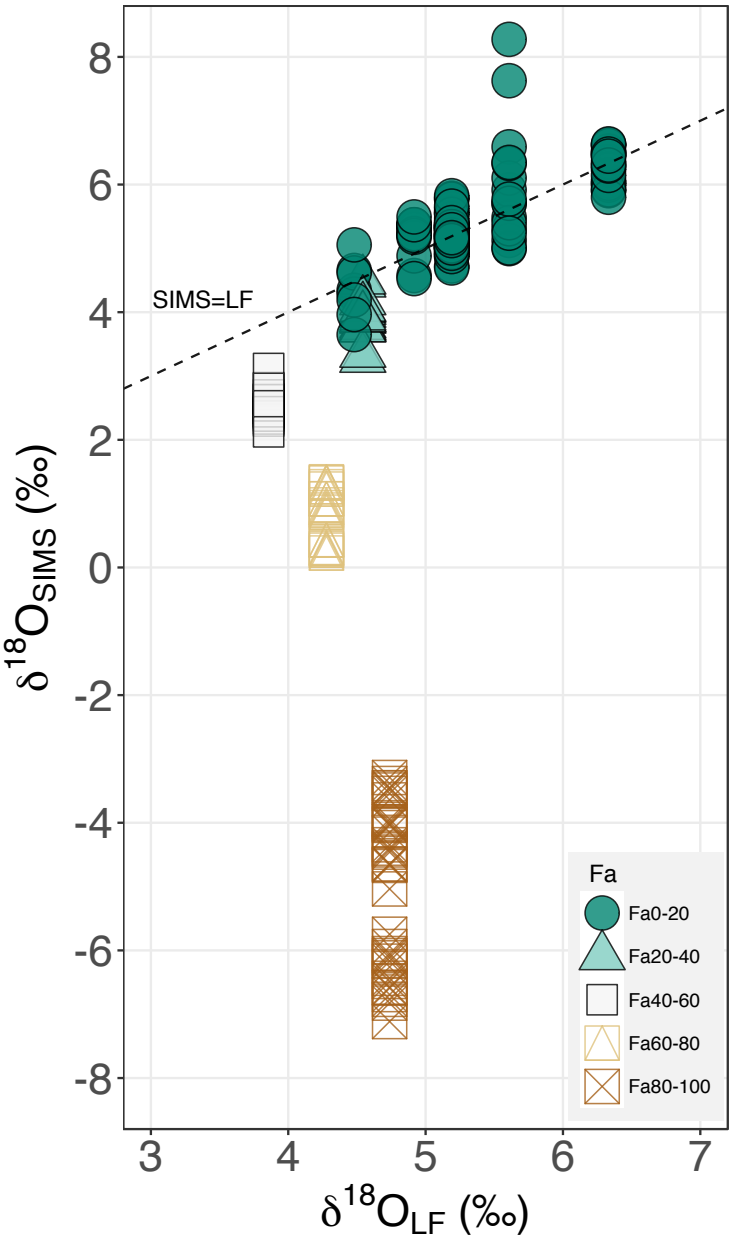

Figure 3-1. $\delta^{18}O$ values of olivine samples measured by SIMS (data as acquired from individual SIMS spots) are plotted as a function of the true $\delta^{18}O$ as determined by laser fluorination (LF). Data are corrected for instrumental mass fractionation during SIMS analyses by comparison with San Carlos olivine (see text). The dashed 1:1 line represents where corrected $\delta^{18}O$ measured by SIMS and LF analyses agree; deviations from the line indicate matrix effects in the SIMS measurements. The Fe concentrations of different olivine samples are indicated in the legend with Fa = Fe/(Mg + Mn + Fe) mol%.

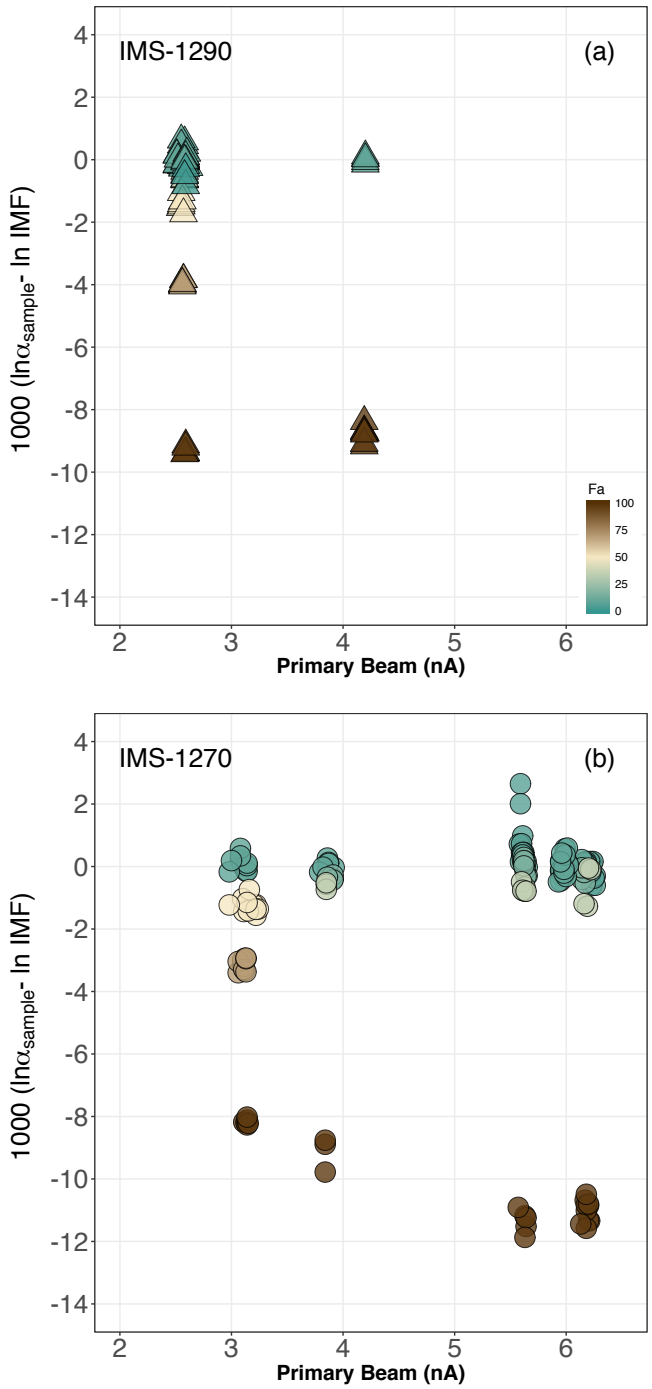

Figure 3-2. O-isotope SIMS matrix effects for different primary beam intensities. The Fe molar fractions are expressed as Fa = Fe/(Mg + Mn + Fe) mol% and color-coded. No primary beam effects were found among ims-1290 analyses (a), whereas data from measurements with ims-1270 indicate primary beam dependent matrix effects in Fe-rich samples (b) (see text). During a given analytical session, fluctuations of primary beam intensities are small.

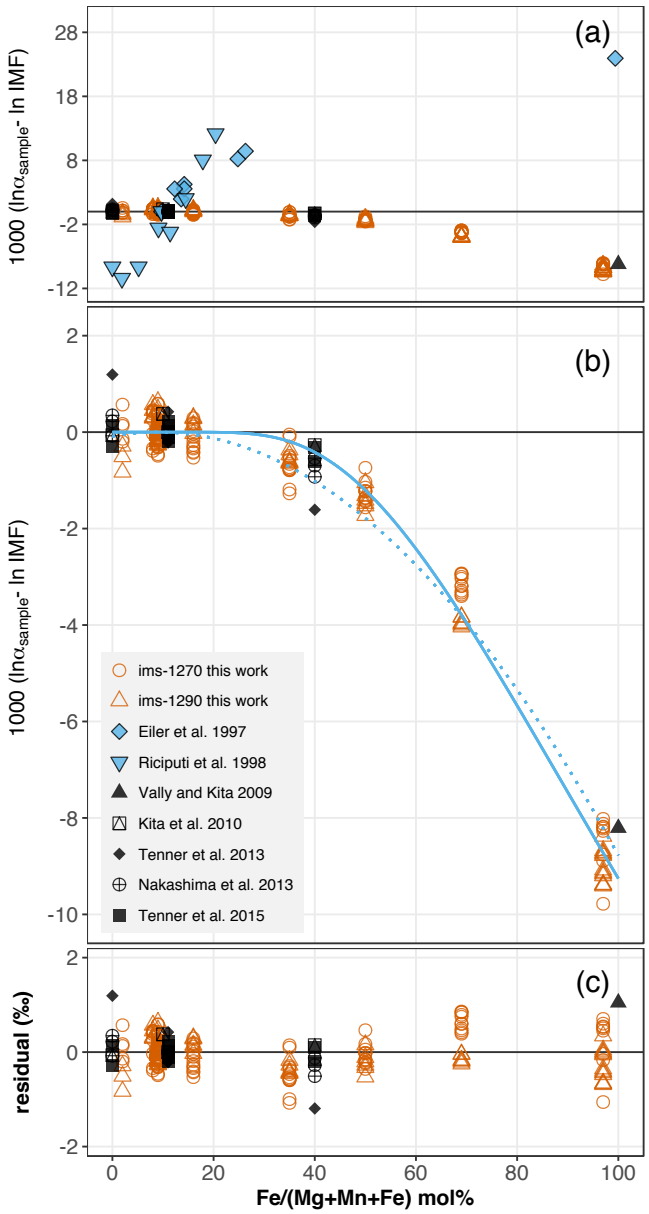

Figure 3-3. O-isotope SIMS matrix effect as a function of Fe molar fractions of olivine. The Fe molar fractions are expressed as Fe/(Fe + Mg + Mn) mol%. **(a)** Plotted are SIMS matrix effects normalized to SC-olivine (this study; also Valley and Kita 2009; Kita et al. 2010; Tenner et al. 2013 and 2015; Nakashima et al. 2013) and extreme energy filtering results (Eiler et al. 1997; Riciputi et al. 1998) which are highlighted in blue. **(b)** SIMS matrix effect (excluding extreme energy filtering data) are fit by a sigmoidal curve, $y = -87.8 / (1 + \exp(2.14 \times (100/Fa))$ (blue solid line). The data can also be fit by a parabola $y = -10.6 \times p^2$ with $p = (Fa/100 - 0.09)$ (blue dash line). (c) The residuals from the best regression curve (sigmoid) as a function of Fa content. The SIMS analytical reproducibility (a standard deviation of duplicated San Carlos olivine analyses) is 0.2‰ (n=77). Most of the data from literature agree within 2 sigma of the fit curve.

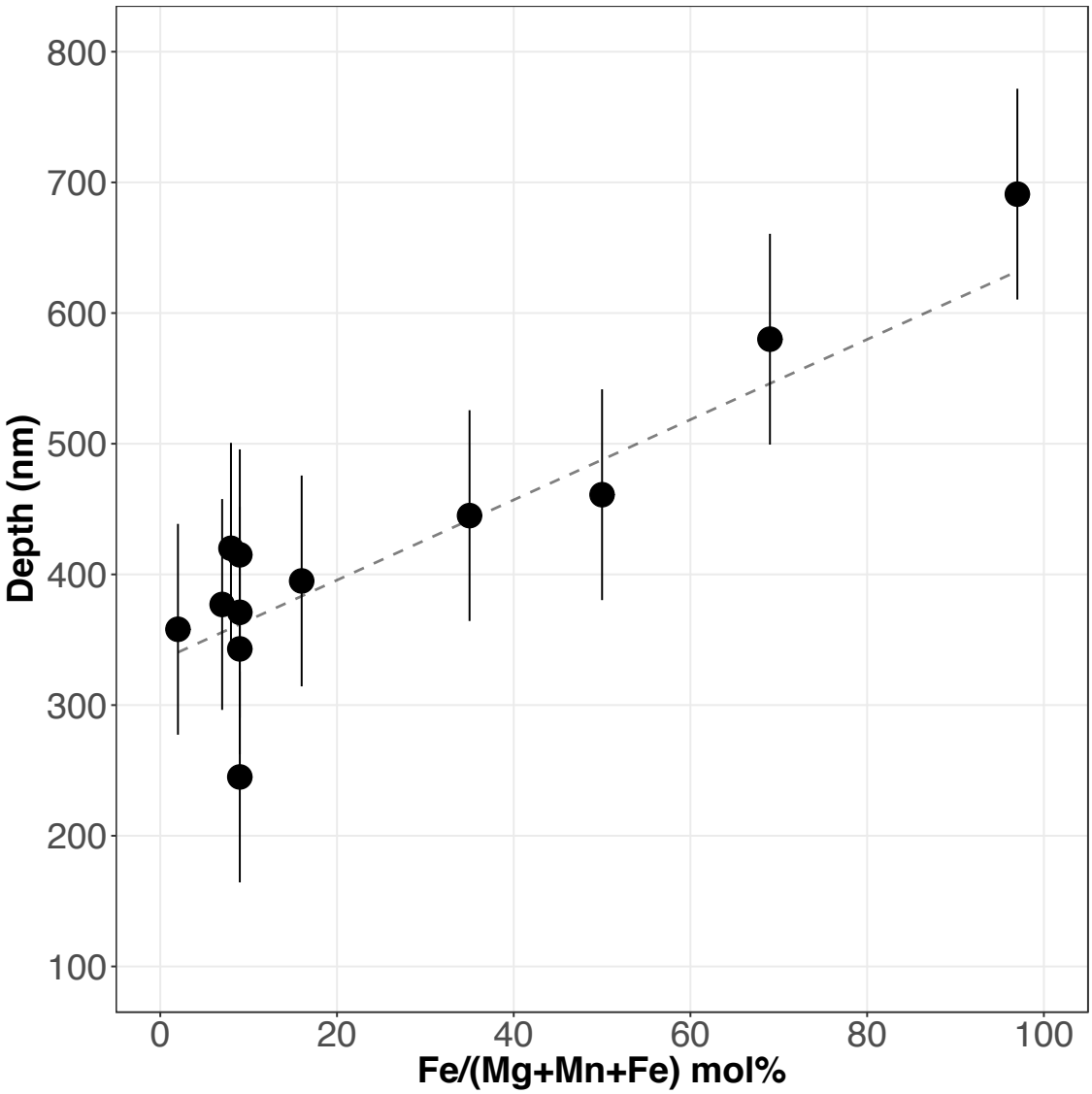

Figure 3-4. Sputtered crater depth vs. molar fraction of Fe in olivine samples sputtered under fixed conditions. Relative sputter rate (proportional to the depth of the crater) is linearly correlated with the molar fraction of Fe in olivine.

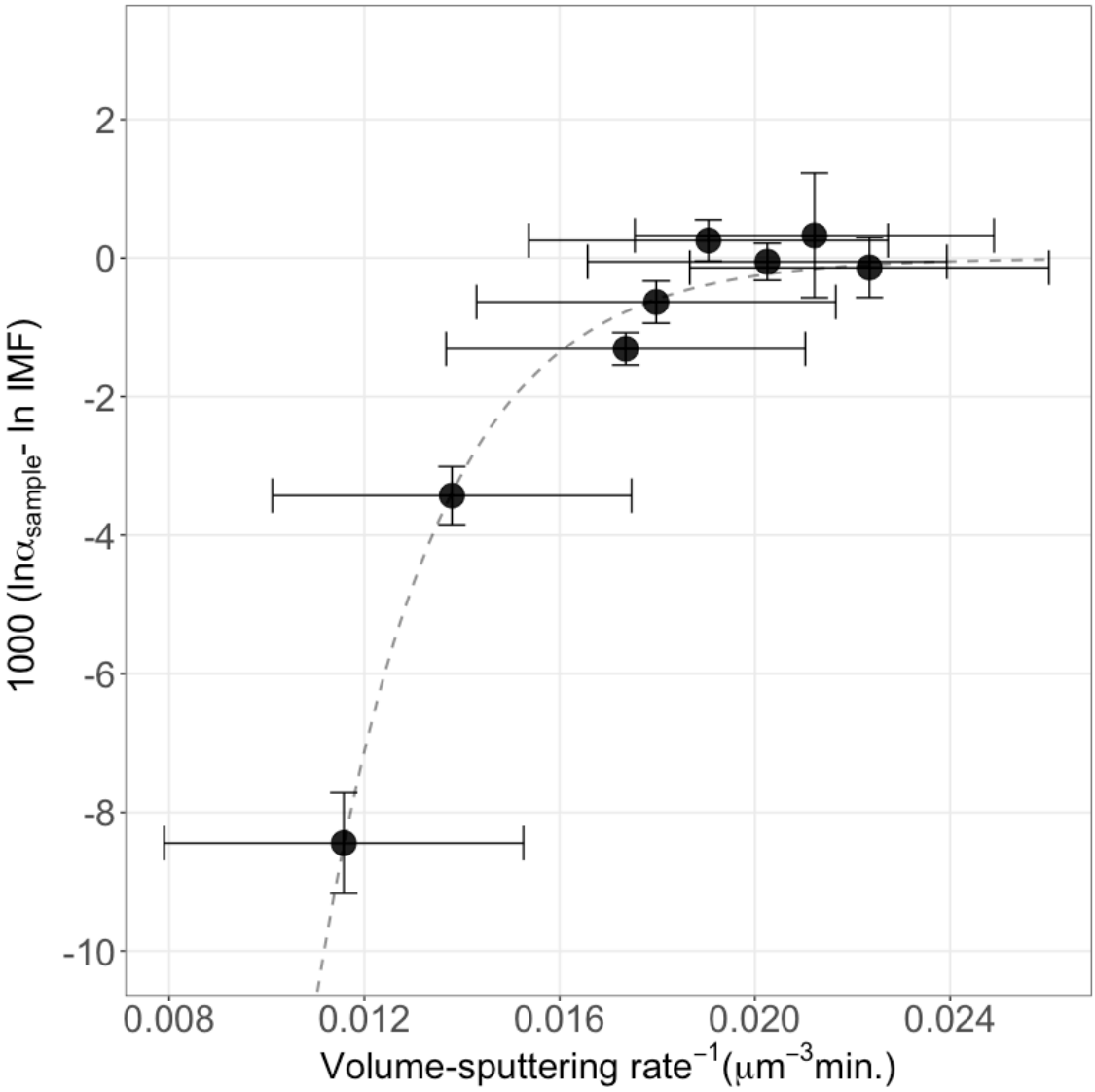

Figure 3-5. Inverse of volume-sputtering rate versus O-isotope SIMS matrix effect. The y-axis uncertainties are propagated errors based on the standard deviation of duplicated measurements for individual samples analyzed with ims-1270 or ims-1290, and a standard deviation of that for SC-olivine 0.2 ‰ (n=77). The SIMS matrix effect is correlated with the inverse sputtering rate which is proportional to the Cs^+ concentration in the near surface of the sputtered sample (Deline et al., 1978). The regression curve is a sigmoid (see text).

3.8 Tables

Table 1. Olivine standard materials used in this study.

Name of sample	Fa	Locality	Source and sample identifier
Pine River IAB iron meteorite	2	N/A	UCLA, IN 314
Day Book dunite	7	Yancey County, North Carolina, USA	NMNH 119138
Mt. Franklin	8	Victoria, Australia	Paul Warren (UCLA)
San Carlos	9	San Carlos, Gila County, Arizona, USA	Christopher Snead (UCLA)
Urals	16	Lake Itkul, Sverdlovsk, Urals, Russia	NMNH 16257-01
Skaergaard EG 5108	35	Skaergaard Intrusion, East Greenland	Oxford U., EG 5108
NWA 6693 achondrite	50	N/A	UCLA, LC 2617 and LC 2618
Skaergaard EG 1907	69	Skaergaard Intrusion, East Greenland	Oxford U., EG 1907
Rockport	97	Essex County, Massachusetts, USA	NMNH 85276

Table 2. Chemical compositions of olivine samples (wt. . %).

	Pine River		**Day Book dunite**		**Mt. Franklin**		**San Carlos**	**Urals**	
	average	std.	average	std.	average	std.	average	average	std.
	n=5		n=3		n=3		n=2	n=3	
SiO_2	41.5	0.6	41.3	0.2	41.2	0.2	41.0	39.71	0.02
TiO_2	-	-	<0.04	-	<0.04	-	<0.04	<0.04	-
Al_2O_3	<0.04	-	<0.04	-	<0.04	-	<0.04	<0.04	-
Cr_2O_3	<0.04	-	<0.04	-	<0.04	-	<0.04	<0.04	-
MgO	54.9	0.8	51.2	0.1	50.6	0.1	49.7	44.6	0.1
CaO	<0.04	-	<0.04	-	0.08	0.01	0.09	<0.04	-
FeO	2.0	0.7	7.3	0.1	7.9	0.2	8.6	15.3	0.1
MnO	0.20	0.04	0.13	0.03	0.09	0.02	0.13	0.17	0.01
NiO	-	-	0.4	0.1	0.42	0.04	0.36	0.33	0.04
Total	98.6		100.2		100.2		99.8	100.2	
Fa mol%	**2.0**		**7.4**		**8.0**		**8.8**	**16.1**	

	Skaergaard EG 5108		**NWA6693**		**Skaergaard EG 1907**		**Rockport**	
	average	std.	average	std.	average	std.	average	std.
	n=3		n=17		n=6		n=15	
SiO^2	37.1	0.1	35.2	0.2	33.2	0.2	29.9	0.3
TiO^2	<0.04	-	-	-	-	-	-	-
Al_2O_3	0.05	0.03	-	-	-	-	-	-
Cr_2O_3	<0.04	-	-	-	-	-	-	-
MgO	32.4	0.1	23.2	0.2	13.4	0.2	0.10	0.03
CaO	0.06	0.02	0.09	0.03	0.09	0.02	0.08	0.02
FeO	31.09	0.04	41.9	0.3	53.9	0.2	67.8	0.2
MnO	0.43	0.03	0.29	0.02	0.79	0.02	2.2	0.1
NiO	0.12	0.03	-	-	-	-	-	-
Total	101.3		100.7		101.4		100.0	
Fa mol%	**34.8**		**50.2**		**68.6**		**96.6**	

Fa mol% $= \mathrm{Fe}/(\mathrm{Mg}+\mathrm{Mn}+\mathrm{Fe})\times 100$
std. a standard deviation (%)

Table 3. $\delta^{18}O$ values measured by the laser-assisted fluorination technique.

Name	Fa	$\delta^{18}O$	Error[§]
Day Book dunite	7	5.61	0.13
Mt. Franklin	8	4.92	0.14
San Carlos	9	5.19	0.13
Urals	16	6.33	0.13
Skaergaard EG 5108	35	4.54	0.14
NWA 6693	50	3.86	0.13
Skaergaard EG 1907	69	4.28	0.13
Rock Port	97	4.74	0.14
Pine River*	2	4.48	

[§] $error\ (‰) = \sqrt{(SD)^2 + (SE)^2}$

*Clayton and Mayeda (1996)

Table 4. $\delta^{18}O$ values measured by SIMS. The isotope ratios are normalized to San Carlos olivine ($\delta^{18}O$=5.2) in each session.

	IMS-1270								
	2012 April			2013 May			2014 April		
Name	$\delta^{18}O$	std.	n	$\delta^{18}O$	std.	n	$\delta^{18}O$	std.	n
Pine River				4.6	0.3	5			
Day Book dunite	5.4	0.3	3	6.0	1.0	14			
Mt. Franklin	4.7	0.2	3	5.3	0.1	6			
San Carlos	≡5.2	0.2	5	≡5.2	0.3	31	≡5.2	0.2	10
Urals	6.0	0.1	3	6.3	0.3	11			
Skaeragard EG 5108	3.9	0.1	3	3.9	0.4	10			
NWA6693							2.6	0.2	11
Skaeragard EG 1907							1.1	0.2	11
Rock Port	-4.4	0.6	3	-6.4	0.4	15	-3.4	0.1	6

	IMS-1290		
	2017 Feb		
Name	$\delta^{18}O$	std.	n
Pine River	3.9	0.3	3
Day Book dunite			
Mt. Franklin	5.3	0.1	5
San Carlos	≡5.2	0.2	31
Urals	6.5	0.1	5
Skaeragard EG 5108	4.0	0.1	5
NWA6693	2.4	0.2	6
Skaeragard EG 1907	0.3	0.1	6
Rock Port	-4.3	0.3	12

n: number of analyses
std.: a standard deviation (‰)

Table 5. Depth of SIMS crater after 20 minutes of sputtering under 50μm ×50 μm raster modes.

Name	Fa	Depth (μm)	I (nA)	5 nA Normalized Depth (μm)
Pine River IAB iron meteorite	2	360	5.1	360
Day Book dunite	7	400	5.2	380
Mt. Franklin	8	440	5.2	420
San Carlos	9	440	5.3	420
San Carlos	9	390	5.2	370
San Carlos	9	350	5.1	340
San Carlos	9	250	5.1	250
Urals	16	400	5.1	400
Skaeragard EG 5108	35	450	5.1	450
NWA 6693 achondrite	50	460	5.0	460
Skaeragard EG 1907	69	610	5.3	580
Rockport	97	710	5.2	690

I: primary beam intensity
normalized depth: measured depth scaled to 5 nA primary beam intensity

3.9 Appendix

Pine River iron meteorite olivine. (UCLA Meteorite Collection, IN314)

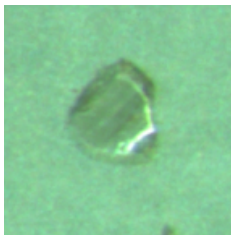

Figure A-1. Pine River

Pine River is an iron meteorite classified as IAB. The total mass 3.6 kg was found in Wisconsin, USA in 1931 or 1894. The detailed of the history, collection, and petrology are described in Buchwald (1975). The olivine Fa value is 2.0. We used the UCLA-Inventory-collection 314 for this study. Olivine grains (pale green) had been separated from iron-nickel metal for previous O-isotope study (Clayton and Mayeda 1996). The photo (Figure A-1) shows an individual grain utilized for analysis ~ 200-300 μm in size. **Day Book dunite, Yancey County, North Carolina, USA. (NMNH 119138)**

The sample was partially metamorphosed but largely consisted of olivine grains (light green). The olivine Fa value is 7.4. The picture at the left (Figure A-2 a) is a polished olivine grain (2-3 mm in size) in a thick section. The picture at the right (Figure A-2 b) is the whole rock sample.

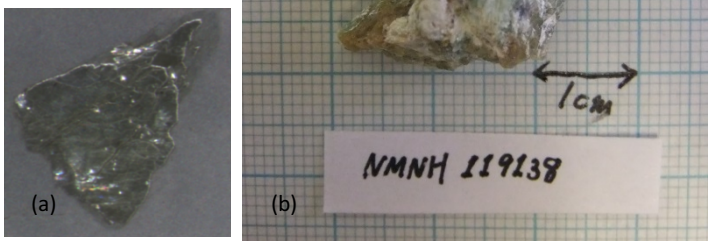

Figure A-2. Day Book dunite

Mt Franklin, Victoria, Australia. (from Paul Warren, UCLA)

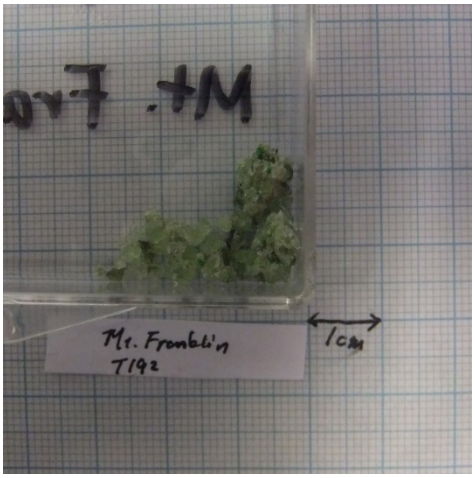

The sample is peridotite containing olivine (light green), enstatite (dark green) and diopside (bright apple green). Olivine grains can be easily identified without using microscope. The olivine Fa value is 8.0. A sample provided by Paul Warren (UCLA). The picture (Figure A-3) is the whole sample including olivine and pyroxene; olivine grains ~ 1 mm in size were used for the SIMS analyses.

Figure A-3. Mt Franklin

Urals, Sverdlovsk, Lake Itkul, Russia. (NMNH 16257-1)

The sample contains large muscovites (transparent minerals at the left in the picture) and olivine. The olivine Fa value is 16.1. Olivine grains were separated from the brown part of the rock (right in the picture). A left picture (Fig A-4 a) is an olivine grain (~ 2 × 2 mm) in a thick section.

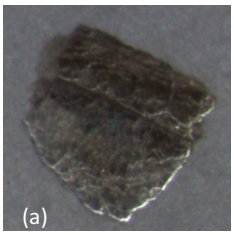

Figure A-4. Urals

Skaergaard Intrusion, East Greenland. (Oxford U. EG 5108) Mostly dark slate gray colored rocks. Sample was originally provided by E. A. Vincent. The olivine Fa value is 34.8 while literature olivine Fa value is 39.7 (Wager and Brown 1967). Left image (Figure A-5 a) shows analyzed an olivine grain (~1.5 to 2 mm) in thick section; right picture (Figure A-5 b) shows the whole sample.

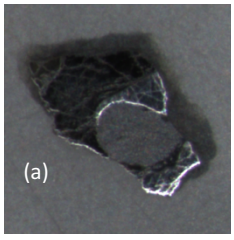

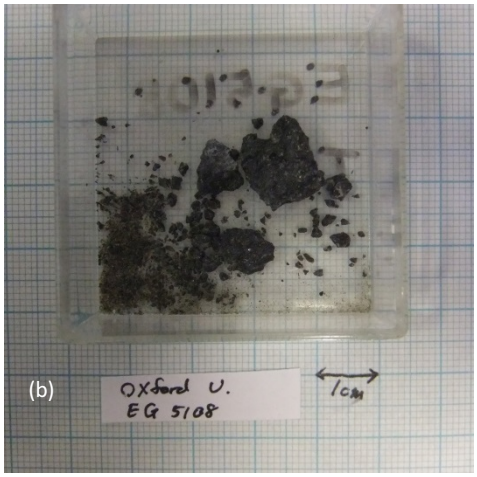

Figure A-5. Skaergaard EG 5108

NWA 6693 achondrite meteorite. (UCLA Meteorite Collection, LC 2617 and LC 2618)

NWA 6693 is as an ungrouped achondrite found in Morocco in 2011 (Figure A-6 b). The total mass is 5.1 kg. Petrology, bulk chemistry, and bulk O-isotope compositions of the rock were studied by Warren et al. (2013). We used olivine grains about 200-400 µm in size. The picture at the left (Figure A-6 a) shows olivine grains after the acid wash. The olivine Fa value is 50.2.

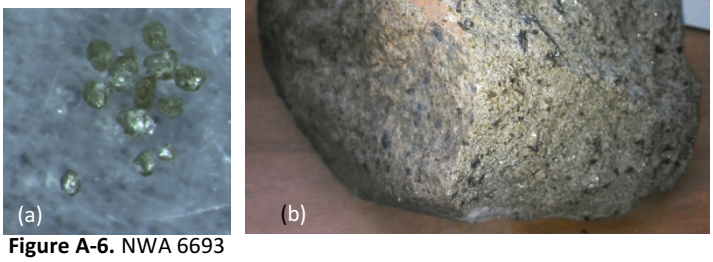

Figure A-6. NWA 6693

Skaergaard Intrusion, East Greenland. (Oxford U. 1907)

Whole rock is very dark brown color containing mostly pyroxene, minor opaque oxides and minor olivine grains (yellow brown). The sample, originally collected by Oxford University, is from the Yoder collection. The olivine Fa value is 68.6. The previous measured olivine Fa value was 60 (personal communication from Yoder). Left image (Figure A-7 a) is olivine grains after the acid wash (less than 50 µm in size); right image (Figure A-7 b) shows whole rock mounted in epoxy resin non-coated and gold-coated thick sections.

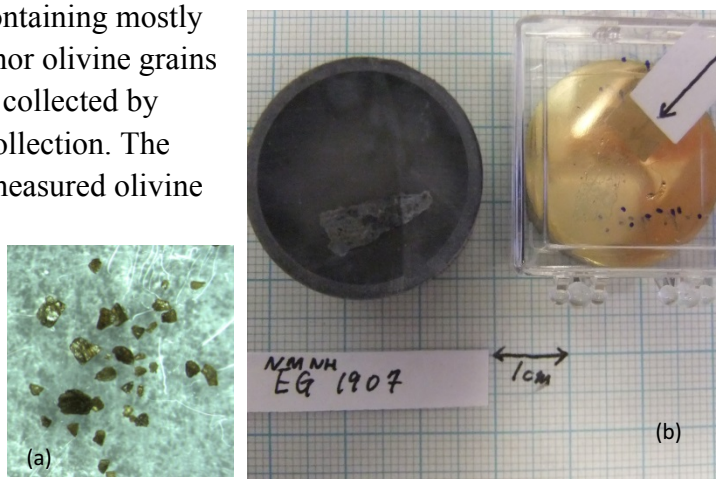

Figure A-7. Skaergaard EG 1970

Rockport Essex County, Massachusetts, USA. (NMNH 85276)

Dark brown with partially weathered rocks that mostly consist of fayalite (dark brown). The olivine Fa value is 96.6; while, the literature olivine Fa value is 98 (Palache 1950; Rose et al., 2009). We used coarse grains at the most 3mm in size. The lower left image (Figure A-8 a) is an analyzed olivine grain (~1 × 1.5 mm) in a thick section. The right image shows whole rock chips (Figure A-8 b).

Figure A-8. Rockport

Table A1. Sample weight, sample conditions and three oxygen isotope compositions measured by the laser-assisted fluorination technique.

Name	Date	Weight (mg)	$\delta^{17}O$	S.E.	$\delta^{18}O$	S.E.	$\delta^{17}O$	S.E.	Block #	Sample Phase
Day Book dunite	22-May-13	1.23	2.955	0.022	5.608	0.027	-0.006	0.015	4	olv
Mt. Franklin	22-May-13	1.34	2.586	0.008	4.916	0.037	-0.010	0.013	4	olv
San Carlos	2-Jun-16	2.85	2.738	0.007	5.190	0.004	-0.003	0.007	7	olv
Urals	20-May-13	1.65	3.305	0.017	6.332	0.029	-0.038	0.012	4	olv
Skaeragard Fa34	14-May-13	1.62	2.381	0.027	4.543	0.037	-0.018	0.011	4	olv
NWA 6693	8-Jun-16	0.67	0.994	0.014	3.857	0.013	-1.043	0.018	6	olv
Skaeragard Fa70	24-Jun-14	1.93	2.251	0.011	4.278	0.007	-0.008	0.012	4	olv
Rock Port	14-May-13	1.3	2.480	0.011	4.738	0.04	-0.021	0.014	4	olv

S.E.: standard error ‰
olv: olivine

Table A2: SIMS analyses. SC-olivine is the standard which are defined as 16/18=2.01561✕10-3

sample name	year	date	Primary beam (nA)	Fa	n	SIMS _18/16 ratios_SCnomalized	se	1000ln(α(SIMS-LF))
Day Book dunite	2012	April	3.86	7	15	0.002016634	0.06	0.09
Day Book dunite	2012	April	3.86	7	15	0.002015478	0.09	-0.48
Day Book dunite	2012	April	3.86	7	15	0.002016193	0.07	-0.13
Mt. Franklin	2012	April	3.89	8	15	0.002014371	0.07	-0.34
Mt. Franklin	2012	April	3.92	8	15	0.002014989	0.08	-0.03
Mt. Franklin	2012	April	3.91	8	15	0.002014276	0.05	-0.39
San Carlos	2012	April	3.86	9	15	0.002016155	0.07	0.27
San Carlos	2012	April	3.87	9	15	0.002015864	0.06	0.13
San Carlos	2012	April	3.87	9	15	0.002015807	0.09	0.10
San Carlos	2012	April	3.79	9	15	0.002015249	0.07	-0.18
San Carlos	2012	April	3.82	9	15	0.002015561	0.07	-0.02
Urals	2012	April	3.91	16	15	0.002017346	0.06	-0.27
Urals	2012	April	3.91	16	15	0.002017036	0.05	-0.43
Urals	2012	April	3.86	16	15	0.002017211	0.04	-0.34
Skaeragard Fa34	2012	April	3.85	35	15	0.002013168	0.07	-0.57
Skaeragard Fa34	2012	April	3.85	35	15	0.002012841	0.06	-0.73
Skaeragard Fa34	2012	April	3.85	35	15	0.002013256	0.05	-0.52
Rockport	2012	April	3.84	97	15	0.001995100	0.08	-9.78
Rockport	2012	April	3.84	97	15	0.001996877	0.06	-8.89
Rockport	2012	April	3.84	97	15	0.001997121	0.07	-8.76
Pine River	2013	May	5.95	2	15	0.002013908	0.09	-0.14
Pine River	2013	May	5.96	2	15	0.002013788	0.14	-0.20
Pine River	2013	May	5.95	2	15	0.002014533	0.14	0.17
Pine River	2013	May	6.01	2	15	0.002014455	0.16	0.13
Pine River	2013	May	5.99	2	15	0.002015336	0.17	0.57
Day Book dunite	2013	May	5.60	7	15	0.002017065	0.09	0.31
Day Book dunite	2013	May	5.61	7	15	0.002018417	0.08	0.98
Day Book dunite	2013	May	5.60	7	15	0.002017435	0.07	0.49
Day Book dunite	2013	May	5.59	7	15	0.002021794	0.10	2.65
Day Book dunite	2013	May	5.58	7	15	0.002017895	0.08	0.72
Day Book dunite	2013	May	5.60	7	15	0.002017927	0.10	0.73
Day Book dunite	2013	May	5.59	7	15	0.002020493	0.10	2.01
Day Book dunite	2013	May	6.23	7	15	0.002015218	0.10	-0.61
Day Book dunite	2013	May	6.26	7	15	0.002015243	0.09	-0.60
Day Book dunite	2013	May	6.26	7	15	0.002015841	0.11	-0.30
Day Book dunite	2013	May	6.22	7	15	0.002016031	0.09	-0.21
Day Book dunite	2013	May	6.23	7	15	0.002016645	0.10	0.10
Day Book dunite	2013	May	6.24	7	15	0.002016775	0.10	0.16
Day Book dunite	2013	May	6.25	7	15	0.002015704	0.11	-0.37
Mt. Franklin	2013	May	5.61	8	15	0.002015911	0.06	0.42
Mt. Franklin	2013	May	5.60	8	15	0.002015934	0.07	0.43
Mt. Franklin	2013	May	5.62	8	15	0.002015966	0.11	0.45
Mt. Franklin	2013	May	5.62	8	15	0.002015828	0.08	0.38
Mt. Franklin	2013	May	5.61	8	15	0.002015572	0.09	0.26
Mt. Franklin	2013	May	5.61	8	15	0.002015959	0.10	0.45
San Carlos	2013	May	5.59	9	15	0.002015909	0.07	0.15
San Carlos	2013	May	5.65	9	15	0.002015571	0.06	-0.02
San Carlos	2013	May	5.65	9	15	0.002015026	0.06	-0.29
San Carlos	2013	May	5.63	9	15	0.002015611	0.08	0.00
San Carlos	2013	May	5.64	9	15	0.002015954	0.08	0.17
San Carlos	2013	May	5.63	9	15	0.002015367	0.06	-0.12
San Carlos	2013	May	5.61	9	15	0.002015929	0.07	0.16
San Carlos	2013	May	5.61	9	15	0.002016351	0.09	0.37

sample name	year	date	Primary beam (nA)	Fa	n	SIMS _18/16 ratios_SCnomalized	se	1000ln(α(SIMS-LF))
San Carlos	2013	May	5.62	9	15	0.002015827	0.09	0.11
San Carlos	2013	May	6.22	9	15	0.002015350	0.09	-0.13
San Carlos	2013	May	6.21	9	15	0.002014973	0.10	-0.31
San Carlos	2013	May	6.18	9	15	0.002015083	0.12	-0.26
San Carlos	2013	May	6.18	9	15	0.002015383	0.14	-0.11
San Carlos	2013	May	6.16	9	15	0.002014673	0.10	-0.46
San Carlos	2013	May	6.14	9	15	0.002014610	0.11	-0.49
San Carlos	2013	May	6.18	9	15	0.002014969	0.13	-0.32
San Carlos	2013	May	5.96	9	15	0.002015662	0.11	0.03
San Carlos	2013	May	5.97	9	15	0.002016801	0.07	0.59
San Carlos	2013	May	5.98	9	15	0.002015710	0.12	0.05
San Carlos	2013	May	5.95	9	15	0.002015180	0.13	-0.21
San Carlos	2013	May	5.95	9	15	0.002015422	0.13	-0.09
San Carlos	2013	May	5.93	9	15	0.002016346	0.14	0.37
San Carlos	2013	May	6.00	9	15	0.002015918	0.11	0.15
San Carlos	2013	May	5.98	9	15	0.002016473	0.12	0.43
San Carlos	2013	May	6.01	9	15	0.002015261	0.10	-0.17
San Carlos	2013	May	6.02	9	15	0.002015933	0.09	0.16
San Carlos	2013	May	5.98	9	15	0.002015907	0.12	0.15
San Carlos	2013	May	5.98	9	15	0.002015808	0.12	0.10
San Carlos	2013	May	5.99	9	15	0.002015886	0.08	0.14
San Carlos	2013	May	5.95	9	15	0.002016053	0.11	0.22
San Carlos	2013	May	5.96	9	15	0.002015243	0.10	-0.18
Urals	2013	May	5.64	16	15	0.002017271	0.06	-0.31
Urals	2013	May	5.62	16	15	0.002018140	0.07	0.12
Urals	2013	May	5.62	16	15	0.002018485	0.08	0.29
Urals	2013	May	5.63	16	15	0.002018230	0.09	0.17
Urals	2013	May	5.62	16	15	0.002018284	0.05	0.19
Urals	2013	May	5.62	16	15	0.002017943	0.06	0.02
Urals	2013	May	6.13	16	15	0.002017705	0.11	-0.10
Urals	2013	May	6.14	16	15	0.002017067	0.13	-0.41
Urals	2013	May	6.17	16	15	0.002016832	0.09	-0.53
Urals	2013	May	6.16	16	15	0.002017520	0.10	-0.19
Urals	2013	May	6.14	16	15	0.002017813	0.12	-0.04
Skaeragard Fa34	2013	May	5.62	35	15	0.002012752	0.07	-0.77
Skaeragard Fa34	2013	May	5.63	35	15	0.002012978	0.07	-0.66
Skaeragard Fa34	2013	May	5.63	35	15	0.002012710	0.08	-0.79
Skaeragard Fa34	2013	May	5.60	35	15	0.002013325	0.08	-0.49
Skaeragard Fa34	2013	May	5.61	35	15	0.002012786	0.10	-0.76
Skaeragard Fa34	2013	May	5.64	35	15	0.002012710	0.06	-0.79
Skaeragard Fa34	2013	May	6.22	35	15	0.002014117	0.10	-0.10
Skaeragard Fa34	2013	May	6.20	35	15	0.002014212	0.15	-0.05
Skaeragard Fa34	2013	May	6.19	35	15	0.002011751	0.15	-1.27
Skaeragard Fa34	2013	May	6.16	35	15	0.002011909	0.08	-1.19
Rockport	2013	May	5.64	97	15	0.001991631	0.18	-11.52
Rockport	2013	May	5.63	97	15	0.001992293	0.22	-11.18
Rockport	2013	May	5.64	97	15	0.001992192	0.20	-11.24
Rockport	2013	May	5.63	97	15	0.001990933	0.22	-11.87
Rockport	2013	May	5.57	97	15	0.001992831	0.16	-10.91
Rockport	2013	May	6.21	97	15	0.001991981	0.21	-11.34
Rockport	2013	May	6.20	97	15	0.001992934	0.23	-10.86
Rockport	2013	May	6.20	97	15	0.001992011	0.17	-11.33
Rockport	2013	May	6.18	97	15	0.001992647	0.21	-11.01
Rockport	2013	May	6.18	97	15	0.001991512	0.17	-11.58

sample name	year	date	Primary beam (nA)	Fa	n	SIMS _18/16 ratios_SCnomalized	se	1000ln(α(SIMS-LF))
Rockport	2013	May	6.17	97	15	0.001993292	0.20	-10.68
Rockport	2013	May	6.18	97	15	0.001993005	0.23	-10.83
Rockport	2013	May	6.20	97	15	0.001993068	0.24	-10.80
Rockport	2013	May	6.13	97	15	0.001991781	0.16	-11.44
Rockport	2013	May	6.18	97	15	0.001993676	0.26	-10.49
San Carlos	2014	April	3.08	9	12	0.002016000	0.06	0.20
San Carlos	2014	April	3.10	9	12	0.002015661	0.07	0.03
San Carlos	2014	April	3.13	9	12	0.002015299	0.05	-0.15
San Carlos	2014	April	3.14	9	12	0.002015302	0.07	-0.15
San Carlos	2014	April	3.14	9	12	0.002015675	0.05	0.03
San Carlos	2014	April	3.14	9	12	0.002015825	0.05	0.11
San Carlos	2014	April	3.08	9	12	0.002016773	0.03	0.58
San Carlos	2014	April	3.08	9	12	0.002016298	0.05	0.34
San Carlos	2014	April	2.98	9	12	0.002015272	0.07	-0.17
San Carlos	2014	April	3.00	9	12	0.002015982	0.08	0.19
NWA6693	2014	April	3.22	50	12	0.002009803	0.07	-1.56
NWA6693	2014	April	3.11	50	12	0.002010029	0.05	-1.44
NWA6693	2014	April	3.22	50	12	0.002010488	0.06	-1.22
NWA6693	2014	April	3.20	50	12	0.002010490	0.05	-1.22
NWA6693	2014	April	3.24	50	12	0.002010194	0.04	-1.36
NWA6693	2014	April	3.10	50	12	0.002010857	0.06	-1.03
NWA6693	2014	April	3.15	50	12	0.002010069	0.06	-1.42
NWA6693	2014	April	3.16	50	12	0.002011453	0.09	-0.74
NWA6693	2014	April	3.22	50	12	0.002010180	0.05	-1.37
NWA6693	2014	April	3.14	50	12	0.002010621	0.06	-1.15
NWA6693	2014	April	2.98	50	12	0.002010467	0.06	-1.23
Skaeragard_Fa70	2014	April	3.06	69	12	0.002006938	0.06	-3.40
Skaeragard_Fa70	2014	April	3.12	69	12	0.002007082	0.04	-3.33
Skaeragard_Fa70	2014	April	3.10	69	12	0.002007358	0.06	-3.19
Skaeragard_Fa70	2014	April	3.12	69	12	0.002007876	0.04	-2.94
Skaeragard_Fa70	2014	April	3.11	69	12	0.002007357	0.05	-3.19
Skaeragard_Fa70	2014	April	3.10	69	12	0.002007737	0.06	-3.00
Skaeragard_Fa70	2014	April	3.06	69	12	0.002007665	0.05	-3.04
Skaeragard_Fa70	2014	April	3.11	69	12	0.002007167	0.05	-3.29
Skaeragard_Fa70	2014	April	3.13	69	12	0.002007004	0.05	-3.37
Skaeragard_Fa70	2014	April	3.13	69	12	0.002007853	0.05	-2.95
Skaeragard_Fa70	2014	April	3.13	69	12	0.002007890	0.06	-2.93
Rockport	2014	April	3.11	97	12	0.001998281	0.06	-8.18
Rockport	2014	April	3.13	97	12	0.001998270	0.05	-8.19
Rockport	2014	April	3.14	97	12	0.001998412	0.07	-8.12
Rockport	2014	April	3.14	97	12	0.001998102	0.05	-8.27
Rockport	2014	April	3.15	97	12	0.001998208	0.05	-8.22
Rockport	2014	April	3.14	97	12	0.001998601	0.05	-8.02
PineRievr	2017	Feb	2.59	2	10	0.002013603	0.24	-0.29
PineRievr	2017	Feb	2.59	2	10	0.002012516	0.26	-0.83
PineRievr	2017	Feb	2.58	2	10	0.002013148	0.19	-0.51
Mt. Franklin	2017	Feb	2.58	8	10	0.002015674	0.18	0.31
Mt. Franklin	2017	Feb	2.58	8	10	0.002015690	0.16	0.31
Mt. Franklin	2017	Feb	2.58	8	10	0.002015632	0.14	0.29
Mt. Franklin	2017	Feb	2.58	8	10	0.002015968	0.16	0.45
Mt. Franklin	2017	Feb	2.58	8	10	0.002016215	0.15	0.57
San Carlos	2017	Feb	2.59	9	10	0.002015485	0.19	-0.06
San Carlos	2017	Feb	2.59	9	10	0.002015564	0.11	-0.02
San Carlos	2017	Feb	2.59	9	10	0.002015563	0.15	-0.02

sample name	year	date	Primary beam (nA)	Fa	n	SIMS _18/16 ratios_SCnomalized	se	1000ln(α(SIMS-LF))
San Carlos	2017	Feb	2.59	9	10	0.002015668	0.14	0.03
San Carlos	2017	Feb	2.59	9	10	0.002015786	0.11	0.09
San Carlos	2017	Feb	2.59	9	10	0.002015576	0.10	-0.02
San Carlos	2017	Feb	4.20	9	10	0.002015705	0.14	0.05
San Carlos	2017	Feb	4.20	9	10	0.002015333	0.13	-0.14
San Carlos	2017	Feb	4.20	9	10	0.002015841	0.10	0.12
San Carlos	2017	Feb	4.20	9	10	0.002015486	0.15	-0.06
San Carlos	2017	Feb	4.20	9	10	0.002015670	0.08	0.03
San Carlos	2017	Feb	2.56	9	10	0.002015217	0.12	-0.19
San Carlos	2017	Feb	2.56	9	10	0.002015198	0.16	-0.20
San Carlos	2017	Feb	2.55	9	10	0.002015606	0.14	0.00
San Carlos	2017	Feb	2.55	9	10	0.002015230	0.16	-0.19
San Carlos	2017	Feb	2.62	9	10	0.002015106	0.18	-0.25
San Carlos	2017	Feb	2.56	9	10	0.002015601	0.13	0.00
San Carlos	2017	Feb	2.56	9	10	0.002015070	0.17	-0.27
San Carlos	2017	Feb	2.55	9	10	0.002016881	0.07	0.63
San Carlos	2017	Feb	2.55	9	10	0.002016554	0.17	0.47
San Carlos	2017	Feb	2.51	9	10	0.002015271	0.33	-0.17
San Carlos	2017	Feb	2.51	9	10	0.002015307	0.19	-0.15
San Carlos	2017	Feb	2.51	9	10	0.002015903	0.25	0.15
San Carlos	2017	Feb	2.51	9	10	0.002015905	0.07	0.15
San Carlos	2017	Feb	2.52	9	10	0.002015649	0.21	0.02
San Carlos	2017	Feb	2.60	9	10	0.002016034	0.23	0.21
San Carlos	2017	Feb	2.59	9	10	0.002015811	0.30	0.10
San Carlos	2017	Feb	2.59	9	10	0.002015240	0.17	-0.18
San Carlos	2017	Feb	2.59	9	10	0.002015524	0.18	-0.04
San Carlos	2017	Feb	2.58	9	10	0.002015471	0.14	-0.07
San Carlos	2017	Feb	2.58	9	10	0.002015562	0.18	-0.02
Urals	2017	Feb	2.58	16	10	0.002018456	0.16	0.28
Urals	2017	Feb	2.58	16	10	0.002018508	0.13	0.30
Urals	2017	Feb	2.58	16	10	0.002018190	0.19	0.15
Urals	2017	Feb	2.58	16	10	0.002017845	0.18	-0.03
Urals	2017	Feb	2.58	16	10	0.002018124	0.19	0.11
SKA34	2017	Feb	2.58	35	10	0.002013559	0.08	-0.37
SKA34	2017	Feb	2.58	35	10	0.002013017	0.13	-0.64
SKA34	2017	Feb	2.58	35	10	0.002013356	0.14	-0.47
SKA34	2017	Feb	2.58	35	10	0.002013026	0.11	-0.64
SKA34	2017	Feb	2.58	35	10	0.002013082	0.11	-0.61
NWA6693	2017	Feb	2.54	50	10	0.002009865	0.21	-1.53
NWA6693	2017	Feb	2.55	50	10	0.002010826	0.10	-1.05
NWA6693	2017	Feb	2.55	50	10	0.002009958	0.10	-1.48
NWA6693	2017	Feb	2.55	50	10	0.002010093	0.09	-1.41
NWA6693	2017	Feb	2.56	50	10	0.002010280	0.18	-1.32
NWA6693	2017	Feb	2.57	50	10	0.002009462	0.17	-1.73
SKA70	2017	Feb	2.57	69	10	0.002006075	0.10	-3.83
SKA70	2017	Feb	2.57	69	10	0.002006061	0.16	-3.84
SKA70	2017	Feb	2.56	69	10	0.002005790	0.08	-3.97
SKA70	2017	Feb	2.56	69	10	0.002005743	0.15	-4.00
SKA70	2017	Feb	2.56	69	10	0.002005655	0.23	-4.04
SKA70	2017	Feb	2.56	69	10	0.002005825	0.18	-3.96
Rockport	2017	Feb	2.59	97	10	0.001996380	0.10	-9.13
Rockport	2017	Feb	2.59	97	10	0.001995873	0.16	-9.39
Rockport	2017	Feb	2.59	97	10	0.001995886	0.14	-9.38
Rockport	2017	Feb	2.58	97	10	0.001995840	0.14	-9.41

MicroXAM Depth Measurement

SIMS Sputtering Condition:
Cs+ beam: 50 µm raster
Analytical duration: 20 min

Rockport Olivine (Fa97)
Primary beam before the analysis: 2.920 nA
Primary beam after the analysis: 2.940 nA

San Carlos Olivine (Fa9)
Primary beam before the analysis: 2.920 nA
Primary beam after the analysis: 2.900 nA

Rockport Olivine

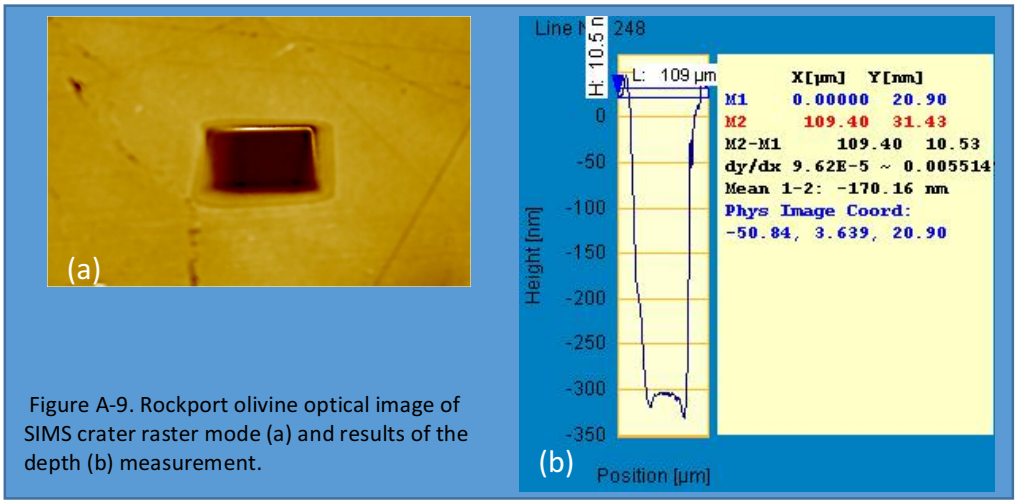

Figure A-9. Rockport olivine optical image of SIMS crater raster mode (a) and results of the depth (b) measurement.

San Carlos Olivine

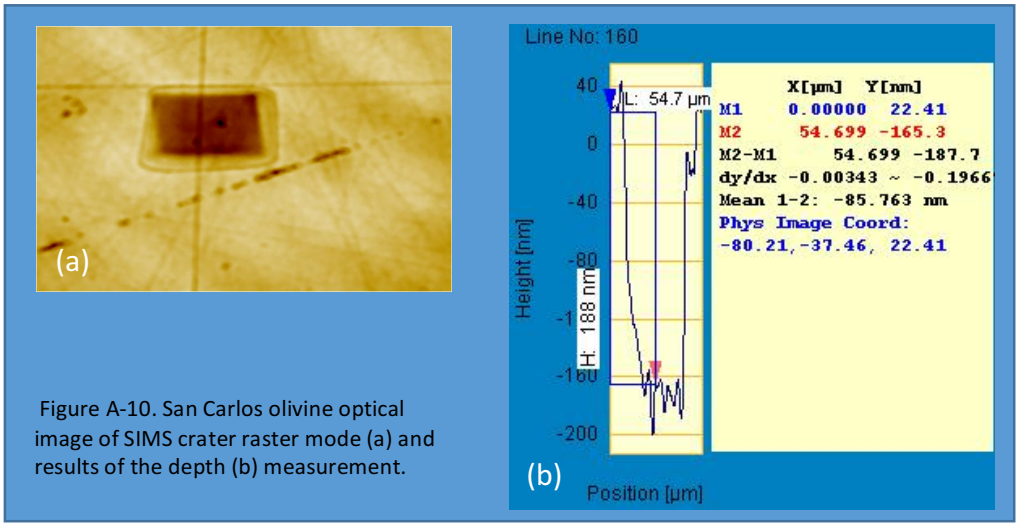

Figure A-10. San Carlos olivine optical image of SIMS crater raster mode (a) and results of the depth (b) measurement.

3.10 References

Andersen, C.A., (1970). Analytic methods for the ion microprobe mass analyzer. Part II. *Int. J. Mass Spectrom. Ion Phys*. **3**, 413-428.

Baertschi, P., (1976). Absolute ^{18}O content of standard mean ocean water. *Earth Planet. Sci. Lett.* **31**, 341-344.

Bernherim, M., Rebière, J., Slodzian, G., (1979). Negative Ion Emission from Surfaces Covered with Cesium and Bombarded by Noble Gas Ions. In *Secondary Ion Mass Spectrometry SIMS II* (pp. 40-43). Springer Berlin Heidelberg.

Chelgren, J.E., Katz, W., Deline, V.R., Evans Jr, C.A., Blattner, R.J., Williams, P., (1979). Surface cesium concentrations in cesium-ion-bombarded elemental and compound targets. *J. Vac. Sci. Technol*. **16**, 324.

Criss, R.E., (2008). Terrestrial oxygen isotope variations and their implications for planetary lthospheres. *Rev. Mineral. Geochemistry* **68**.

Deline, V.R., Katz, W., Evans, C.A., Williams, P., (1978). Mechanism of the SIMS matrix effect. *Appl. Phys. Lett*. 33, 832-835.

Eiler, J.M., Graham, C., Valley, J.W., (1997). SIMS analysis of oxygen isotopes: Matrix effects in complex minerals and glasses. *Chem. Geol*. **138**, 221-244.

Huberty, J.M., Kita, N.T., Kozdon, R., Heck, P.R., Fournelle, J.H., Spicuzza, M.J., Xu, H., Valley, J.W., (2010). Crystal orientation effects in $\delta^{18}O$ for magnetite and hematite by SIMS. *Chem. Geol*. **276**, 269-283.

Jogo, K., Nagashima, K., Hutcheon, I.D., Krot, A.N., Nakamura, T., (2012). Heavily metamorphosed clasts from the CV chondrite breccias Mokoia and Yamato-86009. *Meteorit. Planet. Sci.* **47**, 2251-2268.

Keil, K., (2012). Angrites, a small but diverse suite of ancient, silica-undersaturated volcanic-plutonic mafic meteorites, and the history of their parent asteroid. *Chemie der Erde - Geochemistry*. **72**, 191-218.

Kita, N.T., Nagahara, H., Tachibana, S., Tomomura, S., Spicuzza, M.J., Fournelle, J.H., Valley, J.W., (2010). High precision SIMS oxygen three isotope study of chondrules in LL3 chondrites: Role of ambient gas during chondrule formation. *Geochim. Cosmochim. Acta* **74**, 6610-6635.

Kita, N.T., Ushikubo, T., Fu, B., Valley, J.W., (2009). High precision SIMS oxygen isotope analysis and the effect of sample topography. *Chem. Geol*. **264**, 43-57.

Kolodny, Y., Bar-Matthews, M., Ayalon, A., McKeegan, K.D., (2003). A high spatial resolution $\delta^{18}O$ profile of a speleothem using an ion-microprobe. *Chem. Geo*l. **197**, 21-28.

Mikouchi, T., Miyamoto, M., McKay, G., (2001). Mineralogy and petrology of the Dar al Gani 476 martian meteorite: Implications for its cooling history and relationship to other shergottites. *Meteorit. Planet. Sci*. **36**, 531-548.

Nakashima, D., Kita, N.T., Ushikubo, T., Noguchi, T., Nakamura, T., Valley, J.W., (2013). Oxygen three-isotope ratios of silicate particles returned from asteroid Itokawa by the Hayabusa spacecraft: A strong link with equilibrated LL chondrites, *Earth and Planetary Science Letters.* **379**, 127-136.

Page, F.Z., Kita, N.T., Valley, J.W., (2010). Ion microprobe analysis of oxygen isotopes in garnets of complex chemistry. *Chem. Geol*. **270**, 9-19.

Riciputi, L.R., Paterson, B.A., Ripperdan, R.L., (1998). Measurement of light stable isotope ratios by SIMS, *Int. J. Mass Spectrom*. **178**, 81-112.

Rollion-Bard, C., Marin-Carbonne, J., (2011). Determination of SIMS matrix effects on oxygen isotopic compositions in carbonates. *J. Anal. At.* **26**, 1285-1289.

Śliwiński, M.G., Kitajima, K., Kozdon, R., Spicuzza, M.J., Fournelle, J.H., Denny, A., Valley, J.W., (2016a). Secondary ion mass spectrometry bias on isotope ratios in dolomite-ankerite, Part II: $\delta^{13}C$ Matrix Effects. *Geostand. Geoanalytical Res*. **40**, 173-184.

Śliwiński, M.G., Kitajima, K., Kozdon, R., Spicuzza, M.J., Fournelle, J.H., Denny, A., Valley, J.W., (2016b). Secondary ion mass spectrometry bias on isotope ratios in dolomite-ankerite, Part I: $\delta^{18}O$ Matrix Effects. *Geostand. Geoanalytical Res*. **40**, 157-172.

Tenner, T.J., Nakashima, D., Ushikubo, T., Kita, N.T., Weisberg, M.K., (2015). Oxygen isotope ratios of FeO-poor chondrules in CR3 chondrites: Influence of dust enrichment and H_2O during chondrule formation. *Geochim. Cosmochim. Acta* **148**, 228-250.

Tenner, T.J., Ushikubo, T., Kurahashi, E., Kita, N.T., Nagahara, H., (2013). Oxygen isotope systematics of chondrule phenocrysts from the CO3.0 chondrite Yamato 81020: Evidence for two distinct oxygen isotope reservoirs. *Geochim. Cosmochim. Acta* **102**, 226-245.

Treble, P.C., Schmitt, A.K., Edwards, R.L., McKeegan, K.D., Harrison, T.M., Grove, M., Cheng, H., Wang, Y.J., (2007). High resolution secondary ionisation mass spectrometry (SIMS) $\delta^{18}O$ analyses of Hulu Cave speleothem at the time of Heinrich Event 1. *Chem. Geol*. **238**, 197-212.

Valley, J.W., Kita, N.T., (2009). In situ oxygen isotope geochemistry by ion microprobe. Mineral. *Assoc. Canada Short Course* 19-63.

Warren, P.H., Rubin, A.E., Isa, J., Gessler, N., Ahn, I., Choi, B.-G., (2014). Northwest Africa 5738: Multistage fluid-driven secondary alteration in an extraordinarily evolved eucrite. *Geochim. Cosmochim. Acta* **141**, 199-227.

Wasson, J.T., Rubin, A.E., (2003). Ubiquitous low-FeO relict grains in type II chondrules and limited overgrowths on phenocrysts following the final melting event. *Geochim. Cosmochim. Acta* **67**, 2239-2250.

Wirtz, T., Migeon, H.-N., (2004). Work function shifts and variations of ionization probabilities occurring during SIMS analyses using an in situ deposition of Cs^0. *Surf. Sci*. **561**, 200-207.

Young, E.D., Kohl, I.E., Warren, P.H., Rubie, D.C., Jacobson, S.A., Morbidelli, A., (2016). Oxygen isotopic evidence for vigorous mixing during the Moon-forming giant impact. *Science*. **351**, 493-496.

Yu, M.L., (1986). Chemical enhancement effects in SIMS analysis. Nucl. Instruments Methods Phys. Res. Sect. B Beam Interact. with Mater. *Atoms* **15**, 151-158.

Chapter4: R-chondrite bulk-chemical compositions and diverse oxides: Implications for parent-body processes.[1]

[1] This chapter have published at following:

Isa, J., Rubin, A. E., & Wasson, J. T. (2014). *Geochimica et Cosmochimica Acta*, *124*, 131-151.

Available online at www.sciencedirect.com

ScienceDirect

Geochimica et Cosmochimica Acta 124 (2014) 131–151

Geochimica et Cosmochimica Acta

www.elsevier.com/locate/gca

R-chondrite bulk-chemical compositions and diverse oxides: Implications for parent-body processes

Junko Isa [a,b,*], Alan E. Rubin [a,b], John T. Wasson [a,b,c]

[a] Institute of Geophysics and Planetary Physics, University of California, Los Angeles, CA 90095-1567, USA
[b] Department of Earth and Space Sciences, University of California, Los Angeles, CA 90095-1567, USA
[c] Department of Chemistry and Biochemistry, University of California, Los Angeles, CA 90095-1567, USA

Received 8 March 2013; accepted in revised form 15 September 2013; Available online 29 September 2013

Abstract

R chondrites are among the most oxidized chondrite groups; they also have the highest $\Delta^{17}O$ values known in whole-rock meteorites. We analyzed R chondrites (six Antarctic, four hot-desert) by instrumental neutron activation analysis. Data for one of the former and three of the latter show large weathering effects, but the remainder show only moderate scatter and permit us to determine trends and mean compositions for the group. Bulk R-chondrite compositions are similar to those in H and L chondrites, but the concentrations of several volatiles, especially Se and Zn, are higher; the more volatile the element, the higher the enrichment in R chondrites relative to H and L.

Petrologic types in R chondrites extend as low as 3.6. We determined olivine compositional distributions and studied opaque oxides in 15 R-chondrite thin sections, including a newly discovered R4 clast in Bencubbin (adding to the diversity of chondritic clasts in this polymict breccia) and an R clast in CM2 Murchison. Opaque oxides in R chondrites include nearly pure magnetite, Al-rich chromite, magnetite–chromite solid solution, nearly pure chromite, and ilmenite. This diverse set of opaque phases reflects differing aqueous-alteration conditions.

The least equilibrated R chondrites contain nearly pure magnetite but the spinels in metamorphosed R chondrites contain additional components (e.g., Cr_2O_3 and Al_2O_3 and some minor cations). The NiO content in olivine correlates with the magnetite component in magnetite–chromite solid solution in equilibrated R chondrites and is a function of the degree of oxidation. The absence of metallic Fe in A-881988 and LAP 031156 indicates a high degree of oxidation; the relatively low-FeO (Fa35) olivine in these rocks in part reflects the conversion of Fe^{2+} to Fe^{3+} and its partitioning into magnetite. Oxidation trends in R chondrites are affected by both aqueous alteration and thermal metamorphism. The differing degrees of oxidation in this group reflect differences in local environments on the parent asteroid.

1. INTRODUCTION

The Rumuruti (R) chondrite group along with the Karoonda group (CK) of carbonaceous chondrites constitute the two most oxidized chondrite groups. R chondrites have been studied for more than 20 years (e.g., Rubin and Kallemeyn, 1989; Weisberg et al., 1991; Bischoff et al., 1994, 2011; Schulze et al., 1994; Kallemeyn et al., 1996; Greenwood et al., 2000) and are characterized by modally abundant matrix (~35 vol.%), moderate chondrule sizes (~400 μm), abundant sulfides (typically 6–10 wt.% pyrrhotite and pentlandite), high olivine/low-Ca-pyroxene ratios (e.g., Kallemeyn et al., 1996), high $\Delta^{17}O$ values (~2.9‰) (Fig. 1) and rare refractory inclusions (~0.04 vol.%). Most R chondrites have experienced metamorphism; they range in petrologic type from 3.6 (e.g., Allan Hills (henceforth ALH) 85151) to 6 (e.g., Yamato (henceforth Y-) 980702). The high state of oxidation of R chondrites is reflected by

* Corresponding author at: Department of Earth and Space Sciences, University of California, Los Angeles, CA 90095-1567, USA. Tel.: +1 3108253202.
E-mail address: jisa@ucla.edu (J. Isa).

0016-7037/$ - see front matter © 2013 Elsevier Ltd. All rights reserved.
http://dx.doi.org/10.1016/j.gca.2013.09.018

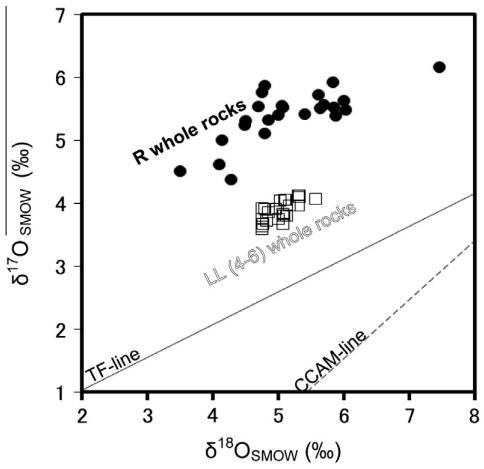

Fig. 1. Three-oxygen-isotope plot of bulk R chondrites (Bischoff et al., 2011 and references therein) and bulk LL chondrites (Clayton et al., 1991). TFL: terrestrial fractionation line, CCAM: carbonaceous chondrite anhydrous mineral line.

the absence (or very low abundance) of metallic Fe-Ni, the high Ni contents of the vast majority of the remaining metal grains (typically awaruite, ~700 mg/g Ni), the abundance of NiO-bearing (typically 1–4 mg/g) ferroan olivine (typically Fa37–40), the presence of Fe^{3+}-bearing, TiO_2-rich chromian spinel, the occurrence of magnetite in some samples, and, in the case of the R6 chondrites LAP 04840 and MIL 11207, moderately abundant hornblende and minor mica (OH-bearing phases) (McCanta et al., 2008; Ota et al., 2009; Gross et al., 2013).

R chondrites share some properties with ordinary chondrites (OC) and carbonaceous chondrites (CC). The proportions of R-chondrule textural types and their FeO/(FeO + MgO) ratios are similar to those of OC, but the high matrix abundance in R chondrites more closely resembles that of CC (matrix abundances: OC 12 vol.% vs. CC 34–60 vol.%; McSween, 1977a,b; Huss et al., 1981; Rubin and Kallemeyn, 1989; Weisberg et al., 1993; Wasson, 2008; Rubin, 2010). As discussed by Kallemeyn and Wasson (1985), chondritic meteorites can be classified on the basis of their refractory lithophile abundances: variations in mean refractory lithophile abundances are relatively small (±2%) within groups, but there is a total range of a factor of 2.5 across all chondrite groups. Refractory lithophile abundances in R chondrites are similar to those in OC and lower than those in CC. The Cr- (or Mg-) and H-chondrite-normalized refractory and common siderophile abundances in R chondrites are at OC levels; however, the volatile elements Se and Zn are significantly enriched relative to OC (Kallemeyn et al., 1996). Similarities in O-isotope compositions between magnetite in R3.8 PCA 91241 and LL3.0 Semarkona imply that these oxides formed in both chondrites by alteration of metallic Fe by high-$\Delta^{17}O$ water (Choi et al., 1998; Greenwood et al., 2000).

Although R chondrites have many similarities to OC, their opaque mineral assemblages differ. Magnetite occurs in R6 LaPaz Icefield (henceforth LAP) 04840 (Righter and Neff, 2007; McCanta et al., 2008) and R3.8 Pecora Escarpment (henceforth PCA) 91241; chromite occurs in other R chondrites (e.g., ALH 85151, Rubin and Kallemeyn, 1989; Rumuruti, Schulze et al., 1994). In contrast, most oxides in equilibrated ordinary chondrites are compositionally relatively uniform chromites (Bunch et al., 1967). Because oxide compositions reflect metamorphic conditions on parent bodies (e.g., bulk chemical compositions, temperatures and degrees of oxidation), and each chondrite group shows different characteristics, the compositions of oxides in R chondrites can provide useful information about the metamorphic and alteration history of this group.

We used instrumental neutron activation analysis (INAA) to determine the bulk chemical compositions of 10 R chondrites to help clarify the relationship between R chondrites and other chondrite groups. We also examined the petrology and mineralogy of 14 R chondrites in addition to two R-chondrite clasts in Bencubbin and Murchison to document R-chondrite parent-body processes, especially focusing on oxide compositions.

2. SAMPLES AND ANALYTICAL TECHNIQUES

We examined thin sections of 14 R chondrites (A-881988,52-2; Dar al Gani (henceforth DaG) 013, PL96037; LAP 02238,20; LAP 031156,8; LAP 03639,20; LAP 03645,8; LAP 04840,29; Meteorite Hills (henceforth MET) 01149,8; Northwest Africa (henceforth NWA) 830, UCLA 1038; NWA 978, UCLA 1411; NWA 2198, UCLA 1572; Mount Prestrud (henceforth PRE) 95404,15; PRE 95411,8; and Y-980702,51-2) as well as two newly discovered R-chondrite clasts from Bencubbin (LC 2491) and Murchison (MZ-R1). The sources of these thin sections are listed in Table 1.

2.1. Petrographic studies

The R-chondrite thin sections were studied with an optical microscope, a LEO 1430 scanning electron microscope (SEM), and the JEOL 8200 electron microprobe at UCLA. Modal analyses were made using a point counter connected to the microscope stage. The stage moves a constant distance (50 μm) with each counted point. Phases larger than ~0.1 μm at the center of the field were identified in reflected light at 500×. The uncertainties in the modal abundances were calculated based on counting statistics (Table 1). These uncertainties do not represent the sampling error and thus are lower limits. Quantitative mineral compositions were obtained by EPMA with 20-s counting times, ZAF corrections and a sample current of ~15 nA at 15 kV. Standards for EPMA are millerite for S, 99.99% of iron metal for Fe in metal and sulfide, magnetite for Fe in silicate and opaque oxides, NBS1156 (NIST) for Co and Ni in metal, chromite (Smithsonian) for Cr, anorthite for Al, albite for Na, diopside for Ca, sphene for Ti, forsterite for Si and Mg, and NiO-bearing olivine for Ni. Cobalt concentrations were measured with a LiF spectrometer; background counts were taken on both sides of the peak. A pure Fe standard (99.99% Fe) was analyzed to determine

Table 1
R-chondrite samples, opaque minerals, weathering category, modal abundances and mode of olivine compositions.

Name	Type	Thin section numbers	Weathering category	INAA data	chr–mgt–hrc–ulv	Other oxides	pn	pyr	mss	Metal	Oxide (vol.%)	Sulfide (vol.%)	Mode olivine (Fa)	Cr/Fe ratio in oxide**
PRE 95404	R3.6	15	wi-3	yes	+	ilm, chm, mgt	+	+	ab	aw, ka	0.4 ± 0.1	n.d.	40	n.d.
LAP 02238	R3.7	20	wi-4	n.d.	+	ab	+	+	ab	ab	n.d.	n.d.	39	n.d.
DAG 013	R3.8	PL96037	wi-5	n.d.	+	chm	+	+	ab	ab	n.d.	n.d.	39	n.d.
LAP 03645	R3.8	8	wi-4	n.d.	+	ab	+	+	ab	ab	n.d.	n.d.	39	n.d.
MET 01149*	R3.8	8	wi-1	yes	+	ab	+	+	ab	ka	n.d.	n.d.	38	n.d.
NWA 978	R3.8	UCLA 1411	wi-5	yes	+	ab	ab	+	ab	tt	n.d.	n.d.	39	n.d.
PRE 95411	R3.8	8	wi-4	n.d.	+	ilm	+	+	ab	aw, ka	0.2 ± 0.1	n.d.	38	n.d.
A-881988	R4	52–2	wi-3	yes	+	ab	ab	ab	+	ab	2.7 ± 0.4	5.3 ± 0.5	35	0.14
Bencubbin clast	R4	LC 2491	n.d.	n.d.	+	ab	ab	+	+	high-Ni	0.7 ± 0.3	6 ± 1	38	0.52
LAP 031156	R4	8	wi-1	n.d.	+	ab	+	ab	+	ab	3.5 ± 0.5	7.2 ± 0.7	35	0.12
NWA 2198	R4	UCLA 1572	wi-1	yes	+	ab	+	+	ab	ab	1.1 ± 0.3	7.6 ± 0.8	39	1.0
LAP 04840	R6	29	wi-0	yes	+	ab	+	+	ab	ab	1.5 ± 0.5	7 ± 1	n.d.	0.28
NWA 830	R5	UCLA 1038	wi-6	n.d.	+	ab	+	ab	+	ab	2.9 ± 0.4	n.d.	39	1.1
Y-980702	R6	51–2	wi-0	n.d.	+	ilm	+	+	+	ab	0.6 ± 0.2	5.3 ± 0.4	38	1.2
Murchison clast	R	–	wi-0	n.d.	+	ab	ab	+	+	high-Ni	0.6 ± 0.6	9	37	0.98
LAP 03639	R4	20	wi-1	yes	n.d.	n.d.	+	+	n.d.	ab	n.d.	n.d.	n.d.	n.d.
NWA 753	R3.9	no section	n.d.	yes	n.d.	n.d.	n.d	n.d	n.d.	n.d.	n.d.	n.d.	n.d.	n.d.
RaS 201	R5	no section	n.d.	yes	n.d.	n.d.	n.d	n.d	n.d.	n.d.	n.d.	n.d.	n.d.	n.d.

chm = chromite; hrc = hercynite; ilm = ilmenite; mgt = magnetite; chr–mgt–hrc–ulv = chromite–magnetite–hercynite–ulvöspinel solid solution.
pn = pentlandite; pyr = pyrrhotite; aw = awaruite; ka = kamacite; tt = tetrataenite; high-Ni = high Ni content Fe-Ni metal; mss = monosulfide solid solution.
Mode olivine (Fa) = the peak in the olivine compositional distribution (Fig. 2).
wi = the weathering categories are based on Rubin and Huber (2005) and were designed specifically for metal-poor meteorites such as R chondrites.
yes = bulk chemical analysis were obtained by INAA in this study.
+ = present; ab = absent.
n.d. = not determined; NWA 830 is too weathered to determine the oxide content.
We classified the oxides into the following categories in this study: ilmenite (ilmenite containing <1% other oxides); magnetite (magnetite containing <1% other oxides); chromite (chromite containing <1% other oxides); Cr-bearing magnetite (magnetite containing 1–5% other oxides); Fe-bearing chromite (chromite containing 1–5% other oxides); Al-rich chromite for spinels containing 17–31 wt.% Al_2O_3 and 29–41 wt.% Cr_2O_3; and magnetite–chromite solid solution for spinels having large chromite and large magnetite components and containing less than ~8 wt.% Al_2O_3 and less than ~7 wt.% TiO_2.
* Previously classified as CK3.
** Mean values of mol Cr/Fe ratios in chr-mgt-hrc-ulv oxide solid solutions.

the interference from the tail of the Fe-K_β peak with the Co-K_α peak; appropriate corrections were made to the analyses. Potential interferences of chromite analyses are from the K_β peak of Ti on the K_α peak of V, and from the K_β peak of V on the K_α peak of Cr. The R-chondrite chromite grains do not contain enough V for these corrections to be significant. Back-scattered electron images (BSE) were made with the LEO 1430 SEM.

2.2. INAA studies

2.2.1. Samples, including possible pairings

The bulk compositions (24 elements) of 10 R chondrites were determined by INAA: LAP 04840 (R6), RaS 201 (R5), A-881988 (R4), LAP 031156 (R4), LAP 03639 (R4), NWA 2198 (R4), NWA 753 (R3.9), MET 01149 (R3.8), NWA 978 (R3.8) and PRE 95411 (R3.8). Samples had masses in the range 250 to 310 mg; when possible, these samples were cut into 3-mm-thick slices but some consisted of powder and crumbs. The sample masses, 250–300 mg, are well suited for our INAA procedure; duplicate analyses have demonstrated that these sample masses are generally sufficient to represent whole rocks. During irradiation the samples and standards were wrapped in aluminum foil or were packed in clean polyethylene vials. The samples and standards were irradiated for 3 h in the TRIGA Mark I reactor of the University of California, Irvine, with a neutron flux of $\sim 1.5 \times 10^{12}$ neutrons cm^2 s^{-1}. Standards included three powders (the Allende CV3 chondrite, the USGS BHVO-1 and/or SCo-1) and a slab of the North Chile IIAB (Filomena) iron meteorite. Gamma-ray spectrometry was performed at UCLA following a protocol similar to that of Kallemeyn et al. (1989). All samples except MET 01149 were analyzed in duplicate runs. With the exception of Ca, Br, Ru, Sb, Yb, Lu and Os, standard deviations attributable to analytical (rather than sampling) errors are 3% or less. Sampling errors were commonly somewhat larger.

It is important to assess probable pairings among the R chondrites from LaPaz Ice Field. Three of these samples were analyzed by INAA in this study: R6 LAP 04840, R4 LAP 031156 and R4 LAP 03639. LAP 04840 contains hornblende and mica (e.g., McCanta et al., 2008) and is paired with R6 LAP 10033 and R6 LAP 10031. All of the other LAP R chondrites are of lower petrologic type and do not contain hornblende; they are not paired with LAP 04840. The Meteoritical Bulletin indicates that R4 LAP 031156 is paired with R4 LAP 031135; several R4 chondrites are listed as being paired with R4 LAP 03639: LAP 03731, LAP 03793, LAP 03902, LAP 031144, LAP 031387, and LAP 04845. Our petrographic observations indicate that the texture of LAP 03639 is very similar to that of LAP 031156. It therefore seems likely that all of these R4 chondrites are paired.

We determined the olivine compositional distributions of two other R chondrites from the LaPaz Ice Field region: R3.7 LAP 02238 (Fa17–48; Fig. 2) and R3.8 LAP 03645 (Fa15–46; Fig. 2). The former appears less recrystallized than the latter; chondrules are better defined and there is less textural integration between chondrules and matrix. We tentatively conclude that the samples are not paired.

Two other unpaired R chondrites from LaPaz Ice Field are listed in the Meteoritical Bulletin: R5 LAP 031275 and R3 LAP 03834. The former is the only LAP R5 chondrite; the latter exhibits significant shock darkening and is thus not paired with the other R3 chondrites. In summary, at this writing, there appear to be six different R chondrites: R6 LAP 04840 (and pairs), R4 LAP 03639 (and pairs including LAP 031156), R3.7 LAP 02238, R3.8 LAP 03645, R3 LAP 03834, and R5 LAP 031275. We treat these samples as six different meteorites since their distinguishable lithologies likely represent different petrogenetic histories. Nevertheless, the possibility exists that some of these samples are paired and are derived from genomict breccias.

3. RESULTS

3.1. Petrography

Mineral compositions and modal abundances are summarized in Tables 1–5; olivine compositional distributions are shown in Fig. 2. Back-scattered electron (BSE) images of type-3 R chondrites are shown in Fig. 3 at two different magnifications. Modes of Fa in olivine range from 35 to 42 among the R3.6 to R6 chondrites. All modes are $\geqslant$Fa37 except those for R4 A-881988 and LAP 031156 (both Fa35); the vertical dashed line in Fig. 2 is drawn at Fa38 (the most common mean Fa composition among R chondrites).

3.1.1. Chondrule and olivine compositions in selected unequilibrated samples

We examined thin sections of seven R3 chondrites. Both low-FeO ($Fa < \sim 4$) and high-FeO ($Fa > \sim 4$) porphyritic chondrules occur in all of these rocks. The low-FeO chondrules in R3 chondrites are similar to those in OCs and CCs and equivalent to type-I chondrules in texture (Fig. 3). The widest olivine compositional range is Fa1–46 in PRE 95404 (Fig. 2). Although PRE 95411 is listed as being paired with PRE 95404 (R3.6), the olivine compositional distribution is much more equilibrated (mostly Fa36–42) in our section of PRE 95411.

DaG 013 (R3.5–6) was well described in previous studies (Jäckel et al., 1996; Bischoff, 2000); Bischoff (2000) observed type-3 lithologies and equilibrated clasts in the Münster thin sections PL95141 and PL96218. The thin section we studied (PL96037) also contains type-3 lithologies with an olivine compositional distribution consistent with petrologic type 3.8 (Fig. 2). Equilibrated clasts were not observed.

MET 01149 is an R3 fragmental breccia that was originally classified as CK. The section includes a 1-mm equilibrated R5 clast. Chondrule sizes (400–500 μm) are typical for R chondrites. The silicate compositions are also typical for R chondrites; most olivines range from Fa37 to Fa42; the mode is at Fa38 (Fig. 2). The low-Ca pyroxene range is Fs8–31, and plagioclase has a mean composition of Ab85Or6.

3.1.2. Olivine compositions in equilibrated samples

Equilibrated R-chondrite samples have peaks in their olivine compositional distributions ranging from Fa35 to Fa39. Mean olivine NiO contents are highly variable, ranging from <1 to 5 mg/g.

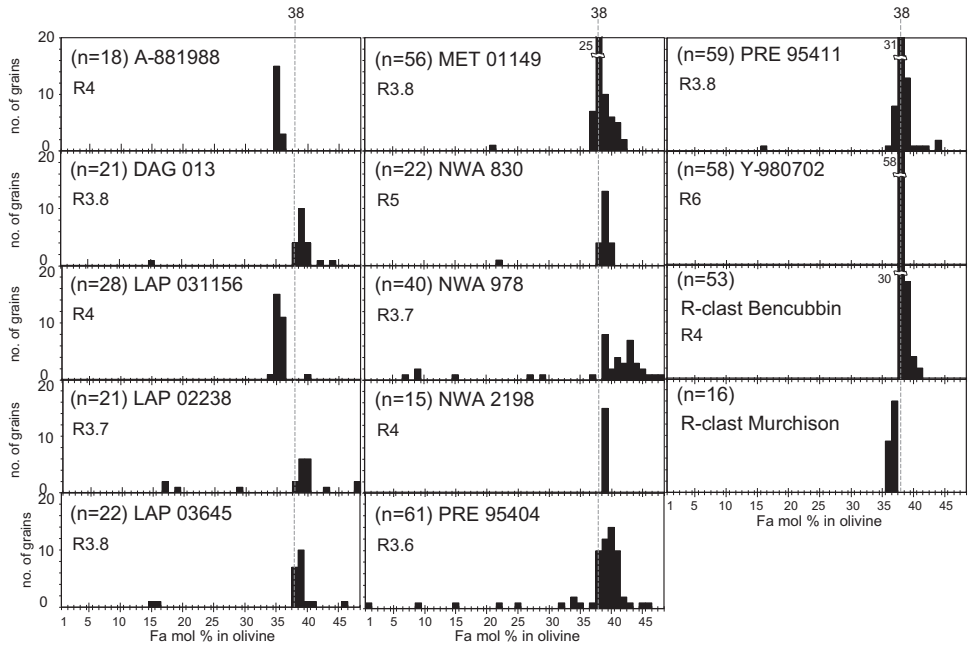

Fig. 2. Olivine compositional distributions in R chondrites. Unequilibrated samples show a wide distribution whereas equilibrated samples show a narrow distribution. The peak varies among R chondrites but does not correlate with petrologic type. A vertical line at Fa38 (the most common R-chondrite Fa value) facilitates the recognition of differences in the modes.

A-881988 and LAP 031156 have the lowest olivine peak Fa values (~Fa35) observed in equilibrated R chondrites; we show below that this is associated with a large fraction of Fe^{3+}. Olivine of similar composition (Fa35–37) was reported in an unequilibrated R-like clast from the Almahata Sitta ureilite (Horstmann and Bischoff, 2010).

3.1.3. Opaque minerals

Opaque mineral compositions and the degree of terrestrial weathering (using the index developed by Rubin and Huber, 2005) are listed in Table 1 and Tables 3–5. Sulfide and oxide assemblages are common in R chondrites (Fig. 4), but the phases differ in different meteorites. Many of the grains have irregular, scalloped boundaries; smaller grains may be fragments of larger assemblages. A few chondrules are rimmed by sulfide. LAP 03639 (R4) contains a bleached cryptocrystalline chondrule (cf. Grossman et al., 2000) with a few 2–4-μm-size sulfides in the bleached zone at the chondrule periphery.

Most of the sulfide grains in equilibrated R chondrites are pentlandite ($(Fe,Ni)_9S_8$) and pyrrhotite ($Fe_{1-x}S$). Monosulfide solid solution ($Fe_{1-x}S$-$Ni_{1-x}S$) is also present in equilibrated R-chondrites as well as in the R-chondrite clasts in Bencubbin and Murchison. Some of the weathered sulfide grains in A-881988 are inferred to have been monosulfide solid solution (mss) based on cation balances, but because of their weathered nature and small grain size, only semi-quantitative data are available. The mss grains in A-889188 contain ~360 mg/g S, ~460 mg/g Fe, ~120 mg/g Ni and minor amounts of Cr, Co and Cu. Pyrite and refractory-enriched (e.g., $(Os,Ru,Ir)S_2$) sulfide grains reported in other R chondrites (e.g., PCA 91002, Y-793575, and Acfer 217; Bischoff et al., 1994; Kallemeyn et al., 1996) were not observed.

Among the samples in this study, metallic Fe-Ni grains occur in PRE 95404, PRE 95411, MET 01149, NWA 978, Bencubbin-R, Murchison-R and Y-980702; most grains are <10 μm in size. The larger (>10 μm) metal grains in R chondrites occur outside of chondrules as isolated grains in the matrix. In contrast to most R chondrites (in which coarse metal was not observed), some of the type-3 R-chondrites contain rare metal grains appreciably greater than 10 μm in size; the largest grain size is 65 × 100 μm. Most grains of metallic Fe-Ni are in the compositional range of awaruite, but rare grains of tetrataenite, kamacite and martensite also occur in type-3 R chondrites (e.g., PRE 95404, PRE 95411, MET 01149, NWA 978 and ALH 85151). In PRE 95404, both kamacite and awaruite (with 700–750 mg/g Ni) are present. A few small grains of low-Ni kamacite (22–53 mg/g Ni) occur within a low-FeO olivine grain (Fig. 5a) in PRE 95404. The interior of this metal-bearing olivine grain is fairly homogeneous (Fa 0.4 ± 0.1) and contains a few small (1–10 μm) grains of Ca,Al-rich pyroxene. Thin section PRE 95411,6 contains ~50 heterogeneously distributed metallic Fe-Ni grains (constituting 0.04 vol.% of the section) (Fig. 5b); most grains are awaruite (with ~700 mg/g Ni), a few are tetrataenite (Table 4). A single tetrataenite grain was found in NWA 978.

Oxide phases include nearly pure magnetite, nearly pure chromite, magnetite-chromite solid solution with low Al and low Ti, chromite–hercynite–ulvöspinel solid solution, and ilmenite. Oxides consisting of nearly pure magnetite

Table 2
Mean compositions (mg/g) of silicates in R chondrites.

Phase	PRE95411			LAP02238				PRE95404				NWA978		LAP03645		
	olv	di	plg	olv	low-Ca px	aug	plg	olv	low-Ca px	aug	pi	olv	low-Ca px	olv	low-Ca px	plg
n.	59	2	6	15	3	1	1	61	23	5	3	20	3	22	1	4
SiO_2	367	537	650	370	571	539	661	366	558	525	541	358	572	369	563	657
TiO_2	<0.2	<0.2	<0.2	<0.2	1.0	2.0	<0.2	<0.2	0.8	3.0	1.3	<0.2	<0.2	<0.2	0.6	<0.2
Al_2O_3	<0.1	3.9	2.1	1.0	4.7	3.5	219	<0.1	5.3	21	15	<0.1	<0.2	0.3	2.0	211
Cr_2O_3	<0.3	6.0	<0.3	1.3	5.9	4.5	<0.3	<0.3	6.6	14	13	<0.3	<0.3	1.7	7.8	<0.3
FeO	326	65	4.7	316	77	69	5.1	323	116	76	124	345	63	318	122	12
NiO	<0.4	1.4	<0.4	1.2	1.3	<0.4	0.9	1.1	<0.4	0.5	<0.4	1.9	<0.4	1.6	<0.4	<0.4
MnO	<0.2	1.3	<0.2	3.8	3.3	1.9	<0.2	3.8	4.8	8.7	7.8	3.5	2.8	3.9	4.5	<0.2
MgO	305	155	<0.3	317	329	157	<0.3	313	303	168	260	283	344	314	302	3.0
CaO	0.5	221	19	1.3	9.7	207	20	0.9	8.2	178	42	0.9	2.3	0.7	3.2	18
Na_2O	<0.1	5.0	101	<0.1	0.4	4.1	103	<0.1	0.6	4.6	0.7	<0.1	<0.1	<0.1	<0.1	103
K_2O	n.a.	n.a.	7.1	n.a.	n.a.	n.a.	n.a.	n.d.	n.d.	n.d.	n.a.	n.a.	n.a.	n.a.	n.a.	n.a.
Total	999	996	992	1012	1003	988	1008	1008	1003	999	1005	992	985	1009	1005	1004
End-member	Fa16–44	Fs18–20 Wo44–46	Ab85–88 Or4	Fa17–48	Fs11–23 Wo0–5	Fs20 Wo43	Ab89	Fa1–47	Fs1–36 Wo0–4	Fs5–32 Wo33–46	Fs13–26 Wo7–10	Fa7–50	Fs3–10 Wo0–1	Fa15–46	Fs19, Wo1	Ab90
Mean	Fa38	Fs19, Wo45	Ab87, Or4	Fa36	Fs12, Wo2			Fa38	Fs18, Wo2	Fs20, Wo38	Fs21, Wo8	Fa38	Fs5, Wo1	Fa36		
s.d.	3		1, 0.3	9	10, 2			8	9, 1	10, 6	7, 2	10	4, 1	7		

	MET 01149			DAG 013			A-889188			R clast in Bencubbin				LAP 031156		
	olv	low-Ca px	plg	olv	low-Ca px	plg	olv	low-Ca px	plg	olv	low-Ca px	di	plg	Olv	low-Ca px	hd
n.	56	2	1	21	1	1	18	3	1	53	2	6	12	28	4	1
SiO_2	367	558	639	363	590	671	365	539	631	359	540	528	641	370	553	468
TiO_2	<0.2	<0.2	<0.2	<0.2	<0.2	0.5	<0.2	<0.2	<0.2	<0.2	<0.2	0.7	<0.2	<0.2	<0.2	8.9
Al_2O_3	<0.1	<0.1	206	<0.1	1.0	216	<0.1	0.9	197	<0.1	1.4	4.9	213	0.9	2.6	132
Cr_2O_3	<0.3	<0.3	<0.3	<0.3	4.6	0.5	<0.3	<0.3	<0.3	<0.3	0.9	3.2	<0.3	<0.3	2.7	2.8
FeO	327	130	4.2	327	25	8	303	178	51	335	196	76	11	311	148	1.8
NiO	1.5	2.2	<0.4	1.7	<0.4	<0.4	4.0	1.2	1.7	4.5	<0.4	2.3	<0.4	4.1	<0.4	0.8
MnO	3.9	3.0	<0.2	4.0	<0.2	<0.2	4.0	3.9	<0.2	4.2	4.1	1.8	<0.2	4.2	3.1	<0.2
MgO	301	294	<0.3	305	381	<0.3	318	257	5.6	305	257	153	1.0	317	285	135
CaO	0.6	6.2	19	0.5	1.4	20	0.4	5.3	18	1.4	5.1	213	23	0.9	4.3	252
Na_2O	<0.1	<0.1	97	<0.1	<0.1	98	<0.1	<0.1	89	0.3	<0.1	5.3	98	<0.1	<0.1	<0.1
K_2O	n.a.	n.a.	9.9	n.a.	n.a.	n.a.	n.a.	n.a.	n.a.	<0.4	<0.4	<0.4	5.5	n.a.	n.a.	n.a.
Total	1001	993	976	1001	1003	1014	994	985	993	1009	1005	988	993	1008	999	1001
End-member	Fa21–42	Fs10–30 Wo1–2	Ab84 Or6	Fa15–44	Fs3 Wo0	Ab88	Fa35–36	Fs28 Wo1	Ab88	Fa38–41	Fs28–32 Wo1	Fs20–30 Wo44–50	An3–23 Or2–17	Fa34–40	Fs16–29 Wo0.3–1.3	Fs1 Wo57
Mean	Fa38			Fa38			Fa35			Fa38	Fs30, Wo1	Fs22, Wo48	An11, Or3	Fa36	Fs23, Wo0.8	
s.d.	3			6			1			1		4,2	5, 4	1	5.6, 0.5	

(continued on next page)

	NWA 2198			NWA 830				LAP 04840		Y-980702				R clast in Murchison		
	olv	di	plg	olv	low-Ca px	aug	pi	olv	low-Ca px	olv	low-Ca px	di	plg	olv	di	plg
n.	15	1	1	22	6	1	1	3	1	58	1	4	10	25	3	2
SiO_2	368	540	676	367	565	545	520	370	548	370	547	541	654	368	519	440
TiO_2	<0.2	1.1	1.0	<0.2	1.0	2.4	3.0	<0.2	<0.2	<0.2	1.5	1.6	<0.2	<0.2	8.5	<0.2
Al_2O_3	<0.1	2.7	212	0.5	2.1	5.4	52	<0.1	1.3	<0.1	1.6	3.6	213	<0.1	23	347
Cr_2O_3	<0.3	4.6	<0.3	<0.3	2.3	7.5	1.8	<0.3	n.d.	<0.3	<0.3	4.5	<0.3	<0.3	9.5	<0.3
FeO	338	68	9.2	326	121	70	142	329	193	330	192	71	3.7	319	60	6.2
NiO	1.7	<0.4	1.2	1.8	<0.4	1.1	<0.4	3.6	1.4	2.5	<0.4	<0.4	n.d.	<0.4	<0.4	<0.4
MnO	4.2	1.5	<0.2	3.9	3.1	1.8	2.8	4.5	3.8	4.0	3.5	1.5	<0.2	3.6	0.9	<0.2
MgO	302	155	<0.1	303	303	155	236	307	254	308	252	155	<0.1	318	141	<0.1
CaO	0.5	211	15.1	0.4	4.5	202	45	0.4	4.0	0.9	9.9	216	22	3.0	229	15
Na_2O	<0.1	4.2	99	<0.1	<0.1	4.9	1.2	<0.1	<0.1	<0.1	<0.1	4.3	99	<0.1	6.7	172
K_2O	n.a.	n.a.	n.a.	n.a.	n.a.	n.a.	n.a.	n.a.	n.a.	n.a.	n.a.	n.a.	9.8	n.a.	n.a.	n.a.
Total	1014	988	1014	1003	1002	995	1004	1015	1006	1015	1008	999	1002	1012	998	980
End-member	Fa39	Fs20 Wo44	Ab 92	Fa22–40	Fs2–30 Wo0–2	Fs12 Wo43	Fs23 Wo9	Fa38	Fs30	Fa38	Fs29 Wo2	Fs11–12 Wo43–45	Ab82–85 Or4–6	Fa36–37	Fs19–20 Wo48–49	Ab95
Mean				Fs18, Wo1				Fa38		Fa38		Fs11,Wo44	Ab84, Or6	Fa36	Fs19, Wo49	Ab95
s.d.				1, 13				0.1		0.2		0.6	1, 1	0.01	0.4	

n.a. = not analyzed.

olv = olivine, di = diopside, hd = hedenbergite, augite = aug, pi = pigeonite, low-Ca pyroxene = low-Ca px, plg = plagioclase,

< = detection limit (1σ).

Element detection limits are 1σ values based on the background count rate: Na_2O 0.1 mg/g, MgO 0.1 mg/g, Al_2O_3 0.1 mg/g, SiO_2 0.1 mg/g, K_2O, CaO 0.1 mg/g, TiO_2 0.2 mg/g, Cr_2O_3 0.3 mg/g, MnO 0.2 mg/g, FeO 0.2 mg/g and NiO 0.4 mg/g.

Table 3
Mean compositions (mg/g) of sulfides in R chondrites.

Phase	PRE 95404			LAP 02238			PRE 95411			NWA 978	LAP 03645		MET 01149	
	pent	low-Ni pent	pyr	pent	low-Ni pent	pyr	pent	low-Ni pent	pyr	pyr	pent	pyr	pent	pyr
n.	3	1	4	2	1	1	1	5	16	3	2	1	6	2
S	328	327	365	329	330	376	333	334	366	374	329	362	326	365
Fe	359	435	608	325	413	602	346	412	629	603	343	617	341	614
Ni	286	205	<0.4	331	237	<0.4	323	240	<0.4	0.7	305	<0.4	308	0.9
Cr	<0.4	0.5	<0.4	<0.4	<0.4	<0.4	<0.4	0.4	<0.4	<0.4	0.4	<0.4	<0.4	<0.4
Co	12	7.1	<0.3	12	8.6	1.1	9.9	16	<0.3	<0.3	11.5	<0.3	12	1.1
Cu	n.a.	n.a.	n.a.	0.8	0.6	<0.4	n.a.	n.a.	n.a.	<0.4	0.7	<0.4	n.a.	n.a.
total	985	975	973	998	988	979	1012	1002	995	978	990	979	987	981

	R clast in Bencubbin			LAP 031156		NWA 2198		NWA 830	Y-980702			R clast in Murchison	
	mss	low-Ni mss	pyr	pent	mss	pent	pyr	pent	pent	low-Ni mss	pyr	mss	pyr
n.	8	1	1	1	11	1	2	2	11	2	7	4	6
S	346	356	381	324	375	331	378	334	329	365	378	325	360
Fe	456	564	586	284	501	333	600	355	334	548	595	358	622
Ni	166	61	5.0	356	100	320	2.0	284	318	60	5.0	281	<0.4
Cr	0.7	<0.4	0.5	<0.4	0.2	<0.4	<0.4	<0.4	<0.4	<0.4	<0.4	<0.4	<0.4
Co	6.0	2.0	<0.3	15	3.0	13	<0.3	11	6.0	2.0	0.5	18	<0.3
Cu	n.a.	n.a.	n.a.	n.a.	n.a.	<0.4	1.0	0.7	n.a.	n.a.	n.a.	n.a.	n.a.
Total	975	983	973	979	979	997	981	985	987	975	979	982	982

n.a. = not analyzed.
pent = pentlandite, pyr = pyrrhotite, mss = monosulfide solid solution.
< = detection limit (1σ of background count rates).
Element detection limits are 1σ values based on the background count rate:
S 0.1 mg/g, Cr 0.4 mg/g, Fe 0.3 mg/g, Co 0.3 mg/g, Ni 0.4 mg/g and Cu 0.4 mg/g.

Table 4
Mean compositions (mg/g) of metal.

Phase	PRE95400		PRE95411		NWA 978
	Awaruite	Kamacite	Awaruite	Taenite	Taenite
n.	2	5	33	3	1
S	<0.4	<0.4	<0.4	<0.4	<0.4
Fe	297	947	301	549	521
Ni	700	37	692	417	464
Cr	<0.4	<0.4	<0.4	<0.4	<0.4
Co	15	4.0	15	19	1.0
Cu	n.a.	<0.4	n.a.	n.a.	<0.4
Total	1012	988	1008	985	986

n.a. = not analyzed.
< = detection limit (1σ of background count rates).
Element detection limits are 1σ values based on the background count rate:
S 0.1 mg/g, Cr 0.4 mg/g, Fe 0.3 mg/g, Co 0.3 mg/g, Ni 0.4 mg/g and Cu 0.4 mg/g.

and nearly pure chromite occur only in samples of petrologic type 3. Fig. 7a shows spinel compositions in R3 chondrites; these have a fairly constant hercynite + ulvöspinel component. Fig. 7b shows spinel compositions in R4, R5 and R6 chondrites; some grains are in the same compositional range as R3 spinel, whereas others are enriched in magnetite. The most magnetite-rich grains occur in the R4 chondrites A-881988 and LAP 031156. We calculated the partitioning of Fe between Fe^{2+} and Fe^{3+} based on stoichiometric and cation-balance considerations; Ti was assumed to be Ti^{4+} for ilmenite and ulvöspinel. Chromite–hercynite solid solution occurs in PRE 95411 and the Murchison clast.

Many of the R chondrites contain quasi-equant oxide grains, 25–150 μm in size. Some of the grains are isolated; others occur at the edges of comparably sized sulfide grains. NWA 2198 (R4) has some porphyritic olivine (PO) chondrules that include a few 5–40-μm-size oxide grains. DaG 013 (R3.8) contains a 40-μm-size oxide-plagioclase assemblage (cf. Rubin, 2003) consisting of

Table 5
Mean compositions (mg/g) of chromite-magnetite solid solution in type 3 R chondrites.

	PRE 95404		LAP 02238		PRE 95411		NWA 978	LAP 03645		MET 01149		DAG 013	
	mean	s.d.	mean	s.d.	mean	s.d.	mean	mean	s.d.	mean	s.d.	mean	s.d.
No.	10		8		11		1	24		12		9	
SiO2	0.6	0.6	1.0	1	<0.5		0.5	<0.5		<0.5		<0.5	
TiO2	54	22	53	9	58	3	58	58	9	49	15	53	10
Al2O3	54	11	53	12	43	4	82	46	9	51	10	59	16
Cr2O3	458	48	374	78	457	73	433	346	37	445	73	426	42
FeO	382	43	471	66	389	65	384	502	34	393	67	423	38
NiO	5.1	0.4	1.0	0.7	<0.9		<0.9	1.1	0.7	0.9	0.7	2.0	1
MnO	11	4	4.8	0.6	5.2	0.5	4.0	4.9	0.5	5.1	0.4	5.0	0.5
MgO	0.7	0.8	12	2.0	15	2	19	11.0	0.9	12	4	12	1
CaO	1.0	1	0.5	0.3	<0.3		<0.3	0.8	0.5	<0.3		<0.3	
Na2O	0.4	0.3	0.7	0.4	0.4	0.3	0.5	0.5	0.3	0.6	0.2	0.5	0.4
Total	967		971		968		981	970		957		981	

Mean compositions (mg/g) of chromite-magnetite solid solution in equilibrated R chondrites

	Y-980702		NWA 830		NWA 2198		Bencubbin		LAP 04840		A-881988		LAP 031156	
	Mean	s.d.	Mean	s.d.	Mean	s.d.	Mean	s.d.	Mean	s.d.	Mean	s.d.	Mean	s.d.
No.	10		4		17		18		17		29		13	
SiO_2	<0.5		2	2	0.6	0.5	<0.5		1.0	0.6	0.5	0.2	0.5	0.3
TiO_2	72	14	57	7	68	4	50	1	14	0.6	21	0.5	17	0.4
Al_2O_3	44	3	51	4	57	2	29	0.6	24	0.5	20	0.4	15	0.5
Cr_2O_3	475	20	470	10	445	6	303	7	200	6	115	2	101	3
FeO	370	11	388	10	402	5	548	14	681	8	752	5	781	4
NiO	1.5	0.7	0.8	0.3	1.0	1	6.0	8	2.8	0.6	3.3	0.6	2.9	0.8
MnO	4.5	0.3	5.4	0.4	5.3	0.2	4.1	0.3	(4)		(4)		(4)	
MgO	34.8	0.5	10	1	10	1	21	2	17.0	0.5	15.9	0.4	12.8	0.4
CaO	<0.3		<0.3		0.4	0.3	0.8	0.8	3.0	5	<0.3		0.5	1
Na_2O	<0.2		<0.2		0.9	0.4	<0.2		<0.2		<0.2		<0.2	
Total	1002		984		990		962		945		929		932	
$Fe_2O_3^*$	40		40		41		254		434		505		535	
FeO*	334		353		365		320		291		297		300	
Total*	1006		989		994		988		987		978		985	

Mean compositions (mg/g) of oxide in an R clast in Murchison

	Murchison	
	Mean	s.d.
No.	7	
SiO_2	<0.5	
TiO_2	43	6
Al_2O_3	211	43
Cr_2O_3	355	32
FeO	343	9
NiO	1.3	0.7
MnO	<4	
MgO	45	7
CaO	<0.3	
Na_2O	<0.2	
Total	1002	

All Fe is given as FeO.
< = detection limit (1σ of background count rates).
The quantitative analytical limit for Mn, (4 mg/g) is given by 10σ of detection limit.
$Fe_2O_3^*$, FeO* and Total* were estimated by cation valances of spinel structure.
Element detection limits are 1σ values based on the background count rate: Na_2O 0.2 mg/g, MgO 0.3 mg/g, Al_2O_3 0.3 mg/g, SiO_2 0.5 mg/g, CaO 0.3 mg/g, TiO_2 0.7 mg/g, Cr_2O_3 0.8 mg/g, FeO 0.4 mg/g and NiO 0.8 mg/g.

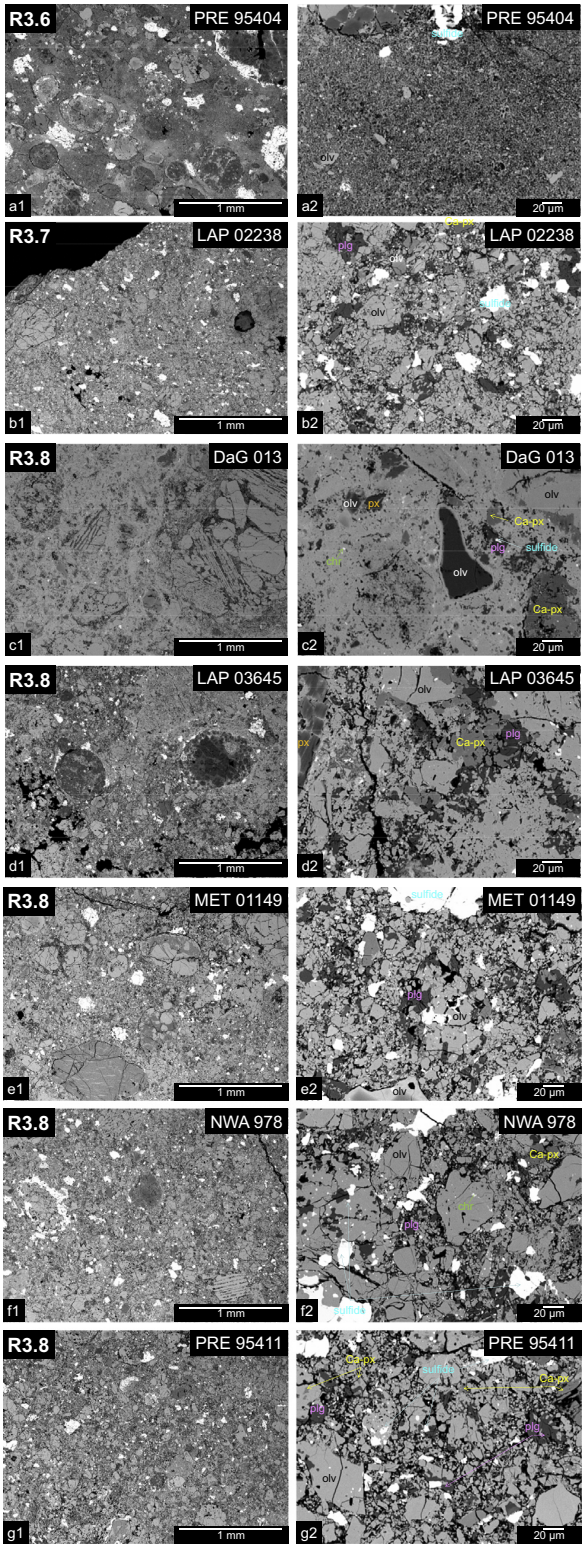

Fig. 3. BSE images of seven type-3 R chondrites. For each meteorite, low-magnification images are on the left and high-magnification image are on the right. FeO-rich olivine grains occur in the fine-grained matrix in most of the meteorites (b2-g2); the sole possible exception is fo PRE 95404 (a2) in which the fine-grained phases in the matrix were not identified. Abbreviations: (plg) plagioclase, (olv) olivine, (px pyroxene, (Ca-px) high-Ca pyroxene, (chr) chromite.

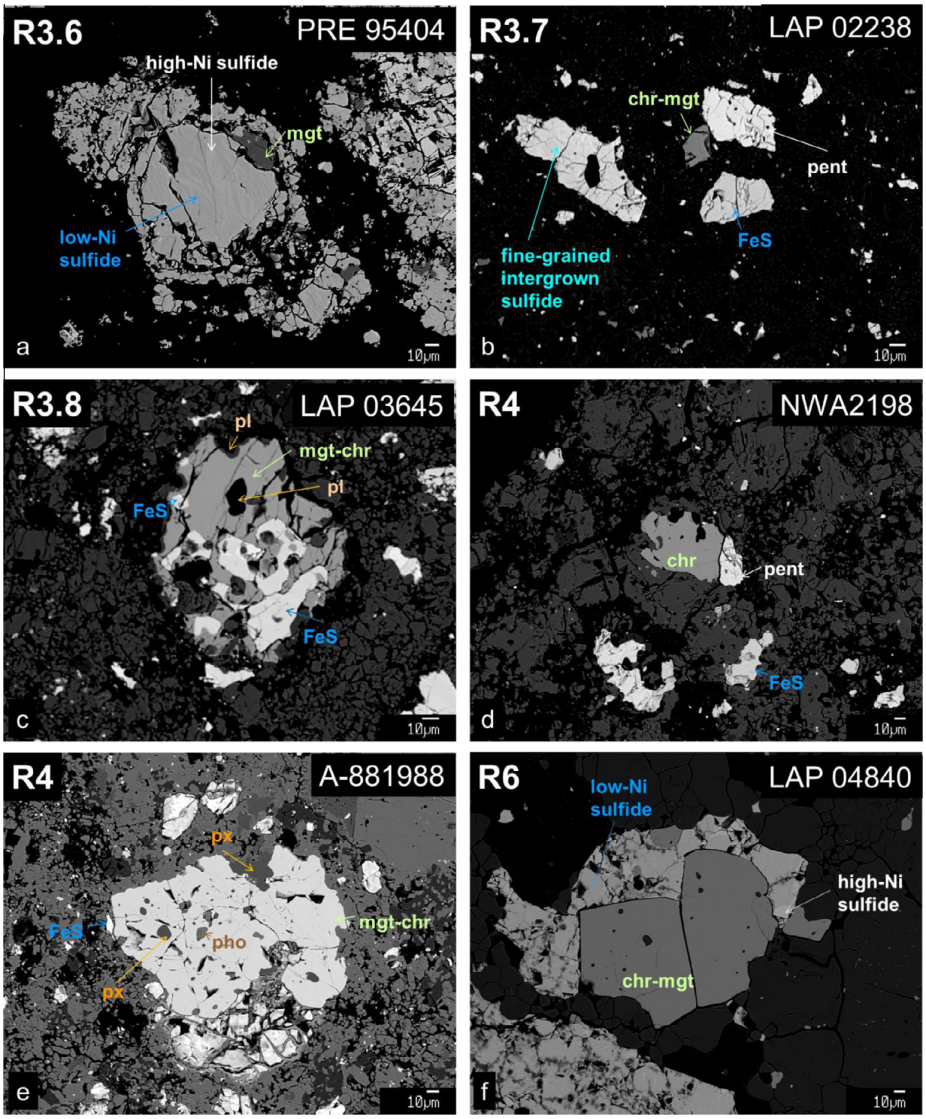

Fig. 4. BSE images of opaque mineral assemblages. (a) Magnetite (mgt) crystal within intergrown sulfides. The sulfide has a lamellar structure with low-Ni (dark gray) and high-Ni (light gray) phases. (b) Magnetite–chromite solid solution (mgt–chr) adjacent to troilite (FeS), pentlandite (pent) and Ni-bearing sulfide. (c) Magnetite–chromite solid solution (mgt–chr) adjacent to troilite (FeS). Plagioclase grains (pl) occur next to mgt–chr. (d) Chromite (chr) near troilite (FeS) and pentlandite (pent). (e) Large magnetite–chromite solid solution (mgt–chr) grain with phosphate and silicate inclusions. Sulfide grains (~10 μm in size) occur near the oxide. (f) Magnetite–chromite solid solution (mgt–chr) near sulfide, which is composed of both low-Ni (dark gray) and high-Ni (light gray) phases.

40 vol.% 2–6-μm oxide grains and 60 vol.% plagioclase or glass of plagioclase composition. MET 01149 (R3.8) contains several layered oxide-sulfide structures. The largest of these is 190 × 270 μm and consists of a large central oxide grain with 25 vol.% sulfide inclusions; this grain is surrounded by fine-grained sulfide-rich layers with small oxide inclusions.

The amphibole-bearing R6 chondrites LAP 04840 (and its paired samples LAP 10031 and LAP 10033) and MIL 11207 (Righter and Neff, 2007; McCanta et al., 2008; Ota et al., 2009), show no significant compositional differences in their sulfides or oxides relative to those in other equilibrated R chondrites.

3.1.4. Clasts in polymict breccias

The R-chondrite clast in Bencubbin is 1.0 × 1.5 cm in size. The boundary between the clast and the meteorite host is fairly sharp, but some mineral intergrowths occur at the interface. The clast contains 400–500-μm-size chondrules, ~40 μm-size feldspar grains, 50–200-μm-size olivine grains and 100–300-μm-size sulfide nodules (most of which contain oxide grains). Sulfide-rich shock-vein networks are

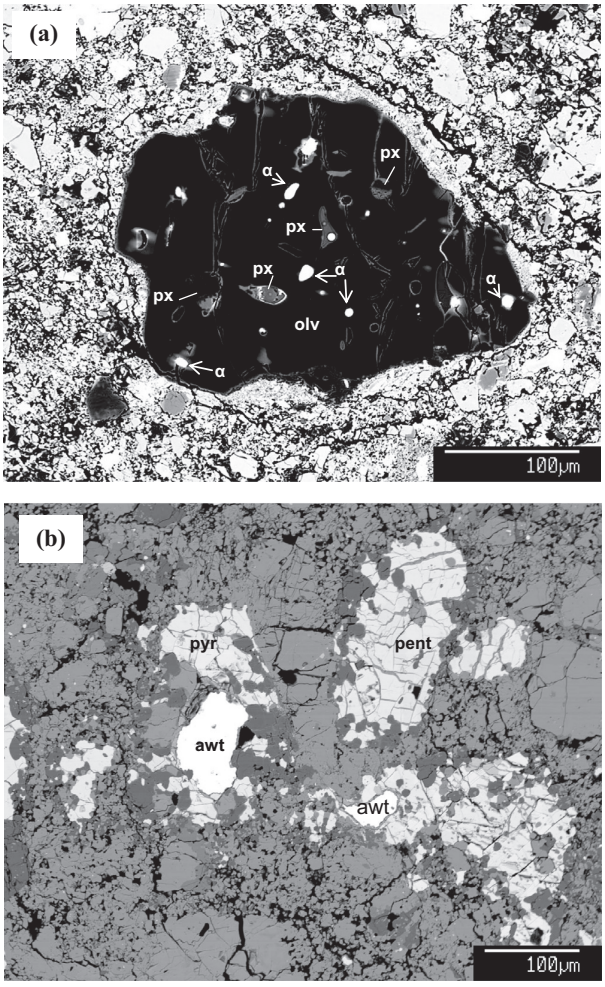

Fig. 5. (a) BSE image of a magnesian olivine grain (Fa 0.5 ± 0.1) in PRE 95404 showing its inclusions of kamacite (α) with 22–53 mg/g Ni and of Ca,Al-rich pyroxene (px). Light patches have olivine compositions up to 8 mol.% Fa. (b) BSE image of relatively large awaruite grains in PRE 95411 associated with pentlandite and pyrrhotite. Also present in the assemblage is plagioclase (dark gray). (awt) awaruite, (pent) pentlandite.

present. Metallic Fe-Ni occurs only as very rare sub-micrometer-size grains. Silicate compositions are typical for R chondrites: olivine Fa38–41 (Fig. 2) with a mode at Fa38; low-Ca pyroxene Fs29–32, Ca-pyroxene Fs19–31 and plagioclase Ab86Or3. Oxide occurs as isolated ~10–25-μm-size grains in the matrix and as ~10–120-μm-size grains within oxide-sulfide assemblages. Oxide compositions are in the range encompassed by the magnetite–chromite (mgt–chr) solid solution. Sub-micrometer-size chlorapatite grains attached to sulfide nodules are also present. Pentlandite and pyrrhotite both occur. The presence of well-defined chondrules and the slightly equilibrated olivine indicates that the clast is R4.

We also analyzed a chondrule-free R-chondrite clast in Murchison (Fig. 6). The boundary between the clast and the host meteorite is sharp. Olivine compositions are in the equilibrated R-chondrite range: Fa36–37 with a mode at Fa37 (Fig. 2). Oxide typically occurs as ~10–100-μm-size grains attached to sulfide. Oxides consist of Al-rich chromite. Sulfide phases include stoichiometric FeS (either troilite or pyrrhotite) and monosulfide solid solution (mss). Pentlandite is absent. There is a single 10-μm-size metallic Fe-Ni grain.

3.2. Bulk compositions

Our INAA data for 24 elements (as well as literature values) are listed in Table 6. The results (normalized to Cr and to the literature composition of H chondrites; Kallemeyn et al., 1989) are shown in Fig. 8. Elements are plotted in terms of increasing volatility to the right. A curve shows the mean composition of L chondrites (Kallemeyn et al., 1989). Because of major weathering effects we excluded from Fig. 8 and from the R-chondrite mean one Antarctic meteorite (MET 01149) and all hot-desert samples except RaS 201. The mean compositions of these samples are listed

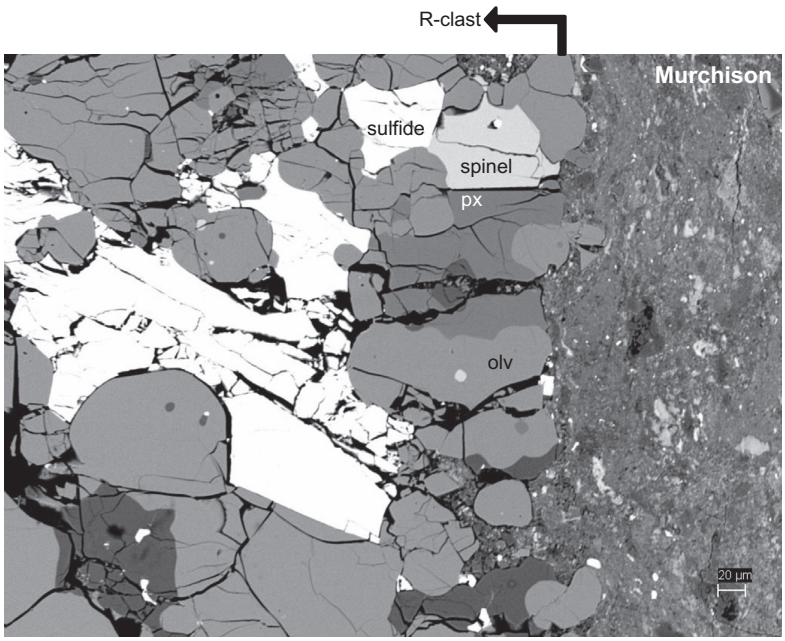

Fig. 6. BSE image of the R-chondrite clast in Murchison.

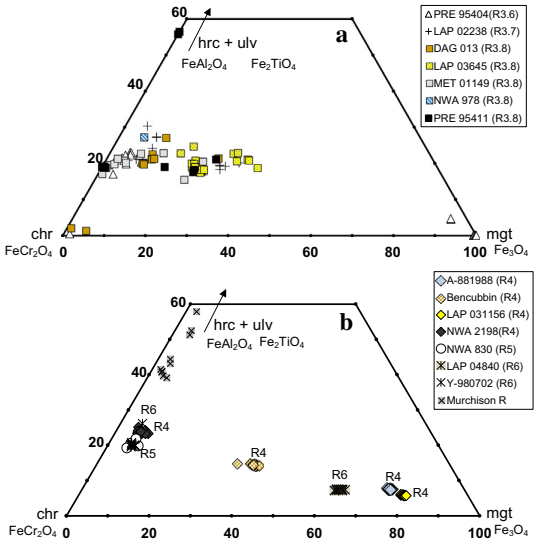

Fig. 7. Spinel compositions in (a) unequilibrated R chondrites and (b) equilibrated R chondrites. The oxides are described as combinations of four end members: ilmenite $(Fe^{2+},Mg)TiO_3$ (ilm), ulvöspinel $(Fe^{2+},Mg)_2TiO_4$ (ulv), chromite $(Fe^{2+},Mg)_2Cr_2O_4$ (chr), magnetite $(Fe^{2+},Mg)_2Fe_2O_4$ (mgt), and hercynite $(Fe^{2+},Mg)_2Al_2O_4$ (hrc). The unequilibrated samples have a fairly constant hercynite + ulvöspinel component. Some of the equilibrated samples contain spinel grains that are much richer in a magnetite component than most unequilibrated samples.

at the bottom of Table 6. In the central portion of Table 6 we list data for Rumuruti and two Antarctic samples (Y-793575 and PCA 91002) from Kallemeyn et al. (1996).

3.2.1. Weathering effects

Huber et al. (2006) noted that many weathered CK chondrites show fractionated abundance patterns, particularly in Ni, Co, Se and Au. The weathering effects were found to be more pronounced among hot-desert samples, but were also observed in a few Antarctic samples. They concluded that the weathering effects are largely attributable to leaching or dissolving of sulfides associated with terrestrial alteration.

The highly oxidized CK and R chondrites are especially sensitive to the weathering of Au and some other siderophiles. As a result of the oxidation of metal during asteroidal aqueous alteration, some siderophile elements are now in fine-grained secondary sulfides that are readily mobilized during weathering.

A challenge is to distinguish asteroidal aqueous alteration effects from those due to terrestrial weathering. The situation is complicated because elemental fractionations differ from element to element and from sample to sample. The main carrier phases of Ni, Co, Se and Au in R chondrites are probably the sulfides pentlandite, pyrite and monosulfide solid solution. Weathering effects for siderophile and chalcophile elements in R chondrites are similar, but not identical, to those in CK chondrites. In particular, Ni, Co and Se seem to be less sensitive to weathering in R chondrites. Abundances of Au are appreciably lower in weathered than unweathered samples (note the position of ALH 85151, PRE 95411, RaS 201 and Y-793575 in Fig. 8b), but a low Ni value is observed only in Y-793575. In contrast, there is almost no scatter in the Se data plotted in Fig. 8b. Nickel and Co are appreciably low only in Y-797575.

Table 6
Concentrations of 24 elements in R chondrites determined by instrumental neutron activation analysis. See text for discussion of weathering effects and analytical biases. Blue (italicized) data given ½ weight in the mean; red (crossed-out) data excluded from the mean. Previous data are from Kallemeyn et al. (1996).

		Na	K	Ca	Sc	Cr	Mn	Fe	Co	Ni	Zn	Ga	As
new data, in mean		mg/g	μg/g	mg/g	μg/g	mg/g	mg/g	mg/g	μg/g	mg/g	μg/g	μg/g	μg/g
Asuka 881988	R4	6.59	730	12.1	7.41	3.38	2.31	223	599	~~*11.4*~~	141	*6.80*	1.92
ALH 85151	R3.6	*6.22*	*641*	*12.9*	*7.30*	*3.53*	*2.38*	*238*	*749*	*15.4*	*147*	*8.20*	*2.21*
LAP 03639	R4	6.18	902	11.3	7.74	3.49	2.31	241	682	14.6	155	8.86	1.97
LAP 04840	R6	*6.77*	*697*	*10.9*	*7.45*	*3.41*	*2.25*	*234*	*648*	*12.8*	*162*	*7.91*	*1.82*
PRE 95411	R3.8	6.23	644	10.4	6.98	3.19	2.08	215	730	17.4	142	8.30	2.00
RaS 201	R5	6.25	696	13.0	8.05	3.66	2.30	243	793	13.8	153	8.39	~~*1.54*~~
previous data, in mean													
PCA 91002	R3.8	6.47	661	12.2	7.70	3.52	2.30	242	692	13.9	141	7.7	1.90
Rumuruti	R3.8	6.28	735	11.4	7.65	3.58	2.26	244	710	14.4	154	8.4	1.82
Yamato 793575	R3.8	6.69	914	11.1	7.6	3.53	2.27	243	~~*483*~~	~~*8.3*~~	138	7.8	1.85
Mean (see text)		6.40	744	11.7	7.56	3.48	2.27	236	701	14.7	147	8.22	1.98
new data, not in mean													
MET 01149	R3.8	6.22	737	10.1	7.70	3.46	2.34	245	659	15.2	147	<11	1.97
NWA 753	R3.9	5.94	1026	15.8	8.28	3.77	2.33	257	730	15.2	160	12.5	7.40
NWA 978	R3.8	4.16	1054	13.8	8.18	3.66	2.11	246	679	10.1	159	8.38	2.68
NWA 2198	R4	6.74	869	11.3	7.98	3.53	2.71	243	695	13.7	160	8.63	3.12

		Se	Br	Ru	Sb	La	Sm	Eu	Yb	Lu	Os	Ir	Au
		μg/g	μg/g	ng/g	ng/g	ng/g	ng/g	ng/g	ng/g	ng/g	ng/g	ng/g	ng/g
Asuka 881988	R4	13.6	0.50	760	85	284	183	76	196	29	520	518	163
ALH 85151	R3.6	*14.2*	*0.67*	*980*	*84*	*305*	*172*	*79*	*203*	*28*	*617*	*585*	~~*80*~~
LAP 03639	R4	13.6	1.00	890	88	276	177	80	218	28	669	550	146
LAP 04840	R6	*13.6*	*2.41*	*1013*	*75*	*323*	*182*	*71*	*226*	*34*	*563*	*528*	*183*
PRE 95411	R3.8	13.6	0.42	860	70	261	153	73	*169*	~~*23*~~	594	542	~~*74*~~
RaS 201	R5	13.6	0.58	*775*	~~*47*~~	299	190	74	233	33	612	565	~~*130*~~
previous data, in mean													
R3.8	R3.8	14.1	1.0	870	76	306	185	73	211	32	623	594	169
Rumuruti	R3.8	15.1	0.7	890	79	296	175	72	207	31	634	614	200
Yamato 793575	R3.8	14.6	0.70	914	67	324	181	72	197	32	658	637	~~*125*~~
Mean (see text)		14.0	0.81	866	78	295	178	75	208	31	613	572	171
new data, not in mean													
MET 01149	R3.8	13.6		1030	51	303	187	91	165	29	746	631	<270
NWA 753	R3.9	13.6		3111	101	420	231	119	302	60	596	641	107
NWA 978	R3.8	13.6		1692	81	477	156	87	325	39	691	618	139
NWA 2198	R4	13.6	0.40	1460	64	424	195	86	270	34	412	570	43

Sources of samples for the new INAA data: Antarctic samples are from NASA-Johnson Space Center (Houston) and the new INAA data: Antarctic Meteorite Working Group, except for Asuka 881988 (supplied by the National Institute of Polar Research, Japan)
RaS 201 is from the Naturhistorisches Museum, Bern. The NWA samples are from the UCLA Meteorite Collection.

As discussed in the next section, we suspect that the observed scatter in K and Br and their low mean concentrations result from terrestrial weathering.

3.2.2. Abundance patterns in R chondrites

The mean refractory lithophile pattern for R chondrites (Fig. 8a) is largely flat. With the exception of Lu in PRE 95411 and several K data, all values plot within 10% of the mean. ALH 85151 and LAP 04840 were given half weight to calculate the mean value. Our data on ALH 15151 were obtained by repeat analysis of the same sample studied by Kallemeyn et al. (1989). The data for LAP 04840 include an analysis that is less precise than our present standards. The curve for mean R chondrites is ~2% higher than those for L and H; this difference may not be outside experimental error considering that that the H and L data are from Kallemeyn et al. (1989), whose standards differed from those used in our study.

The remaining lithophiles are also about the same in R, L and H chondrites. There is some evidence that Mn is higher in R and L relative to H. The mean K is lower in R than in L and H, but there is large scatter among the data points and we speculate that K has been lost by leaching during terrestrial weathering (as is apparently the case for some OC finds; Kallemeyn et al., 1989). The mean Na is higher in R than in H and L; because we suspect that some low Na values reflect minor leaching loss, the R value should be treated as a lower limit. We will discuss these three volatiles further in connection with the volatiles plotted in Fig. 8b.

Siderophile and other (mainly chalcophile) elements are plotted in Fig. 8b; volatility increases to the right. For the elements As through Zn the mean H-normalized R-chondrite abundance (the solid curve) is used as the measure of volatility.

Mean R abundances of refractory siderophiles (Os, Ir), common siderophiles (Ni, Co, Fe) and Au are intermediate between those in L chondrites and H chondrites.

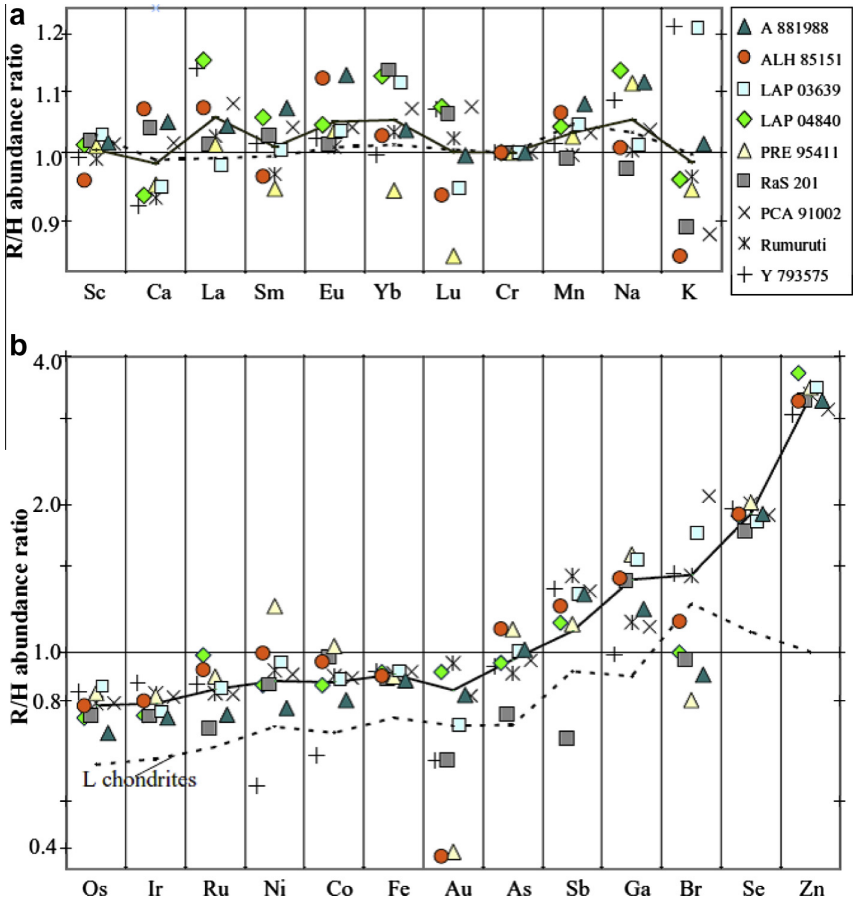

Fig. 8. Cr- and H-chondrite-normalized abundance ratios of R chondrites. Our new data on the mean compositions of six R chondrites are plotted as filled symbols and the three R chondrites from Kallemeyn et al. (1996) as stick symbols. Only those data that show little or minor weathering effects are included. These consist of new data for five cold-desert specimens and one hot desert sample from Oman. A dashed curve shows abundance ratios for L chondrites (Kallemeyn et al., 1989). Elements are ordered from left to right in increasing volatility; lithophiles are shown in the top portion, siderophiles and others in the bottom portion. With the exception of higher volatile abundances, abundance ratios are similar to those for H and L chondrites. Low values in Au, K, Br and, to a lesser degree, a few other elements are attributed to terrestrial weathering. See text for more details.

Abundances of Os and Ir are about 6% lower than those of the common siderophiles. The four lowest Au values appear to be low because of weathering effects; they were excluded from the mean. Unweathered samples have higher Au contents (e.g., 200 ng/g Au in Rumuruti; Kallemeyn et al., 1996).

The mean abundance ratios of six volatiles (As, Sb, Ga, Br. Se and Zn) increase from ~1.0 for As to ~3.3 for Zn. With the exception of a Ga/Sb reversal, abundance ratios of these five elements increase with decreasing condensation temperature (Wasson, 1985; Lodders and Fegley, 1998).

The Br values show appreciable scatter. We suspect that the four lowest values have been reduced by leaching during weathering. We do not report a Br value for MET 01149; one value was lower than any plotted value; the other was about 30× higher. Our H-normalization data were taken from Wasson and Kallemeyn (1988); because of the high scatter in the literature, they reported Br means to only one significant figure. For ordinary chondrites the values are: H chondrites, 0.5 μg/g; L chondrites, 0.8 μg/g; LL chondrites, 0.6 μg/g. We arbitrarily increased the H chondrite Br value to 0.6 μg/g to lower the spread between H chondrites and the other ordinary-chondrite groups; this is well within the uncertainty of the scattered literature data.

In our recent paper on CK chondrites (Wasson et al., 2013) we found that Br in CK chondrites is about 4× lower than that in CV chondrites, the unequilibrated members of the same group; we attributed this to volatile loss during impact heating. In our R-chondrite data we see no evidence of a relationship between Br content and petrologic type, but our sample set is missing types 3.5 and lower.

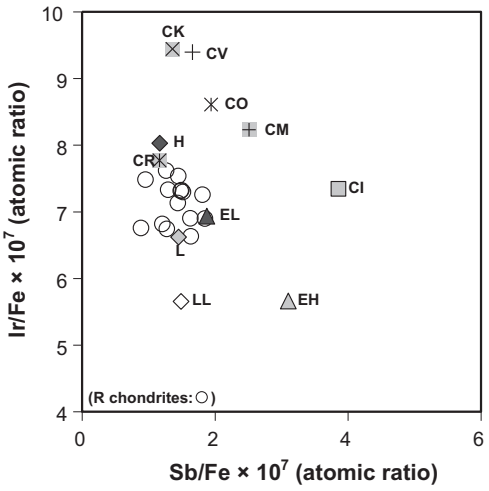

Fig. 9. Volatile and refractory siderophile H-chondrite-normalized abundance ratios in chondrite groups. Our new R-chondrite data and previous data (Kallemeyn et al., 1996) are plotted individually. Refractory and common siderophile abundance ratios are intermediate between those in H and L chondrites.

4. DISCUSSION

4.1. R-chondrite links to ordinary chondrites

Possible links between R chondrites and other chondrite groups have been discussed by previous workers (Clayton et al., 1991; Weisberg et al., 1991; Kallemeyn et al., 1996; Greenwood et al., 2000). The closest petrologic and compositional links are between R chondrites and OC. R chondrites and OC have similar bulk chemical compositions (e.g., Figs. 8 and 9). Our data combined with earlier data from our team (Kallemeyn et al., 1996) show that Cr-normalized refractory-lithophile abundances are similar in R chondrites and OC (Fig. 8a). The R-chondrite siderophile and chalcophile abundances are intermediate between those

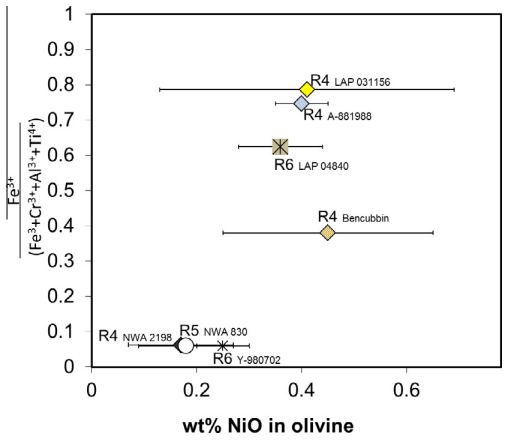

Fig. 10. Equilibrated R chondrites with large fractions of Fe^{3+} have higher NiO concentrations in olivine.

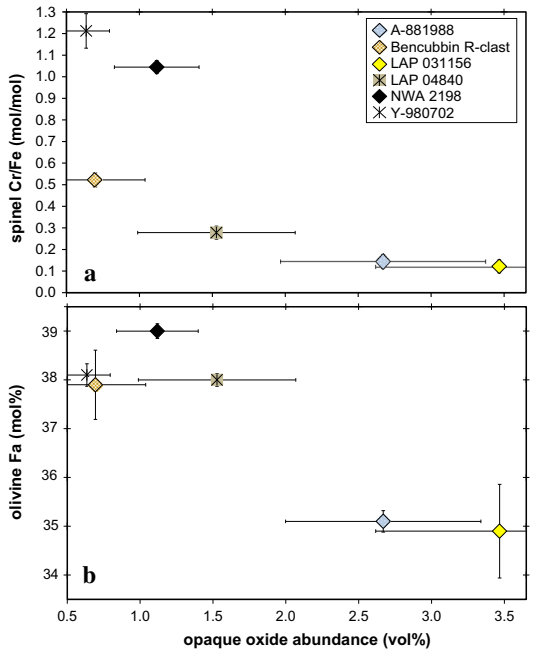

Fig. 11. (a) The Cr/Fe ratio in magnetite–chromite–hercynite–ulvöspinel solid solution and oxide modal abundance in equilibrated R-chondrites. The error bar is 1 sigma for the Cr/Fe ratio. A low Cr/Fe ratio indicates mgt-enriched oxide. Such samples tend to have olivine with lower Fa values (as shown in Fig. 11b). (b) The mean value of Fa in olivine grains and the oxide/silicate ratio in equilibrated R-chondrites. Error bars are 1 sigma. The Fa values decrease with increasing amounts of oxides. Conversion of Fe^{2+} to Fe^{3+} has lowered the activity of Fe^{2+}.

in H and L chondrites except for an enrichment in the R chondrites of the volatiles Sb, Ga, Se and Zn.

Greenwood et al. (2000) suggested that the compositional differences between OC and R chondrites are due to nebular mechanical fractionations associated with differences in the grain-size distributions of the nebular components (i.e., the large difference in their abundance of fines). Also, their O-isotope data confirmed the close relationship of OC and R based on the similarities of chondrule and magnetite compositions. We explore this idea below.

The proportion of RP + C chondrules in R3 chondrites ($2 \pm 2\%$ of chondrules) appears to be in the range of that in carbonaceous chondrites (0.3–3%) and is appreciably below that of noncarbonaceous (i.e., ordinary and enstatite) chondrites (7–18%) (Table 5 of Rubin, 2010 and references therein). Because these small chondrules are easily obscured by crushing and metamorphism, a comprehensive reexamination of these abundances is needed.

Because fines are enriched in volatile elements (e.g., Larimer and Anders, 1967; Wai and Wasson, 1977), it appears that the relatively high R-chondrite modal matrix abundance is responsible for the higher volatile abundances in bulk R chondrites. The estimated matrix content of R chondrites is ~3× that of H chondrites, (~35 vs. ~12 vol.%; Huss et al., 1981; Rubin, 2010); this is similar

to the difference in Zn concentrations, which are ~3× higher in R than in H chondrites (see calculation below). This is the result that would be predicted if the Zn concentration of the matrix were the same in R and H and if all the Zn was in the matrix, i.e., in the fine nebular fraction. At the other extreme, the As abundance in R and H chondrites is the same, the result expected if the As concentration was the same in matrix and non-matrix. The intermediate volatiles appear to be enriched in matrix in variable degrees compared to non-matrix.

The bulk R-chondrite Zn concentration is 147 μg/g (Table 6); if all the Zn is in the matrix and this is 35% of the mass of these chondrites, we obtain a Zn concentration in matrix of 420 μg/g. For comparison, the Zn concentration in the volatile-rich CI chondrites is 312 μg/g (Wasson and Kallemeyn, 1988). If one corrected for the Zn content of chondrule interiors (8.3 μg/g in Semarkona chondrules (Grossman and Wasson, 1987), the two numbers would become somewhat closer.

4.2. Minor chemical fractionations in bulk R chondrites

As discussed in Section 3.2 we calculated the mean composition from our analytical data for the least-weathered chondrites in our set of samples and those of Kallemeyn et al. (1996). This value is listed in Table 6.

R chondrites are compositionally relatively uniform (Fig. 8) despite their range in metamorphic effects. Rochette et al. (2008) suggested the reclassification of A-881988 as a member of a magnetite-bearing R-chondrite subgroup. Our data show that olivine compositions in this meteorite differ from those in other normal R chondrites: A-881988 has one of the lowest mean Fa values among R chondrites, suggesting a higher ferric/ferrous iron ratio.

Our Cr-normalized abundance ratios of refractory and common siderophiles in A-881988 are about 10% lower than those in other R chondrites. These low values cannot be attributed to an anomalously high Cr content because Cr-normalized refractory lithophile abundances are marginally high on average. Rochette et al. (2008) suggested that A-881988 belongs to a magnetite-bearing chondrite class different from R chondrites. Despite the high Au value, we suspect that the relatively low siderophile-element abundances are due to terrestrial weathering and sampling errors.

Because R-chondrite bulk compositions show only minor fractionations, we infer that the aqueous alteration they record occurred late in their history, without affecting their bulk compositions.

4.3. Aqueous alteration, oxidation, thermal metamorphism and the formation of spinel-group minerals

The diverse petrologic characteristics of R chondrites reflect two kinds of alteration: aqueous and thermal. The mineralogical record of low-temperature effects may have been erased in equilibrated R chondrites because of recrystallization. To help assess aqueous and thermal alteration, we studied oxide chemical compositions in both unequilibrated and equilibrated R chondrites.

4.3.1. Nearly pure magnetite in unequilibrated R chondrites with lower degrees of alteration

Until this study, nearly pure magnetite in R chondrites had been previously reported only within a 2-mm-size unequilibrated clast in PCA 91241 (paired with PCA 91002) (Rubin and Kallemeyn, 1994; Greenwood et al., 2000). In fact, grains of nearly pure magnetite are common and grains of Cr-bearing magnetite grains are of minor abundance only in the least-altered R chondrites, e.g., PRE 95404 (R3.6). This suggests that, during metamorphism, spinel compositions gradually evolved to include higher Cr and Al contents.

R3 chondrites still retain relatively primitive materials. Rubin and Kallemeyn (1989) reported martensite with 99 mg/g Ni and rare high-Co kamacite with 370 mg/g Co in R3.6 ALH 85151. We found a low-FeO olivine crystal that contains kamacite grains in PRE 95404. Nickel-rich metal grains occur in the same thin section as well as in PRE 95411 (R3.8) and NWA 978 (R3.8) (two other R chondrites that experienced relatively little metamorphism).

We observed both types of magnetite in PRE 95404. Because metal in unequilibrated R chondrites has low Cr contents, below the detection limit of EPMA (Table 4), it is apparent that the Cr in the magnetite is from a source other than metal (e.g., primary chromite, olivine, pyroxene, matrix fines or chondrule mesostases).

Both nearly pure magnetite and small amounts of chromite-bearing magnetite in PRE 95404 are distinguishable from the magnetite-chromite solid solution observed in equilibrated R chondrites; the PRE 95404 phases have higher Fe (Fig. 7a). The O-isotopic composition of the magnetite in PCA 91002 has slightly higher $\Delta^{17}O$ values than the R-chondrite whole rock (Greenwood et al., 2000). Because of the similarity in $\Delta^{17}O$ values between magnetite in PCA 91002 and in LL3.0 Semarkona (Choi et al., 1998), Greenwood et al. (2000) suggested that, in both cases, the magnetite formed from metallic Fe that was altered by similar ^{17}O-rich aqueous fluids. Magnetite in PRE 95404 probably formed in the same manner, possibly at an earlier stage of alteration compared to the other oxide minerals (after the fluid had exchanged O with the silicates).

4.3.2. Chromite composition in unequilibrated R chondrites

Some R3 chondrites also contain nearly pure chromite as well as chromite grains with relatively high Al and Ti (Fig. 7a). Nearly pure chromite grains occur in type-3 OC, but in equilibrated OC, chromite grains contain variable amounts of minor elements (Bunch et al., 1967). By analogy to the chromite in OC, it seems likely that the nearly pure chromite grains in R3.6 chondrites have been little affected by thermal metamorphism.

4.3.3. Chromite compositions in equilibrated R chondrites

Chemical compositions of oxides have large meteorite-to-meteorite variations in equilibrated R chondrites although oxide phases within individual meteorites are chemically rather uniform (Fig. 7b). The Cr_2O_3 contents of the phases we describe as magnetite-rich chromite to chromite-rich magnetite range from 101 mg/g in R4 LAP 031156 to 475 mg/g in R6 Y-980702.

The R clast in Murchison (CM2) contains Al-rich chromite that does not follow the trend of increasing Fe and decreasing Ti and Al exhibited by the oxides in other R chondrites (Fig. 6b). Because CM chondrites are among the most aqueously altered meteorite groups (e.g., McSween, 1979; Bunch and Chang, 1980; Zolensky et al., 1997; Rubin et al., 2007), it seems unlikely but possible that the composition of oxides in the Murchison clast were not established on the R-chondrite parent body (see more details in Section 4.5). We therefore exclude the R clast in Murchison from the discussion about other equilibrated R chondrites.

4.3.4. Degree of oxidation in the R-chondrite parent body

The magnetite–chromite chemical trend reflecting changes in oxidation state is distinct from compositional variations among spinel-group minerals in other chondrite groups. The Fe/Cr ratios in equilibrated ordinary-chondrite chromite vary systematically with chondrite group, H to L to LL (Bunch et al., 1967), mainly reflecting differences in the degree of oxidation. Differences in chromite compositions among R chondrites most likely result from differences in the degree of oxidation or in equilibration temperature. We considered that sulfide abundance might play a role but rejected this possibility because the less-weathered R-chondrites all show similar abundances of sulfides (~7–8 vol.%; Table 1) indicating that original concentrations of S in R-chondrites were probably rather uniform.

The magnetite components in the mgt–chr solid solution correlate with the NiO content of olivine in the same rock (Fig. 10) as well as with the abundance of oxide (Fig. 11). Because the composition of the mgt–chr solid solution and the NiO concentration in olivine are independent of petrologic type (Fig. 10), it is apparent that oxidation on the R-chondrite parent body is not a simple function of thermal metamorphism; instead it probably resulted from a variety of alteration conditions such as various water vapor pressures present at different locations and/or at different times.

4.3.5. Olivine compositions in highly oxidized equilibrated R chondrites

The high Fa contents in R-chondrite olivine reflect the high degree of oxidation of these rocks (i.e., the FeO/(FeO + MgO ratios). When metallic Fe-Ni slowly oxidizes, Fe (which is less noble than Ni) diffuses out of the metal, making the residual metal Ni rich. If permitted by transport kinetics, this extra FeO is largely partitioned into olivine and pyroxene, respectively raising their Fa and Fs. This raises the divalent-cation/Si ratio, facilitating the formation of $(Mg,Fe)_2SiO_4$ olivine (2:1 ratio) at the expense of $(Mg,Fe)SiO_3$ low-Ca pyroxene (1:1 ratio). If the degree of oxidation reaches a high-enough value, some Fe reaches the +3 oxidation state and magnetite forms, in many cases nucleating at the surfaces of residual metal grains. The conversion of Fe^{2+} to Fe^{3+} reduces the Fe^{2+} activity and thus may reduce the mean Fa content of the olivine.

As Righter and Neff (2007) described, the lower olivine Fa content (Fa33) and much higher modal abundance of magnetite in CK chondrites relative to typical R chondrites are consistent with the higher degree of oxidation and thus with the higher magnetite abundance in CK chondrites. An analogous process may have occurred in R4 A-881988 and R4 LAP 031156. These metal-free rocks have the least-ferroan olivine (Fa35), the second-highest olivine NiO contents (~4.0 mg/g), and the highest modal abundances of oxide among R chondrites (Figs. 10 and 11). This underscores the variability in oxidation processes on the R-chondrite parent body.

4.4. Implications for R-chondrite parent-body processes

We suggest the following scenario: (1) during R-chondrite low-temperature aqueous alteration and oxidation, the modal abundances of metal decreased, the residual metal grew richer in Ni (some transformed into awaruite), and pure (or nearly pure) magnetite formed. (2) With increasing alteration/thermal metamorphism, the magnetite acquired Cr (from olivine, pyroxene, matrix fines and chondrule mesostases), forming Cr-bearing magnetite. (3) With further alteration/thermal metamorphism, low-Al, low-Ti chromite–magnetite solid solutions formed. At each stage, the compositions of other minerals were also changing.

The degree of aqueous alteration/oxidation is not simply correlated with petrologic type. At one extreme in the oxidation sequence, Y-980702 (R6) is relatively reduced; it contains low-NiO olivine, no magnetite and a low modal abundance of oxides. At the other extreme are A-881988 (R4) and LAP 033156 (R4), highly oxidized R chondrites containing high-NiO olivine, chromite-rich magnetite and high modal abundances of oxides. In contrast, Y-980702 (R6), LAP 04840 (R6) and MIL 11207 (R6) are very oxidized; the occurrence of hornblende and coarse grains of mica in these samples implies that at least one region of the R-chondrite parent body experienced a higher pH_2O for a period long enough to grow these hydrous minerals or their precursors (e.g., McCanta et al., 2008; Ota et al., 2009; Gross et al., 2013). It is apparent that aqueous alteration processes were highly variable on the R-chondrite parent body. We note that Fe metal buffers the degree of oxidation but when the metallic Fe is completely oxidized, oxidation levels can greatly increase.

4.5. Aqueous alteration of an R-chondrite clast on the CM parent body

The R-chondrite clast in Murchison (henceforth Murchison R) seems to have been little affected by alteration on the CM parent body. However, Fig. 7 shows that the chromite chemical composition of Murchison R is greatly enriched in Al and scattered (170–300 mg/g Al_2O_3) relative to those of other equilibrated R chondrites (15–57 mg/g Al_2O_3). Three types of spinel-group oxides occur in normal Murchison including Al-rich chromite (32–220 mg/g Al_2O_3) (Fuchs et al., 1973). Because Al is one of the elements mobilized during aqueous alteration, the large spinel component in CM chondrites is likely a product of parent-body alteration. Murchison (CM2.4; Rubin et al., 2007) is more heavily aqueously altered than any R chondrite. The Al-rich phases (e.g., Ca-Al rich inclusions), in Murchison are mostly chemically altered and converted to secondary minerals (e.g., MacPherson et al., 1983). Although aqueous

alteration in the CM parent body may have added Al to the chromite in Murchison R, this seems unlikely because the chromite is coarse and we see no other evidence of aqueous alteration in the clast.

Silicate compositions of the R clast in Murchison (olivine Fa36–37, diopside Fs19–20Wo48–49, plagioclase Ab95) are not distinguishable from those in other R chondrites. Coarse olivine in Murchison was little affected by parent-body aqueous alteration (Rubin et al., 2007) and the Murchison whole rock was not subject to thermal metamorphism. Therefore, olivine and spinel compositions in Murchison R were probably produced on the R-chondrite parent body and were essentially unaffected by subsequent CM parent-body processes.

4.6. Incorporation of R-chondrite clasts into polymict breccias

Most R chondrites are breccias. Impact-related shock effects caused olivine grains to develop undulose extinction and planar fractures and, in some cases, mosaic extinction. Sulfide-rich shock veins and plagioclase-rich melt pockets occur in the R4 clast in Bencubbin as well as in individual R chondrites such as PCA 91002 and Rumuruti (although shock effects in the Bencubbin clast could have been caused during or after incorporation into the Bencubbin parent body). The martensite-troilite mixture in ALH 85151 (Rubin and Kallemeyn, 1989) formed by impact melting and rapid cooling of an unoxidized kamacite–taenite–troilite assemblage similar to those in OC. In PCA 91002, a small grain of metallic Cu enclosed in a pyrrhotite–pentlandite assemblage may also be a product of impact heating (Rubin and Kallemeyn, 1994).

R-chondrite clasts have been reported in other chondrites besides Murchison and Bencubbin including the Kaidun polymict breccia (Zolensky and Ivanov, 2003), the EET 83309 and EET 87720 polymict ureilites (Downes et al., 2008), the Almahata Sitta ureilite (Bischoff et al., 2010; Horstmann and Bischoff, 2010), and the GRO 95551 ungrouped metal-rich chondrite (Weisberg et al., 2012).

The single "R3" fragment in Kaidun contains olivine with low FeO (Fa33), below the normal range of R chondrites; it also contains abundant diopside and lacks fine-grained matrix (Zolensky and Ivanov, 2003), unlike normal R chondrites (Kallemeyn et al., 1996). Consistent with Zolensky's and Ivanov's characterization of the classification of this unusual clast as "tentative," it is unlikely that the clast is a real R chondrite.

Because some of these R-chondrite clasts are of high petrologic type and some appear relatively unshocked, it seems likely that they were thermally metamorphosed before they accreted to their final hosts.

5. CONCLUSIONS

We used INAA to study the bulk chemical compositions of 10 R chondrites and the optical microscope and the electron microprobe to evaluate the petrologic characteristics of 14 R chondrites as well as R-chondrite clasts in Bencubbin and Murchison. Some R-chondrite bulk elemental abundances have relatively high uncertainties because of terrestrial weathering effects. We minimized these by excluding from the means samples that showed large depletions in Au, the key weathering tracer. Mean refractory and lithophile abundance ratios in R chondrites are similar to (or a few percent higher than) those in H and L chondrites. Refractory and common siderophile abundances are intermediate between those in H and L chondrites. It is thus clear that R chondrites are compositionally closely related to these two groups of ordinary chondrites.

Relative to H chondrites R-chondrite volatile abundances increase with decreasing 50%-condensation temperatures. Almost all the Zn in R chondrites is present in the matrix, but moderate fractions of R-chondrite Ga, Se and other volatiles are present in non-matrix components as well (i.e., chondrules, chondrule fragments and coarse sulfide grains). The individual R chondrites have similar bulk compositions despite differences in their petrologic type, extent of brecciation and degree of oxidation/aqueous alteration.

R-chondrite whole rocks were aqueously altered producing nearly pure magnetite by oxidation of metallic Fe-Ni; during subsequent thermal metamorphism, some magnetite acquired Cr from other phases and produced Cr-bearing magnetite. Further alteration/metamorphism caused low-Al, low-Ti chromite–magnetite solid solution to nucleate and grow. These low-temperature processes appear to be similar to those that occurred in OC.

In equilibrated R chondrites, a moderately large range of oxidation states is observed. This reflects the fact that all the Fe metal, a key buffer phase, has been oxidized in some R chondrites. In addition, there may have been differences in the availability of water as well as local differences in temperature and pressure.

The R-chondrite clast in Murchison was little affected by alteration on the CM parent body. Prior to incorporation into the CM asteroid, the clast was thermally metamorphosed on the R-chondrite parent body.

ACKNOWLEDGMENTS

The authors thank Frank Kyte for assistance with EPMA. We also thank Jason Utas and Mike Zolensky for providing samples of R-chondrite clasts. This work was supported mainly by NASA Cosmochemistry grants NNG06GG35G (J.T. Wasson) and NNG06GF95G (A.E. Rubin).

REFERENCES

Bischoff A. (2000) Mineralogical characterization of primitive, type-3 lithologies in Rumuruti chondrites. *Meteorit. Planet. Sci.* **35**, 699–706.

Bischoff A., Geiger T., Palme H., Spettel B., Schultz L., Scherer P., Loeken T., Bland P., Clayton R. N., Mayeda T. K., Herpers U., Meltzow B., Michel R. and Dittrich-Hannen B. (1994) Acfer 217 – a new member of the Rumuruti chondrite group (R). *Meteoritics* **29**, 264–274.

Bischoff A., Horstmann M., Laubenstein M. and Haberer S. (2010) Asteroid 2008 TC3-Almahata Sitta: not only a ureilitic meteorite, but a breccia containing many different achondritic and

chondritic lithologies (abstract). *Lunar. Planet. Sci.* **41**, 1763.pdf.
Bischoff A., Vogel N. and Roszjar J. (2011) The Rumuruti chondrite group. *Chem. Erde* **71**(2), 101–133.
Bunch T. and Chang S. (1980) Carbonaceous chondrites – II: carbonaceous chondrite phyllosilicates and light element geochemistry as indicators of parent body processes and surface conditions. *Geochim. Cosmochim. Acta* **44**, 1543–1577.
Bunch T. E., Keil K. and Snetsinger K. G. (1967) Chromite composition in relation to chemistry and texture of ordinary chondrites. *Geochim. Cosmochim. Acta* **31**, 1569–1582.
Choi B.-G., McKeegan K. D., Krot A. N. and Wasson J. T. (1998) Extreme oxygen-isotope compositions in magnetite from unequilibrated ordinary chondrites. *Nature* **392**, 577–579.
Clayton R. N., Mayeda T. K., Goswami J. N. and Olsen E. J. (1991) Oxygen isotope studies of ordinary chondrites. *Geochim. Cosmochim. Acta* **55**, 2317–2337.
Downes H., Mittlefehldt D. W., Kita N. T. and Valley J. W. (2008) Evidence from polymict ureilite meteorites for a disrupted and re-accreted single ureilite parent asteroid gardened by several distinct impactors. *Geochim. Cosmochim. Acta* **72**, 4825–4844.
Fuchs L. H., Olsen E. and Jensen K. J. (1973) Mineralogy, mineral-chemistry, and composition of the Murchison (C2) meteorite. *Smithson. Contrib. Earth Sci.* **10**, 1–39.
Greenwood J., Rubin A. E., Kallemeyn G. W. and Wasson J. T. (2000) Oxygen-isotopes in R-chondrite magnetite and olivine: links between R chondrites and ordinary chondrites. *Geochim. Cosmochim. Acta* **64**, 3897–3911.
Gross J., Treiman A. H. and Connolly H. C. (2013) A new subgroup of amphibole-bearing R-chondrites: evidence from the new R-chondrite MIL 11207 (abstract). *Lunar Planet. Sci.* **44**, 2212.pdf.
Grossman J. N. and Wasson J. T. (1987) Compositional evidence regarding the origins of rims on Semarkona Chondrules. *Geochim. Cosmochim. Acta* **51**, 3003–3011.
Grossman J. N., Alexander C. M. O'D., Wang J. and Brearley A. J. (2000) Bleached chondrules: evidence for widespread aqueous processes on the parent asteroids of ordinary chondrites. *Meteorit. Planet. Sci.* **35**, 467–486.
Horstmann M. and Bischoff A. (2010) Characterization of spectacular lithologies from the Almahata Sitta breccia (abstract). *Lunar. Planet. Sci.* **41**, 1784.pdf.
Huber H., Rubin A. E., Kallemeyn G. W. and Wasson J. T. (2006) Siderophile-element anomalies in CK carbonaceous chondrites: implications for parent-body aqueous alteration and terrestrial weathering of sulfides. *Geochim. Cosmochim. Acta* **70**, 4019–4037.
Huss G. R., Keil K. and Taylor G. J. (1981) The matrices of unequilibrated ordinary chondrites: implications for the origin and history of chondrites. *Geochim. Cosmochim. Acta* **45**, 33–51.
Jäckel A., Bischoff A., Clayton R. N. and Mayeda T. K. (1996) Dar al Gani 013 – a new Saharan Rumuruti-chondrite (R3–6) with highly unequilibrated (type 3) fragments (abstract). *Lunar. Planet. Sci.* **27**(595–596), 1298.pdf.
Kallemeyn G. W. and Wasson J. T. (1985) The compositional classification of chondrites: IV. Ungrouped chondritic meteorites and clasts. *Geochim. Cosmochim. Acta* **49**, 261–270.
Kallemeyn G. W., Rubin A. E., Wang D. and Wasson J. T. (1989) Ordinary chondrites: bulk compositions, classification, lithophile-element fractionations, and composition-petrographic type relationships. *Geochim. Cosmochim. Acta* **53**, 2747–2767.
Kallemeyn G. W., Rubin A. E. and Wasson J. T. (1996) The compositional classification of chondrites: VII. The R chondrite group. *Geochim. Cosmochim. Acta* **60**, 2243–2256.
Larimer J. W. and Anders E. (1967) Chemical fractionations in meteorites – II. Abundance patterns and their interpretation. *Geochim. Cosmochim. Acta* **31**, 1239–1270.
Lodders K. and Fegley B. (1998) *The Planetary Scientist's Companion*. Oxford University Press, New York, 371pp..
MacPherson G. J., Bar-Matthews M., Tanaka T., Olsen E. and Grossman L. (1983) Refractory inclusions in the Murchison meteorite. *Geochim. Cosmochim. Acta* **47**, 823–839.
McCanta M. C., Treiman A. H., Dyar M. D., Alexander C. M. O'D., Rumble D. and Essene E. J. (2008) The LaPaz Icefield 04840 meteorite: mineralogy, metamorphism, and origin of an amphibole- and biotite-bearing R chondrite. *Geochim. Cosmochim. Acta* **72**, 5757–5780.
McSween H. Y. (1977a) Petrographic variations among carbonaceous chondrites of the Vigarano type. *Geochim. Cosmochim. Acta* **41**, 1777–1790.
McSween H. Y. (1977b) Carbonaceous chondrites of the Ornans type: a metamorphic sequence. *Geochim. Cosmochim. Acta* **41**, 447–491.
McSween H. Y. (1979) Alteration in CM carbonaceous chondrites inferred from modal and chemical variations in matrix. *Geochim. Cosmochim. Acta* **43**, 1761–1770.
Ota K., Mikouchi T. and Sugiyama K. (2009) Crystallography of hornblende amphibole in LAP04840 R chondrite and implications for its metamorphic history. *J. Mineral. Petrolog. Sci.* **104**, 215–225.
Righter K. and Neff K. E. (2007) Temperature and oxygen fugacity constraints on CK and R chondrites and implications for water and oxidation in the early solar system. *Polar Sci.* **1**, 25–44.
Rochette P., Gattacceca J., Bonal L., Bourot-Denise M., Chevrier V., Clerc J. P., Consolmagno G., Folco L., Gounelle M., Kohou T., Pesonen L., Quirico E., Sagnotti L. and Skripnik A. (2008) Magnetic classification of stony meteorites: 2. Non-ordinary chondrites. *Meteorit. Planet. Sci.* **43**, 959–980.
Rubin A. E. (2003) Chromite-plagioclase assemblages as a new shock indicator; implications for the shock and thermal histories of ordinary chondrites. *Geochim. Cosmochim. Acta* **67**, 2695–2709.
Rubin A. E. (2010) Physical properties of chondrules in different chondrite groups: implications for multiple melting events in dusty environments. *Geochim. Cosmochim. Acta* **74**, 4807–4828.
Rubin A. E. and Huber H. (2005) A weathering index for CK and R chondrites. *Meteorit. Planet. Sci.* **40**, 1123–1130.
Rubin A. E. and Kallemeyn G. W. (1989) Carlisle Lakes and Allan Hills 85151: members of a new chondrite grouplet. *Geochim. Cosmochim. Acta* **53**, 3035–3044.
Rubin A. E. and Kallemeyn G. W. (1994) Pecora Escarpment 91002: a member of the new Rumuruti (R) chondrite group. *Meteoritics* **29**, 255–264.
Rubin A. E., Trigo-Rodriguez J. M., Huber H. and Wasson J. T. (2007) Progressive aqueous alteration of CM carbonaceous chondrites. *Geochim. Cosmochim. Acta* **71**, 2361–2382.
Schulze H., Bischoff A., Palme H., Spettel B., Dreibus G. and Otto J. (1994) Mineralogy and chemistry of Rumuruti: the first meteorite fall of the new R chondrite group. *Meteoritics* **29**, 275–286.
Wai C. M. and Wasson J. T. (1977) Nebular condensation of moderately volatile elements and their abundances in ordinary chondrites. *Earth Planet. Sci. Lett.* **36**, 1–13.
Wasson J. T. (1985) *Meteorites: Their Record of Early Solar-System History*. Freeman, New York, 267pp..
Wasson J. T. (2008) Evaporation of nebular fines during chondrule formation. *Icarus* **195**, 895–907.
Wasson J. T. and Kallemeyn G. W. (1988) Compositions of chondrites. *Philos. Trans. R. Soc. London* **A325**, 535–544.

Wasson J. T., Isa J. and Rubin A. E. (2013) Compositional and petrographic similarities of CV and CK chondrites: a single group with variations in textures and volatile concentrations attributable to impact heating, crushing and oxidation. *Geochim. Cosmochim. Acta* **108**, 45–62.

Weisberg M. K., Prinz M., Kojima H., Yanai K., Clayton R. N. and Mayeda T. K. (1991) The Carlisle Lakes-type chondrites: a new grouplet with high $D^{17}O$ and evidence for nebular oxidation. *Geochim. Cosmochim. Acta* **55**, 2657–2669.

Weisberg M. K., Prinz M., Clayton R. N. and Mayeda T. K. (1993) The CR (Renazzo-type) carbonaceous chondrite group and its implications. *Geochim. Cosmochim. Acta* **57**, 1567–1586.

Weisberg M. K., Ebel D. S., Nakashima D. and Kita N. T. (2012) Petrology and oxygen isotopes of chondrules in NWA 5492 and GRO 95551: a new type of metal-rich chondrite. *Lunar Planet. Sci. Conf.* 1463.

Zolensky M. E. and Ivanov A. V. (2003) The Kaidun microbreccia meteorite: a harvest from the inner and outer asteroid belt. *Chem. Erde* **63**, 185–246.

Zolensky M. E., Mittlefehldt D. W., Lipschutz M. E., Wang M.-S., Clayton R. N., Mayeda T. K., Grady M. M., Pillinger C. T. and Barber D. (1997) CM chondrites exhibit the complete petrologic range from type 2 to 1. *Geochim. Cosmochim. Acta* **61**, 5099–5115.

Associate editor: Alexander N. Krot

Chapter 5: Oxygen Isotope Studies of PRE 95404,15 R3 Chondrite Components: Implications for Formation Processes of the R Chondrite Parent Body

Abstract

To help understand R-chondrite formation we obtained oxygen isotope and composition data for mafic minerals in R3.6 PRE 95404. We compare our results with data collected from SIMS analysis on olivine phenocrysts in chondrules from several other chondrite groups, including especially LL3.0 Semarkona. The O-isotopic compositions found for the interiors of some olivine phenocrysts have high $\Delta^{17}O$ values that are similar to that of R-chondrite whole rocks (+3 ‰) suggesting that the precursors of chondrules with these O-isotopic compositions already existed when R chondrules formed. We also find that the chondrule populations have a wide diversity in oxygen isotope compositions that can be quantified by a standard measure of population entropy. Many chondrules are unequilibrated but some are equilibrated. Our data show that $\Delta^{17}O$ values in PRE 95404 are similar to those in Semarkona, but that those in the R chondrite record more extreme values (both high and low). Olivine compositions range from values typical of LL chondrite chondrules to Fa40 values typical of equilibrated LL chondrites; there is no correlation between the Fa value of olivine and the $\Delta^{17}O$ value. Petrographic observations of PRE 95404,15 indicate that type R3 chondrites consist of a mixture of chondritic components metamorphosed to different degrees and embedded in fine grained matrix that appears be rather pristine. The existence of equilibrated and intact chondrules and unequilibrated chondrules within a few mm of each other suggests that the final consolidation of PRE 95404 occurred later than the metamorphism of at least some parts of R chondrite parent body(ies) and perhaps after the metamorphism of some ordinary chondrites parent bodies.

5.1 Introduction

Type 3 chondrites are often interpreted as "pristine" rocks. However, non-fragmented type 3 rocks are rare in the Rumuruti (R) chondrite group. Thus, the textures of type R3 prior to fragmentation are not well understood. For this reason, the chemical compositions and O-isotope compositions of R chondrite chondrules are of great interest. This is because the mean bulk R-chondrite $\Delta^{17}O$ value of ~3‰ ($\Delta^{17}O = 2.72 \pm 0.31$‰, n = 24 including finds; Bischoff et al., 2011 and reference therein; the Rumuruti fall, $\Delta^{17}O = 2.88$‰; Schulze et al., 1994) is the highest among asteroidal and planetary objects. Moreover, most R whole rocks have similar $\Delta^{17}O$ values (Bischoff et al., 1994; Greenwood et al., 2000; Kallemeyn et al., 1996; Pack et al., 2004; Rubin and Kallemeyn, 1989; Schulze et al., 1994). Measurements of O-isotope compositions in chondrules from carbonaceous chondrite groups show that $\Delta^{17}O$ values increase with degree of oxidation. Therefore, one might expect that highly oxidized chondrite groups such as the R chondrites would have chondrules with high $\Delta^{17}O$ values.

The O-isotopic compositions of some R chondrules scatter around a mass-fractionation line with $\Delta^{17}O$ = ~2.7‰; however, chondrules from Carlisle Lakes and PCA 91241 plot close to the ordinary chondrite (OC) region with $\Delta^{17}O = 0.68$‰ (Schulze et al., 1994) and -0.4 to 0.7‰ (Greenwood et al., 2000). Most individual olivine and pyroxene grains in R chondrites either plot near an R-chondrite mass-fractionation-line (RFL), defining the intercept ($\Delta^{17}O$ = ~3%) or in the region of unequilibrated ordinary chondrites (UOC) (Greenwood et al., 2000). A few refractory forsterite grains in DAG 013 have low $\Delta^{17}O$ values of ~-3‰ (Pack et al., 2004). Most individual minerals in R-chondrite CAIs plot along a line with slope equal to one. The spinel and hibonite

grains have low $\Delta^{17}O$ values of −20.5‰ to −24.7‰, whereas the fassaite grains and the diopside rims vary in $\Delta^{17}O$: −13.8‰ to +5.1‰ (Rout et al., 2009).

In this chapter, we present the results of SIMS analysis of the least metamorphosed R chondrite, PRE 95404 as found in a prior survey (Isa et al., 2014) of several R chondrite meteorite samples. We utilize thin section #15 from PRE 95404 (that is PRE 95404,15) to determine its chondrule O-isotope compositions. We also present the results of O-isotopic compositions for other chondrite group chondrules in order to clarify the relationship between R chondrites and other chondrite groups.

Previous hypotheses of R-chondrule whole-rock formation held that their precursors had OC-chondrule O-isotopic compositions that later acquired higher $\Delta^{17}O$ values by reaction with nebular gas (Rubin and Kallemeyn, 1989; Weisberg et al., 1991) or by reaction with water derived from parent body fluids associated with the matrix (Greenwood et al., 2000). Unfortunately, bulk R-chondrule O-isotope data are not ideal for testing these hypotheses because many chondrule mesostases were altered by $\Delta^{17}O$-rich parent-body fluids. Therefore, it is necessary to use *in situ* analytical tools to identify the original O-isotopic compositions of R-chondrule precursors.

Furthermore, we investigated accretionary conditions and metamorphism affecting the R chondrite parent body as recorded within the textures, chemical compositions, and O-isotope compositions of this least metamorphosed R3 chondrite, PRE 95404.

5.2 Sample Selection

Mount Prestrud (henceforth PRE) 95404 is an R3 chondrite. The total weight of PRE 95404 is 39.5 g; other companion samples include: PRE95412 (14.6 g), PRE95411 (43.0 g), and PRE5410 (41.7 g). R chondrites are, in general, heavily brecciated; many chondrules have been fragmented. PRE95404 is also a regolith breccia (Ludolf Schultz et al., 2005); nevertheless, our thin section (PRE 95404,15) is dominated by a "pristine" clast that retains some largely intact chondrules. In a previous study (Isa et al., 2014), we studied 13 R chondrites (R3.6 to R6) and two R-clasts found within samples from different meteorite groups. Amongst these samples, PRE 95404,15 was found to have the most primitive features. We utilized this thin section for O-isotope studies.

PRE 95404 was previously classified as a petrologic type 3.6. A paired meteorite, PRE95411, was classified as type 3.8. Our previous research did not distinguish the type 3 clasts. The differences of petrologic types between the paired meteorites R3.6 and R3.8 shows that the fraction of unequilibrated materials varies in thin sections (1-3 cm). It should be noted that this absolute petrologic type in R chondrites is not directly comparable with the petrologic types in OCs. For example, the grain size distribution in R chondrites is different from that in OCs due to fragmentation and recrystallization of the matrix components in higher R petrologic types and the mineralogy is also different (e.g. amphibole and hornblende are present in two R chondrites). In PRE95404,15, olivine compositions range from Fa0 to Fa60 with a mode of Fa40, it is more metamorphosed than type 3.0 ordinary chondrites such as Semarkona. However, *in situ* metamorphism effects on O-isotope compositions are minimal in this thin section. This is further discussed below.

Although PRE 95404 is classified as type 3.6 in our previous study, the thin section, 15, contains three different type-3 clasts. Therefore, the petrologic type 3.6 is the upper limit of the petrologic type of this section. A large part of the thin section, consists of less fragmented R3, although some parts are fragmented type 3 lithology (see Figure A1-1 in the Appendix-1). The thin section contains approximately 60% chondrules and silicate fragments with approximately 40% of fine-grained matrix including opaque minerals. This clast is likely a portion of the type 3.2 clast described in Miller et al., (2017, accepted). In our study, many of the R chondrite components are selected from a less fragmented area. Although the texture of this sample is uncharacteristically "pristine" as an R chondrite, it appears to be an R chondrite. The bulk chemical composition of PRE 95411, which is paired with PRE 95404 (Schultz et al., 2005), is consistent with that of an R chondrite (Isa et al., 2014). The chondrite components of the less fragmented area of PRE 95404,15 are also consistent with those of other R chondrites (chondrule sizes, rare in CAIs, abundant sulfides, and a negligible amount of metal grains).

For analysis, we selected chondrules and olivine fragments that included less-altered chondrule olivine and pyroxene phenocrysts, Mg-rich olivine fragments, nearly equilibrated chondrule olivine phenocrysts, and oxide phases within sulfide nodules.

5.3 Procedures

5.3.1 Mineral Chemistry and Petrology

Backscattered electron (BSE) images were taken before and after oxygen-isotope analyses. Cathodoluminescence (CL) images were also taken. Individual chondrules and olivine/pyroxene fragments were examined using a LEO 1430 scanning electron microscope (SEM) equipped with

monochrome CL, a VEGA Tescan SEM equipped with color CL and energy-dispersive X-ray spectroscopy (EDX), and the JEOL 8200 electron microprobe at UCLA. Quantitative mineral compositions were determined with the electron probe micro analyzer (EPMA) with 20 s counting times for peaks and 5 s counting times for backgrounds, ZAF corrections, and a sample current of ~15 nA at 15 kV. Three standard deviations of background counts were used to determine the detection limits for minor elements. The detection limit was determined using a forsterite standard. We inspected all pits created by SIMS analyses with the SEM and the chemical compositions within the SIMS-analyzed area were measured with the EPMA.

5.3.2 SIMS Analyses

Secondary ion mass spectrometry (SIMS) analyses were performed on the UCLA 1270 ion microprobe using a primary Cs^+ beam and analyzing negative secondary ions. The measurements were carried out during three different analytical sessions: in the years 2010, 2012 and 2015. Samples were sputtered with Cs^+ primary beam intensities of about 0.3 nA, 5-8 nA, and 7 nA, respectively (by year), with impact energies of 20 keV focused on spots with a diameter in the range of 20-40 μm. A normal incident electron gun was used to compensate for possible sample charging. Oxygen isotopes ^{16}O, ^{17}O, and ^{18}O were measured simultaneously by a multi-collector system. A Faraday cup (detection for ^{16}O) and two electron multipliers (EM) (for detection of ^{17}O and ^{18}O) were used in the 2010 analysis while three Faraday cups were used in the 2012 and 2015 analysis. In the 2010 studies, dead time corrections of 21 ns were applied for counting the $^{17}O^-$ secondary ions at the axial EM detectors (after a 90° deflection through the projection system). Fixed 65 ns dead time corrections were applied for counting $^{18}O^-$ at an EM detector on the multi-collection system. The dead time for the axial EM was determined by a fit curve

between $^{17}O/^{16}O$ isotope ratios and different secondary ion count rates with different primary beam currents. The supplying voltage to the amplifier of the axial EM detectors was adjusted to keep the peak of the pulse height distribution constant through the analyses. A mass resolving power greater than 5000 was used to resolve the interference of a ^{16}OH at mass 17. A nuclear magnetic resonance (NMR) sensor regulated the magnetic field throughout the analyses.

We utilized Springwater pallasite olivine (2010) and San Carlos olivine (2012, 2015) as standards and SIMS matrix effects were corrected. The SIMS matrix effects are discussed in more detail in the Appendix. The counting time and waiting time were 10 s and 0.5 s, respectively, for 30 cycles measurements in 2010 and 2012. The counting time and waiting time was 10 s and 1 s, respectively, for 20 cycles measurements in 2015. The internal precision of an individual measurement for $\delta^{18}O$ and $\delta^{17}O$ in 2010 was about 1.0‰ and 2.3‰, and the reproducibility on $\delta^{18}O$ and $\delta^{17}O$ was around 0.6‰ and 1.2‰ (at one standard deviation, 1SD), respectively. The internal precision of an individual measurement for $\delta^{18}O$ and $\delta^{17}O$ in 2012 was about 0.6‰ and 0.4‰, and the reproducibility on $\delta^{18}O$ and $\delta^{17}O$ was around 0.3‰ and 0.4‰ at 1SD, respectively. The internal precision of an individual measurement for $\delta^{18}O$ and $\delta^{17}O$ in 2015 was about 0.2‰ and 0.3‰ and the reproducibility on $\delta^{18}O$ and $\delta^{17}O$ was around 0.3‰ and 0.2‰ at 1SD, respectively. The external reproducibility of $\Delta^{17}O$ values ($\Delta^{17}O = \delta^{17}O - 0.52 \times \delta^{18}O$) in standards are 1.1‰, 0.5‰, and 0.3‰ in 2010, 2012 and 2015, respectively.

5.3.3 Histograms and Entropy

We constructed histograms to depict the frequency distributions of mass-independent oxygen isotope variations in $\Delta^{17}O$ values across chondrules in PRE 95404 (this study) and literature data

(Kita et al., 2010; Libourel and Chaussidon, 2011; Tenner et al., 2013). We chose a bin width of 0.25‰.

In addition to histograms, we also quantitatively expressed the diversity of chondrule populations by using Shannon-Wiener entropy (Shannon, 1948) that is used for expressing diversity in populations of interest in ecology, economics, and information theory. The Shannon-Weiner entropy is given by $H' = \sum p_i \cdot \log p_i$ where H' is entropy and p_i is the probability of a bin *i*. In our study, we calculated entropy based on the distributions of averaged $\Delta^{17}O$ values in olivine or pyroxene phenocrysts in individual chondrules and isolated silicate fragments that were determined by SIMS. The data gathered for this analysis include data from this study and data from prior studies of type 3 chondrules that appear in the published literature. The p is a relative frequency of $\Delta^{17}O$ values in a bin *i*. The width of bins used in entropy calculations was 2‰, which is approximately 2 standard deviations of the largest external reproducibility of our measurements.

5.4 Results

We analyzed chondrite components including 12 chondrules and chondrule fragments, 8 olivine and pyroxene fragments, and five silicate fragments in 2 sulfide nodules in the thin section PRE 95404,15. We first describe 1) structural and petrological observation of the primary and secondary features of the chondrite components and survey the compositions and textures of chondrules, 2) O-isotope compositions of individual components. We summarize the BSE images (Figure 5-1 to 5-4) and data of the chemical compositions (Table A2) of the chondrite components observed in this study, and 3) diversity of chondrule populations constructed as

histogram and entropy. O-isotopic compositions are shown in Figure 5-5 to 5-9 and those data are listed in Table 1. The olivine compositions are shown as Fa values (Fa = molar Fe /molar (Fe+Mg) × 100).

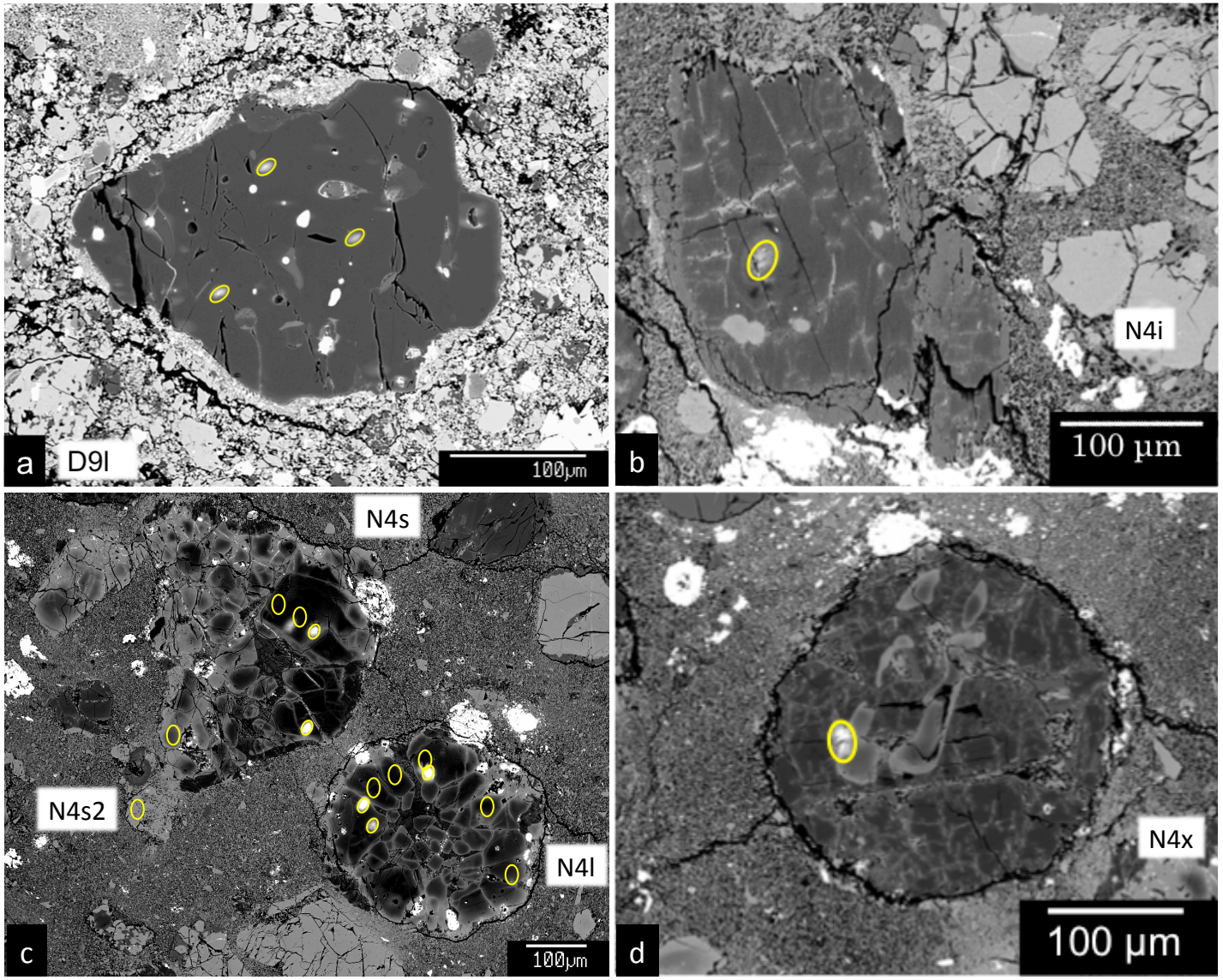

Figure 5-1. a-d

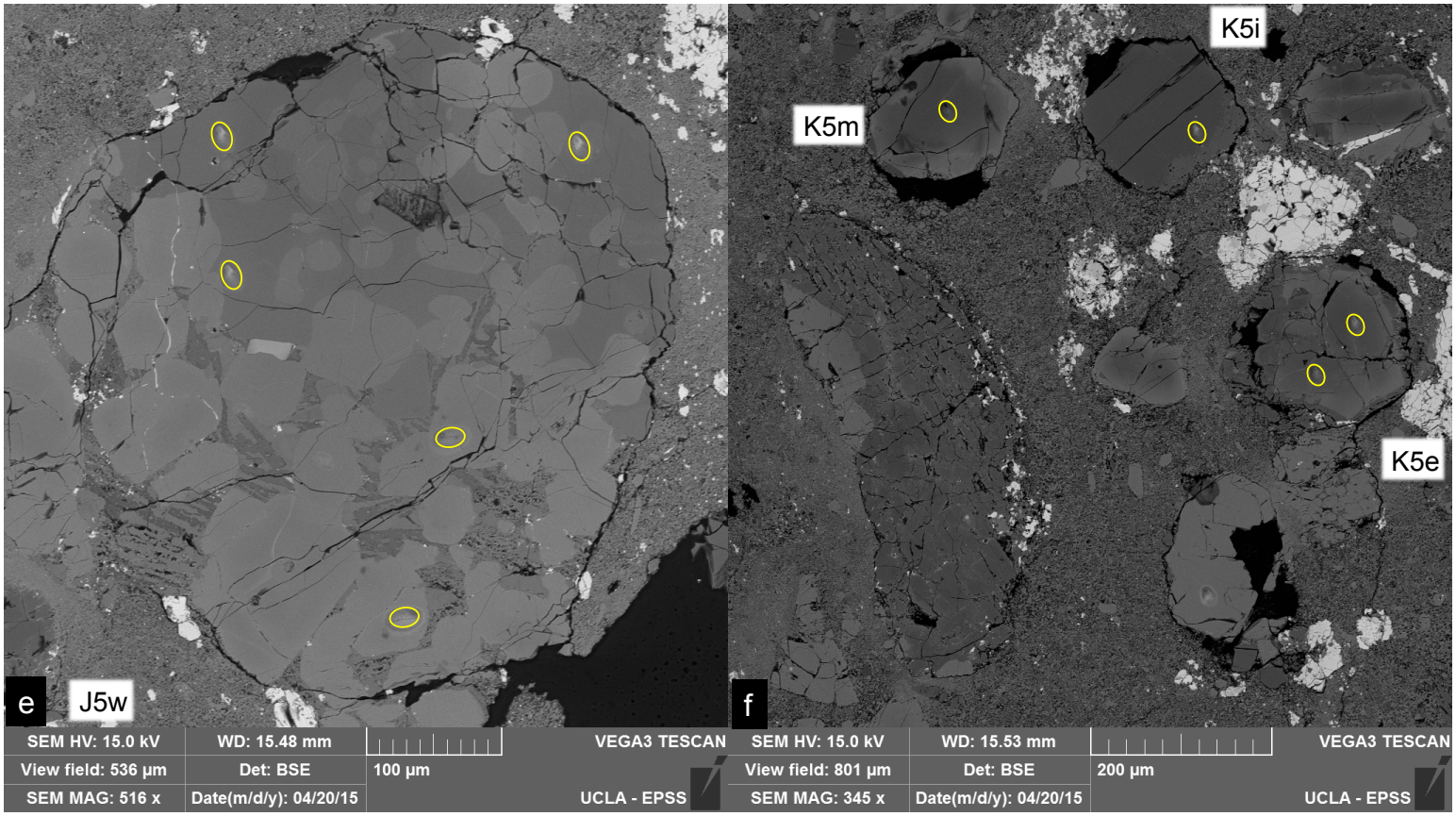
e
J5w
SEM HV: 15.0 kV
WD: 15.48 mm
VEGA3 TESCAN
View field: 536 µm
Det: BSE
100 µm
SEM MAG: 516 x
Date(m/d/y): 04/20/15
UCLA - EPSS
f
K5i
K5m
K5e
SEM HV: 15.0 kV
WD: 15.53 mm
VEGA3 TESCAN
View field: 801 µm
Det: BSE
200 µm
SEM MAG: 345 x
Date(m/d/y): 04/20/15
UCLA - EPSS

Figure 5-1. e-f

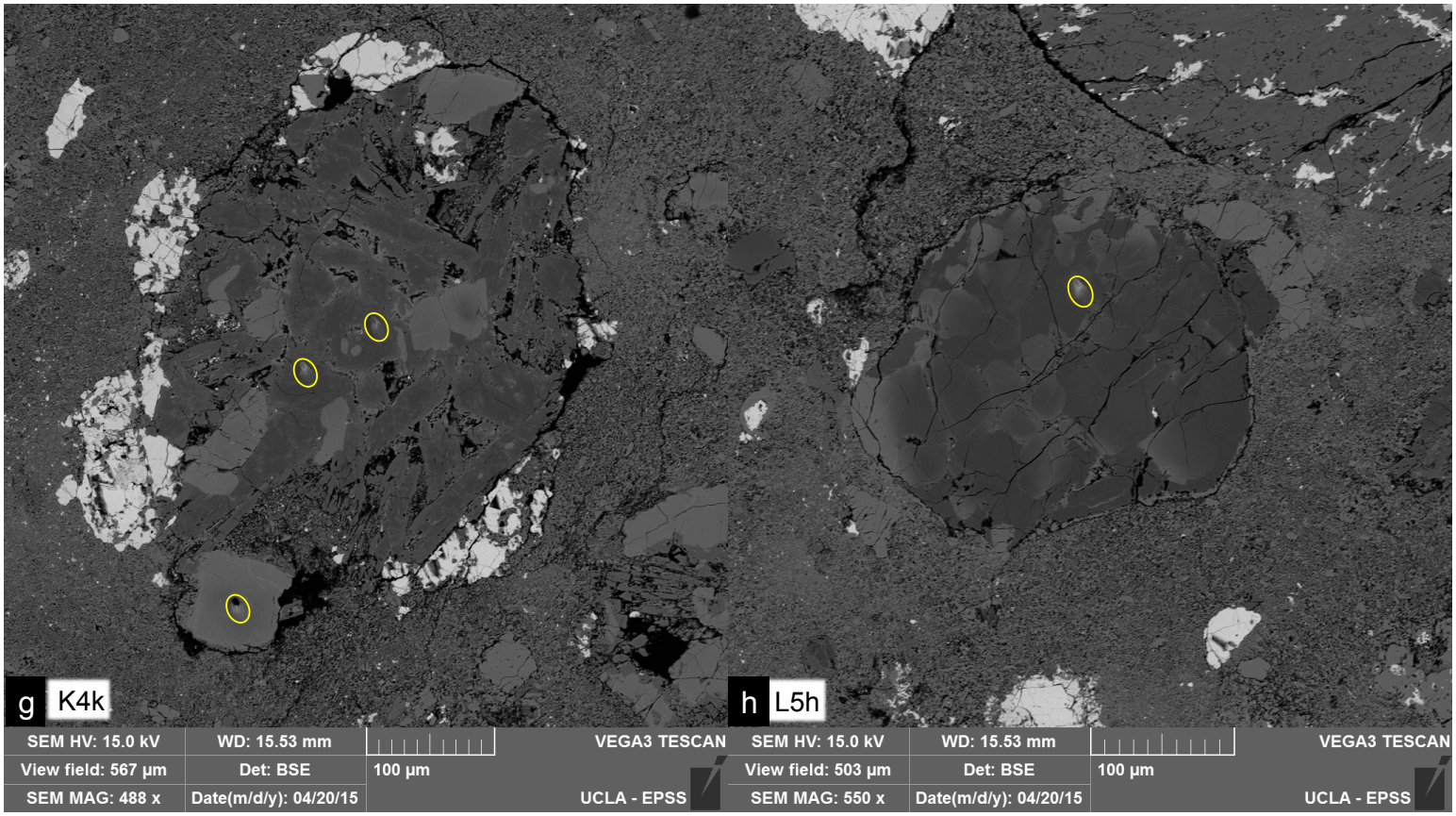
g K4k
SEM HV: 15.0 kV
WD: 15.53 mm
VEGA3 TESCAN
View field: 567 µm
Det: BSE
100 µm
SEM MAG: 488 x
Date(m/d/y): 04/20/15
UCLA - EPSS
h L5h
SEM HV: 15.0 kV
WD: 15.53 mm
VEGA3 TESCAN
View field: 503 µm
Det: BSE
100 µm
SEM MAG: 550 x
Date(m/d/y): 04/20/15
UCLA - EPSS

Figure 5-1. g-h

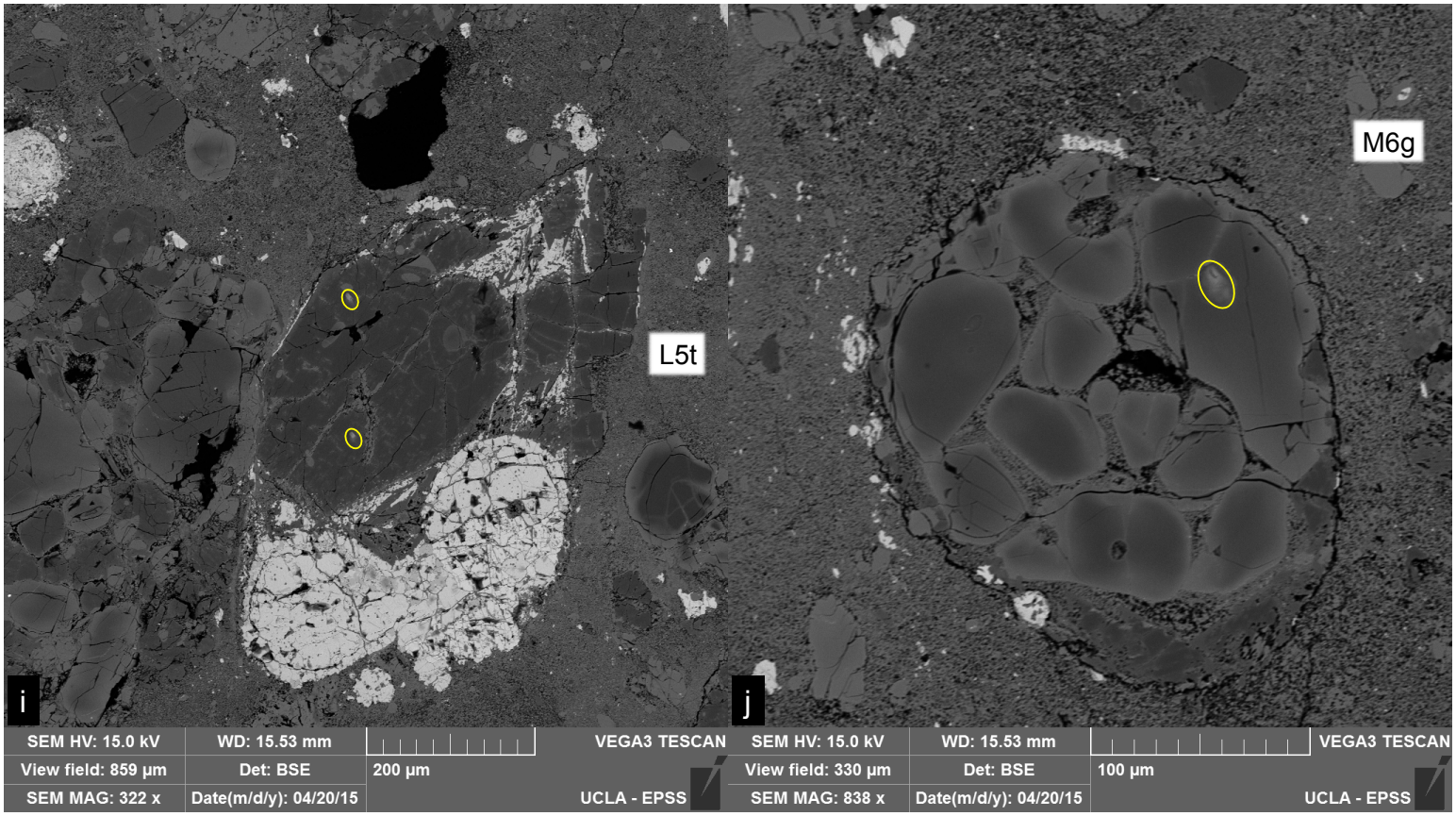
L5t
M6g
i
j
SEM HV: 15.0 kV
WD: 15.53 mm
VEGA3 TESCAN
View field: 859 µm
Det: BSE
200 µm
SEM MAG: 322 x
Date(m/d/y): 04/20/15
UCLA - EPSS
SEM HV: 15.0 kV
WD: 15.53 mm
VEGA3 TESCAN
View field: 330 µm
Det: BSE
100 µm
SEM MAG: 838 x
Date(m/d/y): 04/20/15
UCLA - EPSS

Figure 5-1. i-j

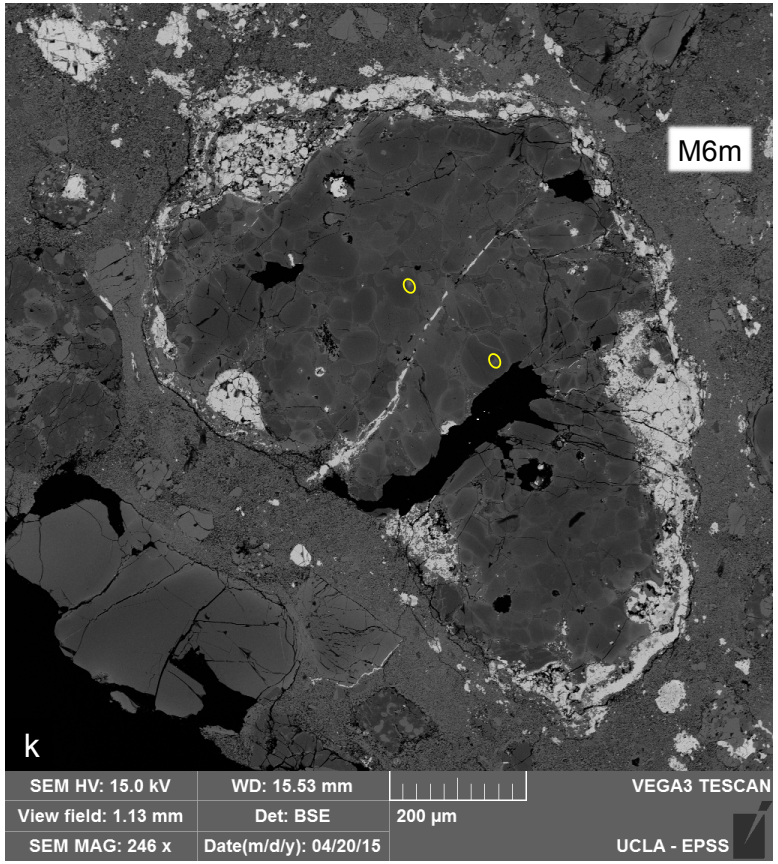

Figure 5-1. k

Figure 5-1. BSE images of FeO-poor olivine and pyroxene fragments or chondrules that were measured with the SIMS to determine O-isotope compositions. Yellow ovals indicate the location of SIMS measurements. (a) D9l, kamacite-bearing olivine fragments (see Isa et al., 2014). (b) N4i, pyroxene fragment. (c) N4s, porphyritic olivine (PO) chondrule; N4s2, a metamorphosed amoeboid olivine inclusion (AOI) (see three O-isotope diagram in Figure 11); and N4l, PO chondrule. The white round nodules are sulfide grains. (d) N4x, porphyritic pyroxene-olivine (PPO) chondrule. (e) J5w, porphyritic olivine- pyroxene (POP) chondrule. (f) K5e, a chondrule or olivine fragments; K5i, olivine fragments; K5m, olivine fragments. (g) K4k, POP chondrule. (h) L5h, PPO chondrule. (i) L5t, PO chondrule with sulfide nodules (appears light gray in the image). (j) M6g, PO chondrule. (k) M6m, PO chondrule with sulfide nodules (appears light gray in the image.

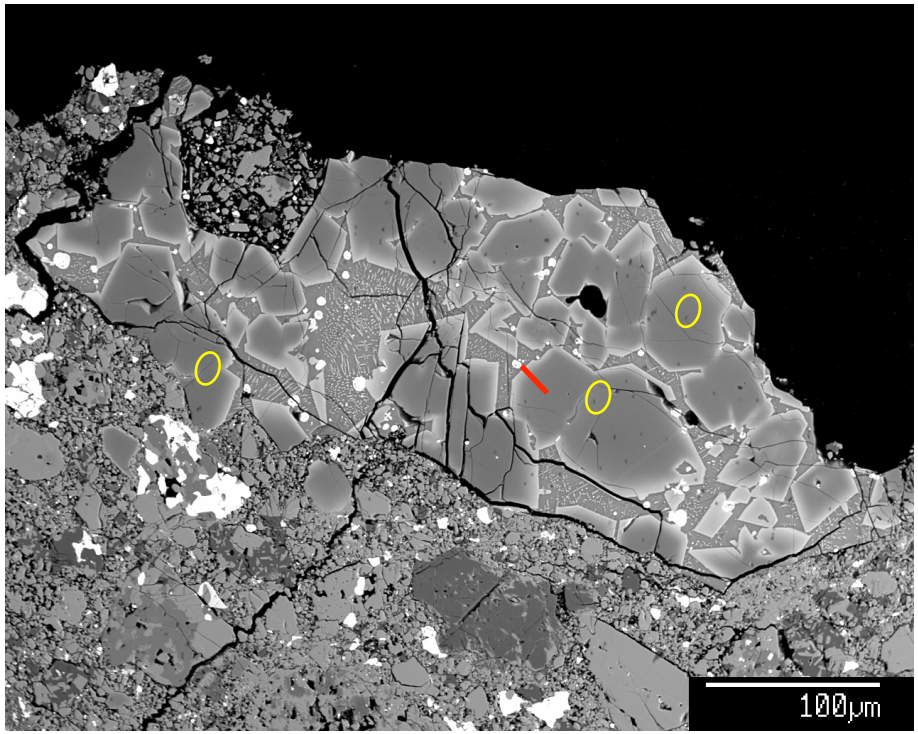

Figure 5-2. BSE images of FeO-rich PO chondrule, D10t, that was measured to determine O-isotope compositions. Yellow ovals indicate the location of SIMS measurements. Olivine phenocrysts are zoned (Fa16-60). Mesostases include sulfide blobs and acicular pyroxene and Cr-bearing oxide. The edge of an olivine phenocryst includes an inclusion in negative olivine shape.

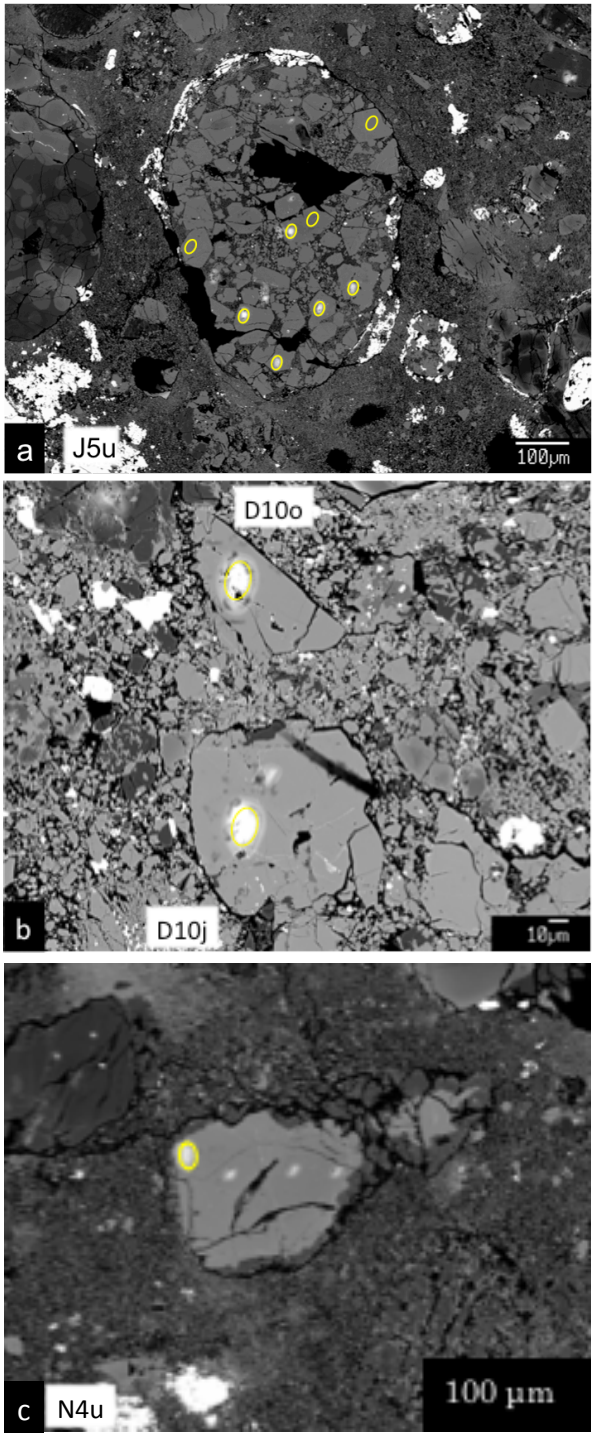

Figure 5-3. (a) BSE images of equilibrated chondrule and (b and c) olivine fragments. Yellow ovals indicate the location of O-isotope SIMS measurements in this study.

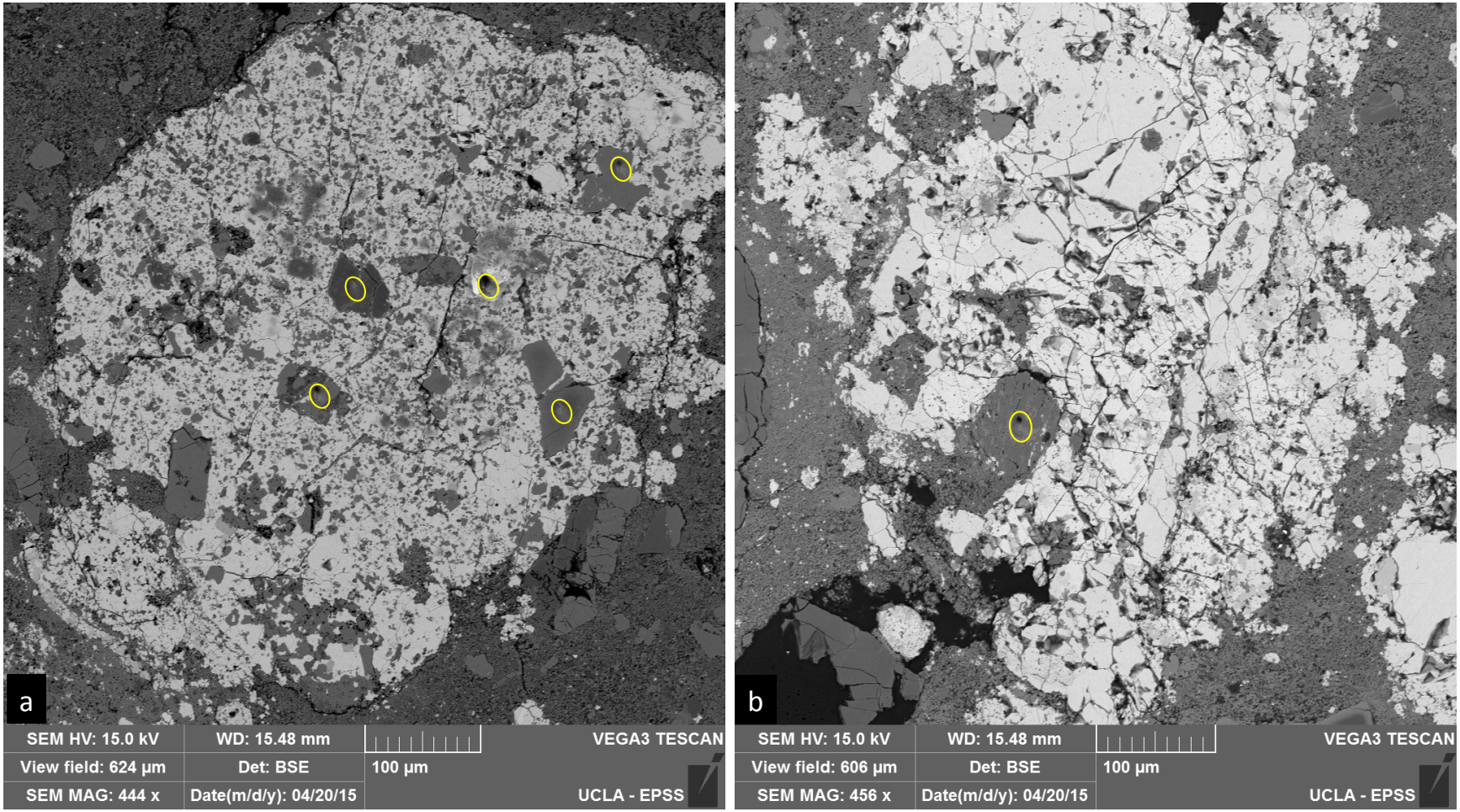

Figure 5-4. BSE images of sulfide nodules. Yellow ovals indicate the location of O-isotope SIMS measurements. (a) K5l, sulfide nodule-1 and (b) J5i, sulfide-2. The main component of these nodules is sulfide minerals. Light gray areas are sulfide minerals. Darker grays are oxides, which include opaque oxide, Cr-spinel, phosphate, silicate and alteration product of sulfide.

Table 1: O-isotope compositions measured by SIMS. And Fa or Fs values measured by EPMA.

		$\delta^{18}O$	error_$\delta^{18}O$	$\delta^{17}O$	error_$\delta^{17}O$	$\Delta^{17}O$		Fa or Fs
chondrules and olivine fragments								
D9l_1	**isolated fragment**	-2.9	0.3	-5.4	0.6	-3.8	olv	0.5
D9l_2		-2.6	0.3	-5.6	0.6	-4.3	olv	0.5
D9l_3		-2.4	0.3	-4.9	0.6	-3.6	olv	0.3
D10j	**isolated fragment**	5.8	0.4	4.1	0.6	1.1	olv	38
D10o	**isolated fragment**	4.3	0.3	4.6	0.6	2.3	olv	38
D10t_1	**PO-fragment**	5.6	0.3	5.8	0.6	2.9	olv	17
D10t_2		5.7	0.4	6.3	0.6	3.3	olv	18
D10t_3		5.7	0.3	6.3	0.6	3.4	olv	16
J5u_1	**PO**	2.2	2.2	2.3	1.6	1.1	olv	40
J5u_2		4.3	2.3	3.5	1.6	1.2	olv	38
J5u_3		3.2	2.2	3.2	1.6	1.5	olv	40
J5u_4		6.3	0.8	4.0	0.5	0.7	olv	40
J5u_5		7.4	0.8	4.8	0.5	1.0	olv	39
J5u_6		6.2	0.9	4.0	0.5	0.8	olv	39
J5u_7		6.0	0.9	3.9	0.5	0.7	olv	39
J5w_1	**POP**	5.3	0.9	2.8	0.5	0.0	olv	29
J5w_2		6.3	0.8	3.3	0.5	0.0	olv	36
J5w_3		2.4	0.3	2.1	0.3	0.9	px	21
J5w_4		2.6	0.3	2.2	0.3	0.9	px	21
K4k_1	**PPO**	2.2	1.2	2.6	0.9	1.5	olv	25
K4k_2		1.8	0.3	3.0	0.3	2.1	px	18
K4k_3		2.9	0.3	3.2	0.6	1.7	px	11
K5e	**PO**	5.2	0.7	2.9	0.5	0.1	olv	18
K5i	**Isolated fragment**	3.1	0.3	4.9	0.4	3.3	px	15
K5m	**Isolated fragment**	4.0	0.3	2.5	0.5	0.4	olv	16
L5h	**PPO**	3.0	0.3	1.9	1.0	0.4	px	5.3
L5t_1	**PP**	3.8	0.2	3.9	0.8	1.9	olv	5.2
L5t_2		3.1	0.4	3.9	1.0	2.3	olv	3.0
M6g	**PO**	3.0	0.3	2.3	0.7	0.7	olv	13
M6m_1	**PO**	3.4	0.3	1.9	1.0	0.2	olv	2.9
M6m_2		1.9	0.3	1.7	0.7	0.8	olv	2.7
N4i	**PPO**	6.7	0.6	5.7	1.0	2.2	px	4.2
N4l_1	**PO**	0.9	2.2	3.7	1.6	3.2	olv	1.7
N4l_2		0.9	2.2	4.3	1.7	3.9	olv	18
N4l_3		0.8	2.2	3.4	1.7	3.0	olv	1.4
N4l_4		0.7	2.2	4.2	1.5	3.8	olv	1.4
N4l_5		2.6	0.7	3.9	0.8	2.5	olv	1.1
N4l_6		2.1	0.7	3.8	0.8	2.7	olv	2.0

Table 1, cont.

		$\delta^{18}O$	error_$\delta^{18}O$	$\delta^{17}O$	error_$\delta^{17}O$	$\Delta^{17}O$		Fa or Fs
N4l_7		2.2	0.7	3.8	0.8	2.7	olv	2.1
N4l_8		1.0	0.7	3.2	0.8	2.7	olv	4.2
N4l_9		1.8	0.7	3.9	0.9	2.9	olv	7.2
N4s_1		-6.4	2.2	-6.1	1.5	-2.8	olv	0.6
N4s_2		-6.4	2.2	-7.3	1.5	-3.9	olv	0.4
N4s_3	**PO**	-2.4	0.8	-3.1	1.0	-1.8	olv	23
N4s_4		-4.3	0.6	-4.8	0.8	-2.6	olv	0.5
N4s_5		-4.7	0.6	-5.2	0.8	-2.7	olv	0.5
N4s2	**AOI**	-36.9	0.6	-37.4	0.9	-18.2	olv	40
N4u	**Isolated fragment**	6.0	0.6	6.2	0.8	3.0	olv	40
N4x	**Isolated fragment**	4.2	0.6	5.9	0.9	3.7	olv	13
sulfide nodules								
J5i		2.4	0.5	3.4	0.5	2.1	px/olv intergrowth	
K5l_1		2.5	0.2	1.8	0.7	0.5	olv	16
K5l_2		1.1	0.4	1.7	0.7	1.1	px	12
K5l_3		-15.1	0.4	-17.5	0.9	-9.7	sulfate?	-
K5l_4		-2.6	0.7	-2.4	0.8	-1.1	olv	40
K5l_5		6.9	0.2	3.9	0.7	0.3	olv	41

error: Twice the propagated error in permil. The propagated error includes a standard deviation of duplicated analyses of the standard and standard error of the mean of an individual analytical spot.

In order to reveal individual thermal histories in the chondrite components, we first categorized chondrite silicate components as olivine fragments, chondrules, and silicate fragments in sulfide nodules. Objects were labeled as chondrules if they had igneous textures, consisted of > 50% silicate phases and had rounded surfaces that extended more than 270° of arc; silicate objects that did not meet these criteria were called fragments. Sulfide nodules were defined as igneous objects consisting of > ~50% Fe sulfide. The chondrite components (the chondrules, the isolated olivine grains, and the sulfide nodules) were named based on their coordinates in grids superposed on a section BSE image shown in the online materials. Sulfide nodules in R chondrites were named "sulfide nodules" consistent with the labels of these objects in other chondrite groups (see more in the Discussion section). We also classified chondrite components as equilibrated and unequilibrated based on the range in Fe/Mg ratios of their olivines or pyroxenes.

5.4.1 Petrographic Observations

The chondrules, olivine fragments, and sulfide nodules were studied in detail (see Appendix for images, EDS analyses and some descriptions). The 12 chondrules studied in this paper are porphyritic olivine/pyroxene texture, with apparent diameters ranging from 150- 850 μm in the studied section. Chondrules vary in their Fe/Mg and minor element concentrations. Some chondrules and olivine fragments have nearly equilibrated Fa values (~Fa40), while others have lower Fa and some show blue luminescence or red luminescence in CL images. One olivine fragment, D9l, contains kamacite grains and Ca-Al-rich pyroxene (Isa et al., 2014).

Equilibrated silicates present in chondrules, fragments and sulfide nodules include chondrule olivine phenocrysts that have Fa39±0.9 (J5u); isolated olivine grains have Fa38 (D10o), Fa38

(D10j), Fa40 (N4u); and Fa40 (N4s2); olivine fragments in sulfide nodules (K5l) also have Fa40. These equilibrated olivine grains preserve intact original petrographic textures and they are not porphyroblasts.

Opaque mineral assemblages occur as round droplets to aggregates ranging from a few to 800 μm in size. The main component of these nodules are sulfide minerals. In a couple of 100 μm opaque nodules, we observed opaque oxide, Cr-spinel, phosphate, silicate and alteration products of sulfide. Their large (~50-100 μm) silicate fragments are relatively euhedral. We investigated O-isotope compositions in opaque mineral assemblages in two sulfide nodules (see below). We analyzed large olivine fragments and an altered phase. The chemical formula of alteration products has not yet been determined, but an X-ray element map of this opaque mineral assembly indicates that it consists of a mixture of oxygen and sulfur (Figures in appendix).

In the least metamorphosed clast, matrix components consist of fine grains (Isa et al., 2014) in this section and also another section (Miller et al., 2017, accepted). Under the transmitted light, the matrix appears opaque. Effects from thermal alterations as well as aqueous alterations are not apparent. This of course requires more detailed work with higher resolution techniques. Although many components in this thin section are thermally metamorphosed, some of fine grained materials could be still pristine.

5.4.2 O-Isotopic Compositions of Olivine Phenocrysts and Olivine Fragments

Our O-isotope data are listed in Table 1. Most of the data are for olivine, the most common mafic mineral in R-chondrite chondrules; a few are for low Ca pyroxene. The chondrite components that we analyzed in this study include chondrules, isolated silicate fragments and silicates

embedded in sulfide nodules. The analyzed spots are shown in the BSE images (Figure 5-1 to 5-4).

In a three O-isotopic diagram, most of O-isotope results plot above the terrestrial fractionation (TF) line and some are lower than the TF line. The majority of the O-isotope data near the TF line shown in plots of $\delta^{17}O$ vs. $\delta^{18}O$ in Figure 5-5. The 16 diagrams show three reference lines, the solid TF line at $\Delta^{17}O$ = 0‰, the dotted R-chondrite line at $\Delta^{17}O$ = 3‰, and the dashed carbonaceous-chondrite-anhydrous- minerals (CCAM) line, an empirical line with a slope of 0.94 fitted to minerals most of which were separated from the Allende CV3 chondrite. The names of the samples (based on their positions in the mosaic of the thin section) are shown in the upper left corner. The FeO/(FeO+MgO) ratios (in mol %, shortened to %) are shown by color coding based on the bar on the right side of the diagram. These compositions were measured on the SIMS spot. Ten of the samples were analyzed once, one or more replicate analyses were carried out on six samples.

The $\Delta^{17}O$ values in 16 R chondrite components scatter between the TF and the R lines (Figure 5-5). There is no obvious relationship between the $\Delta^{17}O$ and Fa values. For example, the least altered FeO-rich chondrule, D10t, and the FeO-poor chondrule, N4l, have $\Delta^{17}O$ values (+3.2 ± 0.2 and +3.0 ± 0.5, respectively) similar to those in R whole rocks (+3‰). The olivine of N4x ($\Delta^{17}O$ of 3.7‰; n=1) is Fa 13, whereas one olivine with Fa36 in J5w has $\Delta^{17}O$ of 0.0‰ (Figure 5-6).

In Figure 5-6 we show the O-isotopic data from J5u. The most important feature of these data is the large range in $\delta^{18}O$. In fact, there are two sets of data, each consisting of 3 points. The three points on the left (with large error bars) were taken near the beginning of this study (in 2010) and

the three on the right with small error bars were taken in 2014. We discuss possible instrumental biases in the appendix.

Data for chondrules and olivine fragments that have low $\Delta^{17}O$ values are separately plotted in Figure 5-7).

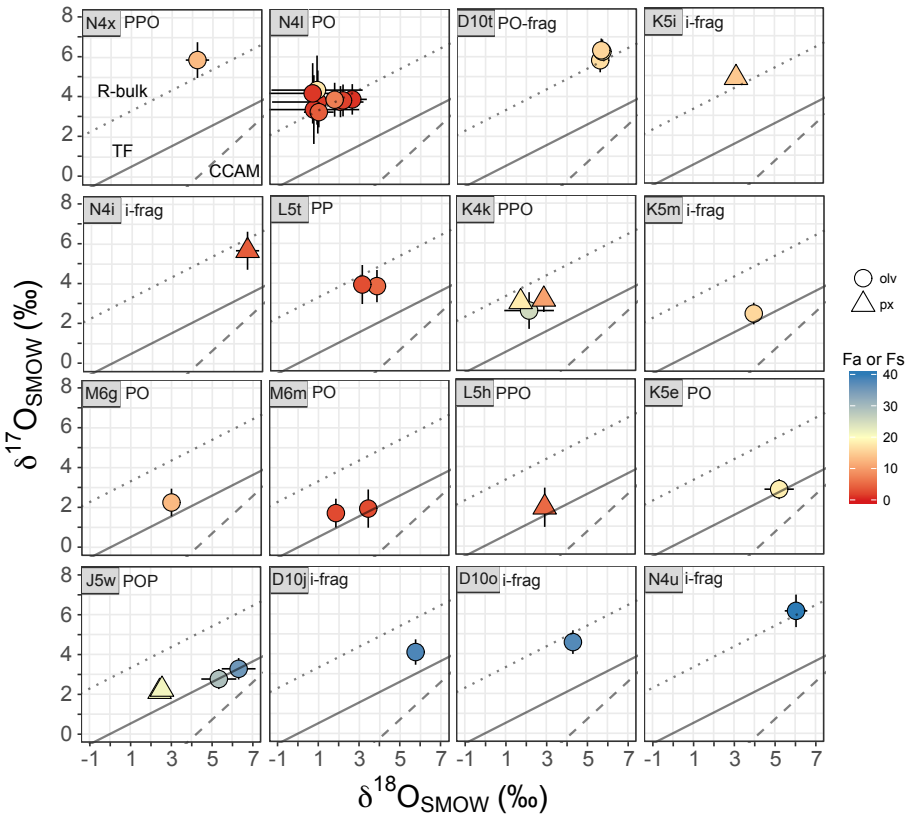

Figure 5-5. Three oxygen isotope plots of individual olivine, pyroxene, and chondrules excluding chondrules and olivine fragments with low $\Delta^{17}O$ values and with significant mass-dependent fractionation. Each data point represents a single SIMS spot measurement. The round and the triangle symbols are olivine and pyroxene, respectively. Olivine Fa or pyroxene Fs values are color coded. Uncertainties of individual measurements are twice of errors. The errors include a standard deviation (SD) of duplicated measurements of a standard and a standard error of the mean (SE) of individual analyses. A solid line, a dashed line, and a dotted line are Terrestrial Fractionation (TF) line, Carbonaceous Chondrite Anhydrous Mineral (CCAM) line, and the mean of R whole rock ($\Delta^{17}O$=2.7; Bischoff et al., 2011) mass-dependent fractionation (R-bulk) line.

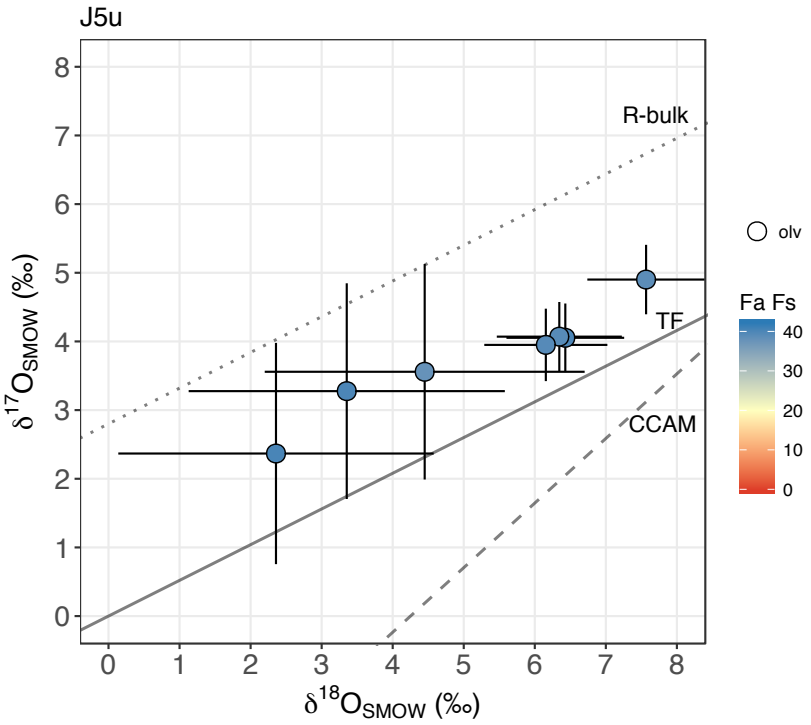

Figure 5-6. Three oxygen isotope of silicates in chondrule J5u. Each data point represents a single SIMS spot measurement. Uncertainties of individual measurements are twice of errors (as stated in the figure captions at Figure 5-5). A solid line, a dashed line, red dashed line, and are blue dashed line are TF-line, CCAM line Y & R line. These chondrule show mass-dependent fractionation.

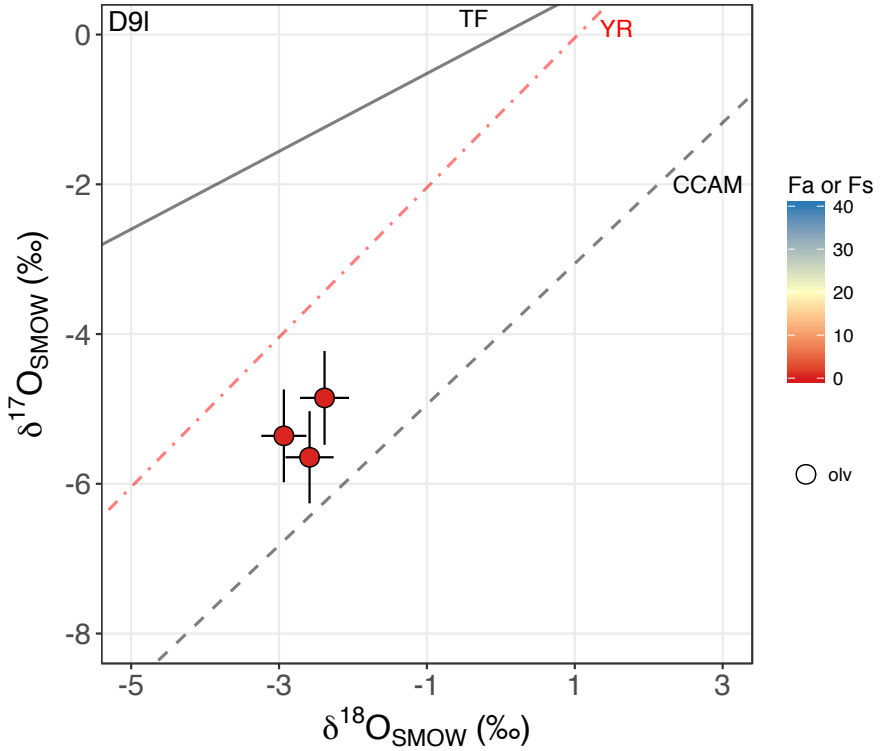

Figure 5-7. Three oxygen isotope of olivine fragment, D9l. Each data point represents a single SIMS spot measurement. Uncertainties of individual measurements are twice of errors (as stated in the figure captions at Figure 5). The three values agree within the experimental uncertainty, and the agreement exhibits homogeneous compositions. A solid line, a gray dashed line, and a red dashed line are TF-line, CCAM line and Y & R line: slope = 1 line (Young and Russell, 1998), respectively. The $\Delta^{17}O$ values are significantly lower than R whole rock or a majority of OC chondrules. The occurrence of kamacite grains and low $\Delta^{17}O$ values of this olivine fragments indicate the associations with the majority of CC chondrules with metal grains and low $\Delta^{17}O$ values.

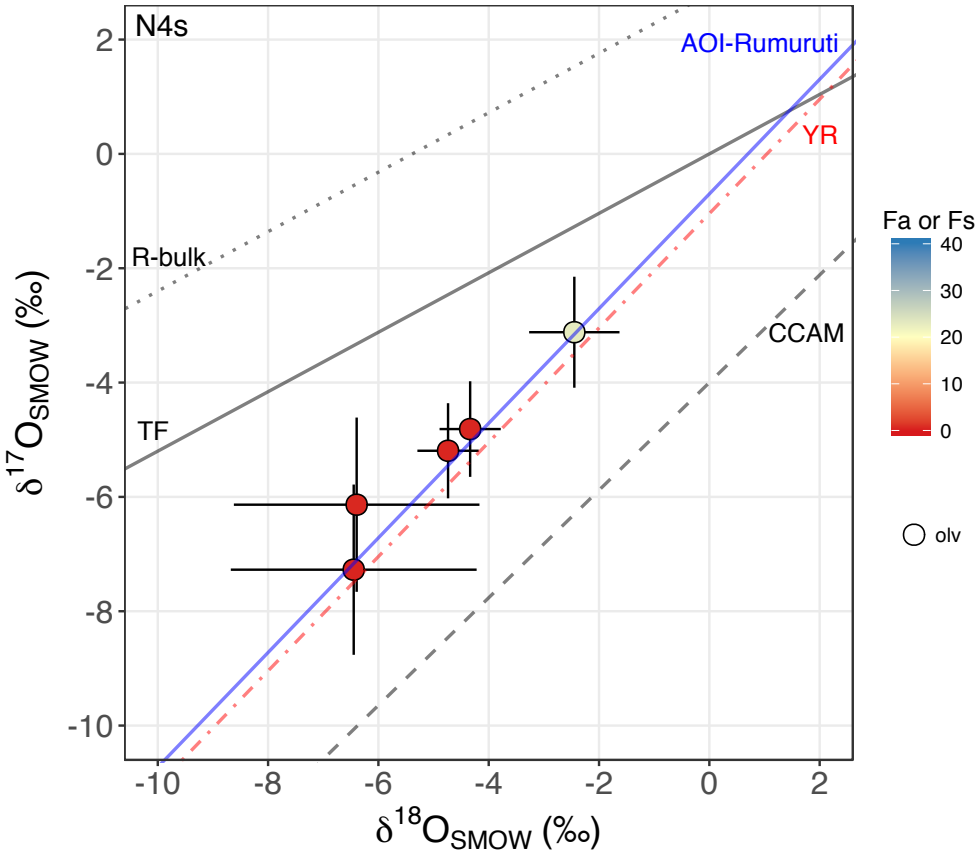

Figure 5-8. Three oxygen isotope of olivine phenocrysts in chondrule N4s. Each data point represents a single SIMS spot measurement. Uncertainties of individual measurements are twice of errors (as stated in the figure captions at Figure 5). A solid line, a dashed line, red dashed line, and are blue dashed line are TF-line, CCAM line Y & R line, and the line between AOI and a data point of Rumuruti (fall) meteorite whole-rock O-isotope compositions, respectively. The $\Delta^{17}O$ values are significantly lower than R whole rock or a majority of OC chondrules. The data show heterogeneous O-isotope compositions.

Data for silicate grains in sulfide nodules are plotted in Figs. 5-9a and 5-9b. The samples from k5l (nodule 1) consist of three olivines and a pyroxene, all of which scatter near the TF line; the total range in $\delta^{18}O$ is quite large, about 9.5 ± 0.8‰. We also have data from nodule 1 for an uncharacterized phase, possibly a sulfate, which plots near the CCAM line at $\delta^{18}O$ = -15 ‰. This point is not plotted because of possible large matrix effects for this phase of unknown mineralogy. The sample from J5l (nodule 2) is an intergrown olivine and pyroxene for which no compositional data are available.

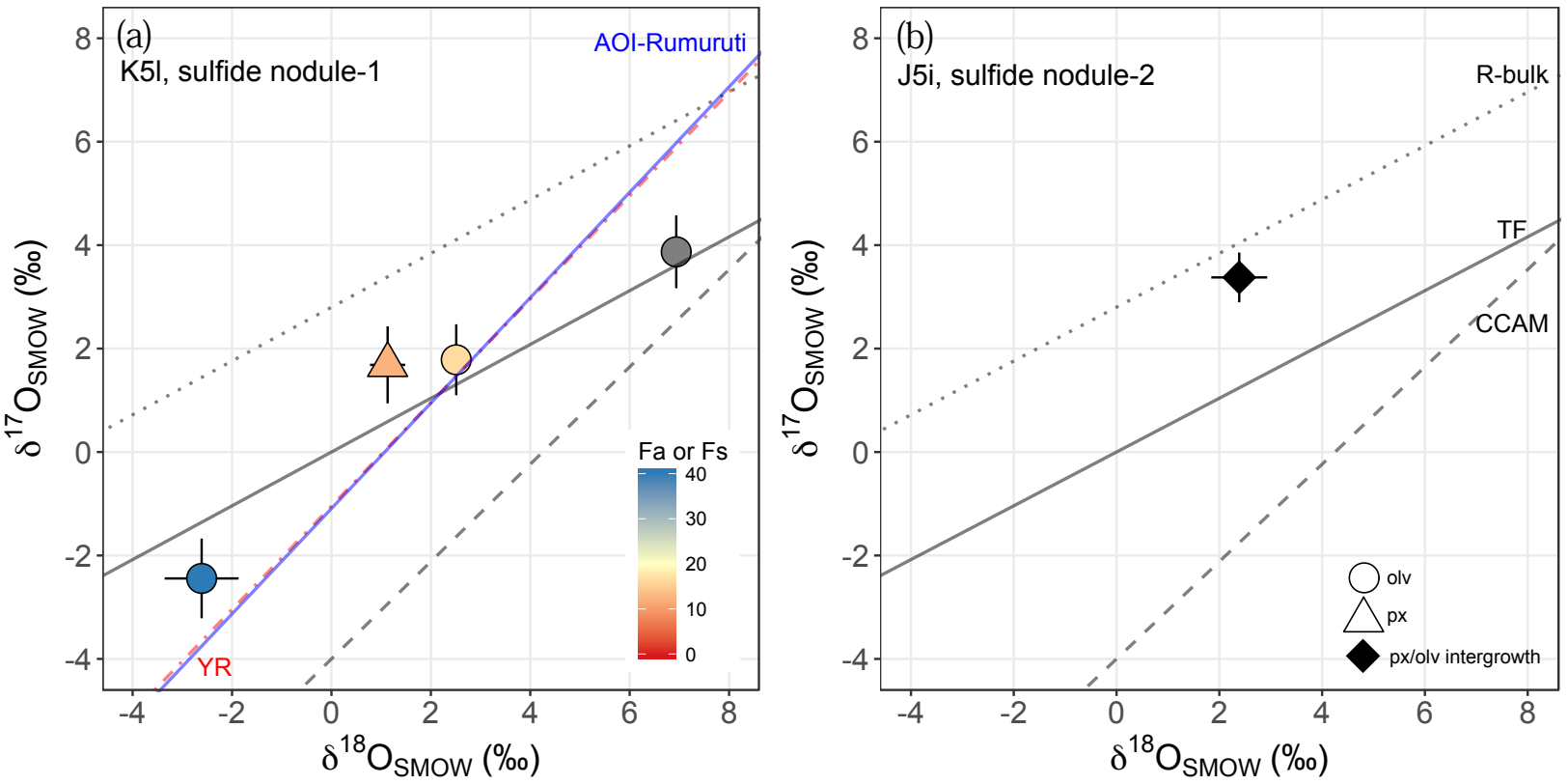

Figure 5-9. Three oxygen isotope of silicates in sulfide nodules, (a) K5l, sulfide-nodule-1 and (b) J5i, sulfide nodule-2. Each data point represents a single SIMS spot measurement. Uncertainties of individual measurements are twice of errors (as stated in the figure captions at Figure 5). A solid line, a dashed line, red dashed line, and are blue dashed line are TF-line, CCAM line Y & R line, and the line between AOI and a data point of Rumuruti (fall) meteorite whole rock O-isotope compositions, respectively. O-isotope data of sulfide nodule-1 exhibit highly unequilibrated heterogeneous compositions. A measured silicate fragment in J5i was pyroxene and olivine intergrowth.

5.4.3 $\Delta^{17}O$ Values in Histograms and of Entropy

Histograms of mean of $\Delta^{17}O$ values acquired by SIMS *in situ* measurements in individual chondrules and silicate fragments in PRE 95404, LL3 and CO chondrite chondrules are shown in Figure 5-10. Included data are unequilibrated chondrule and silicate fragments from this study and the data from the literature (Kita et al., 2010; Libourel and Chaussidon, 2011; Tenner et al., 2013). The data sources are shown in the diagram top left.

For a comparison across the different labs, we used mean $\Delta^{17}O$ values (including heterogeneous samples such as relict olivines). In this way, we can reduce the selection bias and can compare inter-lab analyses under the similar conditions. The mode of individual distributions shows at 0.00 to 0.50 ‰ for PRE 95404, 0.50 to 0.75 ‰ for Semarkona LL3.0, 0.75 to 1.00‰ for Bishunpur LL3.1, and 0.25 to 0.50 ‰ for Krymka LL3.2 in $\Delta^{17}O$ scale. The mode of CO3 chondrule is -5 to -4.75 ‰ in $\Delta^{17}O$.

We constructed relative frequency table of mean of $\Delta^{17}O$ values measured in individual chondrules and silicate fragments (Table A3). The entropy calculation of LL3 (Kita et al., 2010; Libourel and Chaussidon, 2011), E3 (Weisberg et al., 2011), CO3 (Tenner et al., 2013) and R-chondrite chondrules (this study and Greenwood et al., 2000) yields 0.74, 0.30, 1.06, and 1.29, respectively (natural logarithmic scale). Higher number indicates the chondrule populations have more heterogeneous O-isotope compositions in $\Delta^{17}O$ scale.

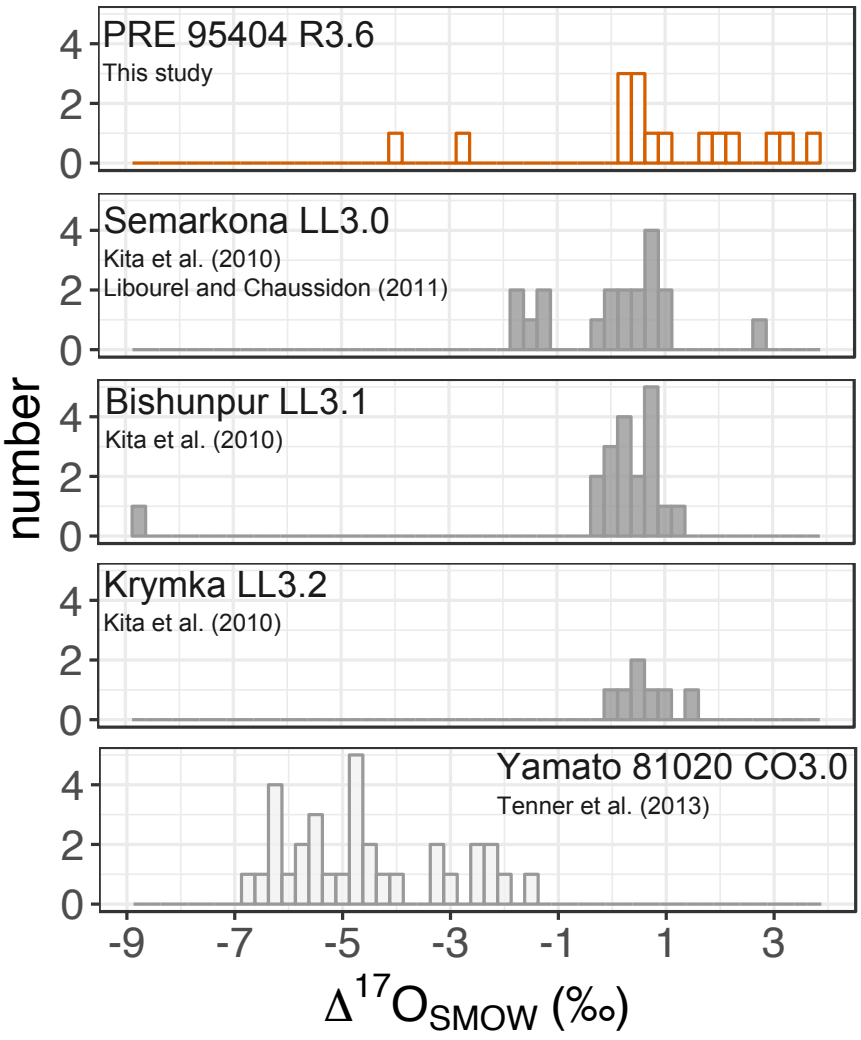

Figure 5-10. Histogram of mean of *in situ* $\Delta^{17}O$ values in individual chondrules in PRE 95404, LL3 and CO chondrite chondrules. The mode of the distribution is 0 to 1 across R and LL3 chondrite chondrules.

5.5 Discussion

A goal of this work is to elucidate the differences between chondrules in R chondrites and those in other chondrite groups in the context of planetesimal formation that includes chondrule formation conditions, chondrite parent body accretionary processes, and parent-body metamorphism. We first discuss O-isotope data comparing with Fa values. We describe diversities of chondrule populations with other chondrite groups in Section 5.6, **O-isotope Compositions between R Chondrite Chondrules and Other Chondrite Chondrules**. Second, we describe in situ metamorphism of PRE 95404 in Section 5.7, **In situ Metamorphism at the Final Lithification Location**. Third, we describe R chondrules and silicate fragments that have O-isotope compositions that have extreme $\Delta^{17}O$ values in Section 5.8, **Petrographic Feature of Selected Chondrules and Isolated Silicate Fragments**. Fourth, we describe metamorphism histories that are recorded in the individual components (FeO-rich chondrule, unequilibrated chondrules, and equilibrated chondrules; sulfide-nodules; and AOI) in Section 5.9, **Individual Histories of R Chondrite Components**. Finally, we discuss potential models of the structure and history of the R-chondrite parent body in Section 5.10, **Story of R Chondrites Parent Body**.

5.6 O-Isotope Compositional Differences between R Chondrite Chondrules and Other Chondrite Chondrules

The main reason for this study was to better understand the formation of the R chondrites and the genetic links to other groups of chondrites. Because the search for taxonomic links is based on chemical and isotopic compositions and physical textures such as chondrule textures and the nature and abundance of fine, nebular matric, it can be approached in a more quantitative way

than the large set of process that may have contributed to the formation of the R-chondrite rocks, and we thus tackle the taxonomic problem first.

It has long been recognized that the R chondrites share several features with the ordinary chondrites (OC) including a high abundance of porphyritic chondrules and $\Delta^{17}O$ values above the TF line. Rubin and Kallemeyn (1994) noted that the distribution of redox states and textural types in R chondrites are similar to those in OC; carbonaceous-chondrite (CC) chondrules are largely low-FeO and frequently have non-spherical shapes indicating formation at lower temperatures resulting in higher viscosities (e.g., lobate chondrules in CO chondrites, Rubin and Wasson, 2005). On the other hand, the R chondrites have much lower abundances of small droplet chondrules such as radial-pyroxene or cryptocrystalline chondrules and abundant sulfide such as sulfide chondrules (Miller et al., 2017, accepted).

5.6.1 Comparison of O-isotopic Compositions in R and Ordinary Chondrites

As can be seen in Figure 5-10, PRE data scatter more than the LL data, but also the mode of PRE is unresolvable from the mode of the LL chondrites. The scatter of R3 data is expressed in larger entropy compared to that of ordinary LL3 or E3. However, CO3.0 has more diversity than R.

LL3.0 Semarkona also shows more scatter than the slightly more equilibrated LL3.1 Bishunpur and LL3.2 Krymka. The standard deviation of Semarkona is about 1‰, that in PRE about 2‰.

The mode of the CO3.0 Yamato is 4.8‰, much lower than that of PRE. This leads to the conclusion that R-chondrite chondrules are much more closely related to LL chondrites than to CO. In fact, although three PRE chondrules have $\Delta^{17}O$ values ≥3.0‰, the distribution clearly

shows a strong resemblance between R and OC $\Delta^{17}O$ values; based only on these data, they could be part of the same population.

However, the set of $\Delta^{17}O$ data for PRE differs from the LL3 chondrites at both ends of the range. The PRE histogram shows points at -2.8 and -4.0‰, only slightly higher than the mode of the CO3.0 Yamato set at -4.8‰. This could imply that PRE sampled chondrules from a reservoir related to that sampled by CO3.0 Yamato but not by LL3.0 Semarkona. And the PRE histogram includes three chondrules in the range 3.0 to 3.8‰, higher than the highest observed in Semarkona, 2.8‰. This discrepancy in the distribution shape implies that the two chondrite groups accreted chondrule populations that originated in the same populations but included some levels of diversity.

5.6.1.1 High $\Delta^{17}O$ Chondrule Precursors in other Chondrite Groups

Silicates with high $\Delta^{17}O$ values approximately equal to the R whole rock field $\Delta^{17}O$ (~3‰) occur in chondrite groups E3 (Weisberg et al., 2011) and LL3 (Libourel and Chaussidon, 2011), indicating that some chondrules formed with $\Delta^{17}O$ ~3‰ regardless of type of parent body. In previous in-situ studies, intermediate distributions of $\Delta^{17}O$ were reported across different types of chondrules (Libourel and Chaussidon, 2011; Tenner et al., 2013; Ushikubo et al., 2012). These heterogeneities have been interpreted as discrete populations of chondrule (or chondrule precursors) reflecting specific reservoirs within the solar nebula. Although our data are not sufficient to comprehensively evaluate the hypothesis of such discrete reservoirs for many chondrule precursors, it does appear that high $\Delta^{17}O$ ~3‰ values are one of the common O-isotope compositions in chondrule precursors.

5.6.1.2 Lack of Correlation in Fe Molar Fraction and $\Delta^{17}O$ Values.

A surprising result of our study is the lack of correlation between Fe molar fractions and $\Delta^{17}O$ values in olivine and pyroxene. It has been known that high FeO contents are indicative of high fO_2 during the chondrule formation and there is an expectation for higher fO_2 conditions to be correlated with high $\Delta^{17}O$ (Connolly and Huss, 2010; Jones et al., 2004; Jonesl et al., 2000; Krot et al., 2006; Kunihiro et al., 2005, 2004; Libourel et al., 2006; Rudraswami et al., 2011; Schrader et al., 2013; Tenner et al., 2013, 2015; Ushikubo et al., 2012). An excellent trend has been observed especially in CR chondrite chondrules (e.g. Connolly and Huss 2010; and Tenner 2015). This was explained by local evolution of gas compositions that increases heavy water vapor with dust enrichment wherein the dust contained ^{17}O- and ^{18}O-enriched water ice.

In R chondrites chondrules, however, we found that even FeO-poor olivine is also enriched in ^{17}O and ^{18}O. It thus seems that chondrule precursors had to form in several regions and/or at different times with different amount of enrichment of Fe or reduction/oxidation reagents. Whereas the well-ordered trend between Fa and $\Delta^{17}O$ values in CR chondrites indicates that those chondrules formed in local regions, the diversity of R-chondrite chondrules points to a lack of systematic local accretion and rather suggests a more chaotic accretionary from a wider nebular region.

In different chondrule formation scenarios, such as chondrule formations from molten differentiated silicate (Asphaug et al., 2011; Sanders and Scott, 2012; Wood and Cameron, 1963; Zook, 1980), the melt could have had high $\Delta^{17}O$ (Libourel and Chaussidon, 2011) and variable Fe/Mg compositions. In this case, $\Delta^{17}O$ and Fa values also do not need to be correlated. This hypothesis requires fewer numbers of assumptions, and thus it has a higher likelihood. However,

our results could be explained by either hypothesis and we do cannot favor any of the chondrule formation scenarios based on our results.

5.6.1.3 Previous Hypothesis R Chondrule Precursors prior to Secondary Processes.

Greenwood et al., (2000) found some low-FeO olivine fragments in R chondrites with O-isotopic compositions similar to UOC. In our study two chondrule phenocryst cores have high $\Delta^{17}O$ ~3‰, indicating the existence of high $\Delta^{17}O$ olivine chondrule precursors when some R chondrules formed. Two earlier models to explain high $\Delta^{17}O$ values thus appear unlikely: (1) reaction with ^{17}O enriched water from the matrix during alteration in the R parent body (Greenwood et al., 2000) and (2) nebular gas-solid exchange. However, other models involving mixtures of precursors cannot be ruled out (Weisberg et al., 1991). A significant problem with the Greenwood et al., (2000) model is an absence of evidence of appreciable aqueous alteration effects in PRE 95404. Weisberg et al., (1991) proposed that low-FeO olivine grains exchanged oxygen with ^{16}O-poor nebular gasses and that this produced fayalitic olivine. The nebular gas was assumed to have high $\Delta^{17}O$-oxygen. However, we found that low-FeO olivine can have high $\Delta^{17}O$ and that there is no simple correlation among Fe concentration and $\Delta^{17}O$ values. Therefore, more complex models are required to explain the lack of correlation of $\Delta^{17}O$ and FeO in R chondrule olivine. Because there are few constraints on the compositions of the individual components among chondrule precursors, it remains possible to assume a small relict component interacted with gas that was $\Delta^{17}O$ rich, for example if chondrule formed by flash melting of gas and dust in the nebula.

5.7 *In Situ* Metamorphism at the Final Lithification Location

Although PRE 95404,15 is one of the least equilibrated R3 chondrites, it does show some evidence of thermal metamorphism. However, this does not mean that O-isotope compositions were affected by metamorphism. Oxygen diffusion rates are much slower than those of Fe and Mg in olivine and pyroxene. It is reasonable to assume that chondrules and coarse (> 60 μm) mafic grains remained closed systems to O after the PRE formed as a rock.

5.8 Petrographic Features of Selected Chondrite Components

We selected chondrules that have high $\Delta^{17}O$ values that are rare in ordinary chondrite chondrules. As we stated above, Fa (or Fs) values do not correlate with $\Delta^{17}O$ values. Since thermal metamorphism can alter Fa or Fs values in mafic minerals and thus obscure the original trends, we focused our attention on two unequilibrated chondrules having high $\Delta^{17}O$ N4l and D10t.

5.8.1 FeO-poor Chondrules with High $\Delta^{17}O$ Values

The round (and thus intact) chondrule N4l is a PO chondrule with low-FeO mafic silicates. Tiny sulfide grains occur inside the chondrule and small (a few tens μm) sulfide nodules are attached to the chondrule (white in Figure A2-6 and A2-7). Several inclusions with sizes up to 10 μm are present in the olivine phenocrysts. Olivine phenocrysts show perhaps both igneous zoning and some zoning due to thermal diffusion. Outer patches of the chondrule show high FeO and the area are appeared in blight gray colored in BSE image (Figure A2-6). Those areas are likely due to Fe-Mg exchange due to thermal metamorphism. Although those FeO-rich areas near at the outer edge of chondrule exchanged Fe-Mg due to thermal metamorphism, the SIMS data were

taken near the centers of several low-FeO chondrules. Some olivines in phenocryst cores show red cathode luminescence indicating that their compositions are nearly pure forsterite. We conclude that the mafics in the phenocryst cores preserve the O-isotope and chemical composition established during chondrule formation.

5.8.2 FeO-rich Unequilibrated Chondrule with High $\Delta^{17}O$ Values

Olivine phenocrysts in the high-FeO chondrules-D10t are highly unequilibrated with cores that are Fa16, rims that go up to Fa60 (Figure 5-11). The overall zoning profile of D10t is consistent with that of a typical FeO-rich (type-II) olivine phenocryst in LL3.00 Semarkona and LL3.3 ALH 81251 in which Fe, Cr, Mn, and Ca are flat at the core, then increasing toward the rim (Jones and Lofgren, 1993). High-FeO chondrules in OC and CO chondrites have mean Fe/Mn ratios of ~ 44 and 99, respectively (Berlin et al., 2011). The Fe/Mn ratio remains constant throughout the olivine phenocrysts 82 ± 11 (1SD). This constant ratio agrees with the Fe/Mn ratios in equilibrated R chondrites within two standard deviations (80 ± 16 based on the data of Isa et al., 2014). The same Fe/Mn ratios between chondrule-D10t and equilibrated R chondrites is consistent with formation from the same mix of materials as equilibrated R chondrites. Most unequilibrated chondrules and olivine do not have the Fe/Mn ratios approximately 80 (Table A2). Bischoff et al., (2011) observed similar texture in an impact melt rock in another R chondrite and also the texture of D10t is typical of highly unequilibrated chondrules (Figure A2-5). Because the chondrule is unequilibrated, the only firm conclusion is that the precursor materials had an R-like Fe/Mn ratio.

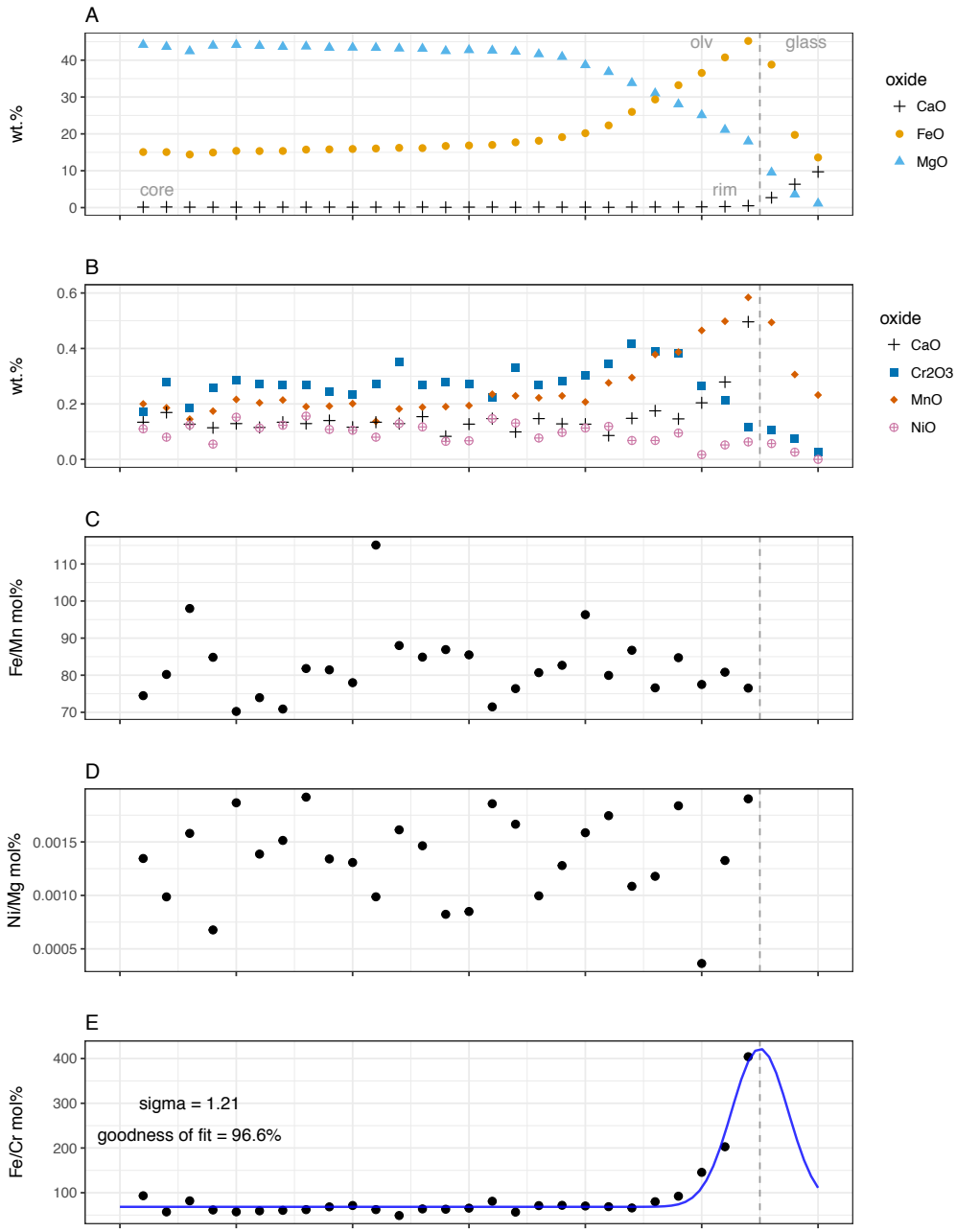

Figure 5-11. Zoning profile of chondrule D10t olivine and mesostasis. The oxide chemical compositions (wt. %) measured with EPMA are plotted in the diagram A and B. The Fe/Mn molar ratios, Ni/Mg molar ratios, and Fe/Cr molar ratios are plotted in C, D, and E. The individual points are measured every 1µm. The dashed line indicates the boundary between olivine phenocryst and mesostasis. The zoning profile of major elements shows a similar pattern in other FeO-rich chondrules in other chondrite groups. The Fe/Mn and Ni/Mg ratios did not significantly change over the crystallization of this olivine phenocrysts. These constant elemental ratios indicate that a lack of remelting under the different environments. Therefore, redox did not significantly evolve over the growth of this mineral. Cr abundance, on the other hand, changed at the edge of the olivine phenocrysts. This zoning profile is consistent with FeO-rich chondrule in Semarkona (LL3.0) chondrite.

5.9 Individual Histories of R Chondrite Components

Petrographic observations of individual chondrules do not show significant differences from reported chondrules in other chondrite groups, and are most similar to those in OC groups. However, the thin section PRE 95404,15 contains multiple "post-accretionary" objects. Following are observations of post-accretionary objects.

5.9.1 Metamorphism of Individual Components

Thermal histories of individual chondrules in PRE 95404,15 have variety. For instance, chondrule J5u that shows properties implying that it experienced thermal metamorphism is located in the same type-3 clast that contains N4l described above. Chondrule J5u is an approximately ~ 400 -600 μm PO chondrule with high FeO concentrations in olivine. It contains only one unequilibrated olivine phenocryst; the FeO-poor olivine phenocrysts have Fa value 30 at the core and that Fa value 39 at the rim (Figure A-32). The FeO composition similar to those in equilibrated R chondrites implies that the relicts were metamorphosed on an R-chondrite body prior to the mixing with the other components of the chondrule. If the uniform composition of the Fa40 reflect metamorphism, it requires a large amount of heat in a body. The recrystallized mesostasis that shows blue luminescence in CL image (Figure A-33) is consistent with this view. The O-isotope compositions of this chondrule J5u are typical of ordinary chondrite chondrules. Because O-isotope compositions of bulk R chondrite compositions are mass-independently different from this chondrules, the metamorphism event recorded in this chondrule, which changed FeO compositions of the chondrule phenocrysts, unlikely affect original $\Delta^{17}O$ values prior to metamorphism on the R chondrite parent body.

It is clear that impact events are common in the early stage of the proto planetary disk evolution. It is easy to invoke that impact processes are responsible for material transports. Intact single chondrule with a lack of silicate clasts implies that the location of metamorphosis was not consolidated. Re-accretion of those metamorphosed chondrules together with fine-grained matrix and other chondrite components could explain this texture in the thin section.

5.9.2 Sulfide Nodules

We observed different O-isotopic compositions in the opaque (mainly FeS and Ni-rich sulfide) mineral assemblages in PRE 95404. The O-isotope compositions of silicate grains in sulfide nodule-1 (K5l) are highly unequilibrated while the O-isotope composition of the silicate fragment in sulfide nodule-2 (J5l) is similar to those of typical chondrules in PRE 95404. The grains (3 ol, 1 px) in nodule-1 have O-isotope compositions near the TF line though the olivines with the most extreme $\delta^{18}O$ values have compositions near Fa 40. We were not able to characterize the alteration phase that has $\Delta^{17}O$ of ~-10‰ and plots near the CCAM line; we infer that this grain likely includes a CAI component.

The oxides in the sulfide nodules have highly diverse chemical compositions and oxygen-isotope compositions. Textually, they are angular fragments whose surface shapes were not controlled by interfacial tension, i.e., they did not form as immiscible liquids as suggested by (Bevan and Axon, 1980; Miller et al., 2016). More or less angular nature of the silicates suggests that these assemblages are results of granular mixing probably due to impact events that likely created the PRE 95404 breccia.

5.10 The Story of the R Chondrite Parent Body

5.10.1 R Chondrite Parent Body Accretion and Mixing

Because chondrites are sedimentary rocks, physical sizes and chemical relationships of chondrite components offer useful information for modeling planetesimal and parent-asteroid formation conditions (Alexander, 2005; Rubin, 2010). The PRE95404 texture preserves chondrules and sulfide nodules in a mix with abundant fine-grained matrix.

As has been summarized in Rubin et al., 2010, chondrite physical properties show clear differences in average size of chondrules between chondrite groups with large size chondrules in the groups CV, CK, and CR and small size chondrules in the groups CM, CO, OC, R, EH, and EL. In the case of R chondrites, the average chondrule size is similar to that of H chondrites (~ 450 μm). Several models have suggested that chondrule size differences among chondrite groups may have been caused by aerodynamic sorting of chondrules in solar nebular gas at different degrees of turbulence (e.g., Clayton, 1980; Cuzzi et al., 2001; Liffman, 2005). As argued by Rubin (2010), transportation of chondritic materials by turbulent mixing within the nebula did not result in the mixing of chondrule populations in OC and E before or during their accretion. Therefore, it is plausible that OC and E planetesimals formed soon after chondrule formation yielding the chondritic asteroids that subsequently experienced metamorphism.

It appears that R chondrites had a somewhat different formation scenario. Chondrules are size sorted regardless of their chemical and isotopic compositions. The chondrule populations are heterogeneous than other ordinary chondrite groups. The $\Delta^{17}O$ and FeO contents in chondrules do not show any correlation. Chondrule compositions include both silicates and sulfides (Miller

et al., 2017, accepted). These observations indicate that the R chondrite parent body accreted from more well mixed source materials than did other chondrite groups.

As described above, PRE 95404,15 contains highly unequilibrated chondrules as well as several post-accretionary materials. These observations imply that PRE 95404 formed from chondrules and matrix having different histories. Also, our observational results require thermal metamorphism before the final lithification of type 3 R chondrites, at least in the case of PRE 95404 which has components that did not experience parent body thermal metamorphism. Such post-accretionary materials are also observed in other chondrite groups (Gibson et al., 1977; Hutchison and Bevan, 1982; Hutchison and Graham, 1975; Tang et al., 2017). Those observations imply that PRE 95404 is not a special case and there are other chondrites that consist of reassembled impact debris surrounded by additional nebular materials. A similar idea has been described in Scott and Taylor (1982) to explain the mixture of various materials in chondrites. The main difference with our idea here is the source of mixing materials. Mixed materials could come from elsewhere during the accretionary processes.

Unfortunately, we do not yet have a reasonable cosmochemical tool to identify the timing of lithification of unequilibrated chondrite materials, and thus, this sorting could have happened during the accretion of R chondrite parent body or long after the establishment of R parent bodies.

5.10.2 R Chondrite Parent Body

R-chondrite parent-body models have evolved over the years (Bischoff et al., 2011, 1994; Isa et al., 2014; Kallemeyn et al., 1996; Khan et al., 2015; Lingemann et al., 2000; McCanta et al., 2008; Righter et al., 2016; Righter and Neff, 2007; Schulze et al., 1994). About half of the R

chondrites are thought to have formed in a regolith (~50% of R chondrites contain solar noble gases; Bischoff et al., 2011; Schultz et al., 2005) and this is also consistent with the occurrence of materials of high petrologic type in host materials of low petrologic type. It has been found that R chondrite parent bodies were heterogeneous in terms of volatile components (e.g. H_2O, CO_2, H_2S etc.) that were not noted in previously reported bulk elemental abundances, but are apparent in petrography in equilibrated R chondrites (Isa et al., 2014; Kallemeyn et al., 1996; Khan et al., 2015; McCanta et al., 2008). The texture and chemical composition of PRE 95404 provides an example that R chondrite parent body could be a mixture of a large range of materials. The heterogeneity in the PRE 95404,15 section could be due to reassembly of various R chondrite parent bodies. And thus, the cause of these chemical variations could be attributed to the parent body size (larger than OC parent bodies) or late formation of the parent body (original materials are well mixed and thus higher entropy).

5.11 Conclusions

We observed O-isotopic compositions of R-chondrite chondrules and olivine fragments. Most of the O-isotopic compositions of R-chondrite chondrules (including previous data) show that there are variations among OC and R whole rock regions, and that $\Delta^{17}O$ values lower than the TFL are rare. Chondrules with $\Delta^{17}O$ ~3‰ in olivine can have very different olivine compositions. This implies that high-$\Delta^{17}O$ R-chondrite chondrule precursors existed prior to chondrule formation and that previous hypotheses of R-chondrule formation invoking reaction with nebular gas (Weisberg et al., 1991) or with water derived from parent-body fluids (Greenwood et al., 2000) are unlikely. The O-isotopic compositions in R whole rock regions have been observed in different chondrite groups and the high-$\Delta^{17}O$ R whole rock region olivine is likely one of the

common silicate precursors across different chondrules. The chondrule populations of R-chondrite chondrule overlapped with that of OCs. The diversity of chondrule silicate precursors in R chondrules is larger than that in OCs in terms of $\Delta^{17}O$ values. Although the R-chondrite group is heavily brecciated, there is a lack of impact annealing or strong compaction unlike most of OCs; the silicate/oxide sulfides are "post-accretionary" fragments readily identified in the matrix. Along with previous observations and based on our new data, we conclude that it is possible that the R-chondrite parent body was larger or that it accreted from planetesimal formed later than those of ordinary chondrites. Further observations and geochronological research are required to quantitatively test the timing of rock formation. From the observations of the diverse thermal histories across the chondritic components, the final lithification of R3 chondrites was later than R chondrite chondrule metamorphism.

5.12 Appendix-1: The Thin Section PRE 95404,15

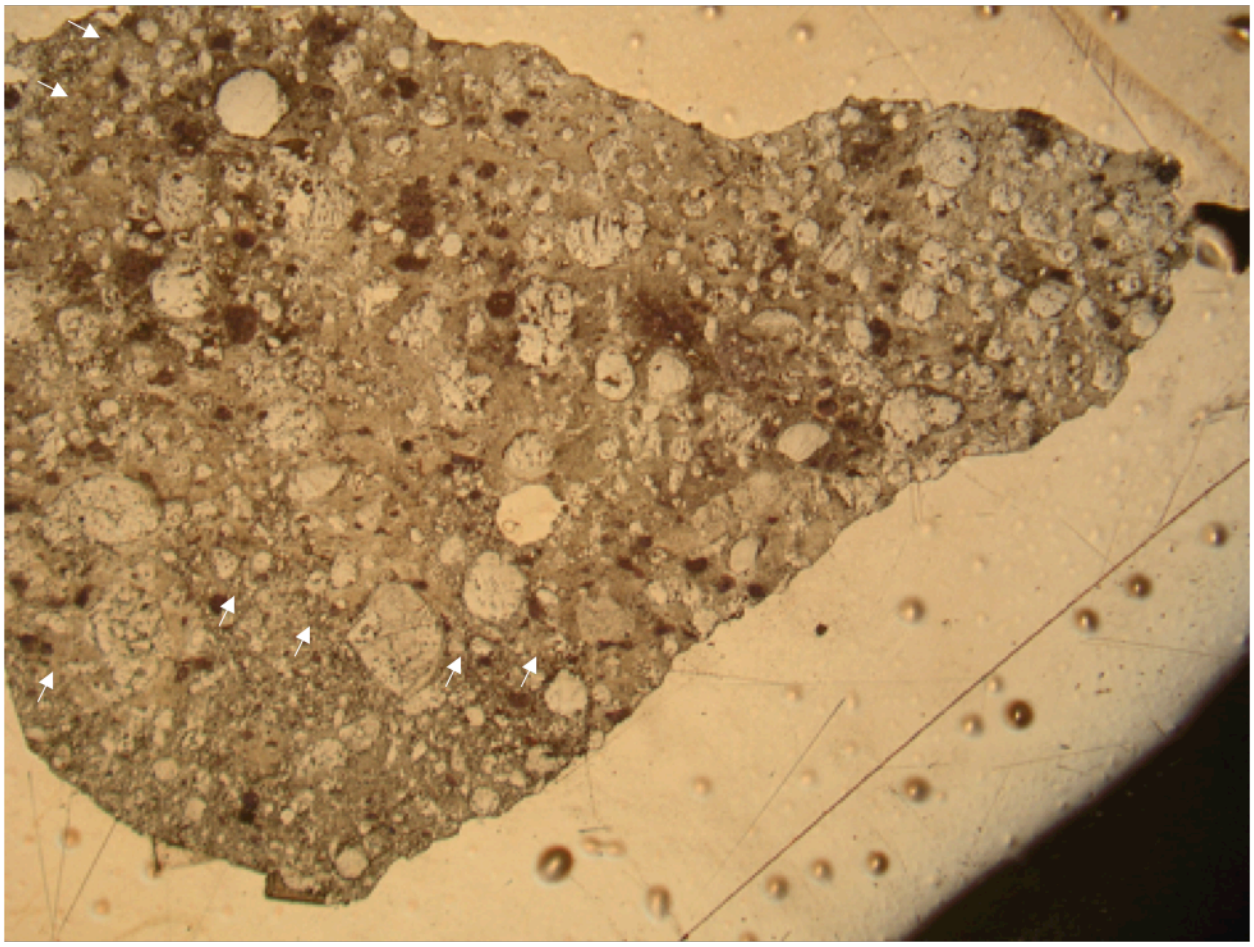

Figure A1-1. A photo of a thin section, PRE 95404,15. Arrows in the picture point the boundaries of two lithologies. The boundaries are not sharp.

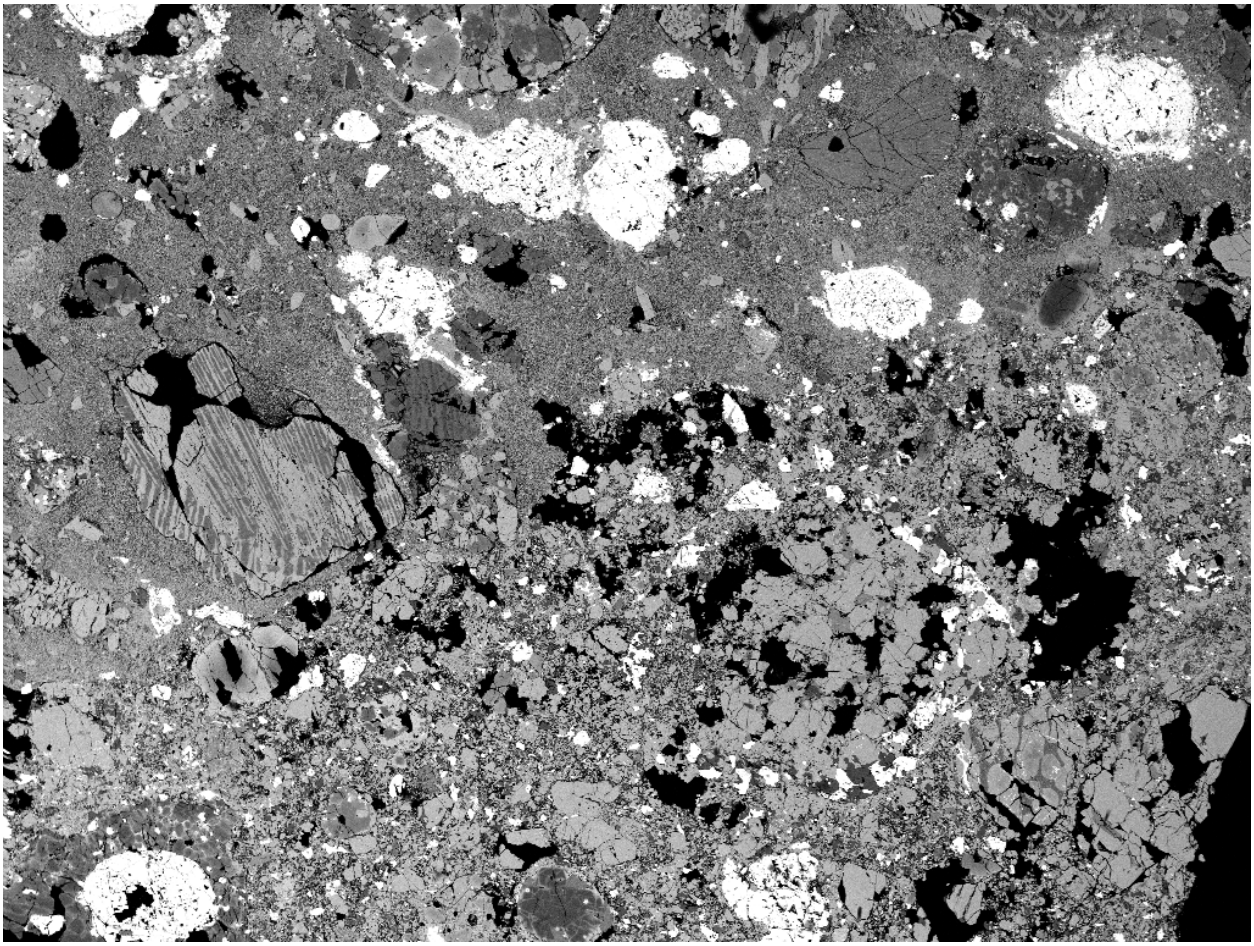

Figure A1-2. BSE image of a thin section PRE 95404,15. A boundary between the two lithologies with fine-grained matrix and fragmented matrix on either side is seen in the image.

5.13 Appendix-2: Petrographic Descriptions of some Chondrules

Table A1: List of chondrule components

name		size	O-isotope measured phase	Fa/Fs at SIMS spot	stdev	note
N4l	PO	~ 300 µm	olv	5	6	The olivine phynocrysts include several compositions of inclusions submicron to tens of microns in size which compositions are sulfide, Ca-phosphate, Al-rich oxide, chromite, silicate with plagioclase-like composition, and pyroxene. Red luminescence in the middle of olivine grains (~Fa1) and blue luminescence from mesostasis.
N4s	PO	~ 300 µm	olv	0.4-40		Blue and red luminescence in a CL image. Edge of olivine phenocrysts altered form original chemical compositions showing Fe zoning.
J5w	POP	~ 500 µm	olv and px	Fa(32)Fs(21)		An euhedral chromite grain and tiny sulfide grains occur in the chondrule and few tens µm size of sulfide nodules attached to the chondrule. Mesostasis are crystalized.
D10t	PO fragment	~150 ×400µm	olv	16-60		It is characterized by presence of large euhedral olivine phenocryst (up to ~100 µm); glassy to microcrystalline mesostasis including dendritic chromite and spherical sulfides with silicate inclusions; and the absence of Fe-Ni metal. The edge of olivine phenocrysts contain melt inclusions with sharp boundaries.
N4x	PPO	~250 ×250 µm	olv	13		A CL image shows that red luminescence in the middle of phenocrysts.
J5u	PO	~400 ×600 µm	olv	39	1	Tiny sulfide grains occur inside of the chondrule. Chondrule rims is discontinuously trimmed by sulfide. Olivine phenocrysts contain high FeO (nearly equilibrated R chondrite Fa values). The most magnesium rich olivine phenocrysts have Fa value 30 at the core and that Fa value 39 at the rim. Mesostasis are recrystallized and show blue luminescence in a CL image .
K4k	PPO	~300×500 µm	olv and px	Fa(25)Fs(14)		Tiny sulfide grains occur inside and up to~ 100 µm size of sulfide nodules attached to the chondrule
L5h	PPO	~200×250 µm	px	5.3		There are no major inclusions in olivine. Olivine phenocrysts has higher FeO contents in contrast MgO-rich pyroxene.
L5t	PP	~200×300 µm	px	4		Silicate consists of more or less spherical chondrule (~150 µm) and an elongated olivine (~50 ×150 µm) fragment. Two sufide chondrules attached to the silicate. It appears like a pair of "tear-dropp-galsses". Sulfide chondrule includes small silicate grains. Sulfide is partially oidized.
M6m	PO	~400×850 µm	olv	3		A CL image shows that red luminescence in the middle of some phenocrysts. The chondrule is framed by a discontinuous sulfide rim. Spherical sulfide nodules (~150 µm and ~80 µm) occur together with silicates.
M6g	PO	~200 µm	olv	13		The core of olivine phenocrysts are Mg rich and rims are Fe-rich due to thermal alteration. The chondrule rims contain sulfide nodule.
K5e	PO	~200 ×200 µm	olv	18		dominated by olivine phynocrysts
K5i	olivine fragment	~200 ×200 µm	olv	15		Isolated olivine fragment with parallel cracks
K5m	olivine fragment	~200 ×200 µm	olv	15		Isolated olivine fragment
D9l	isolated olivine grain	~200 µm	olv	0.4	0.1	The shape of the olivine grain is not circle or ellipse and rather distorted polygon shape but not completely euhedral. The grain contains kamacite metal grains and Al-Ca-rich pyroxene (See Isa et al. 2014). A CL image shows overall red luminescence forsterite indicates lacking of FeO (less than ~ 2% FeO).
D10o	isolated olivine grain	~40 ×100 µm	olv	38		Equilibrated olivine fragment.
D10j	isolated olivine grain	~100 ×100 µm	olv	38		Equilibrated olivine fragment.
N4i	isolated olivine grain	~200 ×250 µm	px	4.2		Mg-rich pyroxene fragment.
N4u	isolated olivine grain	~150 ×150 µm	olv	40		Equilibrated olivine grain
N4s2	AOI	~100 ×200µm	olv	40	1	Includes ~50 µm or so CAI iwthin this AOI. Ca-px inclusions
K5l	sulfide nodule	~500 ×700µm	olv,px, and sulfate?	Fa(16-40)Fs(12)		Mostly consisted of sulfide, silicate and oxide. Sulfide is partially oxidized. Fine grain silicates include Al-K-rich phase.
J5i	sulfide nodule	~450 ×700µm	olv/px intergrowth	Mg-rich		Mostly consisted of sulfide and silicate. Sulfide is partially oxidized and became oxide.

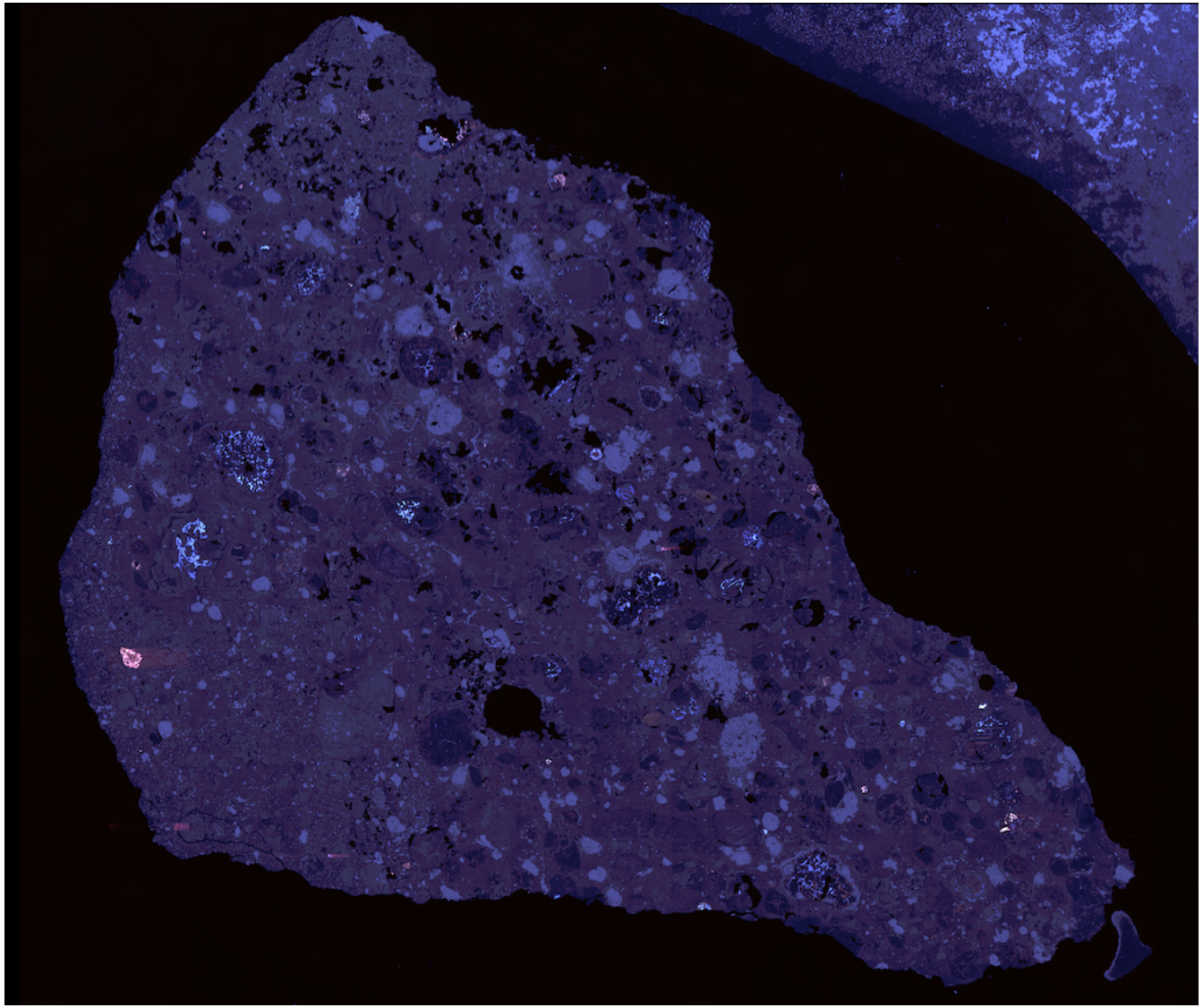

Figure A2-1. Color CL image of the thin section PRE 95404,15.

Chondrule Fragment D10t

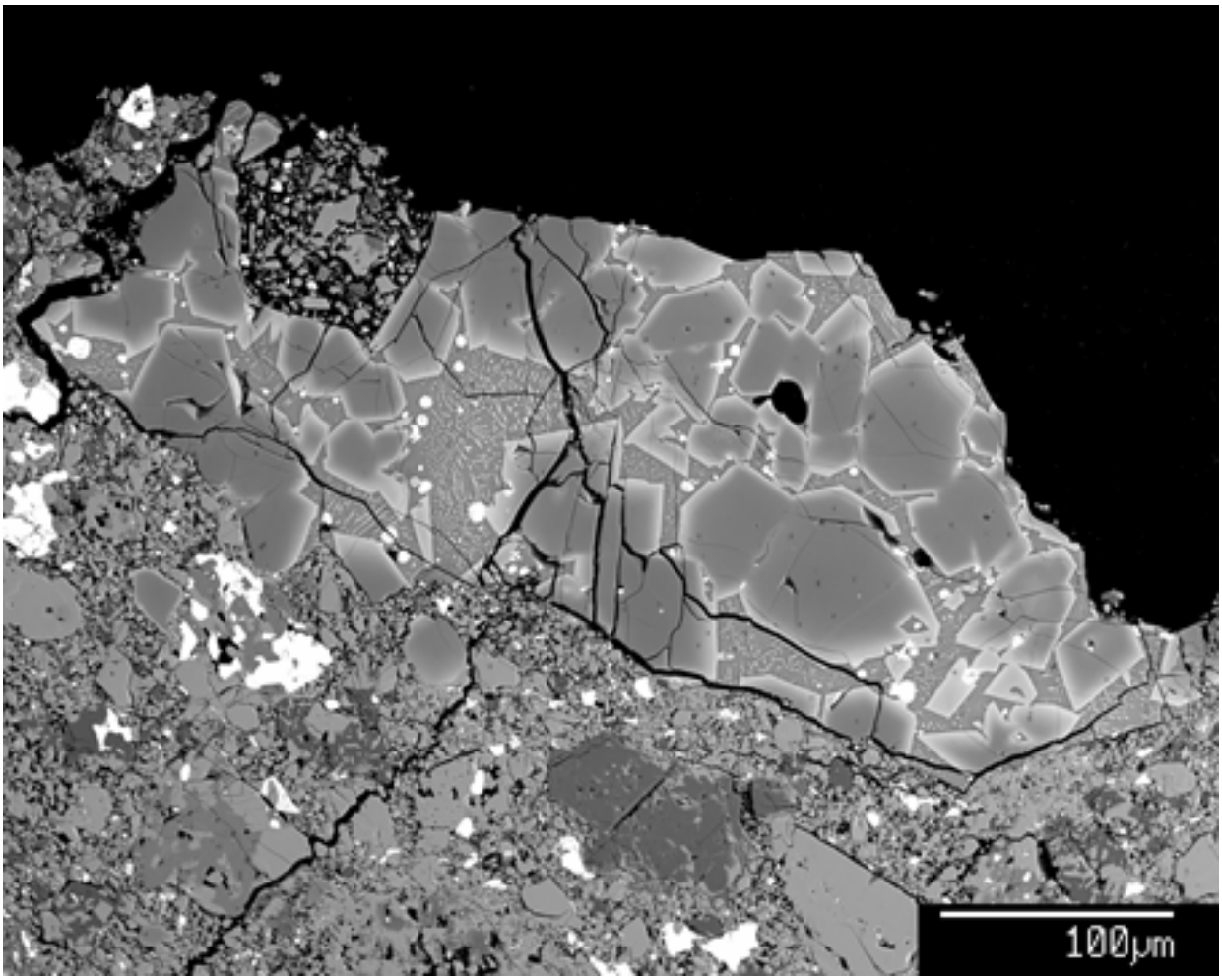

Figure A2-2. BSE image of chondrule D10t

Chondrule D10t is textural aporphyritic olivine chondrule fragment (Figure A2-2) It is characterized by presence of large euhedral olivine phenocryst (up to ~100 μm); glassy to microcrystalline mesostasis including dendritic chromite and spherical sulfides with silicate inclusions (white in Figure A2-3); and the absence of Fe-Ni metal. The edge of olivine phenocrysts contain melt inclusions with sharp boundaries.

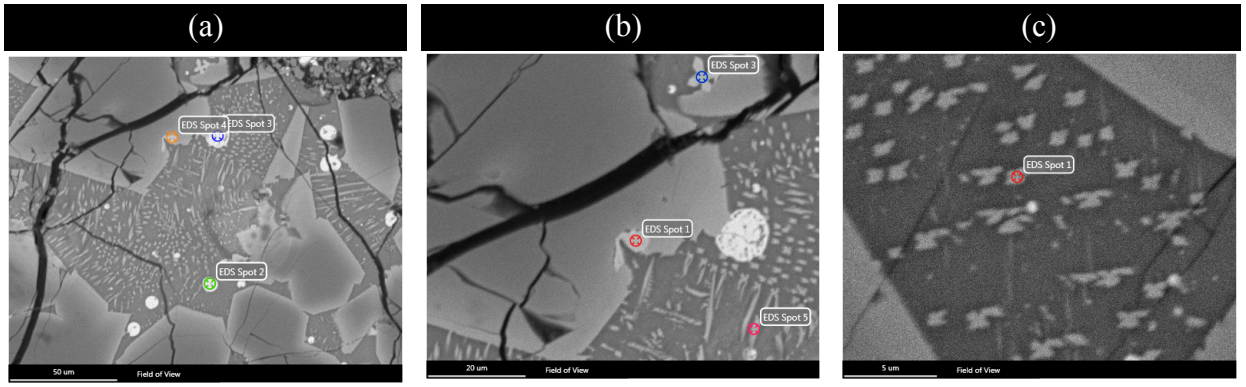

Spot 2 in Figure A2-3 (a) FeS + oxygen

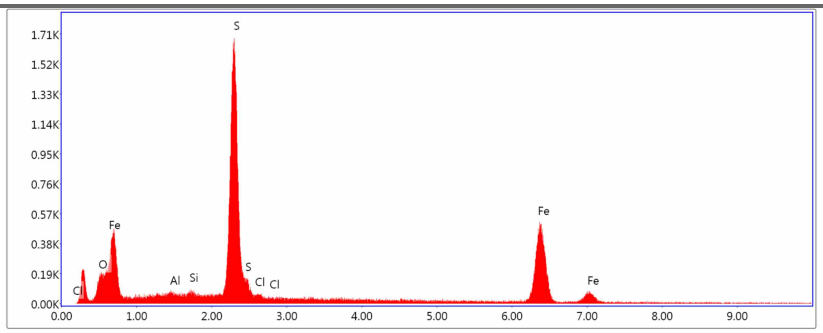

	Weight %	Atomic %	Error %
O K	5.82	14.53	12.45
AlK	0.23	0.35	63.74
SiK	0.23	0.33	61.52
S K	32.98	41.10	3.37
ClK	0.59	0.67	36.77
FeK	60.14	43.03	3.70

Spot 4 in Figure A2-3 (a) FeS + oxygen

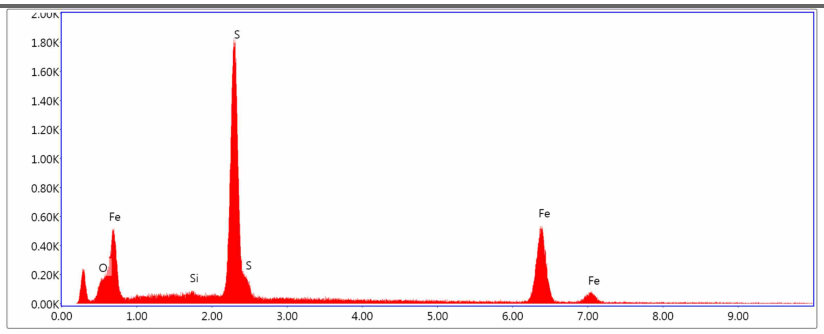

	Weight %	Atomic %	Error %
O K	4.00	10.20	14.40
SiK	0.37	0.54	44.49
S K	35.62	45.37	3.31
FeK	60.01	43.88	3.71

Spot 1 in Figure A2-3 (b) (CrFe)2O3

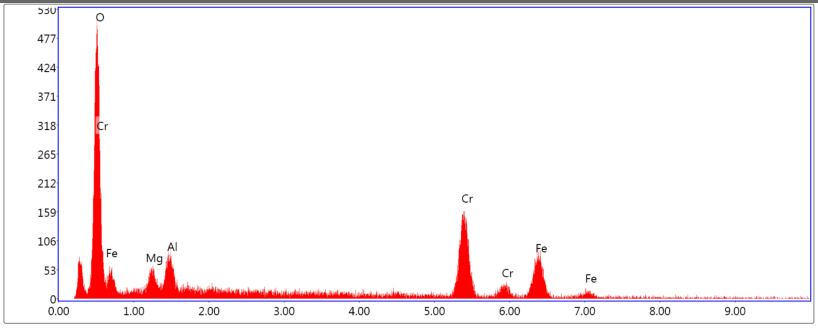

	Weight %	Atomic %	Error %
O K	29.77	56.35	5.92
MgK	2.69	3.35	16.73
AlK	3.97	4.45	12.33
CrK	34.16	19.90	5.31
FeK	29.42	15.95	7.66

Spot 3 in Figure A2-3 (b) Cr-bearing oxide and glass

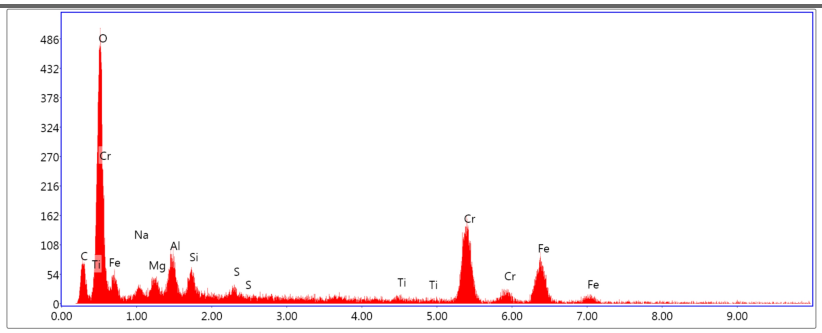

	Weight %	Atomic %	Error %
C K	16.53	30.09	12.12
O K	35.08	47.94	7.66
NaK	0.66	0.63	68.05
MgK	0.93	0.84	30.97
AlK	2.36	1.91	12.69
SiK	1.13	0.88	18.86
S K	0.30	0.20	61.22
TiK	0.31	0.14	63.60
CrK	22.87	9.62	5.90
FeK	19.83	7.76	8.51
Carbon is carbon-coating			

Spot 5 in Figure A2-3 (b) hedenbergite (CaFe2+Si2O6) + glass or esseneite

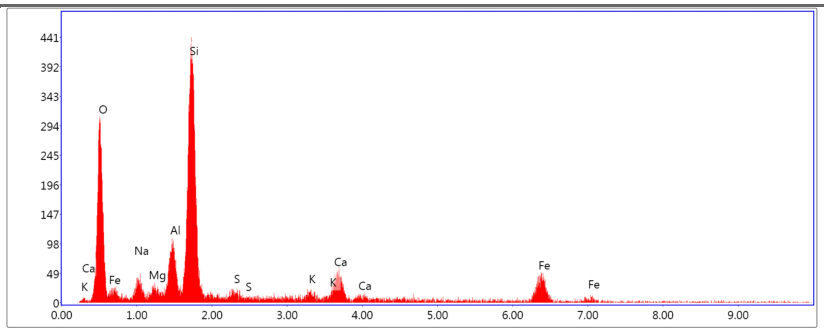

	Weight %	Atomic %	Error %
O K	41.61	60.46	8.81
NaK	1.79	1.81	35.72
MgK	0.28	0.27	70.64
AlK	4.63	3.99	9.66
SiK	25.97	21.49	4.95
S K	0.50	0.36	62.63
K K	0.83	0.49	60.02
CaK	5.94	3.45	13.04
FeK	18.45	7.68	12.64

Spot 1 in Figure A2-3 (c) plg		Weight %	Atomic %	Error %
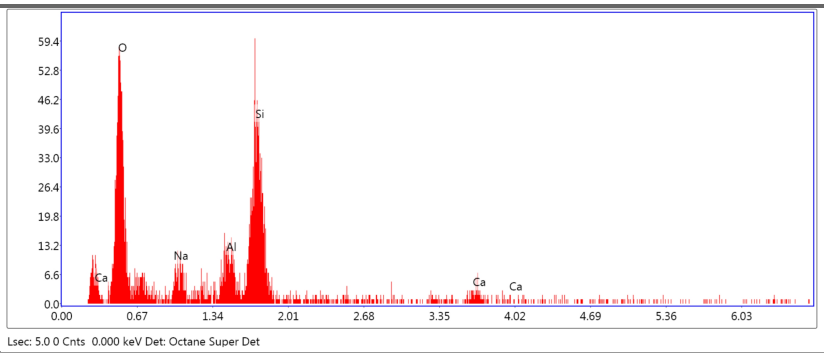	O K	50.80	64.75	10.41
	NaK	4.87	4.32	31.29
	AlK	7.53	5.69	16.32
	SiK	29.95	21.75	8.15
	CaK	6.84	3.48	48.52

Figure A2-3. BSE images and EDS spectra and results of chondrule D10t mesostasis.

Fe/Mg zoning profile shown in Figure A2-4 indicates that the edge of phenocrysts enriched in Fe (Fa value 60) and the center of olivine has moderate FeO compositions (Fa 16 to 17). The both Fe and Mg concentrations are low in chondrule mesostasis glass. These low concentrations of Fe and Mg in the mesostases indicate that the edge of the high Fa olivine is due to overgrowth on the relict olivine grains from the melt (or glass) and thus not due to the diffusions from the mesostasis glass nor fine grain matrix that surrounds the chondrule. Mesostases are mostly glass and tiny acicular high Ca pyroxene, chromite and sulfide drops occur in mesostases.

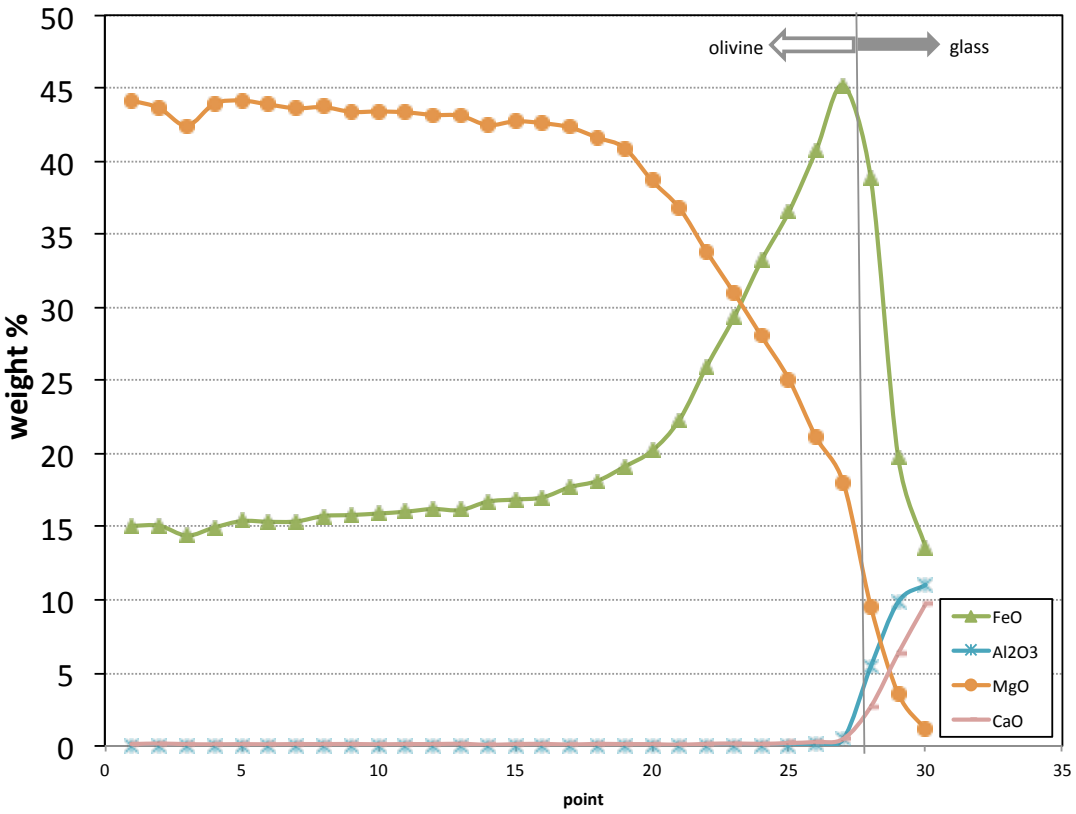

Figure A2-4. Magnified version of zoning profile of chondrule D10t olivine and mesostasis.

We carefully investigated this chondrule because an object with similar igneous texture was interpreted as a typical impact melt rock (Bischoff et al., 2011). In this study, we aim to compare the chondrule components between R chondrite and other chondrite groups. Therefore, recognizing the difference between chondrules and other chondrite components would be useful. The overall zoning profile of D10t is consistent with that of a typical type-II olivine phenocryst in LL3.00 Semarkona and LL3.3 ALH 81251 in which Fe, Cr, Mn, and Ca are flat at the core and enriched in toward the rim; CR is flat across olivine grains in ALH 81251 chondrules (Jones and Lofgren 1993). Olivine Fa values changed significantly from the core (Fa16) to the rim (Fa60). This wide range can be established with changing melt compositions with reducing melt fraction resulted from olivine crystallizing under equilibrium conditions. The Fe concentration of

this type-II olivine phenocryst (Fa60) is higher than that of type-II OC chondrules (Fa40) (Jones, 1990), but is similar to type II chondrules found in CO3.0 Yamato 81020 (Fa55) and ALH A77307 (Wasson and Rubin, 2003).

Olivine Fa values changed significantly from the core (Fa16) to the rim (Fa60). This wide range can be established with changing melt compositions with reducing melt fraction resulted from olivine crystallizing under equilibrium conditions. The Fe concentration of this type-II olivine phenocryst (Fa60) is higher than that of type-II OC chondrules (Fa40) (Jones, 1990), but is similar to type II chondrules found in CO3.0 Yamato 81020 (Fa55) and ALH A77307 (Wasson and Rubin, 2003). If they crystallized from the same elemental compositions, the final crystallization temperature of R and CO type-II chondrules were lower than that of OC; it may have involved a smaller melt fraction or it may have crystallized under disequilibrium conditions. Crystallization temperatures can be constrained with further analyses and free energy minimization calculations such as in the program MELTS. Nonetheless, we assume that the initial and final crystallization temperatures of this chondrule are similar to those of regular type-II OC chondrules because the major elemental compositions of the two chondrules are similar. Type-II chondrule initial crystallization temperatures were estimated to exceed 1700 °C (Hewins and Radomsky, 1990). When the temperature cooled from~1500°C to 1270°C (e.g., Hewins et al., 2005; Hewins and Radomsky, 1990), the amount of olivine increased until orthopyroxene crystallized at lower temperatures (Miyamoto et al., 2009). Using the temperature range and elemental zoning profile, we estimated a thermal history of this olivine phenocryst using Cr/Fe ratios.

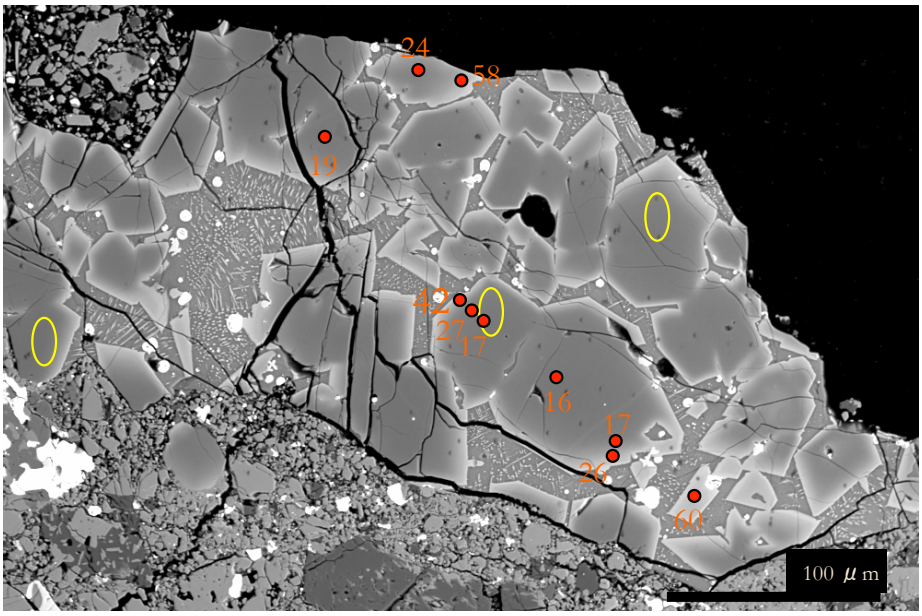

Figure A2-5. BSE image of chondrule D10t with Fa values determined with EPMA (in red values and dots) and locations of SIMS O-isotope measurements (in yellow oval).

Although the texture of chondrule-D10t looks like that of a typical type-II chondrule in CCs and OCs, there are unique aspects in this R type-II chondrule: lack of metal grains, low amount of sulfide, intermediate values in Fe/Mn ratios, higher NiO concentration and higher $\Delta^{17}O$ values. The results imply that chondrule-D10t formed under oxidized conditions.

Olivine Fa values are often used as an indicator of redox conditions of chondrites (Figure16 in Righter and Neff, 2007). Also, the low Ni abundance in olivine is attributed to reduced their formation environment in chondrule (Ruzicka et al., 2008). This is valid if oxidant is the only O and another oxidant such as S is negligible. Therefore, it may not always apply to the R chondrite chondrules, since some chondrule-forming melt saturated in S (e.g., sulfide occur in mesostases in chondrule fragment-D10t). However, in a case of chondrule-fragment D10t, small modal abundance of sulfide, absent of detectable amount of Ni in sulfide, and lack of metal grains, give some sense that it is reasonable to directly compare the Ni abundance in this chondrule and chondrule in other chondrite groups and given the same Ni abundance across the

type-II chondrules. Type-II CO chondrules oxygen fugacity is estimated log fO_2 0.5 below IW (iron-wüstite buffer) (Lofgren 1989). The formation conditions of D10t were higher than this redox condition. We attempted to constraint on oxygen fugacity by investigating Ni compatibilities in olivine. Ni becomes more incompatible with olivine with decreasing log fO_2 over the range of fO_2 from $10^{-9.4}$ to $10^{-10.3}$, (decrease from a value of 6.8 at log fO_2 = -9.4 to a value of 5.5 at log fO_2 = - 10.3, a factor of 1.2.) with no significant change between $10^{-5.5}$ and $10^{-9.4}$ (Ehlers et al., 1992). Because we did not see an apparent Mg/Ni fractionation from the core to rim of the phenocrysts, there was no significant change in Ni partitioning over the formation of this type-II chondrule. Therefore, the oxygen fugacity of formation of this chondrule-D10t did not change dramatically and this is consistent with observed Fe/Mn ratios.

The Fe/Mn ratios in igneous phases have been used for classification tools (Goodrich and Delaney, 2000; Papike et al., 2003; Warren et al., 2014) due to both elements' divalent cations having nearly identical partition coefficient values under a steady redox system and similar diffusion coefficient values in most silicate minerals. The Type-II chondrules in OC and CO chondrites have Fe/Mn ratios of ~ 44 and 99, respectively (Berlin et al., 2011). The Fe/Mg vs. Fe/Mn diagram of type-II R chondrule D10t shows a constant Fe/Mn ratio throughout the olivine phenocrysts 82 ± 11 (1SD). Considering two standard deviations of Fe/Mn ratios in equilibrated chondrites (80 ± 16 n=141 based on the data Isa et al., 2014), this constant ratio indicates that the chondrule formed under a closed system (at least in Fe and Mn) and that changes in its redox conditions were small enough to maintain constant Fe/Mn ratios. This observation implies that the formation of chondrule-D10t did not follow an extensive number of multiple melting chondrule formation model suggested in a previous study (Wasson and Rubin, 2003). We

analyzed O-isotope compositions from the olivine relict that has Fe/Mn ratios of 82, 77, and 91, which reflect melt compositions during chondrule formation.

Chromium concentrations in olivine are known to be one of the most sensitive indicators of thermal metamorphism (Grossman and Brearley, 2005), although the experimental diffusion rate of Cr^{2+} is slow (Ito and Ganguly, 2006). The chondrule D10t relict contains ~0.3 wt. % Cr_2O_3. The zoning profile of Cr showing elevated Cr compositions near the rim and a rapid decline toward the edge of the olivine grain were typically interpreted as a change of melt compositions at the end of the olivine crystallization due to chromite formation (Jones, 1990). The Fe/Cr ratios over the phenocryst are matched by a Gaussian distribution curve. The partition coefficient of Fe, Mn, Cr of olivine in chondritic melts are similar (Kennedy et al., 1993). Therefore, the elemental ratios caused by fractional crystallization are negligible under our EPMA analyses. The goodness of the Gaussian fit is high 96.6%, and this could be due to diffusion (Cr diffusing from olivine to glass). If the Cr deficiency at the edge of the olivine phenocryst is due to crystallization of chromite and perhaps also pyroxene from the melt, the Cr concentration does not necessarily fit the Gaussian curve. If this distribution is due to exsolution of Cr-rich products as seen in metamorphosed chondrules (Grossman and Brearley, 2005), the thermal alterations for this particular olivine phenocrysts are only affected at the edge of the olivine. This zoning profile is the same level with Semarkona chondrite chondrule. From these Cr abundances, it appears that this particular chondrule experienced little thermal alteration on its parent body. Since this zoning profile probably does not traverse the center of the grain as with most of chondrule studies, the diffusion time scale must be considered a lower limit of the heating duration. Using the sigma of the Gaussian fit and the diffusion coefficient of Cr, we find that the diffusion time scale is 1.3-1.7 hours and 3-10 thousand years in 1270 °C and 900 °C respectively (note: this is a

maximum as we stated above). Because O isotopes diffuse slow in olivine, it is likely that the olivine phenocrysts preserved their original O-isotope compositions. In this time scale, oxygen did not exchange between olivine and mesostasis.

Chondrule N4l

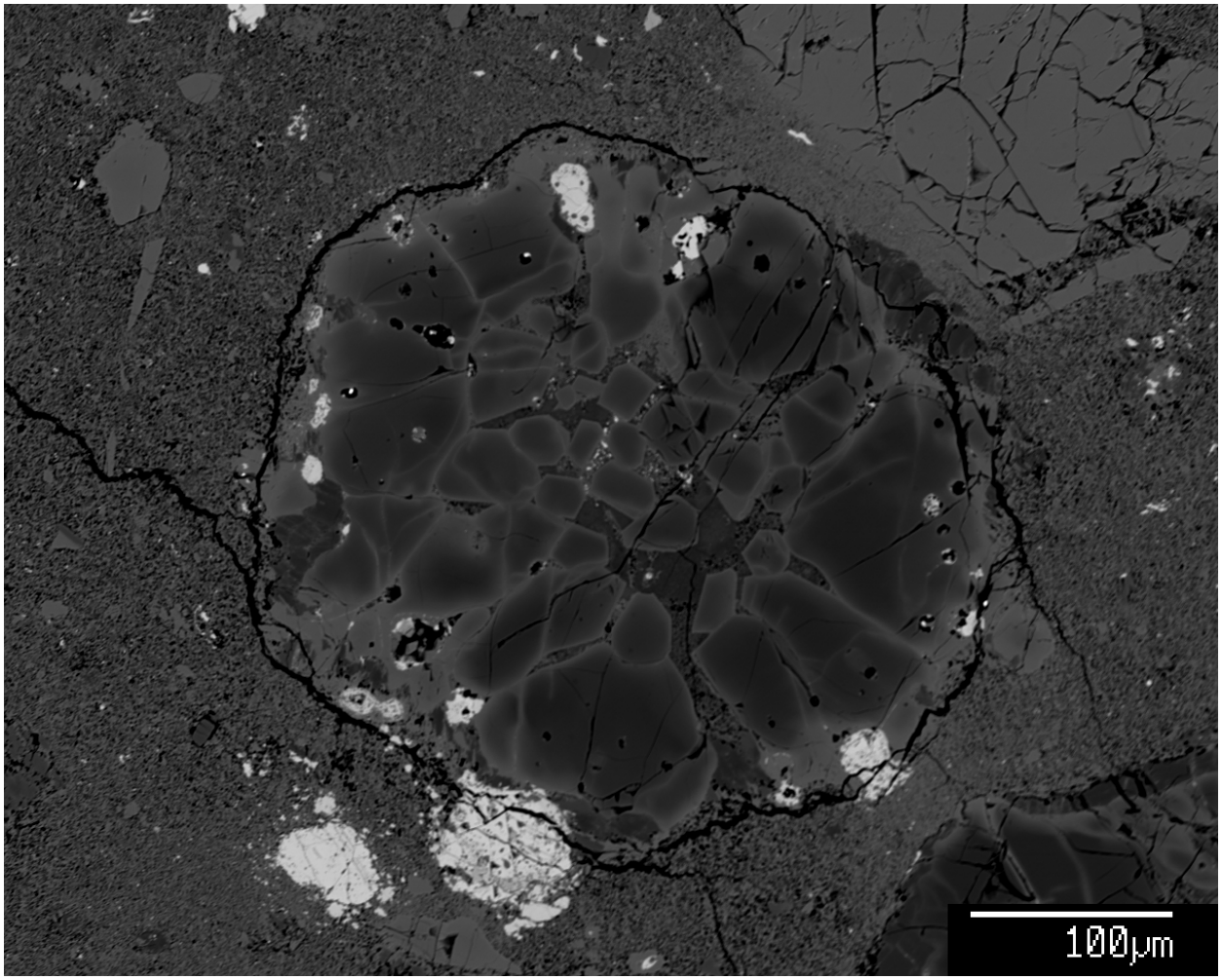

Figure A2-6. Chondrule N4l olivine phenocrysts and mesostasis.

Chondrule N4l is FeO-poor (~ 300 μm) type-I porphyritic olivine chondrule (Figure A2-6). Tiny sulfide grains occur inside and few tens μm size of sulfide nodules attached to the chondrule (white in Figure A2-6 and A2-7). The outer parts of the chondrule have higher FeO contents in contrast to the FeO-poor core. The location of high FeO contents indicates that elevated Fa values are due to parent body thermal metamorphism. The olivine phenocrysts include several compositions of inclusions submicron to tens of microns in size which compositions are sulfide,

Ca-phosphate, Al-rich oxide, chromite, silicate with plagioclase-like composition, and pyroxene (Figure A2-7).

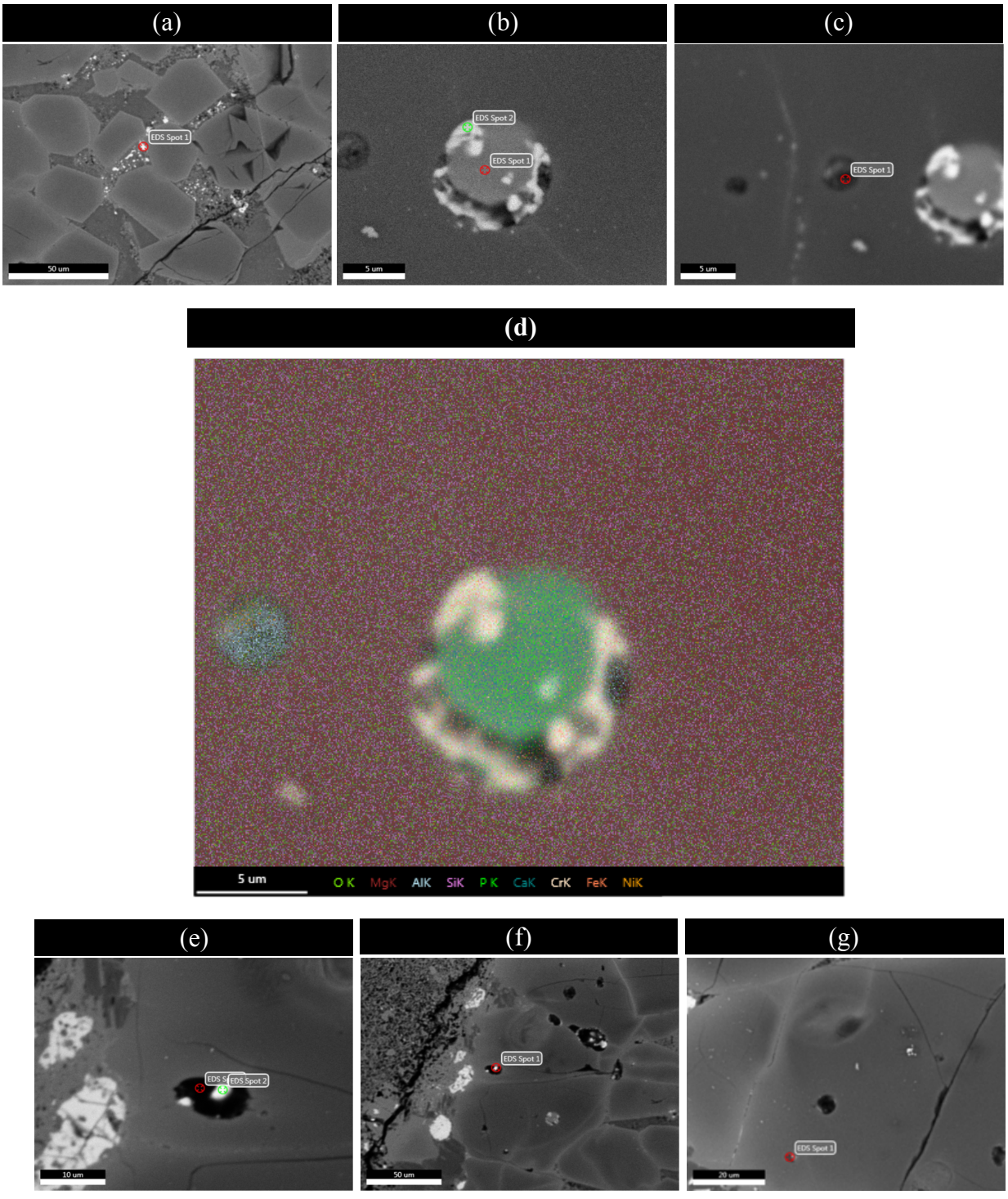

(h)

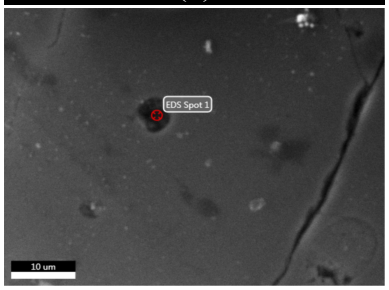

(i)

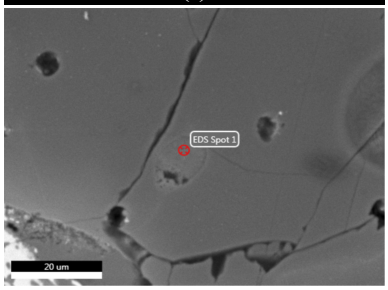

(j)

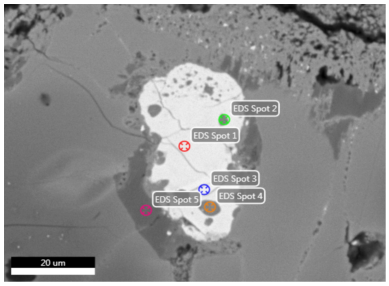

(k)

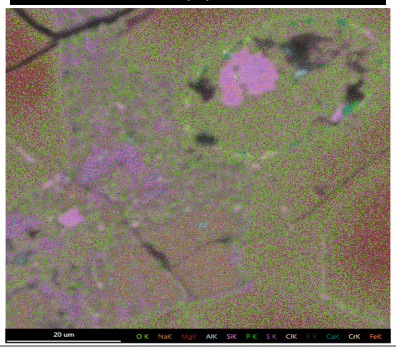

Spot 1 in Figure A2-7 (a) sulfide

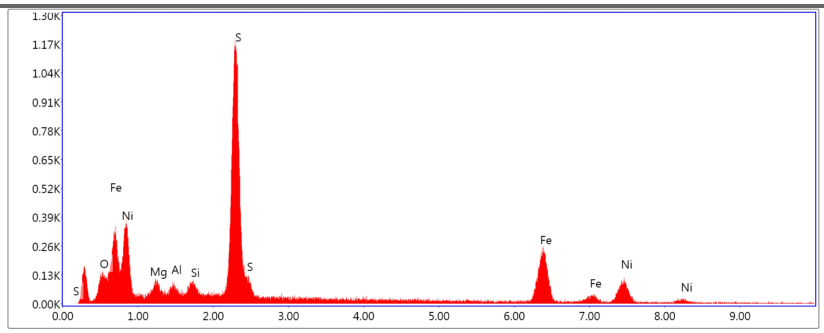

	Weight %	Atomic %	Error %
O K	5.47	13.56	13.95
MgK	2.02	3.30	15.10
AlK	1.01	1.49	19.84
SiK	1.27	1.79	16.36
S K	31.47	38.95	3.73
FeK	34.83	24.75	4.96
NiK	23.93	16.17	7.76

High oxygen concentration is likely due to interference from Fe to O.

Spot 1 in Figure A2-7 (b) Ca-phosphate

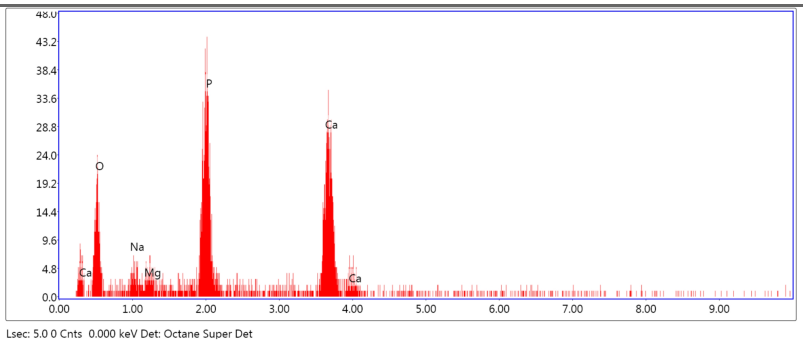

	Weight %	Atomic %	Error %
O K	39.01	58.65	17.83
NaK	2.48	2.59	72.13
MgK	1.66	1.64	69.60
AlK	0.20	0.18	83.86
P K	20.14	15.64	9.31
CaK	32.92	19.75	9.25
FeK	3.59	1.54	67.12

Spot 2 in Figure A2-7 (b) olv + chromite + Fe bearing oxide		Weight %	Atomic %	Error %
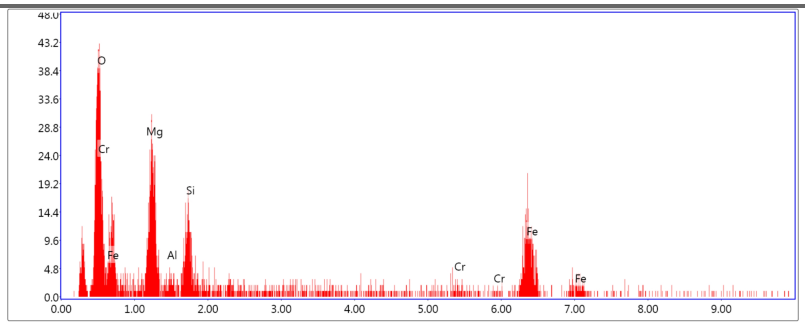	O K	29.89	51.84	10.41
	MgK	15.06	17.18	13.48
	AlK	1.03	1.06	74.78
	SiK	5.97	5.90	19.09
	CrK	3.76	2.01	51.92
	FeK	44.30	22.01	11.35

Spot 1 in Figure A2-7 (c) Ca-px + phosphate + sulfide + aluminum oxide		Weight %	Atomic %	Error %
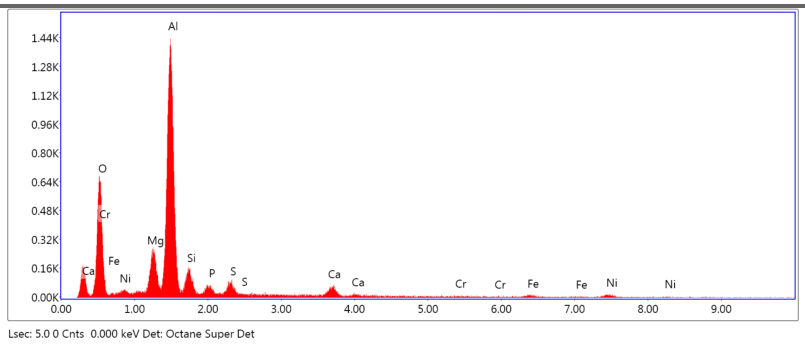	O K	38.24	53.28	7.85
	MgK	6.07	5.57	6.77
	AlK	35.95	29.70	4.40
	SiK	4.41	3.50	8.48
	P K	1.96	1.41	14.14
	S K	2.54	1.77	13.36
	CaK	3.30	1.84	15.24
	CrK	0.71	0.30	58.77
	FeK	2.19	0.88	31.06
	NiK	4.61	1.75	23.96

Spot 1 in Figure A2-7 (e) whole?		Weight %	Atomic %	Error %
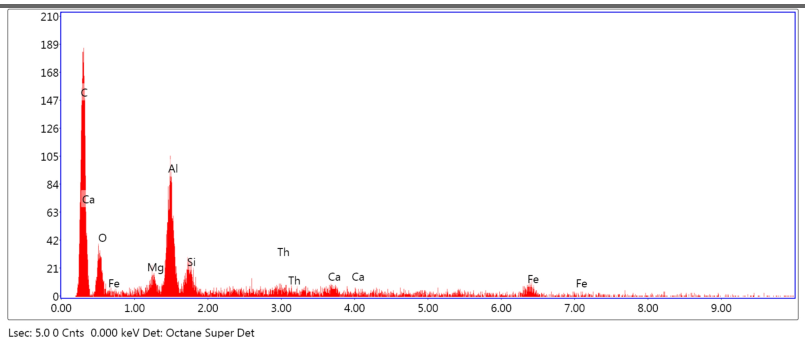	C K	67.75	80.83	9.52
	O K	13.39	11.99	16.56
	MgK	0.83	0.49	27.81
	AlK	6.63	3.52	6.63
	SiK	1.79	0.91	13.62
	ThM	1.92	0.12	49.36
	CaK	1.63	0.58	27.98
	FeK	6.06	1.56	24.87

Spot 2 in Figure A2-7 (e) olv		Weight %	Atomic %	Error %
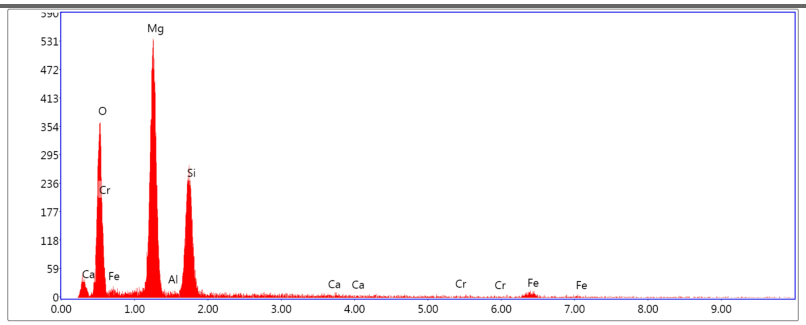	O K	41.61	54.83	7.36
	MgK	32.19	27.91	5.21
	AlK	0.37	0.29	67.25
	SiK	19.00	14.26	5.83
	CaK	0.69	0.36	60.27
	CrK	0.79	0.32	61.68
	FeK	5.35	2.02	23.88

Spot 1 in Figure A2-7 (f) whole?		Weight %	Atomic %	Error %
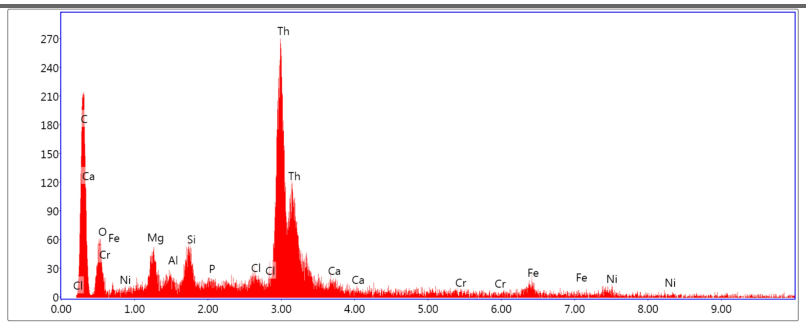				

Spot 1 in Figure A2-7 (g) whole?		Weight %	Atomic %	Error %
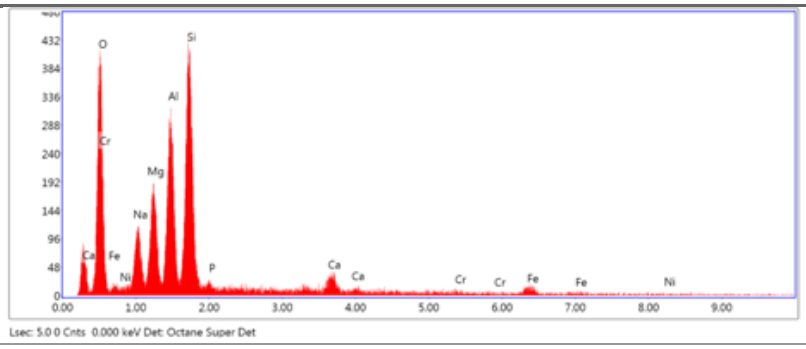	O K	39.62	53.93	8.27
	NaK	6.89	6.53	10.49
	MgK	8.20	7.35	7.82
	AlK	13.95	11.26	6.18
	SiK	20.63	16.00	5.65
	P K	0.72	0.51	46.06
	CaK	3.48	1.89	17.27
	CrK	0.96	0.40	59.88
	FeK	4.38	1.71	25.74
	NiK	1.16	0.43	61.56

Spot 1 in Figure A2-7 (h) whole?		Weight %	Atomic %	Error %
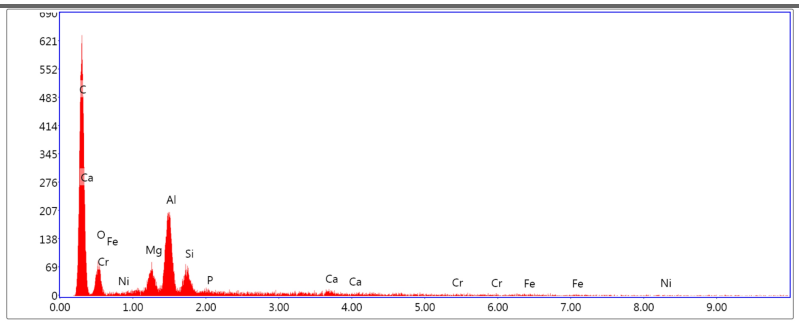	C K	76.05	84.38	7.79
	O K	12.65	10.54	14.42
	MgK	1.53	0.84	10.95
	AlK	5.67	2.80	5.16
	SiK	1.61	0.76	9.51
	P K	0.17	0.07	62.21
	CaK	0.62	0.21	39.86
	CrK	0.33	0.08	62.30
	FeK	0.83	0.20	61.19
	NiK	0.54	0.12	64.31

Spot 1 in Figure A2-7 (i) alb-an-like composition		Weight %	Atomic %	Error %
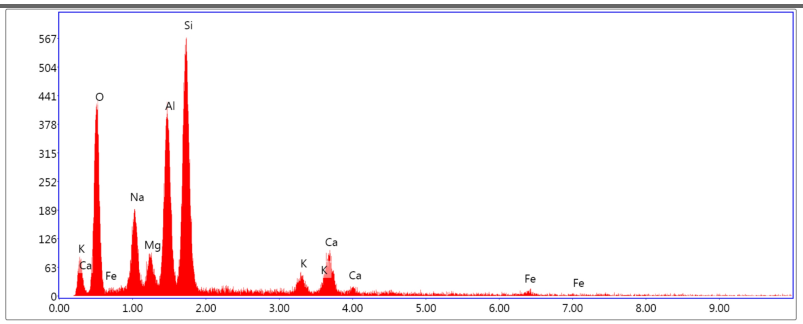	O K	40.66	54.92	8.97
	NaK	9.19	8.64	8.87
	MgK	2.75	2.44	11.29
	AlK	14.44	11.57	5.63
	SiK	21.40	16.47	5.21
	K K	2.37	1.31	15.67
	CaK	7.22	3.89	9.76
	FeK	1.98	0.77	39.19

Spot 2 in Figure A2-7 (j) Ca-phosphate		Weight %	Atomic %	Error %
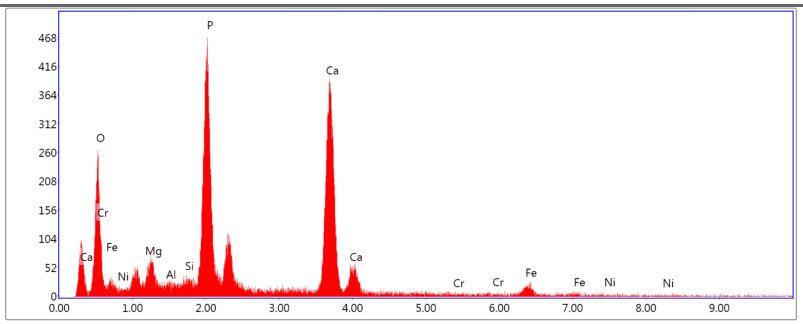	O K	38.16	58.71	11.52
	MgK	2.32	2.35	12.64
	AlK	0.20	0.18	66.76
	SiK	0.46	0.41	43.28
	P K	18.86	14.99	3.94
	CaK	33.15	20.36	3.47
	CrK	0.52	0.25	60.25
	FeK	5.25	2.31	21.52
	NiK	1.06	0.44	61.70

Spot 4 in Figure A2-7 (j) Ca-phosphate		Weight %	Atomic %	Error %
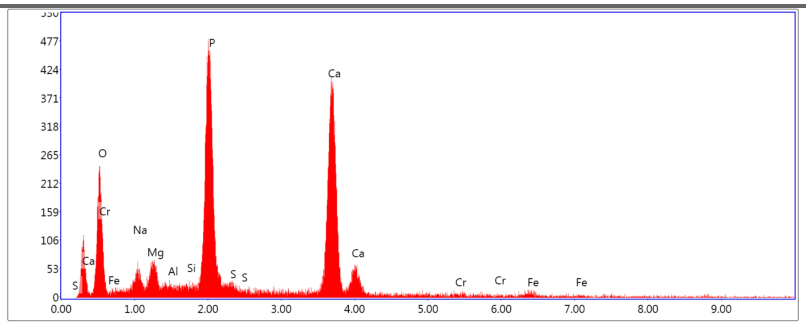	O K	37.21	56.75	11.44
	NaK	2.23	2.36	18.16
	MgK	1.95	1.96	13.38
	AlK	0.18	0.16	66.90
	SiK	0.16	0.14	68.81
	P K	20.17	15.89	3.88
	S K	0.80	0.61	28.56
	CaK	33.68	20.51	3.38
	CrK	1.10	0.52	58.76
	FeK	2.53	1.10	31.65

Spot 5 in Figure A2-7 (j) pyroxene		Weight %	Atomic %	Error %
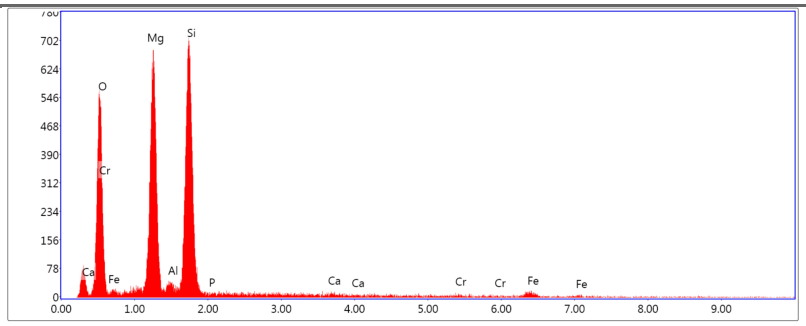	O K	41.19	54.69	7.53
	MgK	23.67	20.68	5.28
	AlK	1.34	1.05	15.77
	SiK	27.95	21.14	4.83
	P K	0.24	0.17	64.42
	CaK	0.69	0.36	54.34
	CrK	0.93	0.38	58.77
	FeK	3.99	1.52	24.50

Figure A2-7. BSE images and EDS spectra and results of chondrule N4l. The chondrule N4l contains numerous round inclusions that composition varies. This could be due to the fast growth of crystals.

CL image of N4l shows red luminescence in the middle of olivine grains and blue luminescence from mesostasis (Figure 2-8). The red luminescence forsterite is consistent with quantitative compositions majored with EPMA managements (Fa ~1).

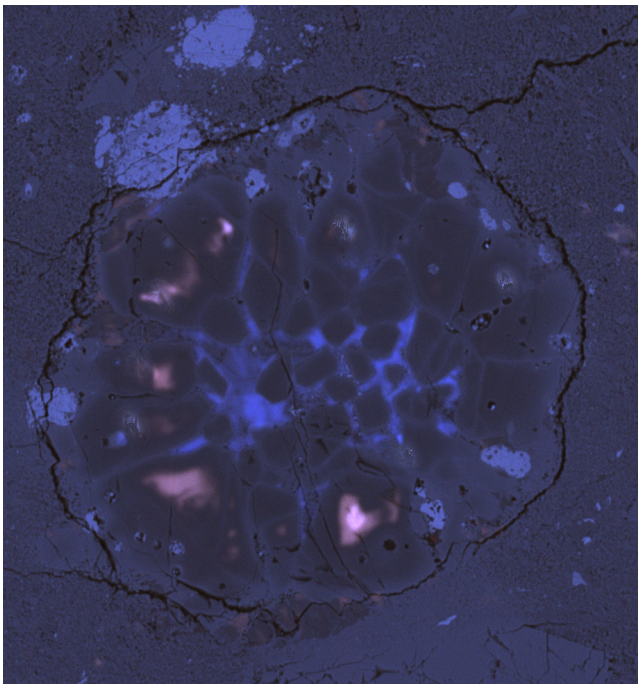

Figure A2-8. Color CL image of chondrule N4l.

Although olivine phenocrysts in chondrule N4l are not large enough to make zoning profiles, the multiple analytical points show large differences from equilibrated chondrites.

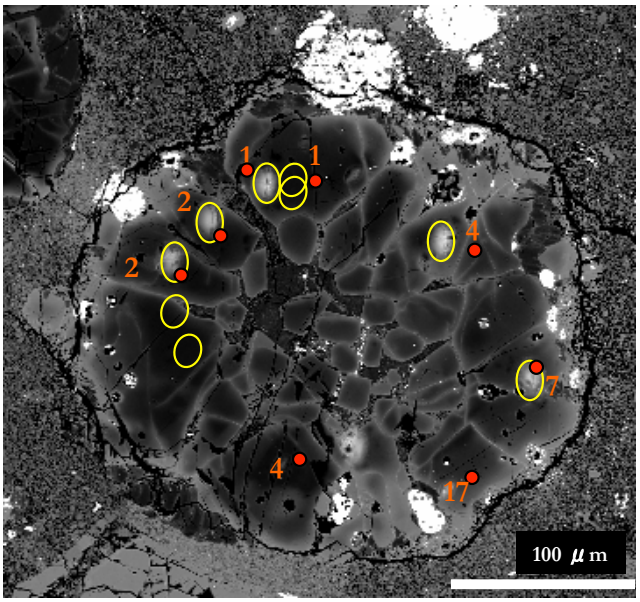

Figure A2-9. BSE image of chondrule N4l with Fa values determined with EPMA (in red values and dots) and locations of SIMS O-isotope measurements (in yellow oval).

Chondrule N4s

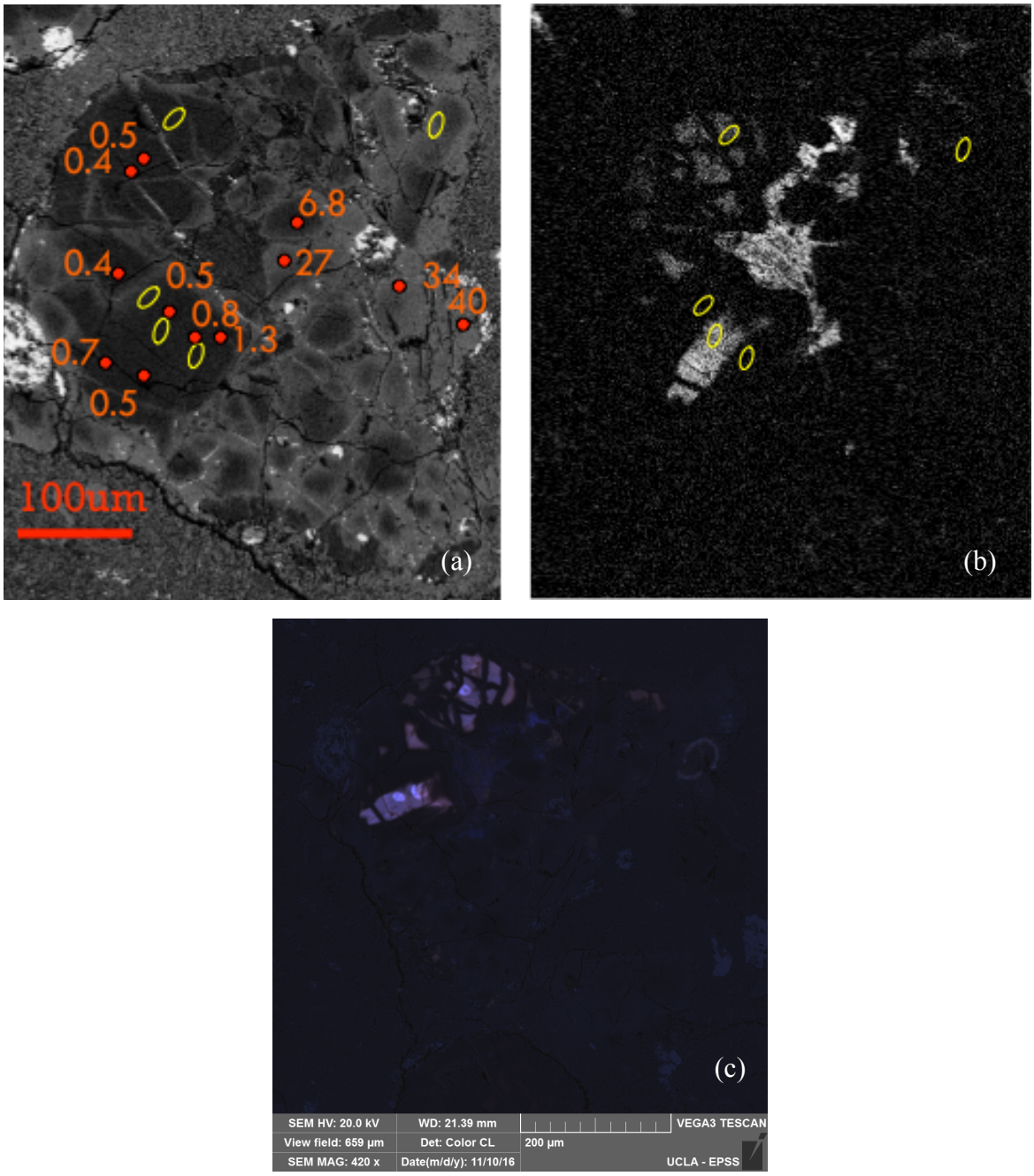

Figure A2-10. BSE image (a), mono monochrome CL image (b) and color CL image (c) of chondrule N4s. The BSE image shows the texture with Fa values determined with EPMA (in red values and dots) and locations of SIMS O-isotope measurements (in yellow oval). The both images (a) and (b) show the same location in the thin section at the same magnification. The edge of chondrules and olivine phenocrysts are metamorphosed and shown in lighter gray in the image (a). The mesostases are also recrystallized and CL luminescence (b). However, olivine cores in several phenocrysts show blue luminescence in color CL (c). These are likely relict olivine grains.

N4s is Mg-rich (~ 300 μm) Type-I porphyritic olivine chondrule (Figure A2-10). A part of chondrule is broken into olivine fragments. Tiny sulfide grains and sulfide veins occur inside of the chondrule and ~60-100 μm size of sulfide nodules are attached to the outside of the chondrule (Figure A2-10). Some of the olivine phenocrysts show blue and red luminescence in a CL image. Edge of olivine phenocrysts altered form original chemical compositions showing Fe zoning (see BSE image A2-10) and high FeO contents that are close to equilibrated R (Fa value 38). Mesostases are mostly recrystallized.

The boundaries of CL active areas are sharp, and the CL-active core is rimmed by CL-active forsterite in chondrule N4s. Zoning of CL-emission was not observed in contrast to previous refractory forsterite study in DAG 013 (Pack et al., 2004).

Blue CL luminescence normally indicates Si-O bonding distortion in silicate crystals. Although chemical compositions of CL blue luminescence are approximately up to 0.5 wt. % Al which composition is not sufficient enough to call this chondrule as an Al-rich chondrule, the blue luminescent is likely due to distortion of tetrahedral silicate due to Al substation. These CL-luminesce relict grains are all nearly pure forsterite and parent body alterations effects are small.

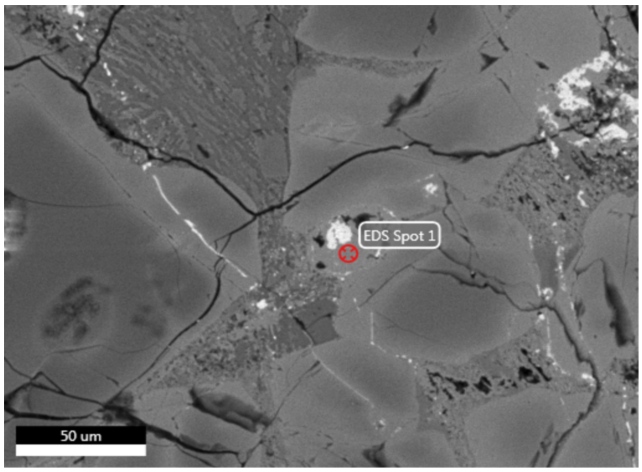

Spot 1 in Figure A2-11 Fe-rich olivine		Weight %	Atomic %	Error %
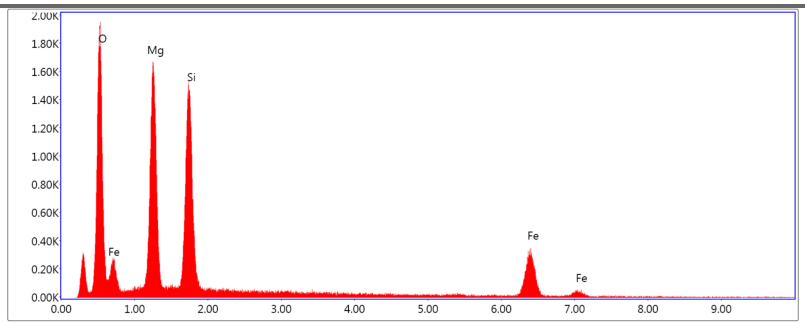	O K	36.07	53.89	6.30
	MgK	20.19	19.85	6.17
	SiK	17.85	15.19	4.97
	FeK	25.89	11.08	4.53

Figure A2-11. BSE image and EDS spectra of chondrule N4s. There is a round object near the center of chondrule N4s. Light gray area in the BSE image is sulfide. The EDS results show that the round inclusion has equilibrated olivine compositions.

Olivine Fragment N4s2

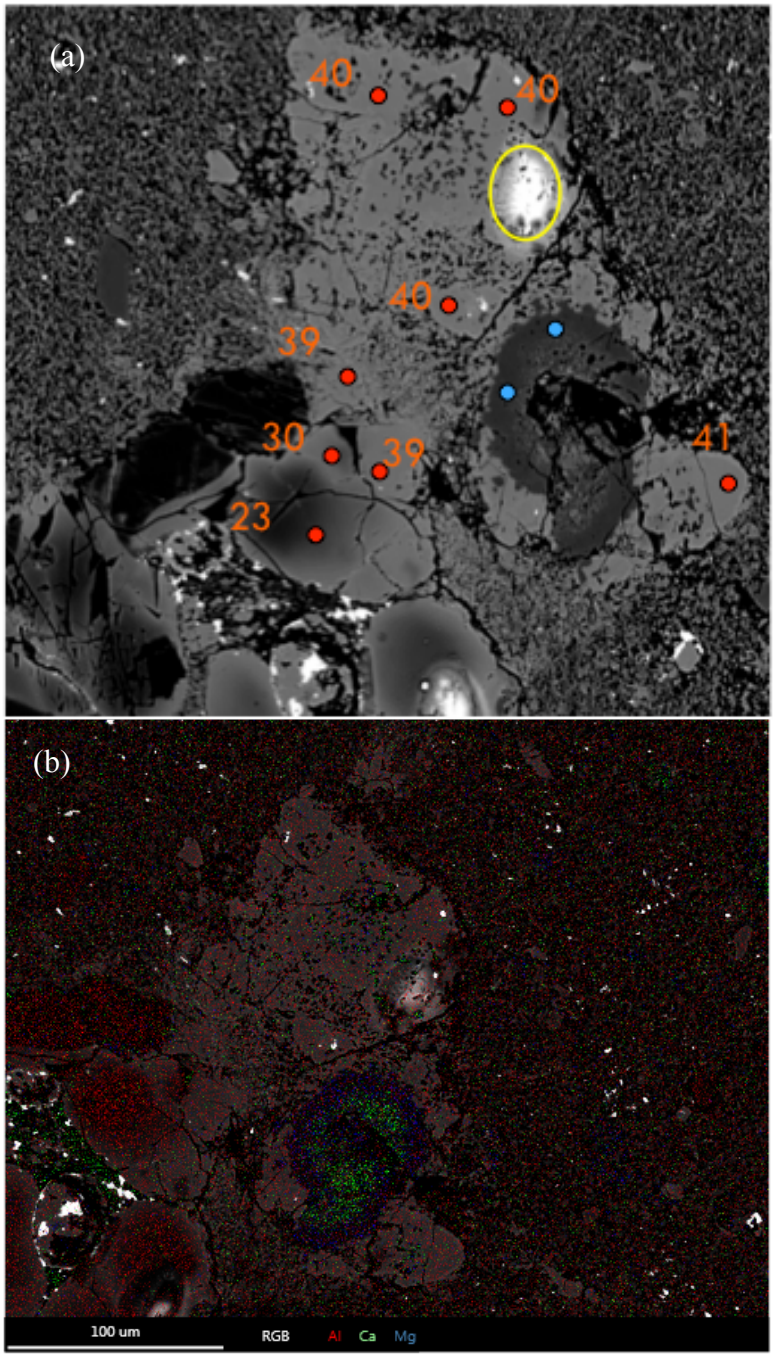

Figure A2-12. BSE image (panel a) and EDS elemental map (panel b) of olivine fragment N4s2. The BSE image shows the texture with Fa values determined with EPMA (in red values and dots) and locations of SIMS O-isotope measurements (yellow ovals). The dark gray areas inside of olivine N4s2 (a) are CAIs. The Ca and Al-rich compositions can be seen in (b). The blue dots in (a) indicate measurement spots of assayed via EPMA in the CAI. The compositions are listed in Table A-1.

Olivine fragment N4s2 has high Fe concentrations containing Al-Ca-rich grains inside of almost equilibrated olivine. We analyzed oxygen isotope compositions of this olivine fragment and the oxygen isotope compositions of the olivine (including minor pyroxene) show significant low $\Delta^{17}O$ values. This spot covers mostly chemically equilibrated olivine but also includes tiny (less than ~3 µm) Ca-Al inclusions which are likely CAIs and the O-isotopic compositions of the spot, thus, represents mixing of pyroxene and olivine.

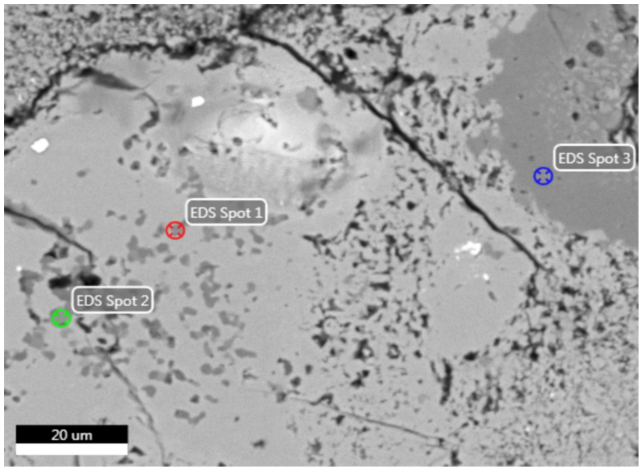

Spot 1 in Figure A2-13 Ca-pyroxene		Weight %	Atomic %	Error %
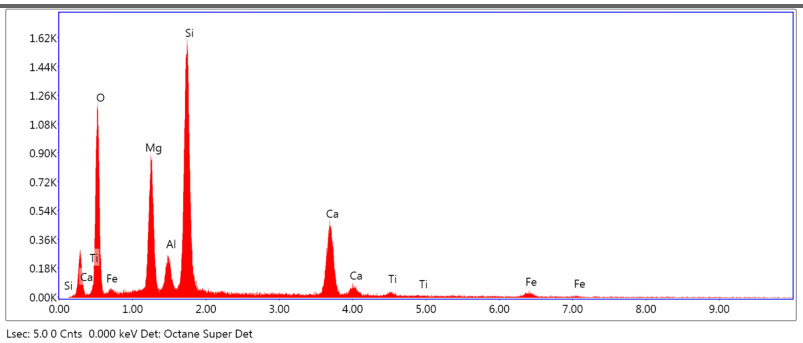	O K	45.43	61.11	8.79
	FeL	1.74	0.67	35.11
	MgK	11.17	9.89	5.70
	AlK	3.20	2.55	7.62
	SiK	22.50	17.24	4.09
	CaK	15.53	8.34	3.97
	TiK	0.43	0.19	59.97

Spot 2 in Figure A2-13 Ca-pyroxene		Weight %	Atomic %	Error %
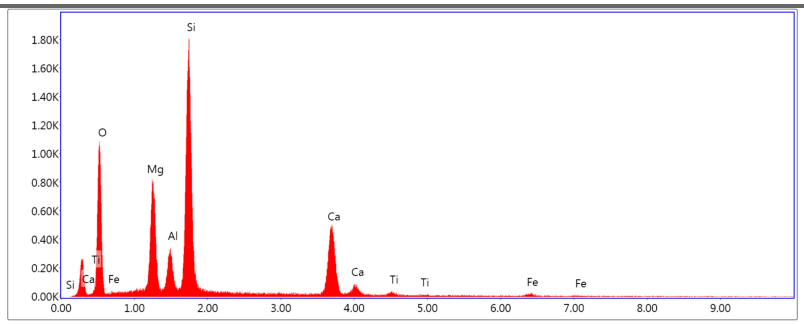	O K	42.57	58.48	9.06
	MgK	10.46	9.46	5.67
	AlK	4.00	3.26	6.77
	SiK	23.69	18.54	4.06
	CaK	17.00	9.32	3.64
	TiK	0.86	0.40	29.83
	FeK	1.41	0.55	34.85

Spot 3 in Figure A2-13 Ca-pyroxene		Weight %	Atomic %	Error %
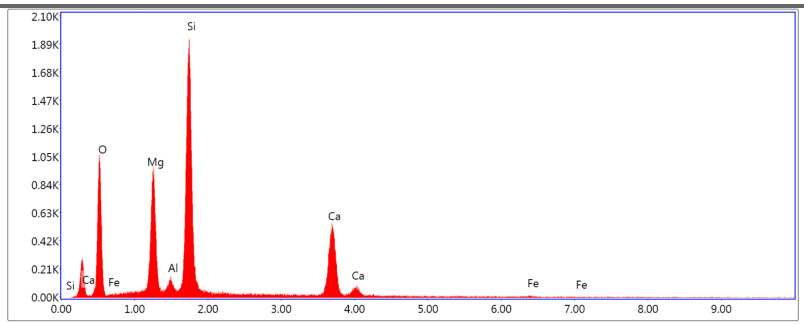	O K	41.96	57.67	9.15
	MgK	11.98	10.83	5.53
	AlK	1.39	1.13	10.37
	SiK	25.42	19.90	3.89
	CaK	18.63	10.22	3.47
	FeK	0.62	0.24	59.79

Figure A2-13. BSE image and EDS spectra results of chondrule N4s2. The tiny inclusions inside of the olivine fragment are Ca-pyroxene. The CAI compositions are confirmed as Ca-pyroxene.

Sulfide nodule K5l

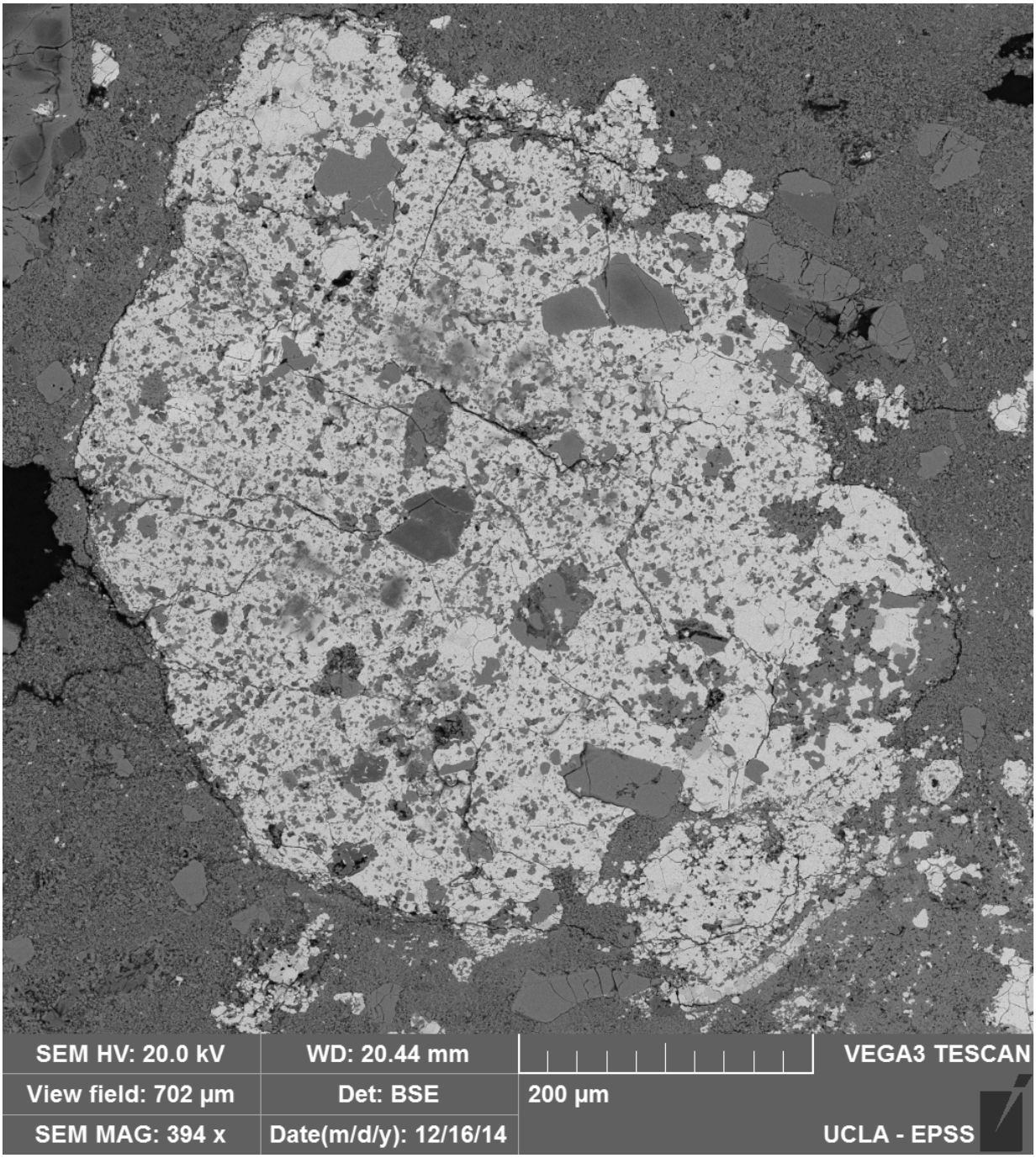

Figure A2-14. BSE image of sulfide nodule K5l. Silicate fragments and opaque oxides are included in the sulfide nodule. Sulfide is partially oxidized.

Opaque nodule K5l is mostly consisted of sulfide, silicate and oxide. Sulfide is partially oxidized (Figure A2-14). This may be due to parent body aqueous alteration or terrestrial weathering.

Large silicate fragments are relatively angular. Fine grain silicates include Al-K-rich phase (Figure A2-15).

(a)

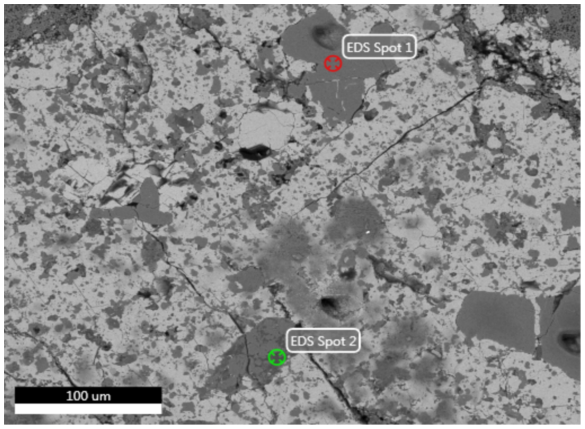

(c)

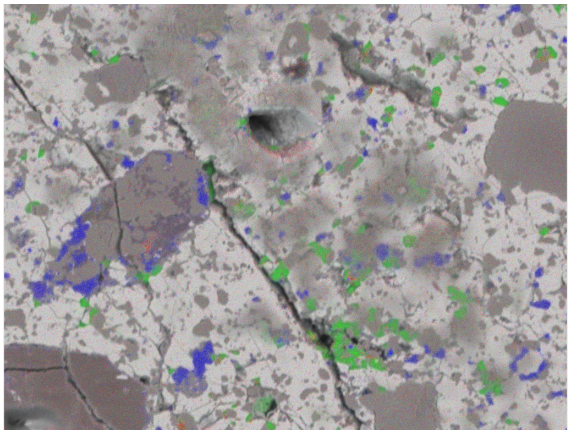

Na (red), K (green) and Al (blue)

(b)

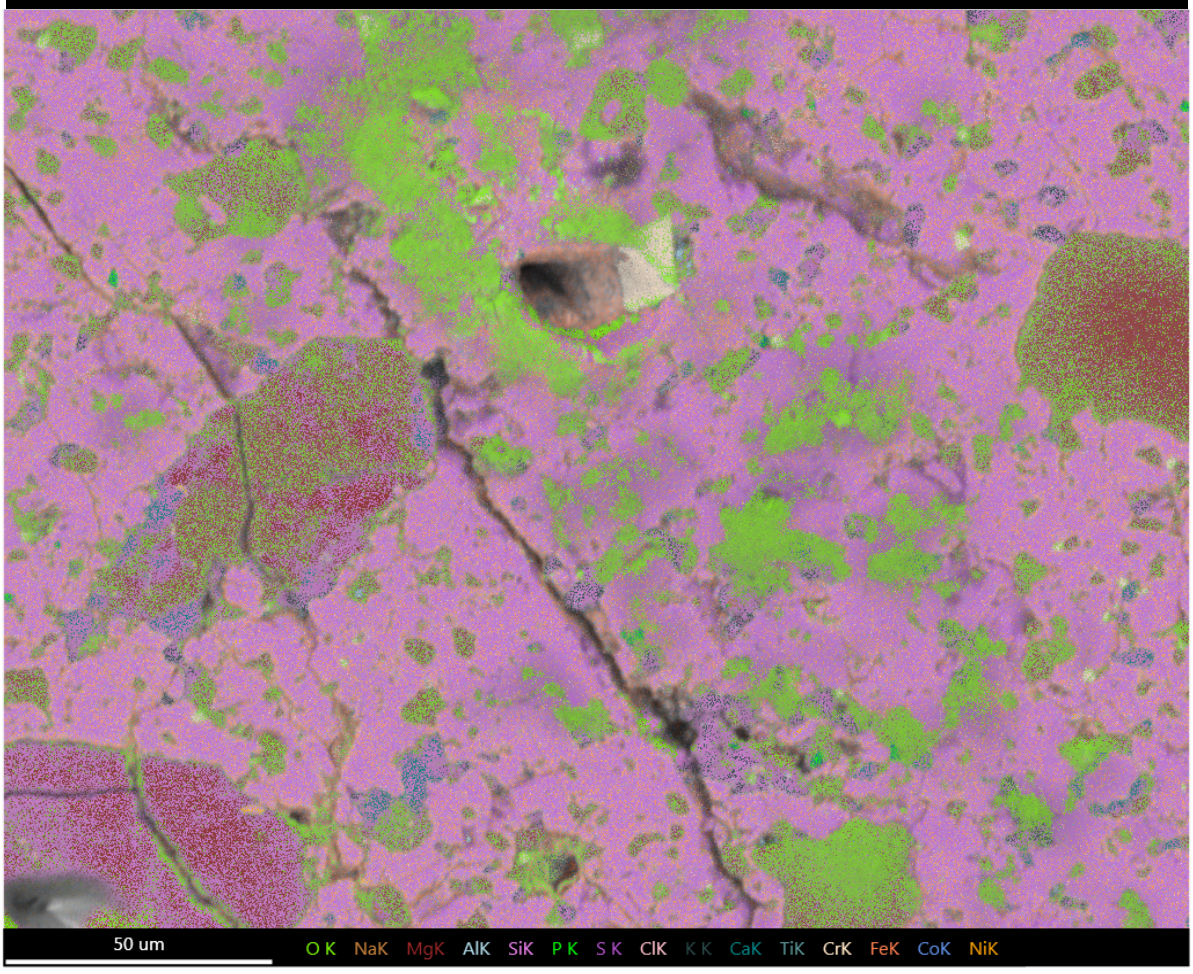

Spot 1 in Figure A2-14 (a) olivine		Weight %	Atomic %	Error %
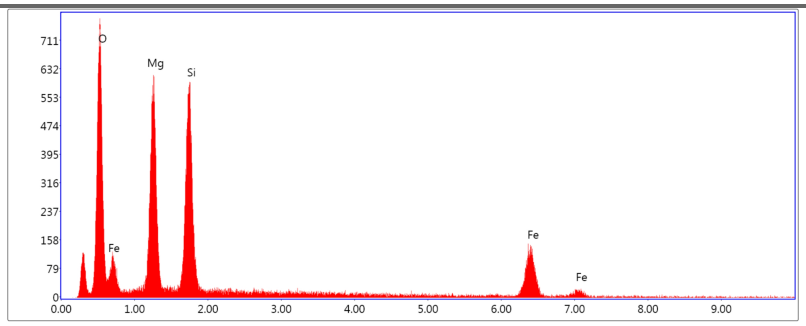	O K	35.83	54.17	6.70
	MgK	18.78	18.69	6.79
	SiK	17.47	15.05	5.55
	FeK	27.92	12.09	5.45

Spot 2 in Figure A2-14 (a) pyroxene		Weight %	Atomic %	Error %
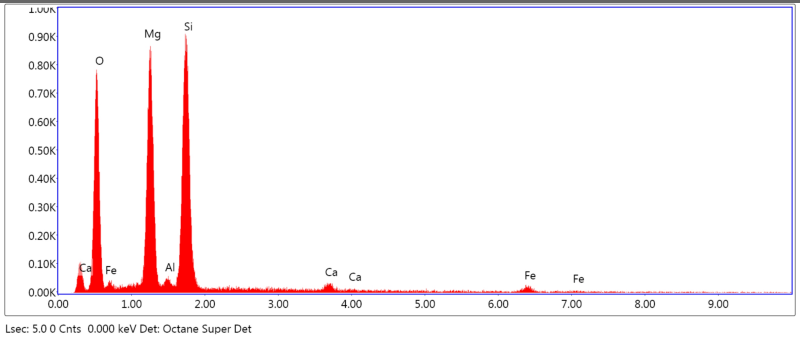	O K	43.51	56.94	7.36
	MgK	22.76	19.61	5.08
	AlK	0.95	0.74	17.31
	SiK	27.47	20.48	4.57
	CaK	1.68	0.88	20.74
	FeK	3.64	1.36	23.03

Figure A2-15. BSE image and EDS spectrum of sulfide nodule K5l. The light pink area is sulfide and altered phase is shown in light green in (b). The phase is not well identified. Silicate in this nodule includes Al-rich perhaps feldspar (c). K-rich phase is not well identified.

Olivine Fragment D9l

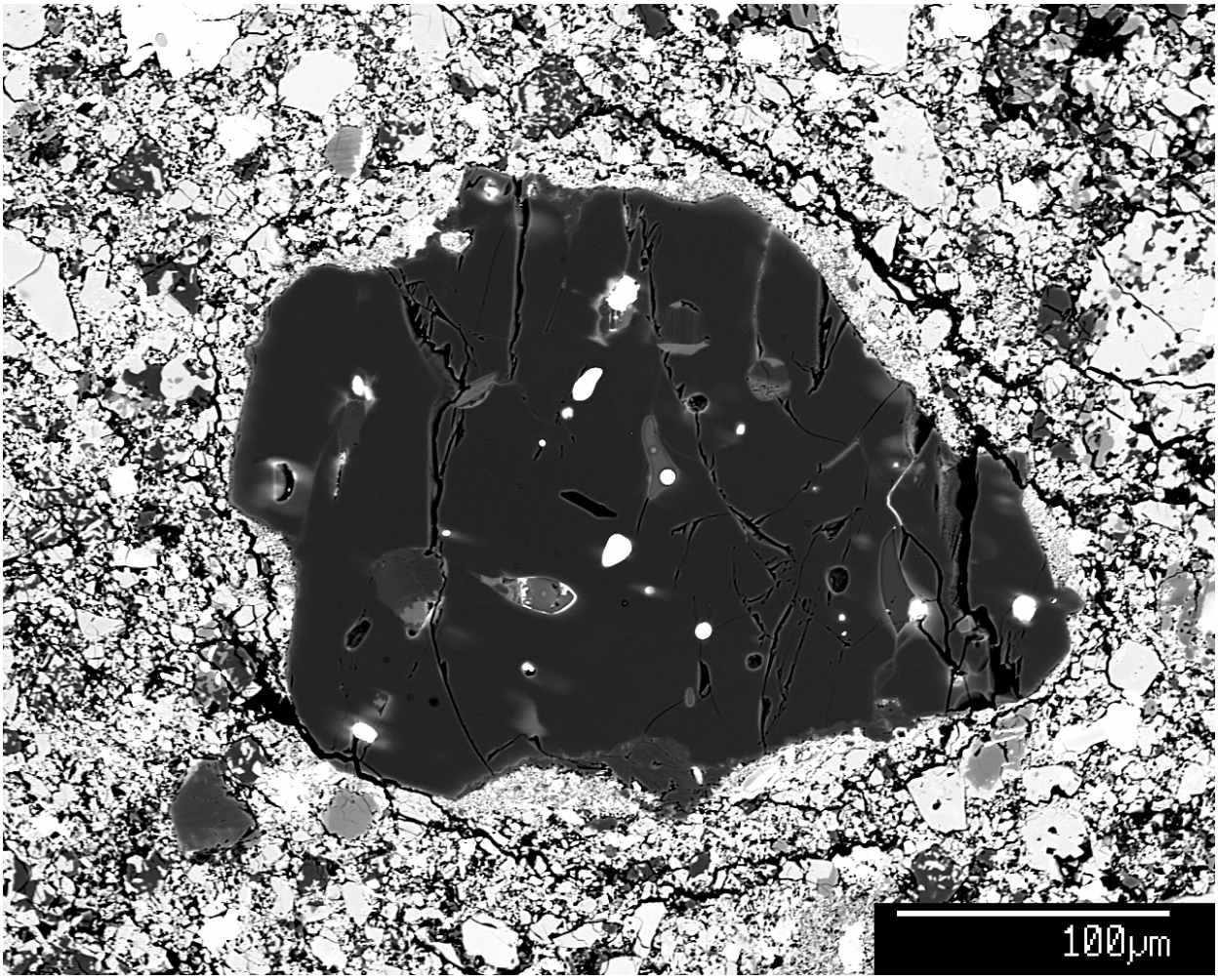

Figure A2-16. BSE image of olivine fragment D9l.

D9l is distinctively (~200µm) large isolated olivine grain. The shape of the olivine grain is not circle or ellipse and rather distorted polygon shape but not completely euhedral. The grain contains kamacite metal grains and Al-Ca-rich pyroxene (See Isa et al., 2014). Although this grain has slightly altered edge and near kamacite showing Fe zoning, the most of olivine composition are similar to a typical Type-I porphyritic olivine phenocrysts in other chondrite groups. This composition was confirmed by a CL image, which shows overall red luminescence forsterite indicates lacking of FeO (less than ~ 2% FeO). As we seen in the compositional zoning

profile, olivine at the edge of the grain and near kamacite grains do not show luminescence and these are due to low degree of thermal alteration. Occurrence of Al-Ca-rich inclusions and implies association with CAIs (e.g., refractory relict grains in Type-I chondrules). CL image indicates lower illumination in the center and the higher illumination at the edge of the grain. This is also likely indicates relict grain boundary.

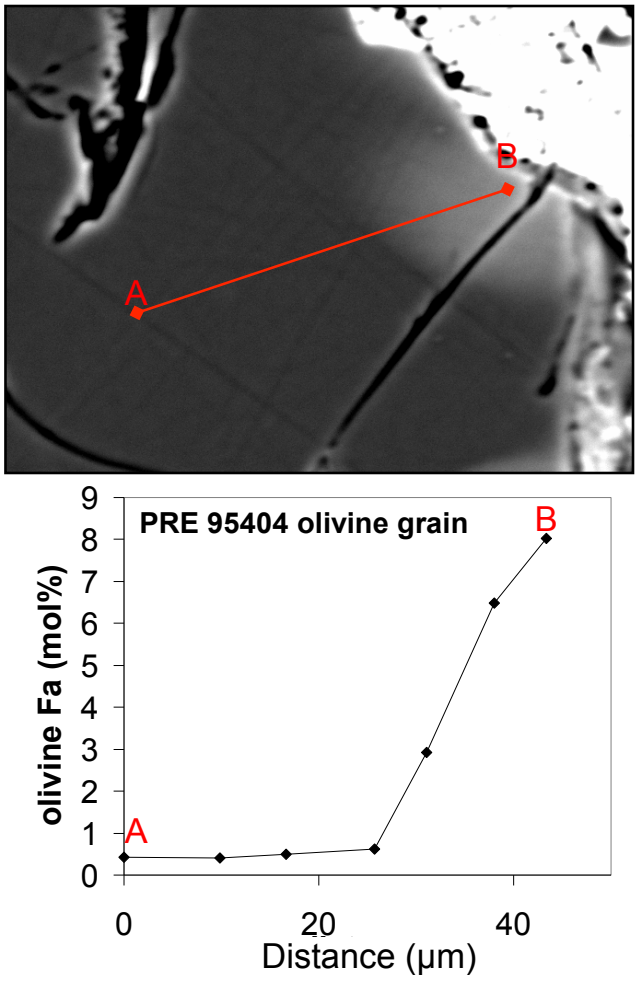

Figure A2-17. BSE image of olivine fragment D9l (upper plot) and its Fa zoning profile (lower plot). This part of the olivine had the most Fe-Mg exchange between this fragment and surrounded matrix. The rest of olivine is nearly pure forsterite.

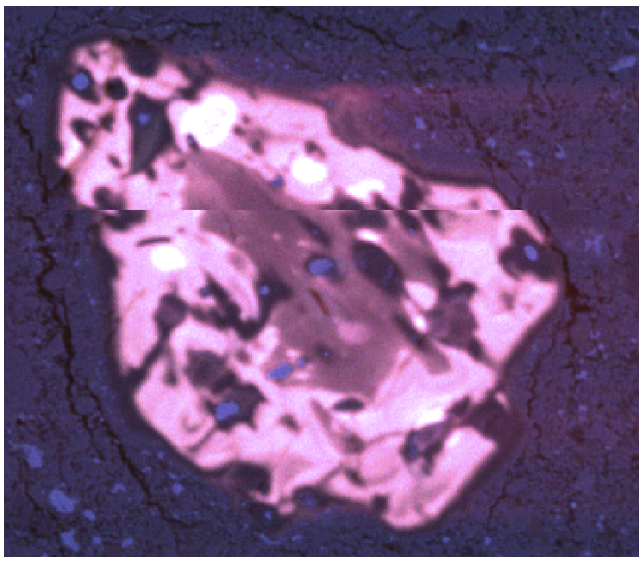

Figure A2-18. Color CL image of olivine fragment D9l. The bright white areas are SIMS spots. The strong red CL luminescence is due to lack of FeO in this forsterite grain. Near the kamacite grains (blue with no luminescence) do not show the red luminescence. This is due to Fe diffusion from metal grains to olivine. Interior of olivine fragment D9l show low red-luminescence and this perhaps due to overgrowth of forsterites. Note that two images are stitched.

Sulfide Nodule J5i

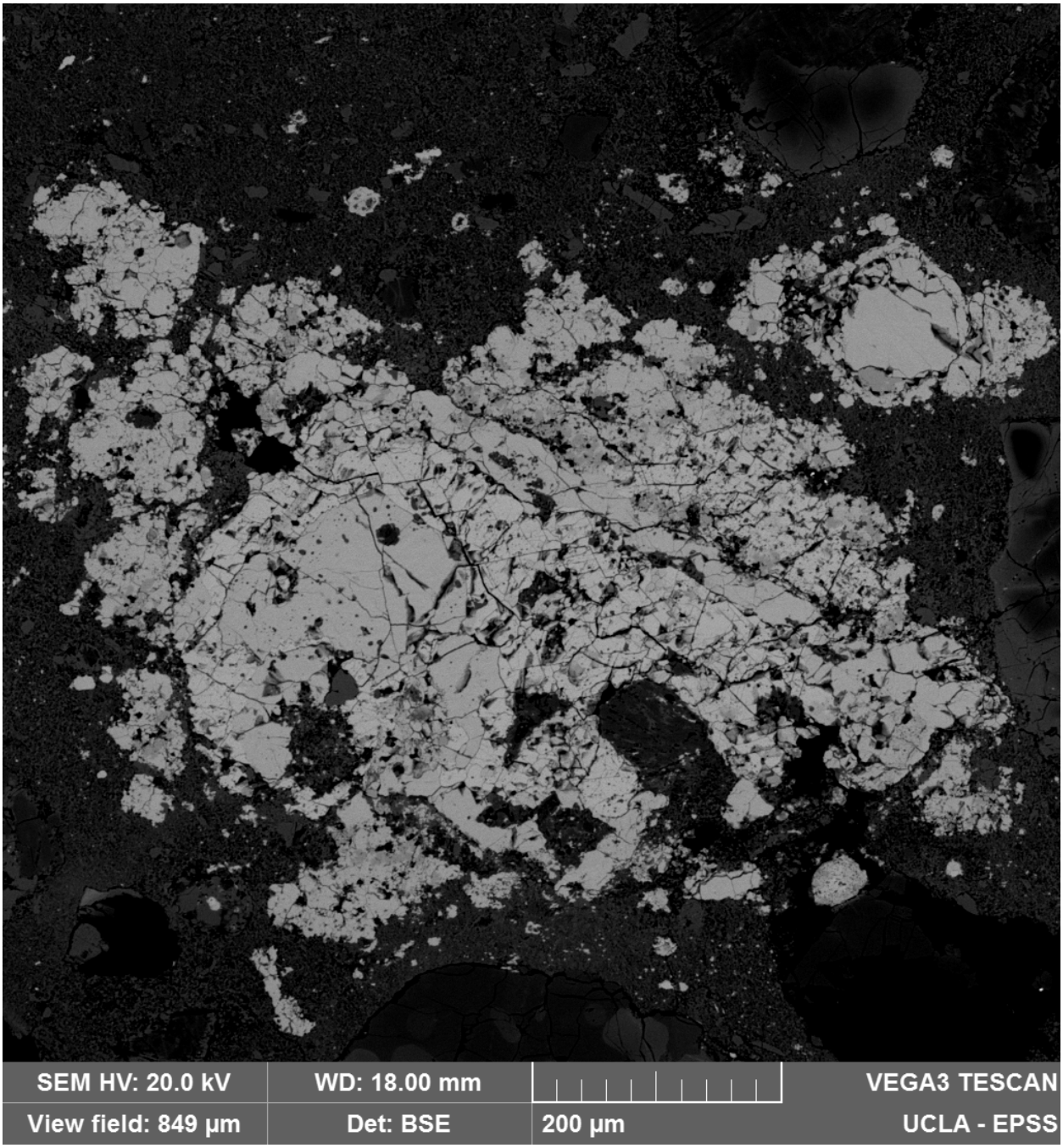

Figure A2-19. BSE image and of sulfide nodule J5i. Silicate fragments and opaque oxides are included in the sulfide nodule. Sulfide is partially replaced as oxide and this is likely due to the parent body alteration. The sulfides are composed of Ni-rich and Ni-poor sulfides.

Sulfide nodule J5i is mostly consisted of sulfide and silicate. Sulfide is partially oxidized and became magnetite (Figure A2-18). This is due to parent body aqueous/thermal alteration.

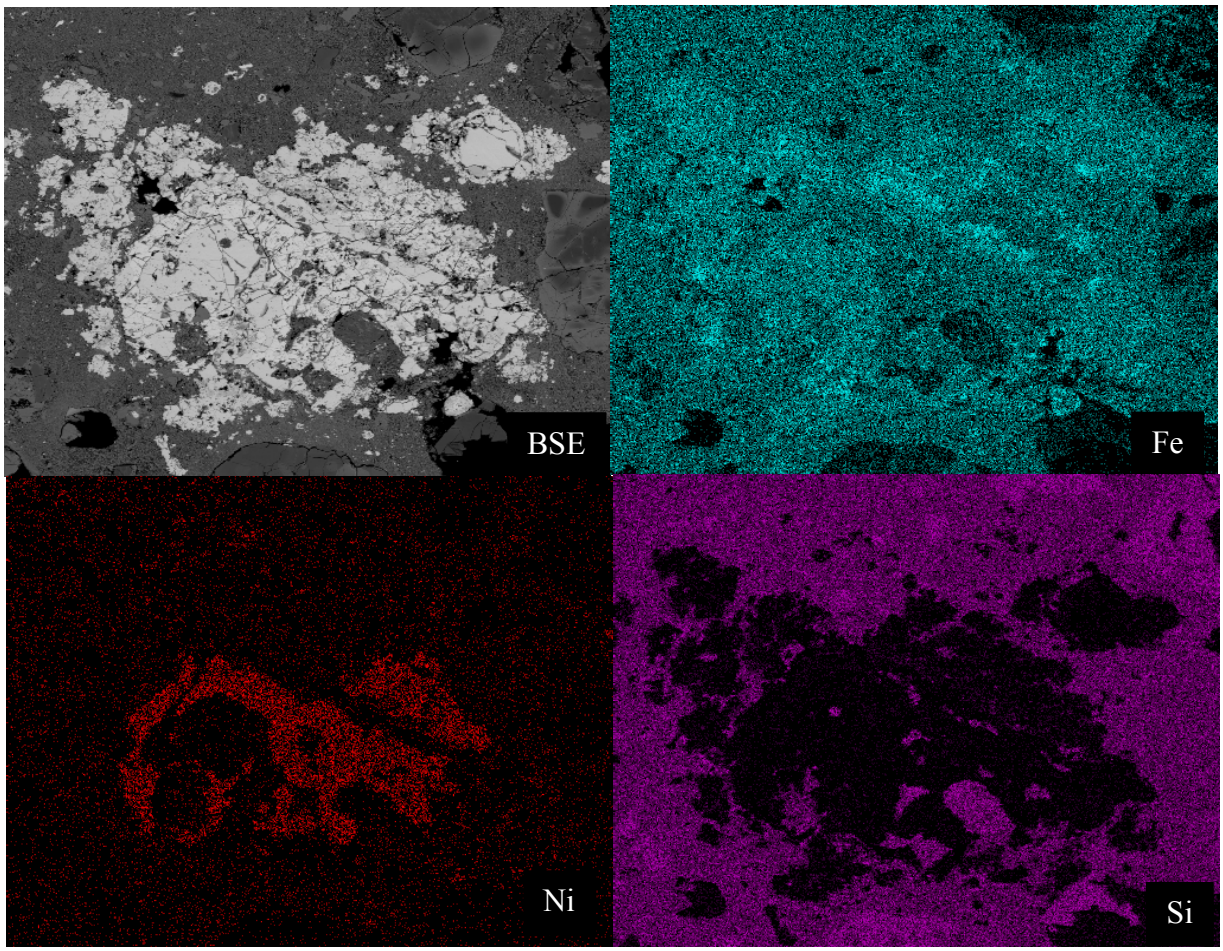

Figure A2-20. BSE image and EDS element maps of sulfide nodule J5i. A structure of this sulfide nodule can be seen well in Ni and Si maps.

Chondrule J5w

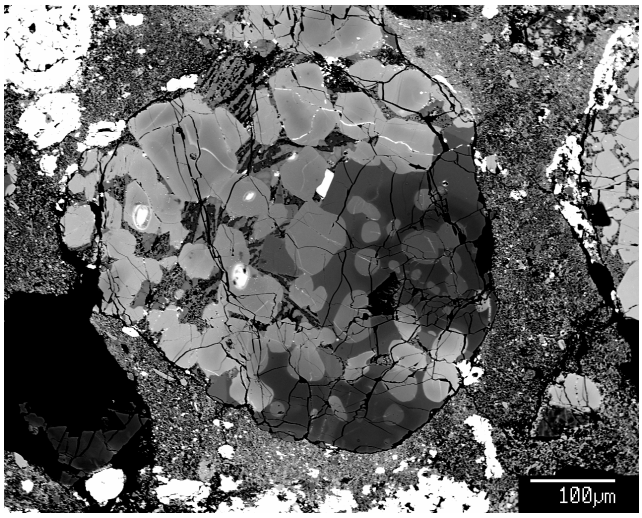

Figure A2-21. BSE image of chondrule J5w.

Chondrule J5w is olivine pyroxene porphyritic chondrule (~ 500 µm) (Figure A2-21). An euhedral chromite grain (lighter gray in a BSE image) and tiny sulfide grains (almost white in a BSE image) occur in the chondrule and few tens µm size of sulfide nodules attached to the chondrule (Figure A2-22). Mesostases are crystalized.

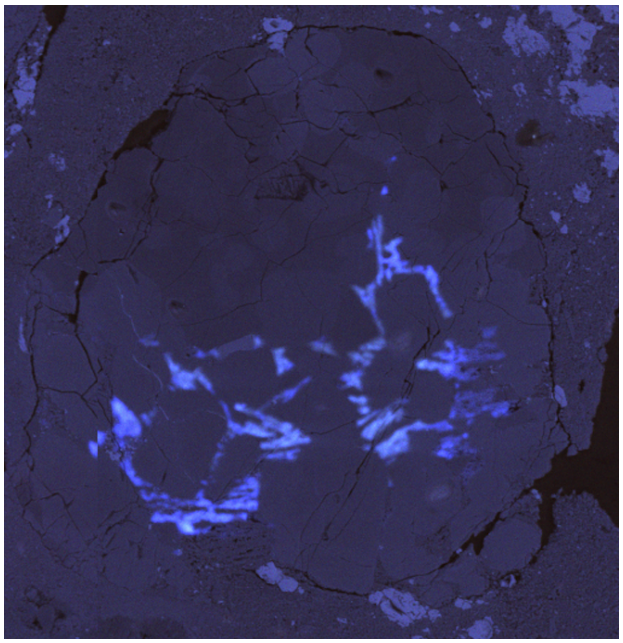

Figure A2-22. Color CL image of chondrule J5w. Mesostases are recrystallized and show blue luminescence.

Chondrule N4x

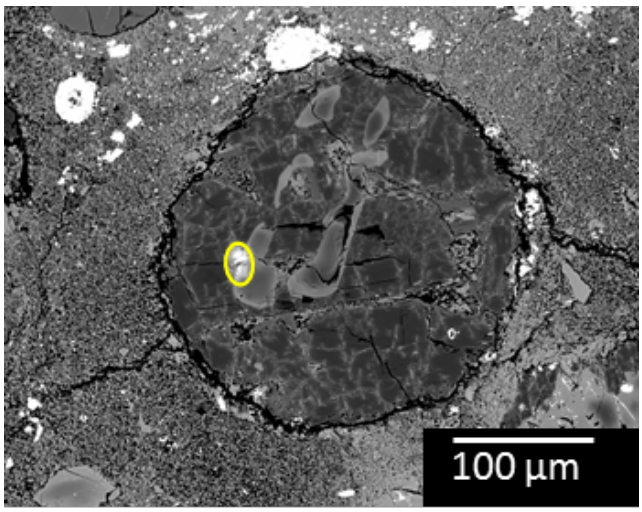

Figure A2-23. BSE image of chondrule N4x.

Chondrule N4x is porphyritic pyroxene olivine chondrule. A CL image shows that red luminescence in the middle of phenocrysts.

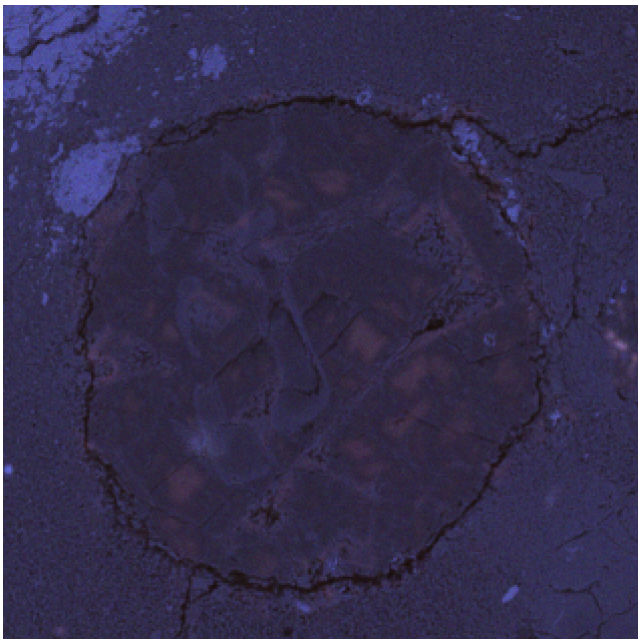

Figure A2-24. Color CL image of chondrule N4x. The pyroxene phenocrysts show red luminescence. This is likely due to the relict grains inside of the phenocrysts.

Olivine Fragment K5m, K5i, and Chondrule K5e

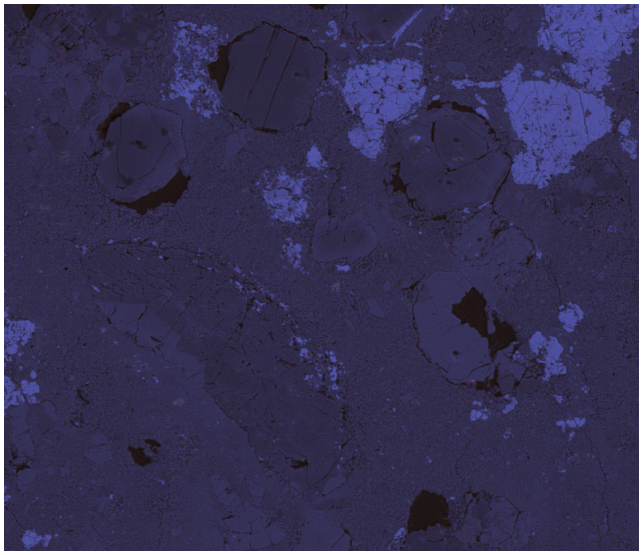

Figure A2-25. Color CL image of chondrule and olivine fragments, K5e, K5i, and K5m. There was no luminescence from those olivine grains. This is consistent with the compositions measured with the EPMA.

Chondrule K4k

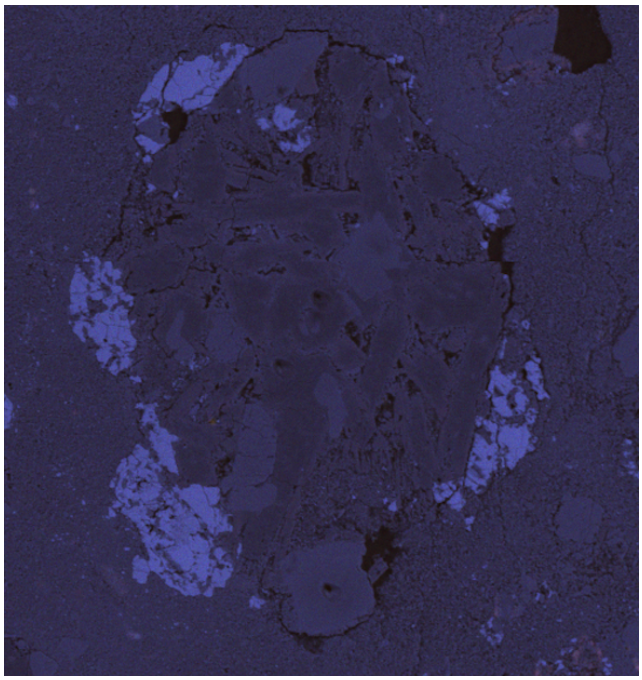

Figure A2-26. Color CL image of chondrule K4k. There was no luminescence from olivine phenocrysts.

Chondrule K4k is porphyritic pyroxene olivine pyroxene chondrule (~300-500 μm) (Figure A2-26). Tiny sulfide grains occur inside and up to~ 100 μm size of sulfide nodules attached to the chondrule (Figure A2-26). Olivine phenocrysts have higher FeO contents in contrast MgO-rich pyroxene.

Chondrule L5h

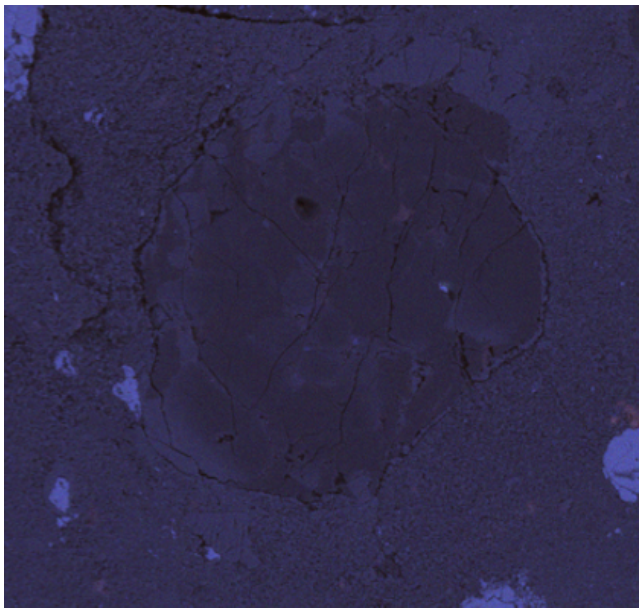

Figure A2-27. Color CL image of chondrule L5h. There was no luminescence from olivine phenocrysts.

Chondrule L5h is porphyritic pyroxene olivine chondrule with a size of ~200-250 μm (Figure A2-27). Olivine phenocrysts have higher FeO contents in contrast MgO-rich pyroxene.

Chondrule L5t

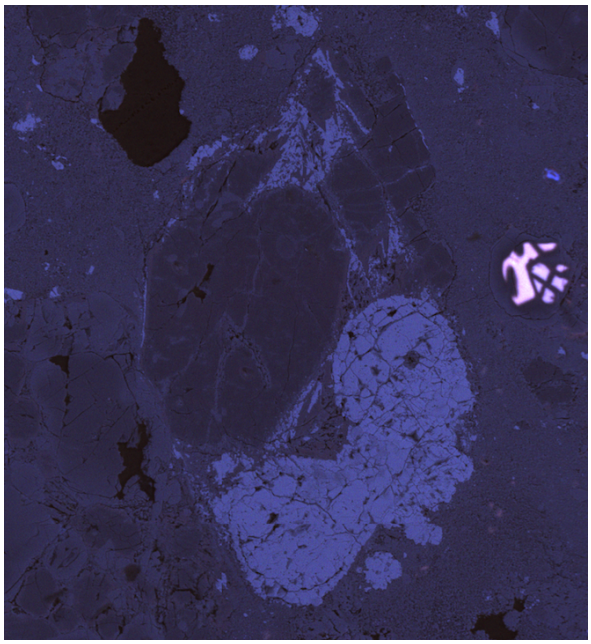

Figure A2-28. Color CL image of chondrule L5t. No luminescence was found in chondrule L5t. Note: the red luminescence is from the chondrule next to the chondrule L5t.

Chondrule L5t is porphyritic pyroxene chondrule with a size of ~200-250 μm (Figure A2-28). The silicate consists of more or less spherical chondrule (~150 μm) and an elongated olivine (~50 ✕150 μm) fragment. Two sulfide chondrules attached to the silicate. It appears like a pair of "tear-drop-glasses". The sulfide chondrule includes small silicate grains and the sulfide is partially oxidized

.

Chondrule M6m

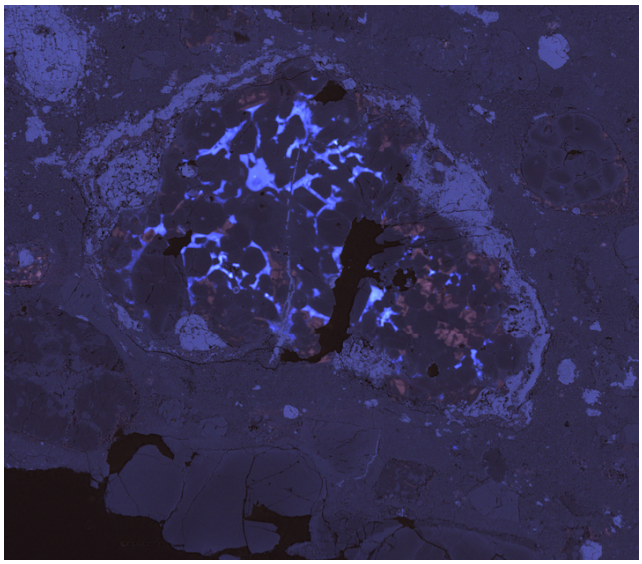

Figure A2-29. Color CL image of chondrule M6m. Olivine phenocrysts shows red luminesces.

Chondrule M6m is a porphyritic olivine chondrule with a size of about 850 × 400 μm (Figure A2-29). A CL image shows that red luminescence in the middle of some phenocrysts. The chondrule is framed by a discontinuous sulfide rim. Spherical sulfide nodules (~150 μm and ~80 μm) occur together with silicates.

Chondrule M6g

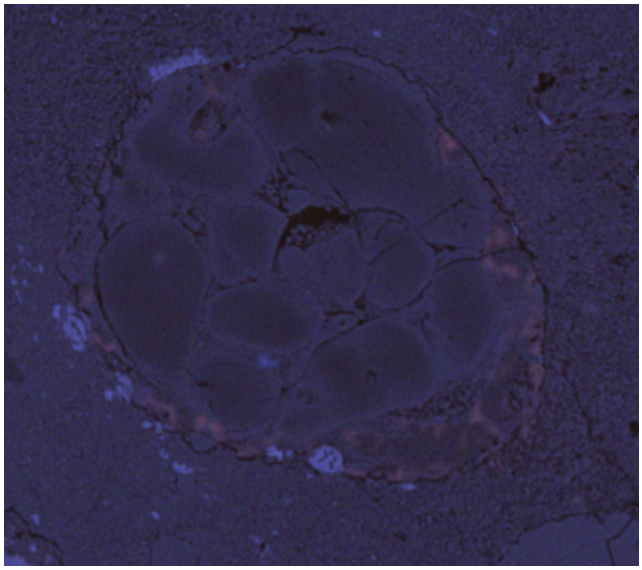

Figure A2-30. Color CL image of chondrule M6g. The edge of chondrule shows red luminesces

Chondrule M6g is an ~200 μm porphyritic olivine chondrule (Figure A2-30). The cores of olivine phenocrysts are Mg-rich and rims are Fe-rich due to thermal alteration. The chondrule rims contain sulfide nodule. Olivine (and perhaps pyroxene) at the rim of chondrule have red luminescence in CL image. Mesostases are recrystallized and show partially blue luminescence in a CL image (Figure A2-30).

Chondrule J5u

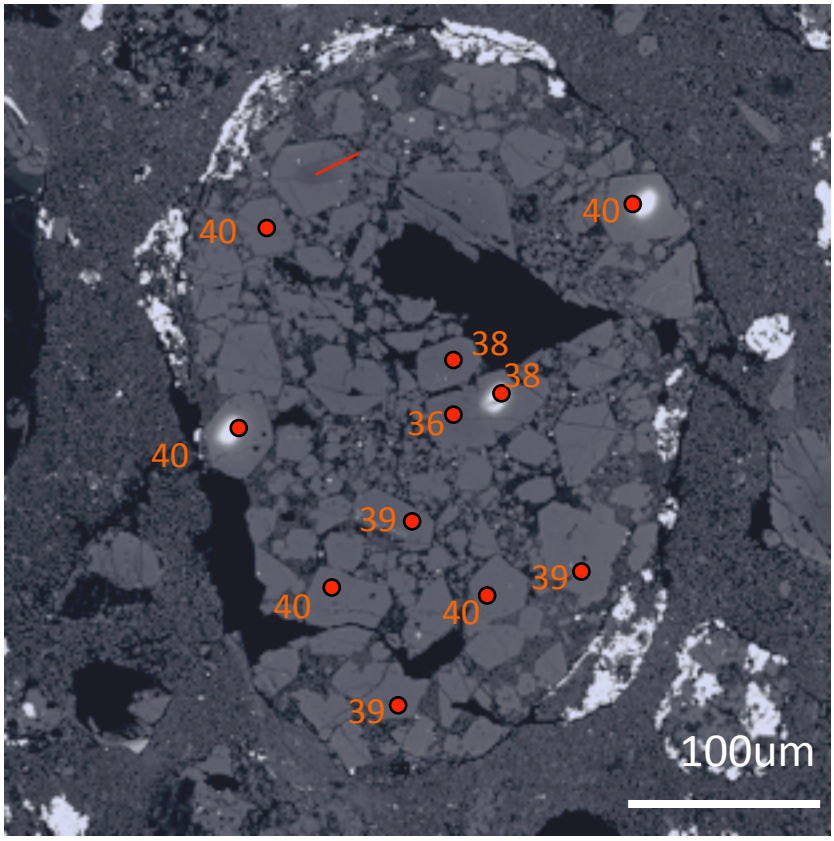

Figure A2-31. BSE image of chondrule J5u. Zoning profile was made across a chondrule phenocrysts indicated as a red line. The red dots are EPMA spots and the number next the dots indicate Fa values.

Chondrule J5u is FeO-rich (~ 400 -600 μm) olivine chondrule (Figure A2-31). Tiny sulfide grains occur inside of the chondrule. Chondrule rims is discontinuously trimmed by sulfide. Olivine phenocrysts contain high FeO (nearly equilibrated R chondrite Fa values). There is the only one highly unequilibrated olivine phenocryst. The most magnesium rich olivine phenocrysts have Fa value 30 at the core and that Fa value 39 at the rim (Figure A2-32). Mesostases are recrystallized and show blue luminescence in a CL image (Figure A2-33).

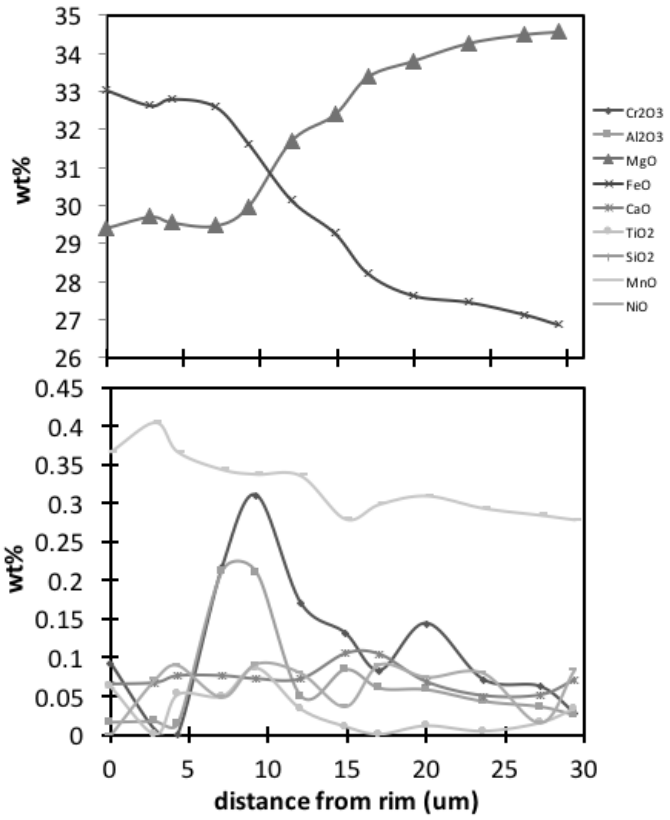

Figure A2-32. Zoning profile of chondrule phenocrysts indicated as a red line in the BSE image. The core of this olivine is FeO-poor.

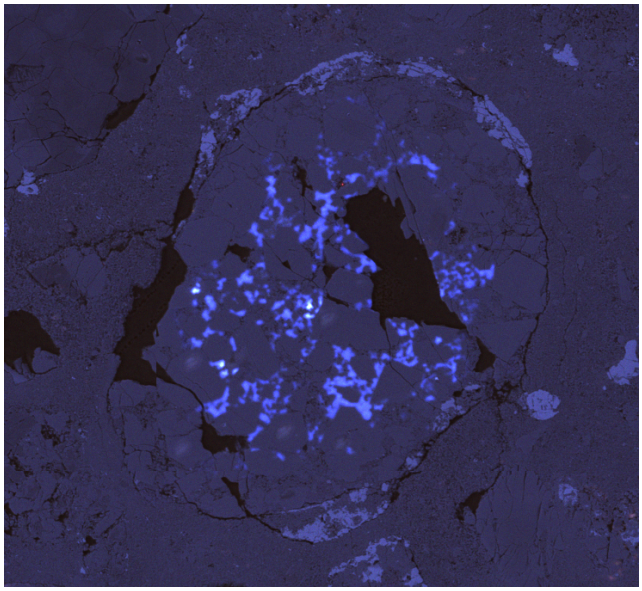

Figure A2-33. Color CL image of chondrule J5u. The mesostases are recrystallized and show blue luminescence.

5.14 Appendix-3: SIMS Data Correction including Matrix Effect Correction

Instrumental machine biases can be caused by sputtering/ionization processes, transmission, and detector amplifiers; most effects are mass dependent. These instrumental mass-dependent fractionations (IMF) for SIMS are calibrated by using standards. We obtained the isotope fractionation factor (alpha) using the following equations:

$$\alpha_{18-SIMS} = \left({}^{18}O/{}^{16}O\right)_{SIMS}/\left({}^{18}O/{}^{16}O\right)_{LF} \qquad (5A-1)$$

$$\alpha_{17-SIMS} = \left({}^{17}O/{}^{16}O\right)_{SIMS}/\left({}^{17}O/{}^{16}O\right)_{LF} \qquad (5A-2)$$

where $({}^{18}O/{}^{16}O)_{SIMS}$ and $({}^{17}O/{}^{16}O)_{SIMS}$ refer to the isotopic ratio in a standard measured by SIMS and $({}^{18}O/{}^{16}O)_{LF}$ and $({}^{17}O/{}^{16}O)_{LF}$ are the "true" values measured by laser-fluorination as $\delta^{18}O_{SMOW}$ (=+5.2‰ for SC-olivine; =+2.95‰ for Springwater pallasite olivine) and $\delta^{17}O_{SMOW}$ (=+2.8‰ for SC-olivine; =+1.26‰ Springwater pallasite olivine) converted to an isotope ratio through the accepted value of ${}^{18}O/{}^{16}O$ and ${}^{17}O/{}^{16}O$ in standard mean ocean water (=0.00200520; (Baertschi, 1976) and (0.000383925), respectively:

$$\delta^{18}O = \left[\left({}^{18}O/{}^{16}O\right)/\left({}^{18}O/{}^{16}O\right)_{SMOW} - 1\right]\times 1000 \qquad (5A-3)$$

$$\delta^{17}O = \left[\left({}^{17}O/{}^{16}O\right)/\left({}^{17}O/{}^{16}O\right)_{SMOW} - 1\right]\times 1000 \qquad (5A-4)$$

In addition to the above corrections, we corrected SIMS mass-dependent instrumental biases caused only by different matrices between samples and standards (so-called matrix effects). These particular mass-dependent fractionations were created by the nature of sputtering/ionization processes of SIMS instruments due to different chemical and crystallinity properties. These corrections were necessary for this study to determine accurate oxygen isotope ratios because their chemical composition of the samples varies from spot to spot even in the

same crystals (i.e., these are unequilibrated assemblages). Several olivine fragments and chondrules in R chondrites contain significantly higher Fe concentrations; this is known to cause larger mass-dependent fractionations during SIMS analyses than well-calibrated standard olivine materials such as San Carlos olivine. We applied a correction curve obtained in a separate study (Isa et al., 2017. in press) to correct these matrix effects. The matrix effects were defined, and the fit curve is as follows:

$$\text{“SIMS matrix effects”} = \left[ln\left\{\left({}^{18}O/{}^{16}O\right)_{measured}/\left({}^{18}O/{}^{16}O\right)_{true}\right\} - \ln(\alpha_{18-SIMS})\right] \times 1000$$

$$= \mathrm{A} \times \left(\frac{Fa}{100} - 0.09\right)^2 \qquad (5A-5)$$

where $({}^{18}O/{}^{16}O)_{measured}$ is the measured O-isotope ratio by SIMS; $({}^{18}O/{}^{16}O)_{true}$ is the true oxygen isotope ratio of the sample; A is a fitting parameter (= -10.6; Isa et al., 2017 in press); Fa/100 is the molar fraction of Fe in the samples; and 0.09 is the molar fraction of Fe in San Carlos olivine. The ratios were corrected using the following equation:

$$\left({}^{18}O/{}^{16}O\right)_{true} = \left[\frac{\left({}^{18}O/{}^{16}O\right)_{measured}}{\alpha_{18-SIMS}}\right] \times e^{\mathrm{f}} \qquad (5A-6)$$

The following equation is applicable to the San Carlos olivine standard:

$$\mathrm{f} = -\mathrm{A} \times \frac{\left(\frac{Fa}{100} - 0.09\right)^2}{1000} \qquad (5A-7)$$

The following equation is applicable to the Spring Water pallasite olivine (Fa 17.5) standard:

$$\mathrm{f} = -\mathrm{A} \times \frac{\left(\frac{Fa}{100} - 0.09\right)^2}{1000} + \mathrm{A} \times \frac{\left(\frac{17.5}{100} - 0.09\right)^2}{1000} \qquad (5A-8)$$

We used the $(^{18}O/^{16}O)_{true}$ ratio to calculate the $\delta^{18}O_{SMOW}$ values:

$$\delta^{18}O_{SMOW} = \left[\left(^{18}O/^{16}O\right)_{true}/\left(^{18}O/^{16}O\right)_{SMOW} - 1\right]\times 1000 \qquad (5A-9)$$

We applied the corrections to $^{17}O/^{16}O$ ratios by assuming the SIMS instrumental fractionation follows an exponential law:

$$\left(^{17}O/^{16}O\right)_{true} = \left[\frac{\left(^{17}O/^{16}O\right)_{measured}}{\alpha_{17-SIMS}}\right]\times e^{f\times 0.52} \qquad (5A-10)$$

We used the $(^{17}O/^{16}O)_{true}$ ratio to calculate the $\delta^{17}O_{SMOW}$ values:

$$\delta^{17}O_{SMOW} = \left[\left(^{17}O/^{16}O\right)_{true}/\left(^{17}O/^{16}O\right)_{SMOW} - 1\right]\times 1000 \qquad (5A-11)$$

5.15 Appendix-4: Definitions of Petrological Terminology and Phenomena

"Relict" grains in chondrules

The relict olivine grains are residual solid materials that remained after the last chondrule-melting events. Relict olivine grains occur in most chondrite groups, e.g., CO3 chondrites (Jones, 1993, 1992; Kunihiro et al., 2004; Wasson and Rubin, 2003) and LL3 chondrites (Ruzicka et al., 2008, 2007); they are also present in R chondrites. Nevertheless, the definition of "relict" is controversial among chondrite researchers. Isotopic and chemical gaps within a single mineral have been used to identify relict grains. O-isotopic studies (e.g., Connolly and Huss, 2010; Kita et al., 2010; Libourel and Chaussidon, 2011; Pack et al., 2004; Ushikubo et al., 2012; Weisberg et al., 2011) have indicated that some relict grains have significantly different O-isotope compositions than their host chondrules. Some relict grains in type-II chondrules appear to be related to type-I chondrules (Jones, 1996). Refractory inclusions also occur as relict grains in type-I chondrules; they contain higher abundances of refractory elements, and low concentrations of FeO (1< wt.%), NiO and MnO. Some refractory inclusions show blue CL luminescence. The blue emission (~420-500 nm) from forsterite is probably due to Al substituting for Si causing distortion of the Si-O bonds (Nishido et al., 2013). Difficulties in identifying relict grains arise because chondrules are igneous assembles and some olivine phenocrysts may have experienced multiple partial melting events and crystal growth during chondrule formation. Single crystallization events could cause chemical fractionations (e.g. normal zoning, oscillatory zoning) and thermal events could cause mobilization of certain elements. We adopt the definition of "relict" regions from Wasson and Rubin (2003a). In this paper we adopt the term relict for phenocrysts that are chemically or isotopically distinct from their host chondrules.

Zoning profiles of phenocrysts in a thin section

In igneous processes, chemical zoning profiles and compositions of mesostasis could be useful parameters for understanding crystallization from silicate melts. For example, mineral textures and chemical zoning potentially archived melt compositions and crystallization histories such as magma recharge or assimilation in magma reservoirs. Unlike terrestrial rock samples in which a number of minerals formed under the same conditions are available, a typical chondrule phenocryst zoning profile traversing the center of a crystal is hard to obtain in a thin section. We are aware that this two-dimensional effect makes it difficult to assess metamorphism which moved elements by diffusion; it can also make it difficult to elucidate fully the crystallization history of a grain (Shea et al., 2015). Nevertheless, the zoning profile of olivine phenocrysts in type II chondrules are widely studied (Jones, 1990), and overall zoning trends such as a comparison between the rim and core of olivine phenocrysts are still useful in identifying relict grains.

"Post-accretionary" and "brecciation"

In chondrite or cometary studies, "pre-accretionary" is a widely used term that could imply both chemical processes in the solar nebula (reactions with ambient gas) and chemical processes in parent bodies before the final lithification. The latter is just called "brecciation" in achondrite studies (CM clasts in HED). Because these terms can be confusing, we do not use the term "pre-accretionary" in this paper.

Brecciation is a very common process in chondrites (Bischoff et al., 2006). A "primitive breccia" is a rock with chondritic clasts situated in a matrix containing chondrules and chondrule fragments (Scott and Taylor, 1982). We avoid this term and only label a chondrite a breccia if it

shows evidence of impact mixing. We just use the term "primitive" to refer to rocks whose components were formed in the nebula and were little modified on their parent body. Most primitive chondrites are known to lack abundant solar-wind gasses which are implanted grains <100 nm from a planetary surface (Goswami et al., 1984). They may also contain grains that exhibit 4π irradiation in space (Zolensky et al., 2003). The terms "regolith breccia" and "fragmental breccia" refer to rocks that were brecciated at parent-body surfaces. The meteorite we analyzed in this study is enriched in solar-wind noble gas and is thus a regolith breccia (Scherer and Schultz, 2000; L Schultz et al., 2005). However, most of the thin section that we studied appeared fresh and contains many largely intact chondrules; we assume that this R3 clast is primitive.

Some brecciated meteorites' parent bodies were defined as "second-generation" (daughter asteroids) formed after collisional destruction of pre-existing "grandparent" bodies (e.g., Bischoff, 1998; Hutchison et al., 1988; Urey, 1967, 1959). It is not, in fact, possible to analyze a meteorite and identify it as a "first-generation" accreted parent body or one from a subsequent generation. Also, distinguishing exotic materials from the host rock is not always easy (e.g. CI chondrites) although there are some obvious lithic "clasts" (e.g. LL5 clasts in LL3) or endogenic components with textual, chemical or isotopic anomalies (e.g., igneous clasts or metamorphosed objects). The latter cases are sometimes referred to "pre-accretionary" objects. Since chondrites are sedimentary rocks and individual components could have been incorporated into their present hosts before or after metamorphism. In this paper, materials that were significantly aqueously or thermally metamorphosed in a planetary setting prior to the final lithification location are termed "post-accretionary."

5.16 Appendix 5: *In Situ* Metamorphism at the Final Lithification Location

The thin section PRE 95404,15 is one of the least equilibrated R3 chondrites and yet texture and olivine FeO compositions at the edge of olivine show some evidence of small amount of *in situ* thermal metamorphism. However, this does not mean that O-isotope compositions are also affected by metamorphism. Oxygen diffusion is slow in olivine and pyroxene and O-isotope exchange due to diffusions are unlikely by the *in situ* thermal alterations. The order of diffusion rates in forsterite is Fe>Mn>Ni>Mg>Ca or Mn>Fe-Mg>Ni; O diffuses more slowly than these elements (Morioka, 1981). Experimentally slow oxygen diffusion is confirmed even after cations exchanged, O isotopes in olivine could retain their initial compositions (Boesenberg, 2007). This is confirmed by analyzing probable AOI. We located metamorphosed AOI, N4s2 (Figure A5-1). This AOI embedded in fine grained matrix with clear boundary but olivine grains next to chondrule are fuzzy boundary. In addition to this AOI, the edge of adjacent chondrule olivine phenocrysts also thermally metamorphosed showing high FeO concentrations. Therefore, it would be possible that this AOI and the chondrule together thermally altered before the final lithification location. Regardless of metamorphism location at either *in situ* or anterior to the lithified, O-isotope compositions ($\delta^{17}O$ =-36.9±0.6 and $\delta^{18}O$=-37.4±0.9) likely did not change (Figure A5-2). This ^{16}O-rich composition is similar to regular CAIs including those in R chondrites (Ito et al., 2004; Rout et al., 2009). Remarkably, however, this olivine Fa value is as the same as that in equilibrated Rs and yet it retains its original ^{16}O-rich compositions. This indicates that the *in situ* O-isotope alterations of this chondrule is minimum unlike Allende AOI that are Fe-rich olivine with ^{16}O-poor compositions (Imai and Yurimoto, 2003). This observation ensures that oxygen isotope compositions of individual components are established elsewhere before the final lithification location.

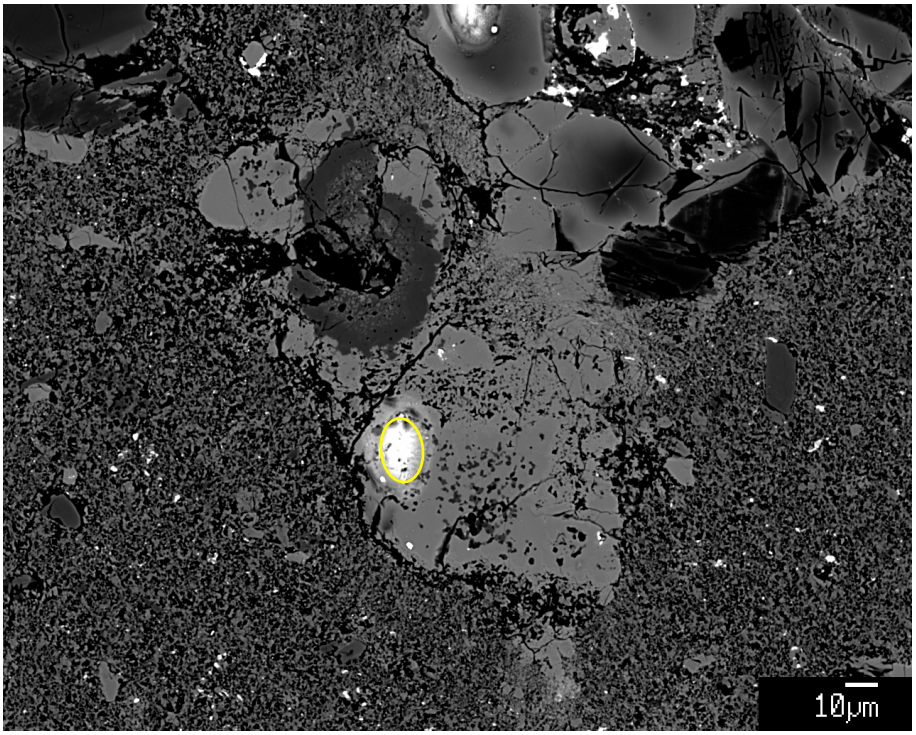

Figure A5-1. BSE image of olivine N4s2. Yellow ovals indicate the location of O-isotope SIMS measurements.

The FeO-rich olivine fragment (middle gray) contains a fragmented CAI 3/2 π of a circular sector and a half π of a circular sector (dark gray inside of the middle gray). The CAI were measured with the EPMA. The results are listed in a Table in the Appendix. Small (few µm or less) Ca-rich pyroxene grains (darker gray) occur in the olivine as inclusions. The compositions were confirmed by characteristic X-ray spectrum determined with EDX equipped with the SEM. This AOI is attached to the chondrule N4s. A SIMS spot at the top of the image is the measurement spot for chondrule N4s.

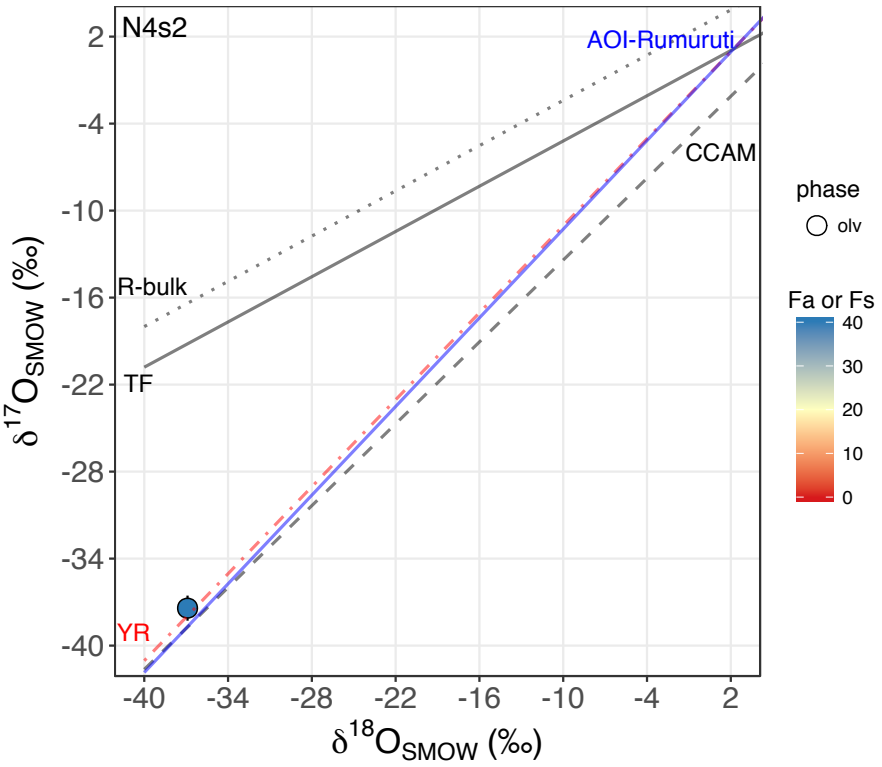

Figure A5-2. Three oxygen isotopes of olivine fragment, N4s2. Each data point represents a single SIMS spot measurement. Uncertainties of individual measurements are twice of errors (as stated in the figure captions at Figure 5). A solid line, a dashed line, red dashed line, and are blue dashed line are TF-line, CCAM line Y & R line, and the line between AOI and a data point of Rumuruti (fall) meteorite whole-rock O-isotope compositions, respectively. The $\Delta^{17}O$ values are significantly lower than R whole rock or a majority of OC chondrules. The oxygen isotope compositions are similar to that of AOI in ordinary chondrites (see text). Nearly equilibrated high FeO is likely due to metamorphism on the parent body.

5.17 Appendix Tables

Table A2: Chemical compositions (wt%) detemined with EPMA.

name		SiO2	s.d.	TiO2	s.d.	Al2O3	s.d.	Cr2O3	s.d.	MgO	s.d.	CaO	s.d.	MnO	s.d.	FeO	s.d.	NiO	s.d.	Na2O	s.d.	Total	**Fa or Fs**
D10t_1	(n=3)	39.4	0.1	-*		0.03	0.01	0.26	0.01	43.9	0.4	0.10	0.02	0.19	0.06	15.7	0.4	0.10	0.03	ND		99.6	**16.7**
D10t_2	(n=3)	39.0	0.5	-		0.08	0.08	0.29	0.03	42.6	1.7	0.20	0.14	0.22	0.05	16.9	2.2	0.26	0.22	ND		99.6	**18.2**
D10t_3		39.5		-		-		0.24		44.6		0.13		0.16		15.0		0.10				99.7	**16**
D10j	(n=3)	36.2	0.1	0.03	0.04	-		0.03	0.02	29.9	0.0	0.05	0.01	0.38	0.03	32.7	0.2	0.13	0.03	ND		99.4	**38.1**
D10o		36.2		0.01		-		-		30.4		0.04		0.39		32.6		0.06		ND		99.7	**38**
J5w-1		37.2		0.07		-		-		35.4		0.26		0.28		25.8		0.03		0.00		99.1	**29**
J5w-2	(n=3)	36.5	0.1	-	-	-		0.04	0.01	31.4	0.4	0.17	0.03	0.35	0.01	30.7	0.6	0.07	0.08	ND		99.2	**35.46**
J5w-3		54.3		0.14		1.22		1.00		28.3		1.03		0.21		13.3		0.04		0.03		99.5	**21**
J5w-4		53.4		0.15		2.35		1.60		27.4		1.49		0.23		13.3		0.06		0.03		100.0	**21**
J5u-1		36.3		-		-		0.04		29.1		0.08		0.40		34.8		0.08		0.02		100.8	**40**
J5u-2		36.8		0.01		0.02		0.06		30.5		0.03		0.35		33.0		0.02		-		100.8	**38**
J5u_3		36.0		0.04		0.01		0.01		28.6		0.11		0.37		34.0		0.05		ND		99.1	**40**
J5u_4		35.5		-		0.02		0.07		28.5		0.08		0.34		34.0		0.10		ND		98.7	**40**
J5u_5		36.0		0.00		-		-		29.3		0.05		0.38		33.0		0.03		ND		98.7	**39**
J5u_6		36.0		-		-		0.03		29.3		0.07		0.39		33.5		-		ND		99.4	**39**
J5u_7		36.0		-		0.04		0.09		29.0		0.11		0.41		33.3		-		ND		98.9	**39**
N4u		36.0		-		-		-		29.1		0.00		0.37		34.2		0.15		0.03		99.9	**40**
N4x		40.1		-		0.05		0.09		46.6		0.31		0.06		12.5		0.12		0.01		99.8	**13**
M6g		39.9		0.04		0.08		0.02		46.8		0.24		0.05		12.5		0.04		ND		99.7	**13**
M6m-1		41.9		0.05		0.05		0.09		54.6		0.05		0.01		2.94		-		ND		99.7	**3**
M6m-2		41.6		0.07		0.13		0.11		54.2		0.30		0.02		2.73		0.03		ND		99.2	**3**
L5h		56.6		0.17		2.24		0.97		34.0		1.85		0.07		3.36		-		ND		99.2	**5**
L5t		58.1		0.05		0.24		0.46		36.3		0.24		0.24		3.55		0.05		ND		99.3	**5**
L5t		58.5		0.05		0.17		0.48		37.6		0.10		0.14		2.05		0.02		ND		99.1	**3**
K4k		37.7		-		0.00		0.02		38.5		0.05		0.29		23.4		0.07		ND		99.9	**25**
K4k		54.4		0.08		0.66		1.11		29.9		0.40		0.38		11.8		0.19		ND		98.9	**18**
K4k		56.6		0.06		0.34		0.65		33.7		0.29		0.42		7.16		0.01		ND		99.3	**11**
K5i		56.2		0.01		0.18		0.61		31.8		0.35		0.28		9.65		-		ND		99.1	**15**
K5m		39.0		0.07		0.16		0.59		44.5		0.06		0.22		15.1		0.06		ND		99.8	**16**
K5e		39.2		-		-		0.02		43.0		0.05		0.39		17.3		0.03		ND		100.0	**18**
D9l-1		41.6		0.05		0.18		0.15		55.5		0.35		-		0.33		0.03		-		98.1	**0**
D9l-2		42.3		0.04		0.12		0.14		56.8		0.35		0.06		0.49		0.04		-		100.3	**0**
D9l-3		42.8		-		0.00		0.09		57.1		0.17		0.03		0.35		-		-		100.5	**0**
N4l-1		41.9		0.04		0.17		0.10		54.7		0.47		0.01		1.66		0.17		-		99.3	**2**
N4l-2		39.1		0.03		0.05		0.16		43.5		0.03		0.16		16.6		0.12		0.01		99.8	**18**
N4l-3 and -4		55.0		0.03		0.18		0.11		41.7		0.06		0.51		1.40		0.11		0.01		99.0	**1**
N4l-5		41.8		-		0.19		0.11		55.0		0.48		0.04		1.11		0.04		0.03		98.8	**1**
N4l-6		41.5		-		0.24		0.16		54.6		0.47		0.01		2.00		0.05		0.01		99.0	**2**
N4l-7		41.5		-		0.23		0.14		54.7		0.46		0.02		2.07		0.07		-		99.1	**2**
N4l-8		41.0		-		0.18		0.22		53.0		0.45		0.06		4.13		-		0.00		99.0	**4**
N4l-9		40.7		-		0.14		0.17		50.8		0.22		0.03		7.03		0.12		0.01		99.2	**7**
N4s-1	(n=2)	41.9		-		0.14		0.16		55.7		0.50		-		0.65		0.03		-		99.1	**1**
N4s-2		42.0		0.08		0.16		0.14		55.4		0.64		0.02		0.44		0.03		0.00		98.9	**0**
N4s-3		38.1		-		0.01		0.07		39.6		0.07		0.15		21.2		0.08		0.00		99.3	**23**
N4s-4		42.0		0.16		0.52		0.12		55.3		0.38		0.02		0.46		-		0.07		99.0	**0**

name		SiO2	s.d.	TiO2	s.d.	Al2O3	s.d.	Cr2O3	s.d.	MgO	s.d.	CaO	s.d.	MnO	s.d.	FeO	s.d.	NiO	s.d.	Na2O	s.d.	Total	**Fa or Fs**	**s.d.**
N4s-5		42.1		0.12		0.29		0.12		55.7		0.58		-		0.51		0.04		-		99.4	**1**	
N4s2	(n=3)	35.8	0.4	-		0.02	0.02	-		28.8	0.2	0.04	0.01	0.37	0.02	34.5	0.1	0.08	0.05	-		99.6	**40**	**0.3**
K5l-1		38.8		0.11		0.19		0.27		45.2		0.15		0.11		15.8		0.05		ND		100.7	**16**	
K5l-2		57.1		-		0.05		0.18		34.1		0.06		0.11		8.52		-		ND		100.1	**12**	
K5l-3																								
K5l-4		35.4		0.01		-		-		29.3		0.01		0.34		34.8		0.07		ND		100.0	**40**	
K5l-5		36.1		0.01		-		0.04		28.7		0.06		0.36		35.1		0.05		ND		100.4	**41**	
	olv/px intergr																							
J5i	owth	57.7		-		0.20		0.37		36.7		0.15		0.26		3.48		0.05		0.02		98.9	**5**	

ND: not detemined

*: under detection limit

Table A3: Chemical composition of pyroxene in a CAI

name	SiO2	TiO2	Al2O3	Cr2O3	MgO	CaO	MnO	FeO	NiO	Na2O	Total	**Fs**	**mol Fe/Mn**
px-N4s2	51.7	-	3.02	0.05	24.5	17.6	-	0.93	0.03	-	97.9	**16**	**-**
px-N4s2	53.9	-	1.52	0.01	24.5	18.6	0.03	0.92	0.05	0.02	99.6	**16**	**97**

Table A4. Relative frequency table of mean Δ17O values of olivine and pyroxene phenocrysts in a chondrule.

	probability		
Δ17O	R3	LL3	E3
-15 to -13	0	0	0
-13 to -11	0	0	0
-11 to -9	0	0	0
-9 to -7	0	0.02222222	0
-7 to -5	0	0	0
-5 to -3	0.03030303	0	0
-3 to -1	0.09090909	0.11111111	0
-1 to 1	0.48484848	0.77777778	0.90909091
1 to 3	0.27272727	0.08888889	0.09090909
3 to 5	0.12121212	0	0

5.18 References

Alexander, D., (2005). From supernovae to planets: The view from meteorites and interplanetary dust particles. In *Chondrites and the Protoplanetary Disk* (Vol. 341, p. 972).

Asphaug, E., Jutzi, M., Movshovitz, N., (2011). Chondrule formation during planetesimal accretion. *Earth Planet. Sci. Lett.* **308**, 369-379. doi:10.1016/j.epsl.2011.06.007

Baertschi, P., (1976). Absolute ^{18}O content of standard mean ocean water. *Earth Planet. Sci. Lett.* **31**, 341-344. doi:10.1016/0012-821X(76)90115-1

Berlin, J., Jones, R.H., Brearley, A.J., (2011). Fe-Mn systematics of type IIA chondrules in unequilibrated CO, CR, and ordinary chondrites. *Meteorit. Planet. Sci*. **46**, 513-533. doi:10.1111/j.1945-5100.2011.01171.x

Bevan, A.W.R., Axon, H.J., (1980). Metallography and thermal history of the Tieschitz unequilibrated meteorite – Metallic chondrules and the origin of polycrystalline taenite. *Earth Planet. Sci. Lett*. **47**, 353-360. doi:10.1016/0012-821X(80)90022-9

Bischoff, A., (1998). Aqueous alteration of carbonaceous chondrites: Evidence for preaccretionary alteration-A review *Meteoritics & Planetary Science*, **33**, 1113-1122.

Bischoff, A., Geiger, T., Palme, H., Spettel, B., Schultz, L., Scherer, P., Loeken, T., Bland, P., Clayton, R.N., Mayeda, T.K., Herpers, U., Meltzow, B., Michel, R., Dittrich-Hannen, B., (1994). Acfer 217-A new member of the Rumuruti chondrite group (R). *Meteoritics* **29**, 264-274. doi:10.1111/j.1945-5100.1994.tb00680.x

Bischoff, A., Scott, E.R.D., Metzler, K., Goodrich, C.A., (2006). Nature and origins of meteoritic breccias, in *Meteorites and the Early Solar System II*. 679-712.

Bischoff, A., Vogel, N., Roszjar, J., (2011). The Rumuruti chondrite group. *Chemie der Erde - Geochemistry* **71**, 101-133. doi:10.1016/j.chemer.2011.02.005

Clayton, D.D., (1980). Chemical and isotopic fractionation by grain size separates. *Earth Planet. Sci. Lett*. **47**, 199-210. doi:10.1016/0012-821X(80)90036-9

Connolly, H.C., Huss, G.R., (2010). Compositional evolution of the protoplanetary disk: Oxygen isotopes of type-II chondrules from CR2 chondrites. *Geochim. Cosmochim. Acta* **74**, 2473-2483. doi:10.1016/j.gca.2010.01.005

Cuzzi, J.N., Hogan, R.C., Paque, J.M., Dobrovolskis, A.R., (2001). Size-selective concentration of chondrules and other small particles in protoplanetary nebula turbulence. *Astrophys. J.* **546**, 496-508. doi:10.1086/318233

Ehlers, K., Grove, T.L., Sisson, T.W., Recca, S.I., Zervas, D.A., (1992). The effect of oxygen fugacity on the partitioning of nickel and cobalt between olivine, silicate melt, and metal. *Geochim. Cosmochim. Acta* **56**, 3733-3743. doi:10.1016/0016-7037(92)90166-G

Gibson, E.K., Lange, D.E., Keil, K., Schmidt, T.E., Rhodes, J.M., (1977). The Kramer creek, Colorado meteorite: A new L4 chondrite. *Meteoritics* **12**, 95-107.

Goodrich, C.A., Delaney, J.S., (2000). Fe/Mg–Fe/Mn relations of meteorites and primary heterogeneity of primitive achondrite parent bodies. *Geochim. Cosmochim. Acta* **64**, 149-160. doi:10.1016/S0016-7037(99)00107-6

Goswami, J.N., Lal, D., Wllkening, L.L., (1984). Gas-rich meteorites: Probes for particle environment and dynamical processes in the inner solar system. *Space Sci. Rev*. **37**, 111-159.

Greenwood, J.P., Rubin, A.E., Wasson, J.T., (2000). Oxygen isotopes in R-chondrite magnetite and olivine: Links between R chondrites and ordinary chondrites. *Geochim. Cosmochim. Acta* **64**, 3897-3911. doi:10.1016/S0016-7037(00)00452-X

Grossman, J.N., Brearley, A.J., (2005). The onset of metamorphism in ordinary and carbonaceous chondrites. *Meteoritics & Planetary Science*, **40**, 87-122. doi:10.1111/j.1945-5100.2005.tb00366.x

Hewins, R.H., Connolly, H.C., Lofgren, G.E., Libourel, G., (2005). Experimental constraints on chondrule formation. In *Chondrites and the protoplanetary disk* (Vol. 341, p. 286)

Hewins, R.H., Radomsky, P.M., (1990). Temprature conditions for chondrule formation. *Meteoritics* **25**, 309-318.

Hutchison, R., Bevan, A.W.R., (1982). Conditions and time of chondrule accretion, In *Chondrules and their origins* (pp. 162-179)

Hutchison, R., Graham, A.L., (1975). Significance of calcium-rich differentiates in chondritic meteorites. Nature. ***255***, 471.

Hutchison, R., Williams, C.T., Din, V.K., Clayton, R.N., Kirschbaum, C., Paul, R.L., Lipschutz, M.E., (1988). A planetary, H-group pebble in the Barwell, L6, unshocked chondritic meteorite. *Earth Planet. Sci. Lett*. **90**, 105-118. doi:10.1016/0012-821X(88)90094-5

Imai, H., Yurimoto, H., (2003). Oxygen isotopic distribution in an amoeboid olivine aggregate from the Allende CV chondrite. *Geochim. Cosmochim. Acta* **67**, 765-772. doi:10.1016/S0016-7037(02)01174-2

Isa, J., Kohl, I.E., Liu, M.C., Wasson, J.T., Young, E.D., McKeegan, K.D., (2017). Quantification of oxygen isotope SIMS matrix effects in olivine samples: Correlation with sputter rate. *Chemical Geology* (in press).

Isa, J., Rubin, A.E., Wasson, J.T., (2014). R-chondrite bulk-chemical compositions and diverse oxides: Implications for parent-body processes. *Geochim. Cosmochim. Acta* **124**, 131-151.

Ito, M., Ganguly, J., (2006). Diffusion kinetics of Cr in olivine and ^{53}Mn–^{53}Cr thermochronology of early solar system objects. *Geochim. Cosmochim. Acta* **70**, 799-809. doi:10.1016/j.gca.2005.09.020

Ito, M., Nagasawa, H., Yurimoto, H., (2004). Oxygen isotopic SIMS analysis in Allende CAI: Details of the very early thermal history of the solar system. *Geochim. Cosmochim. Acta* **68**, 2905-2923. doi:10.1016/j.gca.2004.02.001

Jones, R.H., (1990). Petrology and mineralogy of Type II, FeO-rich chondrules in Semarkona (LL3.0): Origin by closed-system fractional crystallization, with evidence for supercooling. *Geochim. Cosmochim. Acta* **54**, 1785-1802. doi:10.1016/0016-7037(90)90408-D

Jones, R.H., (1992). On the relationship between isolated and chondrule olivine grains in the carbonaceous chondrite ALHA 77307. *Geochim. Cosmochim. Acta* **56**, 3593. doi:10.1016/0016-7037(92)90403-6

Jones, R.H., (1993). Effect of metamorphism on isolated olivine grains in CO_3 chondrites. *Geochim. Cosmochim. Acta* **57**, 2853-2867. doi:10.1016/0016-7037(93)90394-C

Jones, R.H., (1996). FeO-rich, porphyritic pyroxene chondrules in unequilibrated ordinary chondrites. *Geochim. Cosmochim. Acta* **60**, 3115-3138. doi:10.1016/0016-7037(96)00152-4

Jones, R.H., Leshin, L.A., Guan, Y., Sharp, Z.D., Durakiewicz, T., Schilk, A.J., (2004). Oxygen isotope heterogeneity in chondrules from the Mokoia CV3 carbonaceous chondrite. *Geochim. Cosmochim. Acta* **68**, 3423-3438. doi:10.1016/j.gca.2004.01.013

Jones, R.H., Lofgren, G.E., (1993). A comparison of FeO-rich, porphyritic olivine chondrules in unequilibrated chondrites and experimental analogues. *Meteoritics **28***, 213-221

Jones, R.H., Saxton, J.M., Lyon, I.C., Turner, G., (2000). Oxygen isotopes in chondrule olivine and isolated olivine grains from the CO3 chondrite Allan Hills A77307. *Meteoritics & Planetary Science*, **35**, 849-857. doi:10.1111/j.1945-5100.2000.tb01468.x

Kallemeyn, G.W., Rubin, A.E., Wasson, J.T., (1996). The compositional classification of chondrites: VII. The R chondrite group. *Geochim. Cosmochim. Acta* **60**, 2243-2256.

Kennedy, A.K., Lofgren, G.E., Wasserburg, G.J., (1993). An experimental study of trace element partitioning between olivine, orthopyroxene and melt in chondrules: Equilibrium values and kinetic effects. *Earth Planet. Sci. Lett*. **115**, 177-195. doi:10.1016/0012-821X(93)90221-T

Khan, R., Shirai, N., Ebihara, M., (2015). Chemical characteristic of R chondrites in the light of P, REEs, Th and U abundances. *Earth Planet. Sci. Lett*. **422**, 18-27. doi:10.1016/j.epsl.2015.04.008

Kita, N.T., Nagahara, H., Tachibana, S., Tomomura, S., Spicuzza, M.J., Fournelle, J.H., Valley, J.W., (2010). High precision SIMS oxygen three isotope study of chondrules in LL3 chondrites: Role of ambient gas during chondrule formation. *Geochim. Cosmochim. Acta* **74**, 6610-6635. doi:10.1016/j.gca.2010.08.011

Krot, A.N., Libourel, G., Chaussidon, M., (2006). Oxygen isotope compositions of chondrules in CR chondrites. *Geochim. Cosmochim. Acta* **70**, 767-779. doi:10.1016/j.gca.2005.08.028

Kunihiro, T., Rubin, A.E., McKeegan, K.D., Wasson, J.T., (2004). Oxygen-isotopic compositions of relict and host grains in chondrules in the Yamato 81020 CO3.0 chondrite. *Geochim. Cosmochim. Acta* **68**, 3599-3606. doi:10.1016/j.gca.2004.02.011

Kunihiro, T., Rubin, A.E., Wasson, J.T., (2005). Oxygen-isotopic compositions of low-FeO relicts in high-FeO host chondrules in Acfer 094, a type 3.0 carbonaceous chondrite closely related to CM. *Geochim. Cosmochim. Acta* **69**, 3831-3840. doi:10.1016/j.gca.2005.01.031

Libourel, G., Chaussidon, M., (2011). Oxygen isotopic constraints on the origin of Mg-rich olivines from chondritic meteorites. *Earth Planet. Sci. Lett*. **301**, 9-21. doi:10.1016/j.epsl.2010.11.009

Libourel, G., Krot, A., Tissandier, L., (2006). Role of gas-melt interaction during chondrule formation. *Earth Planet. Sci. Lett*. **251**, 232-240. doi:10.1016/j.epsl.2006.09.011

Liffman, K., (2005). Chondrule and metal grain size sorting from jet flows. *Meteoritics & Planetary Science*, **40**, 123-138. doi:10.1111/j.1945-5100.2005.tb00367.x

Lingemann, C.M., Berlin, J., Stöffler, D., (2000). Rumuruti chondrite: Origin and evolution of primitive components. *Meteoritics & Planetary Science*, Supplement, A98.

McCanta, M.C., Treiman, A.H., Dyar, M.D., Alexander, C.M.O., Rumble, D., Essene, E.J., (2008). The LaPaz Icefield 04840 meteorite: Mineralogy, metamorphism, and origin of an amphibole- and biotite-bearing R chondrite. *Geochim. Cosmochim. Acta* **72**, 5757-5780. doi:10.1016/j.gca.2008.07.034

Miller, K.E., Lauretta, D.S., Connolly, H.C., Berger, E.L., Domanik, K., (2016). Chondrules and opaque phases in unequilibrated R chondrites: A comprehensive assessment of their formation. *Lunar Planet. Sci. Conf.*

Miller, K.E., Lauretta, D.S., Connolly, H.C., Berger, E.L., Nagashima, K., Domanik, K., (2017). Formation of unequilibrated R chondrite chondrules and opaque phases. *Geochim. Cosmochim. Acta.* (In press)

Miyamoto, M., Mikouchi, T., Jones, R.H., (2009). Cooling rates of porphyritic olivine chondrules in the Semarkona (LL3.00) ordinary chondrite: A model for diffusional equilibration of olivine during fractional crystallization. *Meteoritics & Planetary Science* **44**, 521-530. doi:10.1111/j.1945-5100.2009.tb00748.x

Morioka, M., (1981). Cation diffusion in olivine–II. Ni-Mg, Mn-Mg, Mg and Ca. *Geochim. Cosmochim. Acta* **45**, 1573-1580. doi:10.1016/0016-7037(81)90286-6

Nishido, H., Endo, T., Ninagawa, K., Kayama, M., Gucsik, A., (2013). Thermal effects on cathodoluminescence in forsterite. *Geochronometria* **40**, 1897-1695. doi:10.2478/s13386-013-0116-7

Pack, A., Yurimoto, H., Palme, H., (2004). Petrographic and oxygen-isotopic study of refractory forsterites from R-chondrite Dar al Gani 013 (R3.5-6), unequilibrated ordinary and carbonaceous chondrites. *Geochim. Cosmochim. Acta* **68**, 1135-1157. doi:10.1016/j.gca.2003.07.014

Papike, J.J., Karner, J.M., Shearer, C.K., (2003). Determination of planetary basalt parentage: A simple technique using the electron microprobe. *Am. Mineral*. **88**, 469-472.

Righter, K., Cosca, M.A., Morgan, L.E., (2016). Preservation of ancient impact ages on the R chondrite parent body: $^{40}Ar/^{39}Ar$ age of hornblende-bearing R chondrite LAP 04840. *Meteoritics & Planetary Science* **51**, 1678-1684. doi:10.1111/maps.12692

Righter, K., Neff, K.E., (2007). Temperature and oxygen fugacity constraints on CK and R chondrites and implications for water and oxidation in the early solar system. *Polar Sci.* **1**, 25-44. doi:10.1016/j.polar.2007.04.002

Rout, S.S., Bischoff, A., Nagashima, K., Krot, A.N., Huss, G.R., Keil, K., (2009). Oxygen- and magnesium-isotope compositions of calcium-aluminum-rich inclusions from Rumuruti (R) chondrites. *Geochim. Cosmochim. Acta* **73**, 4264-4287. doi:10.1016/j.gca.2009.04.006

Rubin, A.E., (2010). Physical properties of chondrules in different chondrite groups: Implications for multiple melting events in dusty environments. *Geochim. Cosmochim. Acta* **74**, 4807-4828. doi:10.1016/j.gca.2010.05.018

Rubin, A.E., Kallemeyn, G.W., (1989). Carlisle Lakes and Allan Hills 85151: Members of a new chondrite grouplet. *Geochim. Cosmochim. Acta* **53**, 3035-3044. doi:10.1016/0016-7037(89)90179-8

Rubin, A.E., Kallemeyn, G.W., (1994). Pecora Escarpment 91002: A member of the new Rumuruti (R) chondrite group. *Meteoritics* **29**, 255-264. doi:10.1111/j.1945-5100.1994.tb00679.x

Rubin, A.E., Wasson, J.T., (2005). Non-spherical lobate chondrules in CO3.0 Y-81020: General implications for the formation of low-FeO porphyritic chondrules in CO chondrites. *Geochim. Cosmochim. Acta*. **69**, 211-220. doi:10.1016/j.gca.2004.06.019

Rudraswami, N.G., Ushikubo, T., Nakashima, D., Kita, N.T., (2011). Oxygen isotope systematics of chondrules in the Allende CV3 chondrite: High precision ion microprobe studies. *Geochim. Cosmochim. Acta* **75**, 7596-7611. doi:10.1016/j.gca.2011.09.035

Ruzicka, A., Floss, C., Hutson, M., (2008). Relict olivine grains, chondrule recycling, and implications for the chemical, thermal, and mechanical processing of nebular materials. *Geochim. Cosmochim. Acta* **72**, 5530-5557. doi:10.1016/j.gca.2008.08.017

Ruzicka, A., Hiyagon, H., Hutson, M., Floss, C., (2007). Relict olivine, chondrule recycling, and the evolution of nebular oxygen reservoirs. *Earth Planet. Sci. Lett*. **257**, 274-289. doi:10.1016/j.epsl.2007.02.037

Sanders, I.S., Scott, E.R.D., (2012). The origin of chondrules and chondrites: Debris from low-velocity impacts between molten planetesimals? *Meteoritics & Planetary Science* **47**, 2170-2192. doi:10.1111/maps.12002

Scherer, P., Schultz, L., (2000). Noble gas record, collisional history, and pairing of CV, CO, CK, and other carbonaceous chondrites. *Meteoritics & Planetary Science* **35**, 145-153. doi:10.1111/j.1945-5100.2000.tb01981.x

Schrader, D.L., Connolly, H.C., Lauretta, D.S., Nagashima, K., Huss, G.R., Davidson, J., Domanik, K.J., (2013). The formation and alteration of the Renazzo-like carbonaceous chondrites II: Linking O-isotope composition and oxidation state of chondrule olivine. *Geochim. Cosmochim. Acta* **101**, 302-327. doi:10.1016/j.gca.2012.09.045

Schultz, L., Weber, H.W., Franke, L., (2005). Rumuruti chondrites: Noble gases, exposure ages, pairing, and parent body history. *Meteoritics & Planetary Science* **40**, 557-571. doi:10.1111/j.1945-5100.2005.tb00963.x

Schulze, H., Bischoff, A., Palme, H., Spettel, B., Dreibus, G., Otto, J., (1994). Mineralogy and chemistry of Rumuruti: The first meteorite fall of the new R chondrite group. *Meteoritics* **29**, 275-286. doi:10.1111/j.1945-5100.1994.tb00681.x

Scott, E.R.D., Taylor, G.J., (1982). Primitive breccias among type 3 ordinary chondrites - origin and relation to regolith breccias. In *Lunar Breccias and Soils and their Meteoritic Analogs* (p. 130).

Shannon, C.E., (1948). A Mathematical Theory of Communication. *Bell Syst. Tech. J.* **5**, 3-55. doi:10.1002/j.1538-7305.1948.tb01338.x

Shea, T., Lynn, K.J., Garcia, M.O., (2015). Cracking the olivine zoning code: Distinguishing between crystal growth and diffusion. *Geology.* **43**, 935-938. doi:10.1130/G37082.1

Tang, H., Liu, M.-C., McKeegan, K.D., Tissot, F.L.H., Dauphas, N., (2017). In situ isotopic studies of the U-depleted Allende CAI Curious Marie: Pre-accretionary alteration and the co-existence of ^{26}Al and ^{36}Cl in the early solar nebula. *Geochim. Cosmochim. Acta* **207**, 1-18. doi:10.1016/j.gca.2017.03.001

Tenner, T.J., Nakashima, D., Ushikubo, T., Kita, N.T., Weisberg, M.K., (2015). Oxygen isotope ratios of FeO-poor chondrules in CR3 chondrites: Influence of dust enrichment and H_2O during chondrule formation. *Geochim. Cosmochim. Acta* **148**, 228-250. doi:10.1016/j.gca.2014.09.025

Tenner, T.J., Ushikubo, T., Kurahashi, E., Kita, N.T., Nagahara, H., (2013). Oxygen isotope systematics of chondrule phenocrysts from the CO3.0 chondrite Yamato 81020: Evidence for two distinct oxygen isotope reservoirs. *Geochim. Cosmochim. Acta* **102**, 226-245. doi:10.1016/j.gca.2012.10.034

Urey, H.C., (1959). Primary and secondary objects. *J. Geophys. Res.* **64**, 1721-1737. doi:10.1029/JZ064i011p01721

Urey, H.C., (1967). Parent bodies of the meteorites and the origin of chondrules. *Icarus* **7**, 350-359. doi:10.1016/0019-1035(67)90079-6

Ushikubo, T., Kimura, M., Kita, N.T., Valley, J.W., (2012). Primordial oxygen isotope reservoirs of the solar nebula recorded in chondrules in Acfer 094 carbonaceous chondrite. *Geochim. Cosmochim. Acta* **90**, 242-264. doi:10.1016/j.gca.2012.05.010

Warren, P.H., Rubin, A.E., Isa, J., Gessler, N., Ahn, I., Choi, B.G., (2014). Northwest Africa 5738: Multistage fluid-driven secondary alteration in an extraordinarily evolved eucrite. *Geochim. Cosmochim. Acta* **141,** 199-227. doi:10.1016/j.gca.2014.06.008

Wasson, J.T., Rubin, A.E., (2003). Ubiquitous low-FeO relict grains in type II chondrules and limited overgrowths on phenocrysts following the final melting event. *Geochim. Cosmochim. Acta* **67**, 2239-2250. doi:10.1016/S0016-7037(03)00023-1

Weisberg, M.K., Ebel, D.S., Connolly, H.C., Kita, N.T., Ushikubo, T., (2011). Petrology and oxygen isotope compositions of chondrules in E3 chondrites. *Geochim. Cosmochim. Acta* **75**, 6556-6569. doi:10.1016/j.gca.2011.08.040

Weisberg, M.K., Prinz, M., Kojima, H., Yanai, K., Clayton, R.N., Mayeda, T.K., (1991). The Carlisle Lakes-type chondrites: A new grouplet with high Δ^{17}O and evidence for nebular oxidation *Geochim. Cosmochim. Acta* **55**, 2657-2669.

Wood, J.A., Cameron, A.C.W., (1963). On the origin of chondrules and chondrites. *Icarus* **2**, 152-180.

Young, E.D., Russell, S.S., (1998). Oxygen reservoirs in the early solar nebula inferred from an Allende CAI. *Science* **282**, 452-455. doi:10.1126/science.282.5388.452

Zolensky, M., Nakamura, K., Weisberg, M.K., Prinz, M., Nakamura, T., Ohsumi, K., Saitow, A., Mukai, M., Gounelle, M., (2003). A primitive dark inclusion with radiation-damaged silicates in the Ningqiang carbonaceous chondrite. *Meteoritics & Planetary Science* **38**, 305-322.

Zook, H.A., (1980). A new impact model for the generation of ordinary chondrites, A new impact model for the generation of ordinary chondrites. *LPI Contributions*, **412,** 143.

Chapter6: Joegoldsteinite: A new sulfide mineral ($MnCr_2S_4$) from the Social Circle IVA iron meteorite[1]

[1] This chapter have published at following:

Isa, J., Ma, C., & Rubin, A. E. (2016). *American Mineralogist*, *101*(5), 1217-1221.

American Mineralogist, Volume 101, pages 1217–1221, 2016

Joegoldsteinite: A new sulfide mineral ($MnCr_2S_4$) from the Social Circle IVA iron meteorite

Junko Isa[1,*], Chi Ma[2,*], and Alan E. Rubin[1,3]

[1]Department of Earth, Planetary, and Space Sciences, University of California, Los Angeles, California 90095, U.S.A.
[2]Division of Geological and Planetary Sciences, California Institute of Technology, Pasadena, California 91125, U.S.A.
[3]Institute of Geophysics and Planetary Physics, University of California, Los Angeles, California 90095, U.S.A.

Abstract

Joegoldsteinite, a new sulfide mineral of end-member formula $MnCr_2S_4$, was discovered in the Social Circle IVA iron meteorite. It is a thiospinel, the Mn analog of daubréelite ($Fe^{2+}Cr_2S_4$), and a new member of the linnaeite group. Tiny grains of joegoldsteinite were also identified in the Indarch EH4 enstatite chondrite. The chemical composition of the Social Circle sample determined by electron microprobe is (wt%) S 44.3, Cr 36.2, Mn 15.8, Fe 4.5, Ni 0.09, Cu 0.08, total 101.0, giving rise to an empirical formula of $(Mn_{0.82}Fe_{0.23})Cr_{1.99}S_{3.95}$. The crystal structure, determined by electron backscattered diffraction, is a *Fd*3*m* spinel-type structure with $a = 10.11$ Å, $V = 1033.4$ Å^3, and $Z = 8$.

Keywords: Joegoldsteinite, $MnCr_2S_4$, new sulfide mineral, thiospinel, Social Circle IVA iron meteorite, Indarch EH4 enstatite chondrite

Introduction

Thiospinels have a general formula of AB_2X_4 where A is a divalent metal, B is a trivalent metal, and X is a –2 anion, typically S, but in some cases Se or Te. Some thiospinels are magnetic semiconductors and have been studied extensively by materials scientists. Synthetic $MnCr_2S_4$ is known to be a ferrimagnetic insulator (Menyuk et al. 1965; Darcy et al. 1968; Lotgering 1968; Plumier 1980; Denis et al. 1970) and recent single-crystal measurements have documented two different anomalies in heat capacity that correlate with magnetic phase transformations (Tsurkan et al. 2003). The complex behavior of thiospinel magnetism results from ferrimagnetic ordering of the Cr and Fe sublattices (Bertinshaw et al. 2014).

Joegoldsteinite is the first known natural occurrence of $MnCr_2S_4$. It is present as two 13–15 μm size subhedral inclusions in the Social Circle IVA iron meteorite. The meteorite itself was found as a single ~100 kg mass in Georgia, U.S.A., in 1926 during plowing (Buchwald 1975).

The IVA irons constitute the third largest "magmatic" iron-meteorite group; each magmatic group is modeled as having formed by fractional crystallization in the metallic core of a differentiated asteroid (e.g., Scott et al. 1996). IVA iron meteorites are fine octahedrites showing Widmanstätten patterns (Buchwald 1975). The bulk Ni concentrations range from ~60 to ~120 mg/g. Studies of the metallographic cooling rates in IVA iron meteorites have been controversial for several decades (e.g., Willis and Wasson 1978a, 1978b; Moren and Goldstein 1978). Relative to other magmatic irons, the IVA group has large depletions in S, Ga, and Ge (Wasson and Richardson 2001). The Ir-rich IVA samples are characterized by lower bulk Ir/Au ratios than comparable members of other iron-meteorite groups (Wasson and Richardson 2001).

The Mn-Cr thiospinel, joegoldsteinite, was approved as a new mineral by the International Mineralogical Association (IMA 2015-049) in August 2015. It was named in honor of Joseph (Joe) I. Goldstein (1939–2015), Distinguished Professor emeritus of mechanical and industrial engineering and former dean of the College of Engineering at the University of Massachusetts, Amherst. Before arriving at Amherst, Goldstein was the T.L. Diamond Distinguished Professor of Metallurgy and R.D. Stout Professor of Materials Science and Engineering at Lehigh University; he served as vice president for graduate studies and research and as director of Lehigh's Electron Optical Laboratory. Goldstein was well known for his fundamental contributions to research on iron meteorites, metallographic cooling rates, Fe-Ni phase equilibria, electron microscopy, and microanalysis.

Samples and analytical methods

A polished thick section of Social Circle (TK 724) was made from a 2 × 3 × 5 mm size aliquot from the UCLA meteorite collection. It was examined in reflected light with an Olympus BX60 petrographic microscope and by backscattered electron (BSE) imaging using a VEGA Tescan SEM at UCLA and a Zeiss 1550VP field emission SEM at Caltech. Phases were analyzed by energy-dispersive X-ray spectroscopy (EDX) with the SEM and by a JEOL 8200 electron microprobe (EPMA) (WDS mode, 15 kV, 15 nA, focused beam mode using ZAF corrections) at UCLA. The chemical composition is shown in Table 1. A synthesized $FeCr_2S_4$ single crystal, grown by a chemical transport reaction method similar to that of Tsurkan et al. (2001), was used as a standard for S, Cr, and Fe measurements.

Single-crystal electron backscatter diffraction (EBSD) analyses at a submicrometer scale using methods described in Ma and Rossman (2008, 2009) were performed using an HKL EBSD system on the Zeiss 1550VP SEM at Caltech, operated at 20 kV and 6 nA in focused-beam mode with a 70° tilted stage and

Table 1. Analytical data for type specimen of joegoldsteinite

Constituent	wt%	Range	S.D.
S	44.3	43.6–44.7	0.4
Cr	36.2	35.7–36.5	0.3
Mn	15.8	15.4–16.0	0.2
Fe	4.5	4.2–5.2	0.3
Ni	0.09	0.02–0.13	0.04
Cu	0.08	0.05–0.11	0.02
Co	<0.03	–	–
Total	101.0		

*E-mail: jisa@ucla.edu and chi@gps.caltech.edu

0003-004X/16/0005–1217$05.00/DOI: http://dx.doi.org/10.2138/am-2016-5594

in a variable-pressure mode (20 Pa). The EBSD system was calibrated using a single-crystal silicon standard. The structure was determined and cell constants were obtained by matching the experimental EBSD patterns with structures of synthetic $MnCr_2S_4$ and daubréelite.

Results

Petrography and mineral chemistry

Joegoldsteinite occurs as two subhedral inclusions, 13 and 15 μm in diameter, in Social Circle thick section TK 724 (Fig. 1). Physical properties were not measured because of the small grain size; however, they are likely to be close to those of daubréelite. Optical properties of joegoldsteinite were assessed in reflected light and compared to daubréelite grains that are adjacent to metallic Fe-Ni in the Aliskerovo and NWA 4704 IIIE iron meteorites (e.g., Breen et al. 2015). Both minerals have similar reflectivity and color. More accurate comparisons could be made if a single section were available that contained grains of both phases. Electron microprobe data indicate that the empirical formula (based on 7 atoms) is $(Mn_{0.82}Fe_{0.23})Cr_{1.99}S_{3.95}$; the general formula is $(Mn,Fe)Cr_2S_4$ and the end-member formula is $MnCr_2S_4$. The calculated density, based on the empirical formula, is 3.71 g/cm^3.

Joegoldsteinite is a thiospinel, the Mn analog of daubréelite ($Fe^{2+}Cr_2S_4$), and a new member of the linnaeite group. In joegoldsteinite and daubréelite, Fe and Mn probably have a 2+ valence and occupy the tetrahedral (A) sites. Chromium may have a 3+ valence and occupy the octahedral (B) sites. Because joegoldsteinite is *Fd*3*m* spinel type, we do not think there is S-S bonding in the structure (a requirement if Cr were 2+; McCoy et al. 2014). It thus seems likely that Cr in both daubréelite and joegoldsteinite is located in the octahedral site; Cr^{3+} should thus be thermodynamically stable at a sufficiently high sulfur fugacity. It seems reasonable that enstatite chondrites could contain both Cr^{3+} and Cr^{2+} in different minerals. (Along with nearly pure forsterite and enstatite, some E3 chondrites contain oxidized mafic silicates, i.e., moderately ferroan olivine (Fa11) and low-Ca pyroxene (Fs18) grains (Weisberg and Kimura 2012).

Some tiny grains of joegoldsteinite associated with troilite (FeS) and niningerite [(Mg,Fe)S] were also observed in the Indarch EH4 enstatite chondrite (Fig. 2), but the grains are too small for accurate quantitative analysis by EPMA.

Crystal structure

The EBSD patterns match the cubic space group *Fd*3*m* spinel-type structure (a = 10.11, V = 1033.4 Å^3, Z = 8) and give a best fit using the $MnCr_2S_4$ structure from Raccah et al. (1966) (Fig. 3), with a mean angular deviation of 0.40 to 0.45°. The cell parameters are taken from data for the matching phase in Raccah et al. (1966). X-ray powder diffraction data (Table 2, in angstroms for Cu$K\alpha_1$, Bragg-Brentano geometry) were calculated from the cell parameters of Raccah et al. (1966) with the empirical formula, using Powder Cell version 2.4.

Discussion

Other Mn- and Cr-bearing phases in irons and reduced meteorites

The only known phases with detectable Mn in IVA irons besides joegoldsteinite are daubréelite (~0.2–0.8 wt% Mn) in Maria da Fé (this study) and orthopyroxene (~0.5–0.6 wt% MnO) and clinopyroxene (~0.5 wt% MnO) in Steinbach and São João Nepomuceno (Scott et al. 1996).

Social Circle contains a few Cr-rich phases in addition to joegoldsteinite; these include daubréelite ($FeCr_2S_4$), chromite ($FeCr_2O_4$), and possibly, brezinaite (Cr_3S_4) (Buchwald 1975). Additional Cr-rich

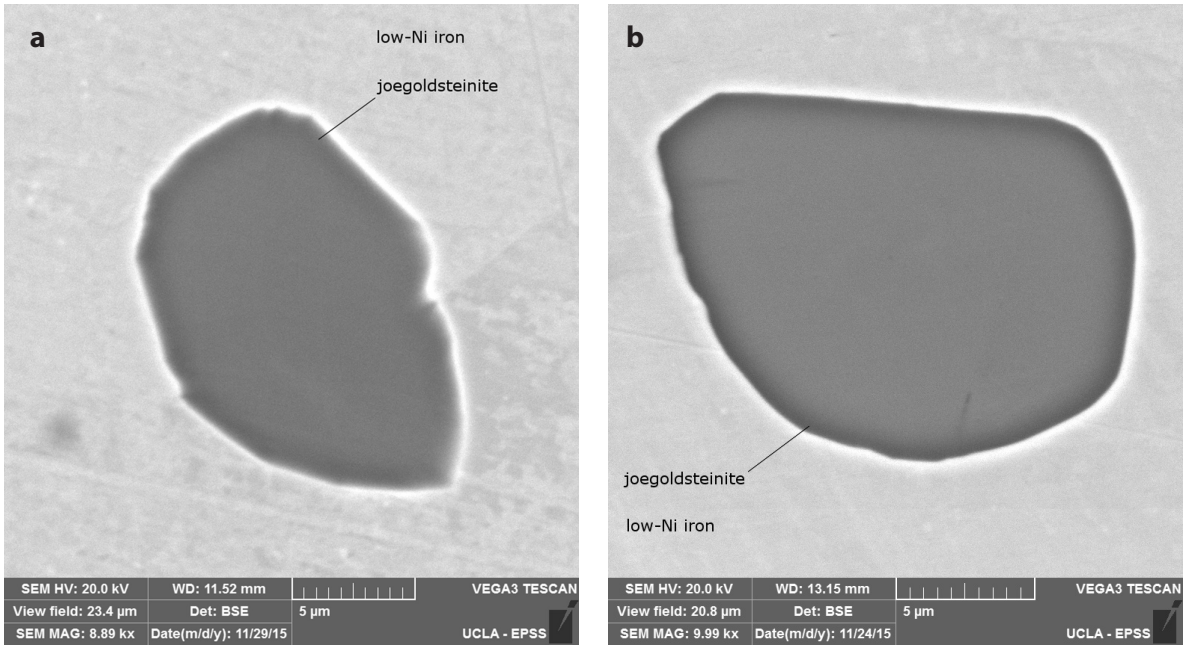

Figure 1. Backscattered electron (BSE) images showing two joegoldsteinite grains in Social Circle thick section UCLA TK 724.

phases reported in magmatic iron meteorites (but not in the IVA group) include carlsbergite (CrN) in several IIIAB samples and kosmochlor ($NaCrSi_2O_6$) in a few IIA samples (Buchwald 1975).

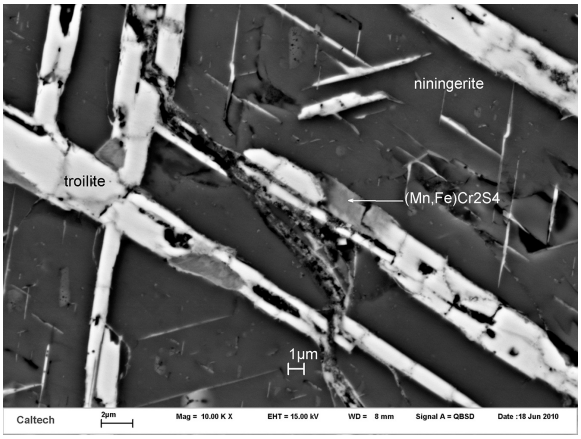

Figure 2. BSE image showing the $(Mn,Fe)Cr_2S_4$ phase in Caltech Indarch section ICM3.

Enstatite chondrites, such as EH4 Indarch (in which small grains of joegoldsteinite were found), formed under low f_{O_2} conditions. These rocks contain mafic silicates (predominantly enstatite, with minor forsterite in unequilibrated samples) with very low FeO, Si-bearing metallic Fe-Ni, and sulfide phases containing cations (e.g., Na, Mg, K, Ca, Ti, Cr, Mn, Fe) that partition mainly into silicates and oxides in more-oxidized assemblages (e.g., Keil 1968; Rubin and Keil 1983; Wasson et al. 1994). For example, sulfide in ordinary chondrites (OC), meteorites that are much more oxidized than enstatite chondrites, is Mn free (e.g., Williams et al. 1985; Rubin et al. 2002); Mn in OC occurs principally in olivine, low-Ca pyroxene, Ca-pyroxene, and chondrule mesostasis (e.g., Brearley and Jones 1998).

Additional Mn-bearing sulfides in enstatite chondrites (and related impact-melt rocks and impact-melt breccias) include daubréelite (with 0.7–4.0 wt% Mn), troilite (FeS: 0.02–0.39 wt% Mn), oldhamite (CaS: 0.18–1.3 wt% Mn), niningerite [(Mg,Fe)S: 6.1–12.9 wt% Mn], keilite [(Fe,Mg)S: 3.4–23.7 wt% Mn], rudashevskyite [(Fe,Zn)S: 1.6–3.6 wt% Mn], buseckite [(Fe,Zn,Mn)S, ~10 wt% Mn], browneite (MnS, ~62 wt% Mn) and pentlandite $[(Fe,Ni)_9S_8$: 0.66–1.1 wt% Mn] (Keil 1968, 2007; Lin et al. 1991; Britvin et al. 2008; Ma et al. 2012a, 2012b).

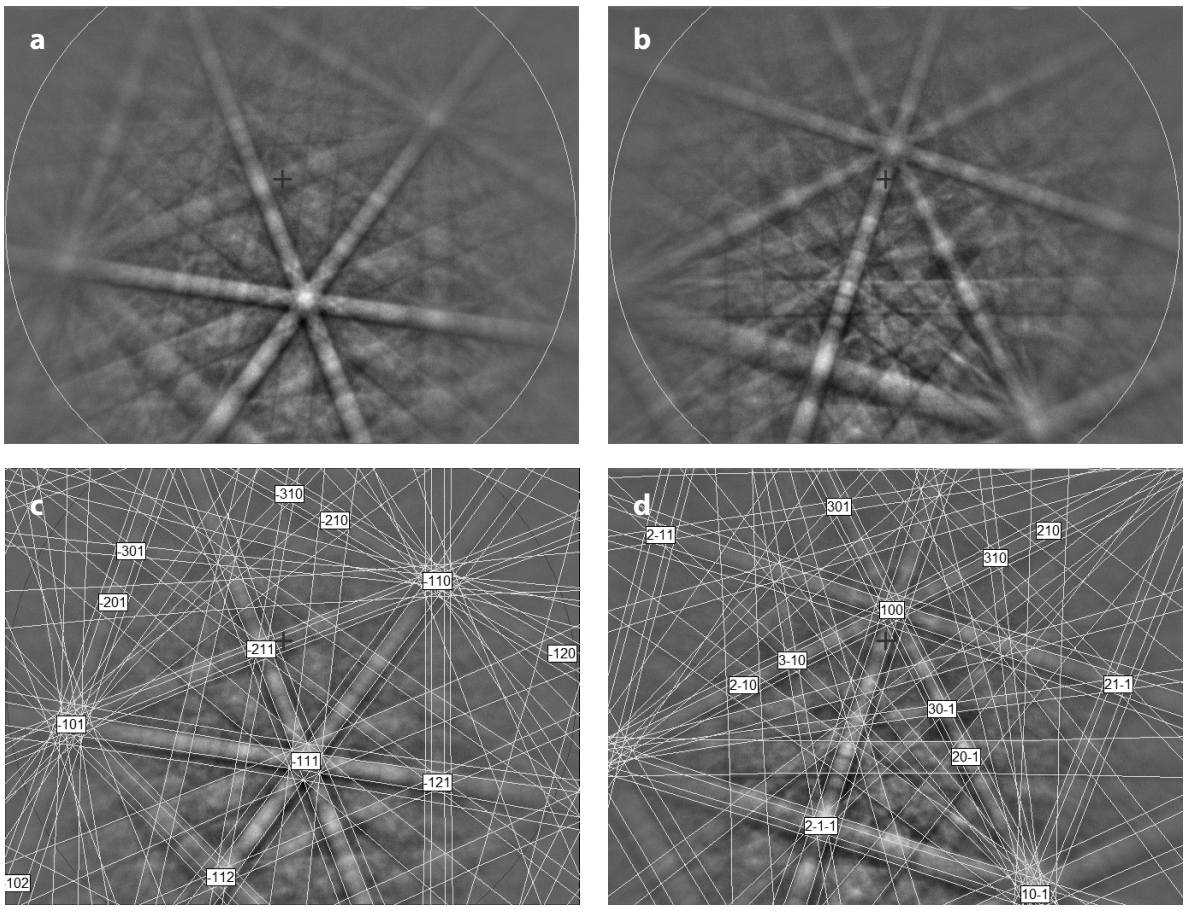

Figure 3. (**a** and **b**) EBSD patterns of the joegoldsteinite crystals in Figure 1, and (**c** and **d**) the patterns indexed with the *Fd*3*m* $MnCr_2S_4$ structure.

Table 2. Calculated X-ray powder diffraction data for joegoldsteinite (I_{rel} > 1)

h	*k*	*l*	*d* (Å)	I_{rel}
1	1	1	5.837	18
2	2	0	3.574	34
3	1	1	3.048	100
2	2	2	2.919	2
4	0	0	2.528	58
4	2	2	2.064	12
3	3	3	1.946	3
5	1	1	1.946	50
4	4	0	1.787	95
5	3	1	1.709	3
6	2	0	1.599	4
5	3	3	1.542	12
4	4	4	1.459	10
5	5	1	1.416	4
6	4	2	1.351	7
5	5	3	1.316	11
7	3	1	1.316	5
8	0	0	1.264	13
7	3	3	1.235	1
8	2	2	1.191	2
6	6	0	1.191	2
7	5	1	1.167	8
5	5	5	1.167	4
8	4	0	1.130	12
9	1	1	1.110	2
9	3	1	1.060	12
8	4	4	1.032	27
7	7	1	1.016	1
10	2	0	0.991	2
8	6	2	0.991	2
9	5	1	0.977	17
9	5	3	0.943	2
10	4	2	0.923	1
11	1	1	0.912	1
7	7	5	0.912	1
8	8	0	0.894	12
11	3	1	0.883	1
9	5	5	0.883	3
8	8	2	0.880	1
8	6	6	0.867	2
9	7	3	0.858	7
12	0	0	0.843	2
8	8	4	0.843	9
7	7	7	0.834	1
12	2	2	0.820	1
10	6	4	0.820	9
9	7	5	0.812	13
11	5	3	0.812	3
12	4	0	0.799	40

Shock effects

The presence of Neumann lines in Social Circle kamacite indicates that the sample was shocked to at least 10 kbar after cooling (Buchwald 1975). A later shock event caused widespread heating of the meteorite: (1) kamacite throughout the mass recrystallized, partially obliterating the Neumann lines (and forming "parallel ghost-lines"), (2) taenite and plessite fields partly decomposed and underwent minor spheroidization, and (3) troilite-metal eutectic shock melts formed (Buchwald 1975). It seems plausible that impact melting of the sulfide assemblages increased the Mn concentration in portions of the S-rich melts, facilitating the crystallization of joegoldsteinite.

After the formation of joegoldsteinite in Social Circle, a minor shock event caused shearing in the grain in the top image of Figure 1. Displacement by ~0.2 μm occurred along a kamacite grain boundary (also probably produced by shearing) running diagonally from SW to NE-ENE.

Implications

It has been shown that $MnCr_2S_4$ can transform from the spinel structure (where two-thirds of the cations are octahedrally coordinated) to the defect NiAs structure (where all cations are octahedrally coordinated) at temperatures of 1000 °C and pressures of 65 kbar (6.5 GPa) (Bouchard 1967). The high-pressure structure is reversible (Vaqueiro et al. 2001). Because of this structural reversibility, empirical observations of thiospinel minerals are unlikely to be useful for constraining the formation temperatures and pressures of asteroidal materials. Nevertheless, chalcospinels, thiospinels, and selenospinels have been used for geophysical studies because their phase transitions are good analogs for those of oxyspinel compounds. These are known to show phase transitions in high-pressure regimes (e.g., 29 GPa for $FeCr_2O_4$, Shu et al. 2007), while thiospinel transitions occur at lower pressure (e.g., 9 GPa for $FeCr_2S_4$, Amiel et al. 2011; and Manjon et al. 2014; Santamaría-Pérez et al. 2012).

It seems probable that additional occurrences of joegoldsteinite in enstatite chondrites and IVA irons could be identified by making Mn X-ray maps of enstatite chondrite thin sections and running EDS scans of sulfide grains in sections of iron meteorites. In enstatite chondrites, joegoldsteinite is most likely to be found in association with other sulfide phases; in IVA irons, it could be found as isolated crystals as in Social Circle or as parts of polymineralic sulfide assemblages.

Acknowledgments

We thank V. Tsurkan for providing a synthesized $FeCr_2S_4$ crystal that greatly facilitated analysis of the new mineral by EPMA. We are grateful to F.T. Kyte and R. Esposito for their patience and for technical support with the electron microprobe. We thank K.D. McKeegan for useful suggestions about finding inclusions in iron meteorites. We also thank J.T. Wasson for comments on the manuscript. Helpful reviews and suggestions were provided by T.J. McCoy, K. Keil, P.R. Buseck, and Associate Editor S.B. Simon. SEM and EBSD analyses were carried out at the Caltech Analytical Facility at the Division of Geological and Planetary Sciences, which is supported, in part, by grant NSF EAR-0318518 and the MRSEC Program of the NSF under DMR-0080065. This work was supported in part by NASA grant NNX14AF39G (A.E. Rubin).

References cited

Amiel, Y., Rozenberg, G.K., Nissim, N., Milner, A., Pasternak, M.P., Hanfland, M., and Taylor, R.D. (2011) Intricate relationship between pressure-induced electronic and structural transformations in $FeCr_2S_4$. Physical Review B, 84(9), 224114.

Bertinshaw, J., Ulrich, C., Günther, A., Schrettle, F., Wohlauer, M., Krohns, S., and Deisenhofer, J. (2014) $FeCr_2S_4$ in magnetic fields: possible evidence for a multiferroic ground state. Scientific Reports, 4, 6079.

Bouchard, R.J. (1967) Spinel to defect NiAs structure transformation. Materials Research Bulletin, 2(4), 459–464.

Brearley, A.J., and Jones, R.H. (1998) Chondritic meteorites. Reviews in Mineralogy, 36, p. 3-1–3-398.

Breen, J.P., Rubin, A.E., and Wasson, J.T. (2015) Shock effects in IIIE iron meteorites: Implications for parent-body history. Meteoritics & Planetary Science, 50, Abstract 5083.

Britvin, S.N., Bogdanova, A.N., Boldyreva, M.M., and Aksenova, G.Y. (2008) Rudashevskyite, the Fe-dominant analogue of sphalerite, a new mineral: Description and crystal structure. American Mineralogist, 93, 902–909.

Buchwald, V.F. (1975) Handbook of iron meteorites, their history, distribution, composition, and structure. Center for Meteorite Studies, Arizona State University.

Darcy, L., Baltzer, P.K., and Lopatin, E. (1968) Magnetic and crystallographic properties of the system $MnCr_2S_4$–$MnInCrS_4$. Journal of Applied Physics, 39(2), 898–899.

Denis, J., Allain, Y., and Plumier, R. (1970) Magnetic behavior of $MnCr_2S_4$ in high magnetic fields. Journal of Applied Physics, 41(3), 1091–1093.

Keil, K. (1968) Mineralogical and chemical relationships among enstatite chondrites. Journal of Geophysical Research, 73(22), 6945–6976.

——— (2007) Occurrence and origin of keilite, $(Fe_{>0.5},Mg_{<0.5})S$, in enstatite chondrite impact-melt rocks and impact-melt breccias. Chemie der Erde, 67, 37–54.

Lin, Y.T., Nagel, H-J., Lundberg, L.L., and El Goresy, A. (1991) MAC88136—The first EL3 chondrite (abstract). Lunar and Planetary Science, 22, 811–812.
Lotgering, F.K. (1968) Spin canting in $MnCr_2S_4$. Journal of Physics and Chemistry of Solids, 29(12), 2193–2197.
Ma, C., and Rossman, G.R. (2008) Barioperovskite, $BaTiO_3$, a new mineral from the Benitoite Mine, California. American Mineralogist, 93, 154–157.
——— (2009) Tistarite, Ti_2O_3, a new refractory mineral from the Allende meteorite. American Mineralogist, 94, 841–844.
Ma, C., Beckett, J.R., and Rossman, G.R. (2012a) Buseckite, (Fe,Zn,Mn)S, a new mineral from the Zakłodzie meteorite. American Mineralogist, 97, 1226–1233.
——— (2012b) Browneite, MnS, a new sphalerite-group mineral from the Zakłodzie meteorite. American Mineralogist, 97, 2056–2059.
Manjon, F.J., Tiginyanu, I., and Ursaki, V. (2014) Pressure-Induced Phase Transitions in AB_2X_4 Chalcogenide Compounds. Springer Series in Materials Science, 189, 243 pp. Springer, Berlin.
McCoy, T.J., McKeown, D.A., Buechele, A.C., Tappero, R., and Gardner-Vandy, K.G. (2014) Do enstatite chondrites record multiple oxidation states? Lunar and Planetary Science, 45, Abstract 1983.
Menyuk, N., Dwight, K., and Wold, A. (1965) Magnetic properties of $MnCr_2S_4$. Journal of Applied Physics, 36(3), 1088–1089.
Moren, A.E., and Goldstein, J.I. (1978) Cooling rate variations of group IVA iron meteorites. Earth and Planetary Science Letters, 40, 151–161.
Plumier, R. (1980) The magnetic structure of sulfur spinel $MnCr_2S_4$ under applied magnetic field. Journal of Physics and Chemistry of Solids, 41(8), 871–873.
Raccah, P.M., Bouchard, R.J., and Wold, A. (1966) Crystallographic study of chromium spinels. Journal of Applied Physics, 37, 1436–1437.
Rubin, A.E., and Keil, K. (1983) Mineralogy and petrology of the Abee enstatite chondrite breccia and its dark inclusions. Earth and Planetary Science Letters, 62, 118–131.
Rubin, A.E., Zolensky, M.E., and Bodnar, R.J. (2002) The halite-bearing Zag and Monahans (1998) meteorite breccias: Shock metamorphism, thermal metamorphism and aqueous alteration on the H-chondrite parent body. Meteoritics and Planetary Science, 37, 125–141.
Santamaría-Pérez, D., Amboage, M., Manjón, F.J., Errandonea, D., Muñoz, A., Rodríguez-Hernández, P., Mújica, A., Radescu, S., Ursaki, V.V., and Tiginyanu, I.M. (2012) Crystal chemistry of $CdIn_2S_4$, $MgIn_2S_4$, and $MnIn_2S_4$ thiospinels under high pressure. Journal of Physical Chemistry C, 116, 14078–14087.
Scott, E.R.D., Haack, H., and McCoy, T.J. (1996) Core crystallization and silicate-metal mixing in the parent body of the IVA iron and stony-iron meteorites. Geochimica et Cosmochimica Acta, 60, 1615–1631.
Shu, J., Mao, L., Hemley, R.J., and Mao, H. (2007) Pressure-induced distortive phase transition in chromite-spinel at 29 GPa. Materials Research Society Symposium Proceedings, 987.
Tsurkan, V., Hemberger, J., Klemm, M., Klimm, S., Loidl, A., Horn, S., and Tidecks, R. (2001) Ac susceptibility studies of ferrimagnetic $FeCr_2S_4$ single crystals. Journal of Applied Physics, 90, 4639–4644.
Tsurkan, V., Mücksch, M., Fritsch, V., Hemberger, J., Klemm, M., Klimm, S., Körner, S., Krug von Nidda, H.-A., Samusi, D., Scheidt, E.-W., and others. (2003) Magnetic, heat capacity, and conductivity studies of ferrimagnetic $MnCr_2S_4$ single crystals. Physical Review B, 68(13), 134434.
Vaqueiro, P., Powell, A.V., Hull, S., and Keen, D.A. (2001) Pressure-induced phase transitions in chromium thiospinels. Physical Review B, 63(6), 064106.
Wasson, J.T., and Richardson, J.W. (2001) Fractionation trends among IVA iron meteorites: contrasts with IIIAB trends. Geochimica et Cosmochimica Acta, 65(6), 951–970.
Wasson, J.T., Kallemeyn, G.W., and Rubin, A.E. (1994) Equilibration temperatures of EL chondrites: A major downward revision in the ferrosilite contents of enstatite. Meteoritics, 29, 658–661.
Weisberg, M.K., and Kimura, M. (2012) The unequilibrated enstatite chondrites. Chemie der Erde, 72, 101–115.
Williams, C.V., Rubin, A.E., Keil, K., and San Miguel, A. (1985) Petrology of the Cangas de Onis and Nulles regolith breccias: Implications for parent body history. Meteoritics, 20, 331–345.
Willis, J., and Wasson, J.T. (1978a) Cooling rates of Group IVA iron meteorites. Earth and Planetary Science Letters, 40, 141–150.
——— (1978b) A core origin for Group IVA iron meteorites: A reply to Moren and Goldstein. Earth and Planetary Science Letters, 40, 162–167.

Manuscript received October 14, 2015
Manuscript accepted January 22, 2016
Manuscript handled by Steve Simon

Chapter 7: Conclusions and Suggestions for Future Study

Summary

From series of meteorite studies and the development of the instrumentation for highly precise and accurate analyses on O-isotope compositions by SIMS, several conclusions can be drawn.

7.1 Conclusions from Chapters 2 and 3: Oxygen Isotope SIMS Matrix Effects

1. SIMS matrix effects on instrumental mass fractionation of oxygen isotopes in olivine, which have compositions that are near the middle of the Fa-Fo solid solution range, can be corrected by using a model curve and a primary standard (e.g. San Carlos olivine as used in this thesis research). Usage of the model curve yields higher precision with an accuracy of ~0.4‰ in δ18O. Because the matrix effects were reproducible between the CAMECA IMS 1270 and 1290 instruments, the correction curve can be generally applied to the O-isotope analyses by the large diameter CAMECA IMS instruments. Moreover, a theoretical model supports the sigmoid correction curve.

2. For SIMS isotopic analyses of samples for which no matching mineral standards exist, one should exercise particular caution due to the potential for large matrix effects especially when very different sputtering rates exist for the samples and standards.

7.2 Conclusions from Chapter 4: Understanding the R Chondrite Parent Body and its Components from a Bulk Chemistry and Petrological Perspective

1. The individual R chondrites have similar bulk compositions despite differences in their petrologic type, the extent of brecciation, and the degree of oxidation/aqueous alteration.

2. At the global scale of the meteorite parent body, refractory elemental abundances in R chondrites and OCs are similar. Bulk refractory and common siderophile abundances in R chondrites are intermediate between those in H and L chondrites. Thus, it is clear that R chondrites are closely related on a compositional basis to these two groups of ordinary chondrites.

3. Differences appear in volatile element abundances. Relative to H chondrites, R-chondrite volatile abundances increase with decreasing 50%-condensation temperatures. Almost all the Zn in R chondrites is present in the matrix, but moderate fractions of R-chondrite Ga, Se, and other volatiles are present in the matrix as well as in non-matrix components.

4. In equilibrated R chondrites, a moderately large range of oxidation states is observed. There may have been differences in the availability of water as well as local differences in temperature and pressure.

7.3 Conclusions from Chapter 5: Oxygen Isotope Studies of a Weakly Metamorphosed R3 Chondrite

1. In R3 chondrites, olivine Fa and $\Delta^{17}O$ are not simply correlated across chondrite components. An oxidant beside oxygen, such as sulfur, could explain the lack of correlation in Fe molar fractions of silicate and $\Delta^{17}O$ values in R chondrite components.

2. O-isotope composition in the least metamorphosed FeO-poor olivine phenocrysts have $\Delta^{17}O$ values ~+3‰ that are similar to R whole-rock $\Delta^{17}O$ values. These high $\Delta^{17}O$ values originated from chondrule precursors, and previous hypotheses cannot explain the diversity of O-isotope composition present in the population of R chondrite chondrules.

3. It is clear that R chondrite chondrule population and OC chondrule population are different. For the R3 type, the thermal histories of individual chondrite components are much more diverse. The $\Delta^{17}O$ values of R chondrite chondrules have a wider range than that of OC chondrules.

4. These significant variations themselves are a reflection of the conditions at the time of formation of the R chondrite parent body. Two scenarios could arise either 1) The R-chondrite parent body was larger than those of the ordinary chondrites, or alternatively, 2) the R chondrite parent body formed later than the ordinary chondrite parent body. Although it is a rough estimate and is also model-dependent, the diverse thermal histories across the chondritic components suggest that the accretion and evolution of chondritic planetesimals lasted at least 10 My.

5. Chondrite components are not always accreted in a simply ordered manner (c.f., chemically and physically sorted ordinary chondrites). Before the final lithification, some chondritic rocks, such as R chondrites, included chaotically mixed collisional debris during their accretionary process.

7.4 Conclusions from Chapter 6: Cr-bearing Sulfides in IVA Iron Meteorites

1. Joegoldsteinite, a new sulfide mineral with the end-member formula $MnCr_2S_4$ that was not known to exist naturally was discovered in the Social Circle IVA iron meteorite.

2. Cr-bearing sulfide phases account for the bulk Cr concentrations in iron meteorites. This knowledge can reconcile the discrepancy between experimentally determined partition coefficients of Cr and bulk chemical Cr concentration observational trends. While finding

Cr-bearing sulfide, chromite inclusions were very rare in IVA iron meteorites. This difference is important because the occurrence of primordial chromite or Cr-bearing sulfide restricts the range of temperatures and of oxygen or sulfur concentrations in the liquid cores of planetesimals during the fractional crystallization.

7.5 Implications and Suggestions for Future Studies

7.5.1 Volatile Components in the Early Solar System:

1. I investigated O-isotope compositions in the outer part of the solar system that was cold and dust-rich environment. However, other volatile components such as H_2, S, N, and C were not very well investigated. Also, the mechanism for the formation of heavy $\delta D = +3700‰$ in hydrated minerals present in R chondrites is still unclear.

2. The origin of water and other volatiles (H_2O, S, C, etc.) on the Earth, as well as other planetary systems, is still unknown. One of the reasons for this is that most of the meteorites have lost their volatile content either during through processes acting on their parent bodies or due to a lack of volatiles during parent body accretion. However, some phases in meteorites still retain geochemical evidence of chemical interactions with volatile species either directly or indirectly. Those phases normally occur as micron scale secondary minerals or as fine-grained or amorphous material found in fine grain matrix. Therefore, SIMS is perhaps a suitable measurement technique to study this subject. The O-isotope matrix effect correction curve, empirically developed and outlined in this thesis, could be helpful to analyze such secondary minerals. Also, R chondrites are certainly relevant in the context of such studies. The abundance of light elements O and S (not

necessarily present in volatile compounds) in metallic cores is also not well constrained. The understanding the properties of the metallic cores of planetary embryos is an important research topic because these are also building blocks of the differentiated cores of large planetary bodies cores and could potentially contain non-Fe-Ni components.

7.5.2 Mass-dependent O-Isotope Measurements with SIMS:

Determination of accurate and precise mass-dependent oxygen isotope fractionations in olivine will potentially provide new ways to investigate metamorphic processes on planets or primitive asteroids, and to understand the chemical interactions that were active in the solar nebula at microscopic scale lengths. For example, investigating micro-scale fluid-mineral interactions with oxygen isotopes may constrain volatile element behaviors and fluid-rock systems on asteroids that were previously investigated by petrologists (e.g., Warren et al., 2014). *In situ* determination of accurate equilibrium temperatures or isotope exchanges of small secondary minerals may help us understand metamorphism on undifferentiated or primitive achondrite parent bodies that were previously investigated with UV-laser fluorination techniques (Dyl et al., 2012). Also, models of evaporation and condensation of silicate melts or of solid and ambient gas interaction in the solar nebula at micro-scales could be investigated.

7.5.3 Chondrite Parent Bodies and Asteroids:

1. The occurrence of parent body weathering products provides direct evidence of fluid water and its compositions should indirectly reflect water compositions on asteroids. The origins of weathering on the R chondrites are still unclear. If the weathering also occurred

on the Earth, O-isotope compositions of the weathering products should follow the trend of the TFL. Further investigation is needed to reveal the origin of R chondrite weathering.

2. R chondrites contain amino-like material; other carbonaceous chondrite groups also contain such matter. Besides amino acid study, investigation of other organic compounds found in R chondrites has not yet been attempted. The sulfur-rich compositions of R chondrites may provide local sulfuric acid solutions. These acidic solutions are likely relevant in the weathering of chondrites (VELBEL 2014) and they could dissolve transition metals such as Fe, Ni, and others. These sulfuric acids could have played a role in altering materials on the meteorite parent bodies. Also, sulfuric acids when accompanied by heat are known to work as an electrophile to aromatic hydrocarbon leading to the formation of sulfonic acid. Sulfuric acid could also dehydrate and form some reactive alkene compounds. Note that a lack of heat means that the same chemical reactions were relatively unimportant for most carbonaceous chondrites.

7.5.4 Iron Meteorites:

1. The presence of Cr-bearing sulfides and oxides found in our samples are important potential indicators of enigmatic bulk Cr behaviors during metallic core formations. Since bulk Cr is controlled by these phases, Cr-isotopes in iron meteorites reflect these non-metallic compositions. So what is the origin of these refractory inclusions? If these were of magmatic origin (products of fractional crystallization) these inclusions would be useful analytes to constrain the form of magmatic processes in iron meteorite parent bodies. If instead the refractory inclusions are somehow inherited from chondritic

components, classifications based on bulk Cr isotopic composition are not necessarily reasonable.

2. The crystallization sequence of metallic cores is still not well known. If we could understand the crystallization history for magmatic non-metallic inclusions that could incorporate non-metallic components such as oxygen or sulfur. In addition to planetary processes, those non-metallic inclusions can be used in geochronological studies. I hope to expand on investigations of volatile elements in iron meteorites in the near future by building on the implications of the petrological and bulk chemical compositional studies performed in support of my doctoral research project.